# Etude par télédétection de la précipitation aurorale de protons

*Morphologie, saisonnalité et influence sur l'ionosphère.*


Dissertation présentée
par Valérie COUMANS
en vue de l'obtention
du grade de docteur
en sciences

Université de Liège
Faculté des Sciences

2007

# Avant-Propos

Le travail décrit dans ces pages sous forme de thèse de doctorat représente les recherches que j'ai menées au **L**aboratoire de **P**hysique **A**tmosphérique et **P**lanétaire (LPAP) de L'Université de Liège lors de ces six dernières années. Ce travail s'est déroulé dans le cadre de la mission spatiale IMAGE (**I**mager for **M**agnetopause-to-**A**urora **G**lobal **E**xploration) mise en œuvre par la NASA et porte sur l'utilisation des données acquises par l'instrument FUV (**F**ar **U**ltra **V**iolet). Cet instrument permet l'observation du phénomène auroral à l'échelle de la calotte polaire dans trois bandes spectrales de l'ultraviolet lointain. Les trois caméras qui composent FUV (WIC, SI12 et SI13) ont été assemblées à l'Université de Californie à Berkeley et au **C**entre **S**patial de **L**iège (CSL). C'est dans le contexte de cette collaboration que la thèse a été réalisée. Les données IMAGE-FUV ont été complétées par des mesures provenant d'autres satellites (NOAA, FAST, DMSP, ACE, WIND, GEOTAIL, ARGOS).

L'outil informatique principalement utilisé pour ce travail est le logiciel IDL (**I**nteractive **D**ata **L**anguage) qui a permis le traitement des données brutes et le développement des programmes de modélisation.

# Remerciements

Je tiens à témoigner toute ma reconnaissance au professeur Jean-Claude Gérard, sans qui ce travail ne pourrait être. Il a su, tout au long de ces années, éveiller ma curiosité scientifique et guider mes travaux. Sa disponibilité et son enthousiasme pour la recherche ont permis l'aboutissement de mes travaux.

Je remercie également tous les membres du LPAP qui ne m'ont jamais refusé un conseil ou une aide. Merci à Benoît Hubert, Matthieu Meurant, Caroline Blockx, Denis Grodent, Bertrand Bonfond pour leur apport. Merci à Dimitri Bisikalo et Valera Shematovich pour leur aide concernant les travaux relatifs aux modèles de transport des particules aurorales. Je profite de ces quelques lignes pour remercier Jean-André Sauvaud, Viviane Pierrard, Arlette Noels, Henri-Pierre Garnir, Jean-Claude Gérard et Denis Grodent pour avoir accepté d'être membre de mon jury.

Je remercie aussi toutes les personnes qui m'ont témoigné leur amitié pendant toutes ces années et qui m'ont soutenue pendant mes moments de doutes. Un merci particulier à Hélène, Aline, Evelyne, Caro, Angela, Matthieu.

Enfin, je remercie du plus profond de mon coeur ma famille qui a rendu possible la réalisation de ce travail. Sans leur aide quotidienne, ces écrits n'existeraient pas. Une tendre pensée à Hugo et Noé qui illuminent chacune de mes journées de leur sourire. Un remerciement spécial à Oli sans qui la vie n'aurait pas la même saveur.

*A Hugo, Noé et leurs arrière-grands-pères*

# Table des matières

# Résumé

Les recherches décrites dans ces pages portent sur l'étude de l'aurore à protons par télédétection spatiale en ultraviolet lointain. Ce travail s'inscrit dans le cadre de la mission IMAGE, dont l'instrument FUV offre la possibilité d'observer les émissions aurorales dues à la précipitation d'électrons et de protons. L'imageur spectral SI12, construit au Centre Spatial de Liège, donne une image de la raie Lyman-$\alpha$ déplacée par effet Doppler produite par la désexcitation de l'hydrogène. Il permet l'observation globale de l'ovale auroral avec une résolution temporelle de 2 minutes. Les données couplées à un modèle de transport et de dégration d'énergie des particules qui précipitent ont été utilisées pour étudier l'aurore à protons tant d'un point de vue morphologique que d'un point de vue quantitatif.

La première étape du travail consistait à valider les observations et à calibrer la méthode développée pour obtenir les flux énergétiques des particules accélérées vers l'atmosphère à partir des taux de comptage SI12. Des comparaisons des observations SI12 et des mesures *in situ* de particules des satellites NOAA ont montré un désaccord de 50%, qui a été pris en considération dans la suite du travail.

J'ai ensuite entrepris une étude statistique des caractéristiques morphologiques de l'ovale protonique. Cette statistique présente un très bon accord avec les études précédentes, bien que celles-ci soient basées sur des mesures locales de la précipitation de protons. Les résultats quantitatifs quant à l'intensité de la précipitation des protons ont montré une variation saisonnière, avec un maximum dans l'hémisphère estival. J'ai également mis en évidence l'influence de l'orientation de la composante nord/sud du champ magnétique interplanétaire et de la pression dynamique du vent solaire sur la précipitation de protons tant au point de vue de l'énergie accumulée durant la phase de croissance, que des processus de déclenchement de leur précipitation et des processus de précipitation eux-mêmes. L'analyse de la dynamique de l'ovale auroral protonique durant les phases de croissance des sous-tempêtes magnétiques a montré que le mouvement vers l'équateur des frontières de l'ovale pouvait être local, global ou une superposition des deux. Ce résultat est interprété comme la combinaison d'un étirement global de la magnétosphère dû à l'influence du vent solaire et d'un étirement local trouvant son origine dans le feuillet de plasma interne à la magnétosphère.

Dans la dernière étape du travail, j'ai analysé les conséquences de la précipitation au-

rorale sur l'ionosphère. J'ai montré que les conductivités de Hall et de Pedersen et leur évolution temporelle pouvaient être déduites de la contribution des trois imageurs ultraviolets à une échelle spatiale globale. Le résultat principal de cette partie montre que la contribution des protons à la puissance et aux conductances aurorales ne peut localement pas être négligée par rapport à celle des électrons.

# Summary

The research work described hereafter concerns the study of proton aurorae using far ultraviolet remote sensing techniques from space. This work fits into the IMAGE satellite mission. It largely involves the FUV imagers which observe auroral emissions induced by electron and proton precipitation. The SI12 spectral imager, designed at the 'Centre Spatial de Liège', is sensitive to the Doppler shifted Lyman-$\alpha$ emission produced by auroral protons. The FUV imagers allow one to observe the auroral oval on a global scale with a temporal resolution of 2 minutes. The observations were used to constrain a transport and energy degradation model of precipitating particles. This made it possible to study the proton aurora in both a morphological and a quantitative way.

The first step of the study consisted in validating the observations, as well as calibrating the method providing the energy fluxes of the accelerated particles from the SI12 counts. Comparisons between SI12 results and in situ particles measurements by NOAA satellites lead to a difference of 50%, which has been taken into account in the next steps of the study.

Afterward, I made a statistical study of the morphological characteristics of the proton auroral oval. The results were compatible with previous studies, although the latter were based on local measurements of the proton precipitation. The observed proton precipitation intensities revealed a seasonal variation, with a maximum in the summer hemisphere. I also showed the importance of the North/South component of the interplanetary magnetic field, and of the solar wind dynamic pressure on proton precipitation. These factors affect the accumulation of energy during the growth phase, the precipitation triggering processes, and the precipitation itself. The analysis of proton auroral oval during substorm growth phases suggested that the equatorward motion of the oval boundaries could be local, global, or a combination of both. These results were interprated as the consequence of a solar wind-driven global stretching of the magnetosphere, together with a local stretching resulting from internal changes occuring in the magnetosphere plasmasheet.

In the final part of my work, I analysed the consequences of the auroral precipitation on the ionosphere. I demonstrated that Hall and Pedersen conductivities and their temporal evolution could be deduced from the three imagers of the IMAGE mission on a global spatial scale. The main result of this part is that the protons contribution to the auroral power and conductances is locally not negligible compared to the electron one.

# Introduction

# Préambule

Les aurores [1] boréales : ces lumières qui "dansent" dans le ciel nocturne polaire, ont toujours fasciné les hommes. Les croyances ancestrales de tous les peuples du Nord relatent différentes interprétations. Les Inuits du Groenland et du nord du Canada pensaient que les aurores étaient la trace d'un crâne de morse avec lequel les esprits jouaient au football. En Suède, selon les régions, les gens croyaient que ces lumières étaient des cygnes en vol vers le nord dont les ailes gelaient, ou qu'elles étaient émises par un pont de feu jeté à travers le ciel par lequel les dieux pouvaient passer de la voûte céleste à la Terre [*Sandahl*, 1995]. Au Moyen Âge en Europe, les aurores étaient vues comme le reflet des guerriers célestes, une sorte de récompense posthume. Les guerriers qui donnaient leur vie pour leur pays et leur roi devaient mener la bataille dans le ciel pour toujours. Les aurores étaient le souffle de ces braves guerriers qui racontaient leurs combats dans le ciel. Il y a plus de 100 ans, les prévisions météorologiques étaient parfois basées sur la présence des aurores. Cependant, ces prévisions étaient souvent contradictoires. Au Labrador, les aurores étaient un présage de beau temps, tandis qu'au Groenland elles étaient un signe de vents du sud et de tempêtes. Au début du siècle passé, certains pensaient encore que les aurores étaient produites par la réflexion de la lumière solaire sur les glaces de l'Arctique.

Aujourd'hui, sans en altérer la beauté, nous savons que cet étrange phénomène est le reflet de toute une série de processus physiques impliquant le Soleil, l'environnement magnétique terreste ainsi que l'atmosphère terrestre. Nous commençons par définir quelques notions utiles dans le cadre de ce travail et par expliciter leur rôle dans le phénomène d'*aurora borealis*. Partant du Soleil et nous rapprochant de la Terre, nous définissons, entre autres, les notions de vent solaire, magnétosphère, accélération de particules aurorales et émissions aurorales qui sont cruciales dans la formation du phénomène. De plus, certaines notions telles que la précipitation non-adiabatique de particules aurorales ou les conductivités ionosphériques sont décrites de façon assez explicite car elles sont indispensables pour expliquer les résultats de nos recherches.

[1] Le mot "aurore" provient de la mythologie romaine. "Aurore" était le nom que les Romains donnaient à la déesse de l'aube. En fait, aurore signifie "lumière qui précède le lever du Soleil".

# Du Soleil à la Terre

## Le Soleil et son atmosphère

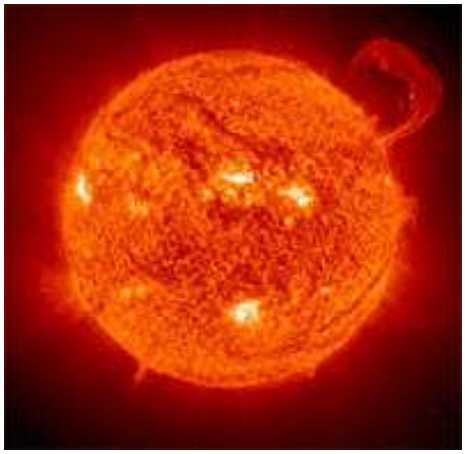

Figure 1: La photosphère du Soleil vu par SOHO

Le Soleil est une étoile parmi d'autres, de taille et de luminosité intermédiaire. Toutefois, elle est particulière pour nous car elle est l'étoile de notre système solaire et que son influence sur notre Terre est permanente. Le Soleil nous éclaire, nous réchauffe. Il est également la cause de beaucoup de processus sur Terre et influence l'environnement. C'est grâce au Soleil que la vie s'est développée sur Terre et c'est également grâce au Soleil que nous pouvons observer des aurores dans le ciel sous les latitudes polaires.

Le Soleil est situé à 1 UA (unité astronomique) de la Terre, ce qui correspond à environ 150 000 000 km. Son rayon est d'environ 696 000 km et il tourne avec une période qui varie en fonction de la latitude. La période de rotation vaut 25 jours à l'équateur et 36 aux pôles. La masse du Soleil est d'environ $2 \times 10^{30}$ kg et est principalement constituée d'hydrogène et d'hélium.

### Structure du Soleil

Le Soleil est constitué de plusieurs couches, comme le schématise la Figure 2. Faisons un petit voyage en partant du centre: nous rencontrons successivement le noyau, la zone radiative, la zone convective, la photosphère et l'atmosphère solaire composée de la chromosphère et de la courone. Le **noyau** est la région la plus chaude de la partie intérieure du Soleil. Sa température s'élève à environ 15 millions de degrés Celsius. L'énergie produite dans le noyau par la fusion nucléaire s'évacue par rayonnement au travers de la **zone de**

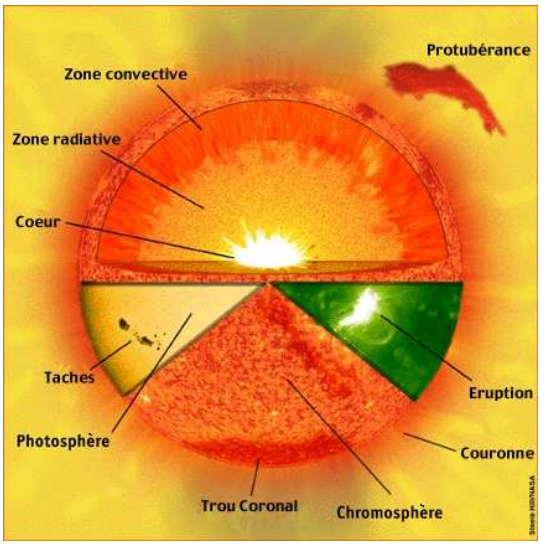


Figure 2: Structure du Soleil

**radiation** jusqu'à environ 7 dixièmes du rayon solaire. Au delà de cette zone, le processus radiatif n'est plus efficace car la température est trop basse ($5\times10^5$°C), l'énergie s'échappe alors vers la surface du Soleil par le processus de convection, via la **zone de convection**. Notons qu'il faut environ $10^6$ ans aux photons produits par les réactions nucléaires pour atteindre la limite supérieure de la zone radiative, alors qu'il leur faut environ 2 mois pour traverser la zone convective. Le sommet de la zone convective forme la **photosphère**, qui est la surface visible du Soleil. Sa température est d'environ 6500°C et est épaisse d'environ 200 km seulement.

Au-dessus de la photosphère se situe l'atmosphère solaire composée de deux couches transparentes : la chromosphère et la couronne. La **chromosphère** est virtuellement invisible à cause de l'importance de la brillance de la photosphère, mais elle peut être observée durant les éclipses solaires. Elle s'étend sur environ 10 000 km au-dessus de la photosphère et sa température atteint 10 000°C. La couche supérieure de l'atmosphère solaire est la **couronne**. Elle s'étend sur une distance de plusieurs rayons solaires, comme on peut également le voir à l'occasion d'une éclipse totale de Soleil, ou plus simplement grâce à un coronographe. La température augmente drastiquement avec l'altitude dans la couronne, atteignant plus de $10^6$°C. Elle est constituée de grands jets de gaz chauds, formant une structure radiale suivant la localisation des régions actives. C'est un milieu en perpétuelle évolution, qui répercute les variations du champ magnétique de la photosphère. C'est dans la couronne qu'est généré le vent solaire. D'autres structures caractéristiques de la couronne sont les trous coronaux.

Les **trous coronaux**, sortes de cavités obscures, sont présents en permanence autour des deux pôles du Soleil tandis que d'autres se dispersent sur le disque et descendent même jusqu'à l'équateur lors des périodes de forte activité solaire. Ces régions moins brillantes sont en fait légèrement plus froides et présentent une plus faible densité que la couronne moyenne et sont donc moins émissives que le reste de la surface avec un champ magnétique moyen de 10 gauss. Les trous coronaux ont un champ magnétique dit "ouvert" et tournent autour du Soleil tel un corps solide, conforme en cela à leur origine magnétique. Ces trous coronaux disparaissent au bout de quelques semaines. Ne pouvant soutenir la pression coronale, cette perte d'énergie doit être équilibrée par une autre force : les trous coronaux offrent en effet la particularité de générer le 'vent solaire' (nous en reparlerons plus loin), dans lequel on retrouve l'énergie cinétique manquante.

### Le champ magnétique du Soleil et son activité

Les quelques phénomènes décrits ci-dessus ont un point commun : le champ magnétique du Soleil et ses caprices. Le champ magnétique du Soleil a une structure extrêmement compliquée. Il est créé et entretenu par un mécanisme de "dynamo" impliquant les déplacements de matière chargée électriquement dans les régions internes de l'enveloppe. Il prendrait naissance dans l'interface, appelée la **tachocline**, qui sépare la zone radiative de la zone convective. Le Soleil est composé de plasma, dont la rotation est variable en fonction de la latitude. Or, dans un tel fluide la forme du champ magnétique est intimement liée aux mouvements de matière (en fait il s'y trouve "gelé"). Il s'ensuit que la rotation différentielle du Soleil va créer un enroulement particulier et des tensions, des contraintes diverses dans l'intensité du champ magnétique. Les lignes de champ se brisent et se renouent alors de manière compliquée suite à la variation de la vitesse des fluides dans la zone de la tachocline. La morphologie complexe qui en résulte est exprimée notamment par l'apparition de taches sombres: les taches solaires, qui marquent la position des points de resserrement des lignes de champ. Ces différentes étapes sont représentées à la Figure 3. La plupart des variations du champ magnétique solaire ne s'étendent pas loin de la surface et le champ magnétique de la couronne extérieure est souvent décrite comme un dipôle ou un quadrupôle.

Cependant, cette description est incomplète car des variations sont tout de même visibles dans le champ magnétique "général" du Soleil. Une variabilité cyclique du champ magnétique solaire peut-être remarquée entre autres sur la fréquence et la position d'apparition des tâches solaires et est le reflet de l'activité du Soleil. La destruction et la re-création de la structure dipolaire du champ magnétique interne a lieu sur une période 11 ans. En fait, on peut expliquer ce cycle de la façon simplifiée suivante : la morphologie complexe du champ magnétique due à la rotation différentielle persiste jusqu'à ce que la situation devienne totalement instable. Le champ magnétique se relaxe alors brusquement et redevient bipolaire. Cette simplification se traduit par une chute abrupte du nombre de taches. Elle est également accompagnée d'une inversion de la polarité globale du Soleil : ce qui

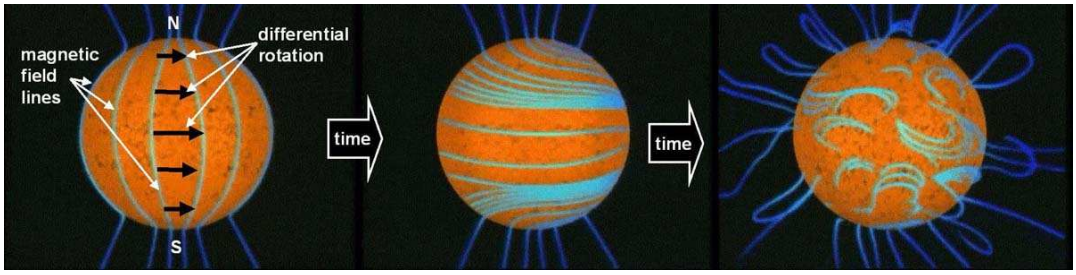


Figure 3: Mécanisme de mise en place du champ magnétique solaire.

était le pôle nord magnétique lors de la phase qui vient de s'achever devient pour les 11 prochaines années le pôle sud, et vice-versa. Après ce second cycle de taches, la situation sera entièrement rétablie, si bien que le cycle magnétique réel du Soleil n'est pas de 11 ans, comme c'est le cas pour le cycle des taches, mais plutôt de 22 ans. Tous les cycles solaires ne sont pas d'intensité égale. Notons que le dernier maximum d'activité solaire a eu lieu en été 2000, et que ce maximum s'est étendu sur une durée anormalement longue, puisqu'en 2003, des phénomènes typiques d'un maximum d'activité ont encore eu lieu.

### Le Soleil : un astre en expansion

Au début du 20$^{e}$ siècle déjà, l'idée que le soleil émettait de la matière avait été proposée. En 1892, *Fitzgerald* [1892] suggère qu'une tache solaire est une source qui projette des émanations du Soleil semblables à la queue des comètes. Quelques années plus tard, suivant les hypothèses de Fitzgerald, *Lodge* [1900] suggère que les tempêtes magnétiques sont causées par un flot ou un nuage d'atomes chargés ou d'ions venant du Soleil. *Chapman and Ferraro* [1930] proposent que le Soleil émet un plasma neutre associé aux protubérances éruptives et qui a pour conséquences de confiner le champ magnétique terrestre.

Jusqu'en 1958, les modèles théoriques développés pour décrire la couronne solaire supposaient généralement que le plasma coronal était en équilibre hydrostatique dans le champ gravifique du Soleil. Le modèle développé par Sidney Chapman s'exprime par l'équation d'équilibre hydrostatique (exprimant que la différence de pression entre deux niveaux est donnée par le poids de la colonne d'air située entre les deux niveaux) :

$$\frac{dp}{dr} = -\rho g = -n\overline{m}g \tag{1}$$

où $\rho$ est la masse moyenne et g l'accélération gravifique. Cette équation est en fait identique à celle d'une atmosphère neutre, à condition de considérer le plasma dans son ensemble (y compris électrons et ions). Comme la température n'est pas constante dans la couronne, Chapman a cherché à déterminer une loi théorique représentant ces variations dans la couronne. Pour ce faire, il a supposé que la chaleur était transportée vers l'extérieur

uniquement par conduction thermique. Il a montré que la distribution de température pouvait alors s'écrire :

$$T = T_0(\frac{r_0}{r})^{2/7} \tag{2}$$

A partir des équations d'équilibre hydrostatique (Equation 1) et de la distribution de température (Equation 2), S. Chapman a obtenu une distribution de la densité de plasma dans la couronne qui possède un minimum à 123 rayons solaires. Au delà de cette distance, la densité augmente indéfiniment avec l'éloignement au Soleil, ce qui physiquement est irréaliste et constitue une situation dynamiquement instable. En effet, on ne peut maintenir en équilibre hydrostatique des couches de densité supérieure au-dessus de couches de densité inférieure. De plus, la distribution de température dans ce modèle conductif devient convectivement instable pour une distance héliocentrique de 34 rayons solaires. Au-delà de cette limite, le gradient de température dans le couronne devient superadiabatique ($\frac{dT}{dr} > (\frac{dT}{dr})_{ad}$). Ceci pourrait être interprété par formation d'une couche convectivement instable, tout en gardant en moyenne l'équilibre hydrostatique. Mais on peut montrer que même le transport par convection turbulente ne permet pas d'évacuer toute l'énergie déposée à la base de la couronne. Pour évacuer plus efficacement cette énergie, une autre explication a été proposée: l'expansion radiale de la couronne solaire dans son ensemble.

Eugene Parker fut le premier, en 1958, à abandonner l'hypothèse d'équilibre hydrostatique et à proposer le premier modèle hydrodynamique d'expansion radiale de la couronne solaire. C'est aussi lui qui introduisit le terme "vent solaire". On peut comparer cette expansion à une explosion continue et stationnaire de la couronne donnant lieu, à grande distance, aux vitesses supersoniques du vent solaire. A partir des équations hydrodynamiques stationnaires de conservation de la masse, du moment et de l'énergie et supposant une couronne isotherme, Parker propose l'équation donnant la vitesse radiale :

$$\frac{d\ln u(s)}{dr}(u^2 - c_0^2) = -\frac{g_0 r_0^2}{r^2} + \frac{2c_0^2}{r} \tag{3}$$

où $u$ est la vitesse d'expansion radiale et $c_0$ une vitesse thermique proportionnelle à la vitesse du son ($v_{son} = \gamma^{1/2} c_0$). Plusieurs solutions sont possibles pour cette équation : un cas infrasonique ($u < c_0$), un cas supersonique ($u > c_0$) et une solution critique ($u = c_0$). Seule la solution critique conduit à une densité et une pression nulles à l'infini. C'est cette solution que Parker proposa pour décrire l'expansion de la couronne solaire. Cette solution donne donc une distribution de densité qui ne possède pas de minimum à une distance finie comme le modèle de Chapman. De plus, comme illustré à la Figure 4, il conduit à une vitesse d'expansion constante située entre 400 et 500 km/s à grande distance du Soleil [2].

Cependant, le modèle de Parker n'est pas entièrement satisfaisant, à cause des hy-

[2]Ce qui aura été confirmé par la sonde MARINER II, qui mesura peu de temps après le travail de Parker, des vitesses du vent solaire entre 300 et 600 km/s

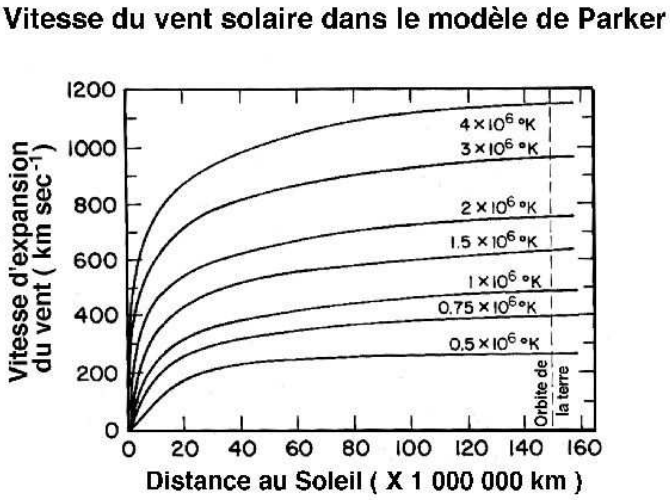


Figure 4: Vitesse du vent solaire selon le modèle de Parker.

pothèses d'isothermie et d'une fréquence de collision élevée [3]. Il faut donc avoir recours à la théorie cinétique basée sur l'équation de Boltzmann pour pouvoir représenter théoriquement l'expansion solaire.

Plusieurs modèles cinétiques ont été proposés : Chamberlain (1960) fut le premier à proposer son modèle de "brise solaire", mais dans ce modèle, les ions s'échappant de la couronne solaire ne sont pas suffisamment accélérés vers l'extérieur et n'atteignent jamais une vitesse moyenne supérieure à celle du son. En 1971, le modèle de Lemaire-Scherer imposant l'égalité du flux d'échappement des électrons et des ions, ainsi que la quasi neutralité du plasma, permet d'obtenir des valeurs supersoniques de la vitesse d'expansion.

### Le vent solaire

Comme expliqué précédemment, la couronne n'a pas de frontière précise et se fond dans le milieu interplanétaire. L'expansion de la couronne se manifeste par un flot de matière ionisée qui baigne tout le système planétaire : le **vent solaire**, nom donné par Parker. Son existence a été vérifiée dès le début des années 1960 par des sondes spatiales russes et américaines, et ses caractéristiques sont mesurées depuis une trentaine d'années. Au niveau de l'orbite terrestre, sa vitesse moyenne est de l'ordre de 400 km $s^{-1}$, mais il existe en fait deux régimes de vent : le vent rapide ($>$ 700 km $s^{-1}$) peu dense et le vent lent (300

[3] approximation de Navier Stokes: le libre parcours moyen des particules est inférieur à la hauteur d'échelle

km $s^{-1}$) et dense. Le vent solaire est constitué essentiellement de protons, d'électrons et de noyaux d'Hélium avec des traces infimes d'ions d'éléments plus lourds, tels que l'oxygène ou le carbone. Il s'échappe continuellement et dans toutes les directions de la surface du Soleil et baigne l'ensemble du système solaire. La densité du vent solaire diminue régulièrement, selon l'inverse du carré de la distance au Soleil. D'environ $10^{12}$ particules/$cm^3$ au niveau de la couronne, elle décroît jusqu'à 10 particules/$cm^3$ au niveau de l'orbite terrestre et de moins d'une particule/$cm^3$ à la distance de Jupiter. Le tableau 1 reprend quelques caractéristiques du vent solaire au niveau de l'orbite terrestre.

| **Paramètres** | **Minimum** | **Moyenne** | **Maximum** |
|---|---|---|---|
| Flux ($cm^{-2}$ $s^{-1}$) | 1 | 3 | 100 |
| Vitesse (km/s) | 200 | 400 | 900 |
| Densité ($cm^{-3}$) | 0.4 | 6.5 | 100 |
| Helium (%) | 0 | 5 | 25 |
| B (nT) | 0.2 | 6 | 80 |

Table 1: Caractéristiques du vent solaire au niveau de la terre

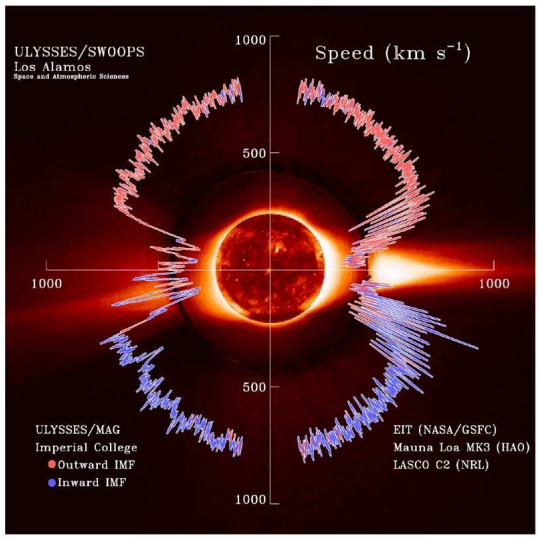


Figure 5: Vitesse du vent solaire et polarité magnétique mesurées par Ulysses, en fonction de la latitude solaire, superposées à trois images concentriques prises avec les instruments NASA/GSFC EIT (centre), le coronagraphe HAO Mauna Loa (anneau intérieur) et le coronographe NRL LASCO C2 (anneau extérieur).

Comme indiqué précédemment, le vent solaire n'est pas uniforme. Sa vitesse et sa com-

position varient. La vitesse du vent solaire est élevée (elle atteint 900 km/s) au niveau des trous coronaux, et plus faible à l'équateur. La Figure 5 présente les mesures de vitesse de vent solaire effectuées par *Ulysses* en fonction de la latitude heliographique. Ce graphique montre que le vent solaire rapide, proche des pôles, est calme et que la transition avec le vent lent est quasi discontinue, ayant lieu, dans ce cas, aux latitudes d'environ +/- 15°. Les vents solaires rapide et lent interagissent l'un avec l'autre et passent alternativement au niveau de la Terre au fur et mesure de la rotation du Soleil.

### Le champ magnétique interplanétaire

Le vent solaire emporte avec lui une infime partie du champ magnétique solaire. Ceci est à l'origine de l'existence du champ magnétique interplanétaire (IMF). Le vent solaire s'échappe radialement du Soleil, mais à cause de la rotation du Soleil sur lui-même (en 27 jours), un jet de plasma ancré en un point donné paraîtra s'enrouler en une spirale analogue à celle d'un jet d'eau sortant d'un tourniquet en rotation. Les lignes de champ magnétique gelées dans le plasma sont emportées par le jet et adoptent la même structure spirale (dite Spirale de Parker). En fait, le plasma ionisé du vent solaire est un conducteur électrique parfait. Une conséquence est que le champ magnétique y subsiste de façon permanente, c'est pourquoi on dit qu'il est gelé dans le plasma. Au niveau de l'orbite terrestre, le champ magnétique interplanétaire fait un angle d'environ 45° avec la direction Soleil-Terre. La Figure 6 schématise la formation de cette spirale de Parker et en donne une représente globale graphique.

Le champ magnétique interplanétaire est originaire de régions du Soleil où le champ magnétique est dit "ouvert". La direction du champ dans l'hémisphère nord étant opposée à celle du champ dans l'hémisphère sud solaire, le long du plan de l'équateur magnétique solaire, les lignes de champ de polarités différentes sont parallèles et sont séparées par une fine couche de courant neutre, appellée "**couche de courant héliosphérique**" ou "couche de courant interplanétaire", comme le montre la Figure 7. Cette couche de courant prend une forme particulière dite en "robe de ballerine" : la couche de courant est inclinée (à cause du décalage entre l'axe du dipôle magnétique du Soleil et son axe de rotation [4]) et déformée (à cause du moment quadrupolaire du champ magnétique solaire). Au niveau de la Terre, des changements périodiques dans la polarité du champ magnétique interplanétaire sont ressentis car elle se trouve tantôt au-dessus, tantôt en dessous de la couche de courant. Ces variations ont des conséquences importantes au niveau de la magnétosphère et influencent fortement l'apparition d'aurores.

[4] Comme expliqué dans le paragraphe portant sur le champ magnétique du Soleil, au commencement d'un cycle, le champ magnétique solaire ressemble à un dipole dont l'axe est aligné avec l'axe de rotation du Soleil. Durant les 5 à 6 années pour se rapprocher du maximum du cycle, cette configuration se transforme et devient anarchique. L'inclinaison du dipole peut être importante. Lorsqu'on se rapproche du minimum du cycle solaire, le dipole retrouve sont orientation initiale, parallèle à l'axe de rotation.

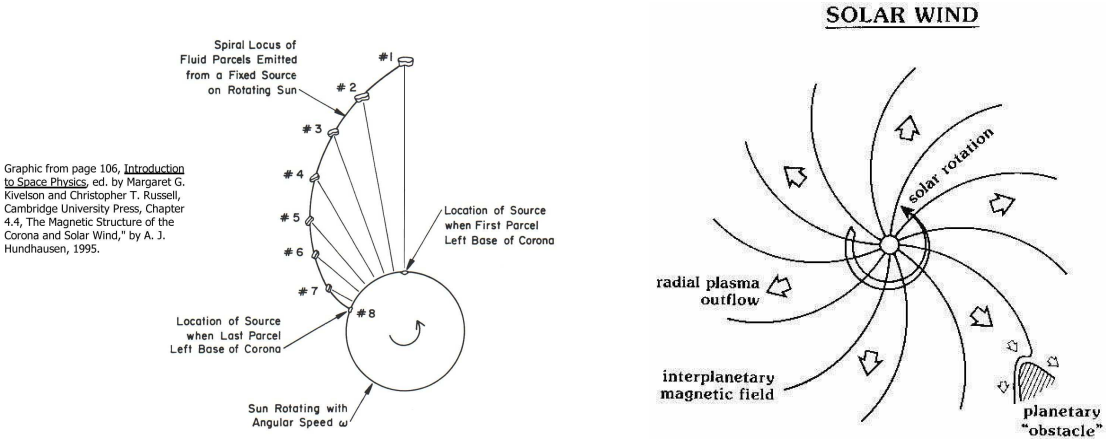


Figure 6: Forme spirale d'une succession de 8 portions de plasma du vent solaire émis à une vitesse constante d'une source fixe du Soleil en rotation. Chaque portion s'écoule radialement du Soleil dans un système fixe (référentiel inertiel). Le champ magnétique du vent solaire suit cette spirale puisque le champ est gelé dans le plasma. La figure de droite schématise cette forme spirale du vent solaire et montre le champ magnétique interplanétaire et le flux de vent solaire.

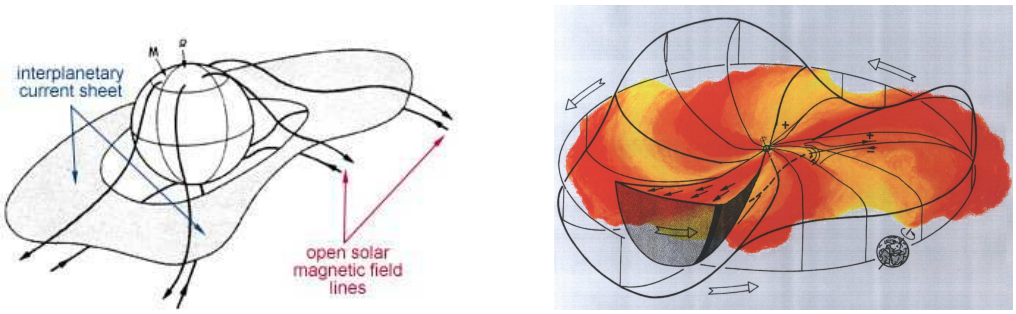


Figure 7: Couche de courant interplanétaire formée entre les lignes de champ ouvertes de direction opposées. Comme on peut le voir sur la figure de droite, cette couche ondule telle une "robe de ballerine".

Le champ IMF peut être représenté par un vecteur **B** dont l'orientation est définie selon trois composantes x, y et z. $B_x$ est dans la direction "Soleil-Terre" et est positif lorsque le vecteur pointe vers le Soleil. $B_y$ est la composante est-ouest (avec $B_y > 0$ pointant vers l'est) et $B_z$ la composante nord-sud (avec $B_z > 0$ pointant vers le nord).

## L'environnement magnétique terrestre

La Terre est une des planètes ayant un champ magnétique interne intense. La région de l'espace où est confiné ce champ magnétique se nomme la **magnétosphère**. La forme de cette région est influencée par la pression du vent solaire et par le champ magnétique interplanétaire. En l'absence du vent solaire, le champ magnétique terrestre peut être approché au premier ordre par un champ dipolaire dont l'axe est incliné de 11 degrés par rapport à l'axe de rotation. Le vent solaire modifie ce champ, le comprimant du côté du Soleil et l'étirant de l'autre côté pour former une longue queue qui s'étend sur plus d'un million de kilomètres. La magnétosphère est ainsi une sorte de cavité protégeant la surface de la Terre des particules de haute énergie du vent solaire. La magnétosphère est divisée en plusieurs régions ayant des propriétés physiques différentes. Ces différentes régions sont décrites ci-dessous et illustrées sur la Figure 8.

- Lorsque le vent solaire entre en collision avec le champ magnétique de la Terre, il est ralenti et, sur une large superficie, dévié autour de lui. Comme le vent solaire rencontre cet obstacle avec une vitesse supersonique, une onde de choc est générée, où le plasma est ralenti et une partie substantielle de l'énergie cinétique des particules est convertie en énergie thermique. La région de plasma thermalisé et subsonique située derrière cette onde de choc, et avant la frontière de la magnétosphère, s'appelle la **magnétogaine** (*magnetosheath*). C'est un milieu turbulent où le plasma est plus dense et plus chaud que dans le vent solaire et où le champ magnétique est plus intense.

- La **magnétopause** est la frontière entre la magnétosphère et le vent solaire. C'est l'équilibre entre la pression du vent solaire et la pression du champ géomagnétique qui définit la position de la magnétopause: du côté face au Soleil, cette limite se situe à une distance moyenne d'environ 10 rayons terrestres (10 Re) de la Terre.

- Sous la magnétopause se trouve une région appelée **manteau de plasma** (*Plasma mantle*) dans laquelle les lignes du champ magnétique sont des lignes "ouvertes". Le plasma dans cette région provient principalement du vent solaire via le processus de reconnexion des lignes de champ IMF et magnétosphériques.

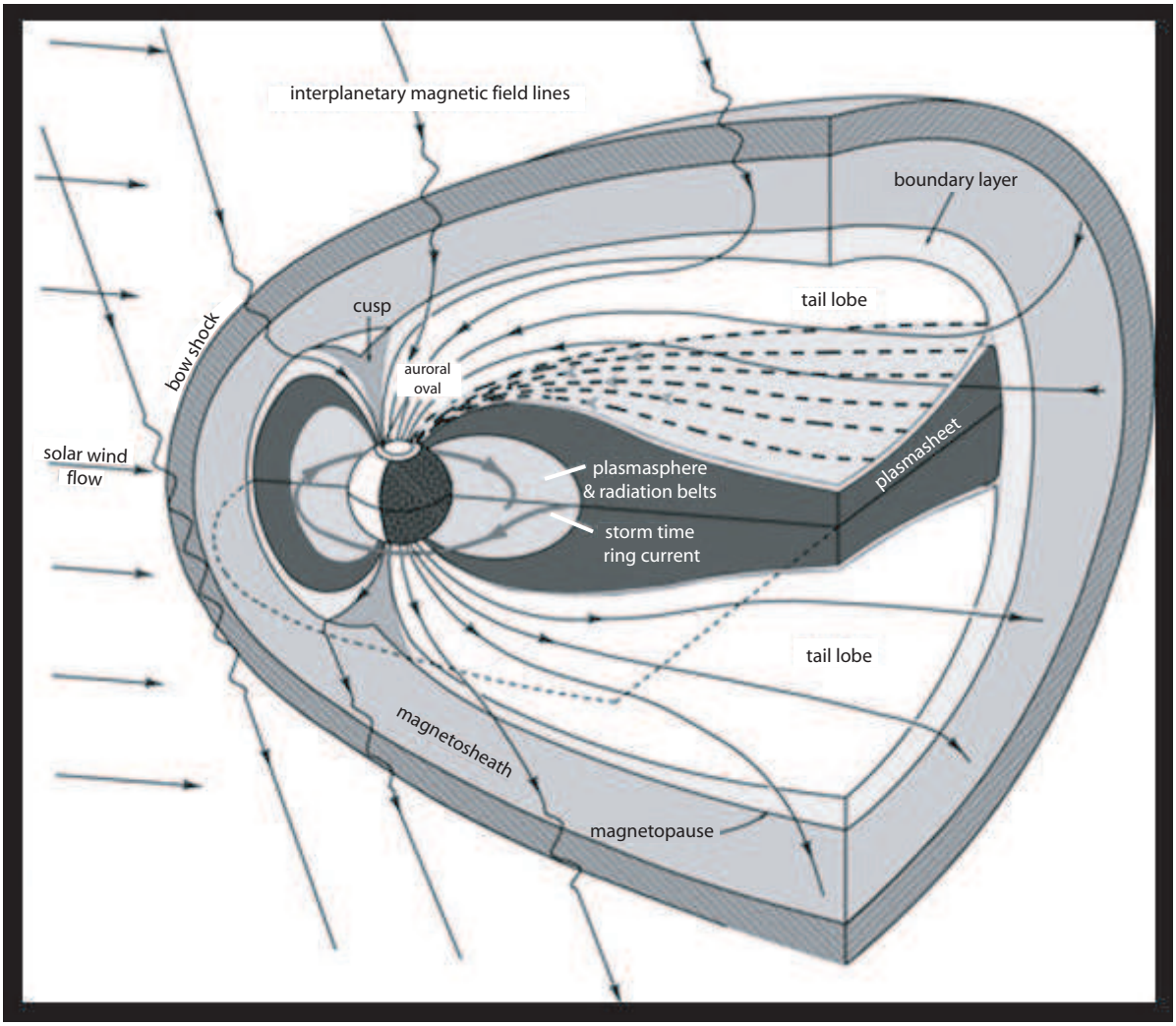


Figure 8: La magnétosphère terrestre et les différentes régions qui la composent. Ces régions sont définies par les caractéristiques du plasma qui les peuple et du champ magnétique qui y règne.

- Les lignes de champ magnétique sous le manteau de plasma sont très instables, parfois "ouvertes", parfois "fermées". Dans la région située au nord de l'équateur, le champ magnétique est dirigé en direction de la Terre, tandis que dans la région au sud de l'équateur, il est dirigé en direction opposée. Ces régions sont relativement vides de plasma et s'appellent les **lobes** (*tail lobes*) nord et sud.

- Entre le plan de l'équateur et le lobe se trouve le **feuillet de plasma** (*plasmasheet*) où les lignes de champ sont fermées mais dont la forme ne peut être décrite par l'approximation dipolaire. Le plasma dans cette région provient en partie de l'ionosphère (ce qui forme le vent polaire) et en partie du vent solaire : particules revenant par la queue après reconnexion des lignes de champ. La densité de plasma dans le feuillet est relativement grande. Ce réservoir se vide lors des sous-tempêtes magnétiques.

- La région entourant la Terre appelée **plasmasphère** est caractérisée par la co-rotation des lignes de champ avec la Terre. Ce mouvement de co-rotation est lié à l'intensité du champ électrique. Les électrons et les ions positifs soumis à l'influence d'un champ électrique dérivent vers l'est. Dans la plasmasphère, la vitesse de dérive est égale à la vitesse angulaire de rotation de la Terre. La frontière de cette région s'appelle la **plasmapause** et se situe à une distance d'environ 5 rayons terrestres ($R_E$) de la Terre.

- Les **ceintures de Van Allen** ou ceintures de radiation sont des régions où les particules sont piégées le long de lignes de champ entre leurs points miroirs. Les particules des ceintures de radiation et du feuillet de plasma dont le vecteur vitesse est dans le cône de perte pénètrent dans l'ionosphère. Elles subissent des collisions avec les constituants ionosphériques neutres, ce qui produit les émissions aurorales. Observée par satellite, cette région forme un anneau radiatif autour du pôle magnétique nord (une région similaire entoure le pôle magnétique sud) et constitue l'ovale auroral. La région intérieure à l'ovale auroral est appelée calotte polaire (*polar cap*). L'ovale auroral s'étend sur une largeur de quelques degrés et sa limite équatoriale descend jusqu'à environ 75° à 65° de latitude géomagnétique[5] selon l'activité magnétique.

- De part et d'autre de la Terre, les lignes de champ convergent vers un point neutre topologique situé au-dessus du pôle magnétique. Les régions de convergence sont les **cornets polaires** ou régions cuspidées (*cusps*). Ils font la séparation entre les

[5]La latitude géomagnétique (magnetic latitude MLAT) est souvent utilisée en géophysique. Elle représente l'angle entre l'axe géomagnétique (joignant les pôles magnétiques) et la verticale du lieu considéré. Une autre coordonnée que nous utilisons au cours de ce travail est l'heure locale magnétique (magnetic local time MLT). Elle est calculée à partir d'un méridien passant par les pôles géomagnétiques, vaut 12:00 (midi local) du côté du Soleil et 00:00 (minuit local) à l'opposé.

lignes dirigées vers le Soleil et celles dirigées vers la queue et sont caractérisés par un champ magnétique faible. Ils sont donc associés à des lignes de champ non connectées, s'ouvrant sur la magnétogaine et permettant l'entrée directe du plasma du vent solaire. Quelques particules du plasma atteignent l'atmosphère et produisent une émission aurorale de faible énergie du côté du jour de l'ovale.

## Le plasma magnétosphérique

Le plasma magnétosphérique est un gaz très peu dense, composé d'un nombre égal d'ions positifs et d'électrons. Le plasma est de charge totale neutre. Il est dit idéal si la densité de particules chargées est assez faible pour que les collisions entre particules soient peu fréquentes. Les particules constituant le plasma sont influencées par les champs électriques et magnétiques qui règnent dans le milieu. Dans le paragraphe suivant est décrit le mouvement d'une particule chargée dans un champ magnétique[6] uniforme et non uniforme, ainsi que le cas où un champ électrique est appliqué. Ensuite, le cas particulier d'une particule chargée dans un champ magnétique dipolaire est traité, puisque le champ magnétique peut, en première approximation, être décrit par un champ dipolaire au voisinage de la Terre.

### Mouvement d'une particule chargée dans un champ magnétique uniforme

Supposons une particule chargée dans un champ magnétique uniforme. La force qui s'exerce sur la particule est donnée par l'équation de Lorentz :

$$\mathbf{F} = q\mathbf{v} \times \mathbf{B} + q\mathbf{E}, \tag{4}$$

Si aucun champ électrique n'est appliqué, l'équation de Newton devient :

$$m\frac{d\mathbf{v}}{dt} = q\mathbf{v} \times \mathbf{B}, \tag{5}$$

Si on projette l'équation 5 sur l'axe parallèle à la direction du champ magnétique, elle devient :

$$m\frac{dv_{\parallel}}{dt} = 0 \Rightarrow v_{\parallel} = Constante, \tag{6}$$

Comme le champ magnétique est tangent en tout point d'une ligne de champ, le mouvement le long d'une ligne de champ dans un champ magnétique uniforme est un mouvement rectiligne uniforme.

Si on projette l'équation 5 dans le plan perpendiculaire à la direction du champ magnétique, elle devient:

$$m\frac{dv_{\perp}}{dt} = qv_{\perp}B. \tag{7}$$

[6]Notons qu'en géophysique, le terme champ magnétique est souvent employé pour décrire l'induction magnétique.

En décomposant cette équation selon les directions x et y du plan, on montre que :

$$\frac{dv_x}{dt} = \frac{qB}{m} v_y \tag{8}$$

$$\frac{dv_y}{dt} = -\frac{qB}{m} v_x \tag{9}$$

Par dérivation et combinaison des équations 8 et 9, nous obtenons :

$$\frac{d^2 v_i}{dt^2} = -\omega_C^2 v_i \tag{10}$$

avec $i = x, y$. Les équations 10 décrivent un mouvement de giration (ou mouvement cyclotronique) de fréquence angulaire $\omega_C$ et de rayon de giration $\rho_C$ définies comme suit:

$$\omega_C = \frac{qB}{m} \tag{11}$$

$$\rho_C = \frac{m v_\perp}{qB}. \tag{12}$$

Le mouvement circulaire se fait dans le sens direct pour les électrons (Figure 9) et dans le sens horlogique pour les ions. De plus, le rayon de giration dépend de la masse de la particule, ce qui entraîne que les protons décrivent un plus grand cercle que les électrons pour une même intensité $B$ et pour une même vitesse $v_\perp$.

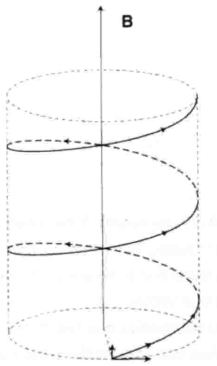


Figure 9: Mouvement d'un électron dans un champ magnétique uniforme et constant.

Considérons le cas où le champ électrique n'est pas nul et que sa direction est perpendiculaire à celle du champ magnétique[7]. Ce champ électrique entraîne une force supplémentaire

[7]Si **E** n'est pas perpendiculaire à **B**, la composante parallèle à **B** annule cette équation et seule la composante perpendiculaire doit être considérée.

agissant sur la particule chargée, ce qui implique un mouvement de dérive du centre de guidage avec la vitesse :

$$\mathbf{v}_E = \frac{\mathbf{F} \times \mathbf{B}}{qB^2} = \frac{\mathbf{E} \times \mathbf{B}}{B^2}. \tag{13}$$

Ce mouvement de dérive, illustré à la Figure 10, dû à la présence d'un champ électrique est identique pour toute particule qu'elle soit chargée positivement ou négativement, puisque la vitesse est indépendante de la charge. Supposons que le champ électrique soit dirigé vers la Terre, la dérive se fait alors vers l'est.

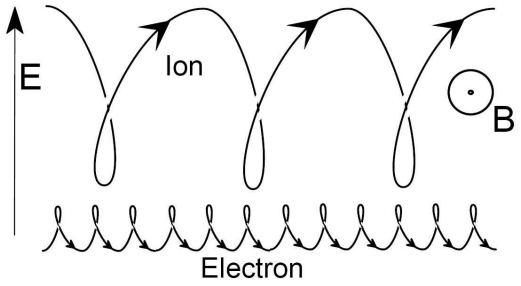


Figure 10: Illustration de la dérive $\mathbf{E} \times \mathbf{B}$, c'est-à-dire de la dérive des particules chargées dans un champ magnétique uniforme et en présence d'un champ électrique.

### Mouvement d'une particule chargée dans un champ magnétique non-uniforme

Un champ magnétique non uniforme peut être décrit par un champ magnétique uniforme auquel est ajouté un gradient de champ. La force due au gradient peut s'écrire :

$$\mathbf{F} = -\mu_B \nabla B \tag{14}$$

où $\mu_B$ est le moment magnétique de la particule et vaut $\mu_B = \frac{\frac{1}{2}mv_\perp^2}{B}$. La vitesse peut alors s'écrire :

$$\mathbf{v} = \frac{\mathbf{F} \times \mathbf{B}}{qB^2} = \frac{-\mu_B \nabla B \times \mathbf{B}}{qB^2} = \frac{1}{2}\frac{mv_\perp^2}{qB^3}\mathbf{B} \times \nabla B \tag{15}$$

Une autre composante de force vient s'ajouter : la force due à la courbure des lignes de champ magnétiques

$$\mathbf{F} = \frac{mv_\parallel^2}{R_C}\mathbf{n} \tag{16}$$

avec $\mathbf{n} = -\frac{R_C \nabla B}{B}$ étant la normale extérieure à la ligne de champ et $R_C$ le rayon de courbure de la ligne de champ. La vitesse de dérive due à cette composante vaut :

$$\mathbf{v} = \frac{\mathbf{F} \times \mathbf{B}}{qB^2} = \frac{mv_\parallel^2}{qB^3}\mathbf{B} \times \nabla B. \tag{17}$$

Ainsi, la variation du champ magnétique entraîne une dérive de vitesse totale :

$$\mathbf{v}_B = \frac{m}{2qB^3}(v_\perp^2 + 2v_\parallel^2)\mathbf{B} \times \nabla B. \tag{18}$$

Dans ce cas, le sens de la dérive est fonction de la charge des particules. Pour le champ magnétique terrestre, elle se fait vers l'est pour les électrons et vers l'ouest pour les protons, comme illustré par la Figure 11. Ce mouvement de charges crée un courant appelé courant annulaire. Comme la masse des électrons est 1836 fois plus faible que celle des protons, la vitesse des protons est beaucoup plus importante que celle des électrons. Le courant annulaire est donc principalement causé par le mouvement des protons.

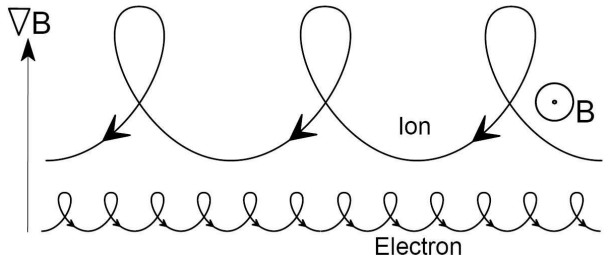


Figure 11: Illustration de la dérive des particules chargées dans un champ magnétique non-uniforme.

Remarquons que la gravité entraîne également un mouvement de dérive des particules chargées. Celui-ci se fait vers l'est pour les ions positifs et vers l'ouest pour les électrons, c'est-à-dire dans le sens opposé à la dérive due à la variation du champ magnétique. La dérive totale est la somme de toutes ces composantes. Leur importance relative dépend de l'énergie des particules, de l'intensité des champs électrique et magnétique et de leurs variations temporelle et spatiale. Notons toutefois que la dérive due au gradient de **B** domine celle due à la force gravifique pour des énergies supérieures à 1 eV.

### Mouvement d'une particule chargée dans un champ magnétique dipolaire

Dans le cas d'un champ dipolaire, l'intensité du champ **B** est proportionnelle à l'inverse du cube de la distance $R^{-3}$, ce qui correspond au cas d'un champ non uniforme. Le mouvement des particules chargées comporte alors 3 composantes :

- un mouvement parallèle à **B** (le long d'une ligne de champ),
- un mouvement de giration centré sur une ligne de force,

- un mouvement de dérive perpendiculaire à **B** (vers l'est pour les électrons et vers l'ouest pour les protons).

Nous introduisons ici la notion d'invariant adiabatique. La théorie générale des invariants adiabatiques indique que la grandeur $I = \frac{1}{2\pi} \oint pdq$ est conservée lors de changements lents dans un système où la variable $q$ est périodique (la variable $p$ étant le moment correspondant). Cette théorie est notamment développée par *Landau and Lifshitz* [1960]. Appliquons-la au cas où le champ magnétique **B** varie lentement.

Considérons d'abord le cas du mouvement de giration : $p = mv_\perp$ et $dq = \rho_C d\theta$ avec $v_\parallel$ désignant la composante de la vitesse des particules dans le plan perpendiculaire au champ magnétique et $\rho_C$ étant le rayon de giration. On peut alors écrire :

$$I_1 = \frac{1}{2\pi} \int_0^{2\pi} mv_\perp \rho_C d\theta = \frac{m^2}{q} \frac{v_\perp^2}{B} = Constante \tag{19}$$

Comme la masse $m$ et la charge $q$ des particules sont constantes, le premier invariant adiabatique lié à la giration s'écrit :

$$\frac{v_\perp^2}{B} = Constante. \tag{20}$$

Comme le moment magnétique vaut $\mu_B = \frac{\frac{1}{2}mv_\perp^2}{B}$, il est lui aussi conservé. Ainsi, si le champ magnétique augmente, l'énergie liée au mouvement de rotation $W_B = \frac{1}{2}mv_\perp^2$ augmente également. Il y a donc une accélération de type bétatron qui entretient le mouvement de giration. La modification de l'énergie associée à la giration des particules est proportionnelle à $R^{-3}$, $R$ étant la distance géocentrique de la ligne de champ. De plus, si l'**angle d'attaque** $\alpha$ est défini par l'angle entre la direction de la vitesse et la direction du champ magnétique, la composante perpendiculaire de la vitesse vaut $v_\perp = v \sin\alpha$. Comme la vitesse totale est conservée, étant donné que la force magnétique ne travaille pas, le premier invariant adiabatique s'écrit :

$$\frac{\sin^2\alpha}{B} = Constante. \tag{21}$$

Le carré du sinus étant maximum pour $\alpha$=90° et $\alpha$=270°, ces points sont équivalents à des maxima du champ magnétique. Ce sont les **points miroirs**. La particule butte sur ces points où $v_\perp$ s'annule et est réfléchie, comme illustré à la Figure 12. La hauteur du point miroir sur une ligne de champ est fonction de la direction du vecteur vitesse et de l'intensité du champ magnétique. La particule se mouvant le long d'une ligne de champ magnétique est piégée entre les deux points miroirs (Figure 12). Cette notion de point miroir, nous permet de définir le concept de **cône de perte** comme étant l'angle solide décrit par les vecteurs vitesses des particules entrant dans l'atmosphère terrestre, c'est-à-dire dont le point miroir est plus bas qu'une altitude de référence posée comme la frontière

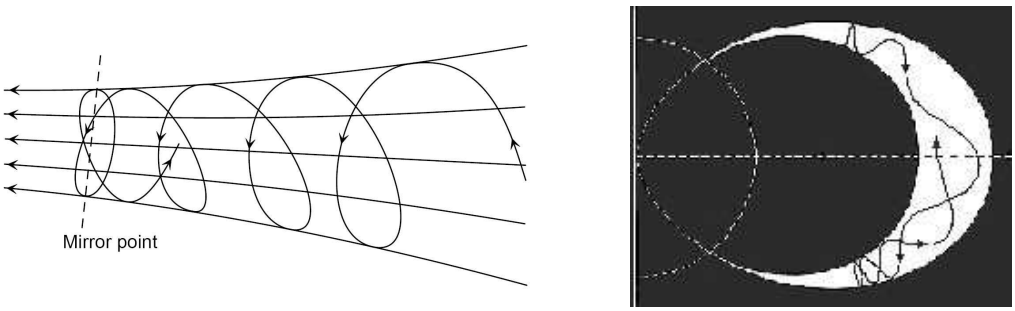


Figure 12: Mouvement d'une particule chargée au voisinage de son point miroir (à gauche) et trajectoire d'une particule dans un champ magnétique non uniforme, entre ses 2 points miroirs (à droite).

de l'atmosphère.

Considérons maintenant le mouvement le long d'une ligne de champ magnétique : $p = mv_{\parallel}$ et $dq = dl$. Si la vitesse $v$ est conservée et si sa composante parallèle au champ magnétique s'écrit $v_{\parallel} = v\cos\alpha = v\sqrt{1-\sin^2\alpha}$, la théorie des invariants adiabatiques donne alors :

$$I_2 = \frac{1}{2\pi}\oint mv_{\parallel}dl. \tag{22}$$

Ce deuxième invariant adiabatique est lié au mouvement d'aller-retour sur une ligne de champ et exprime la conservation de la séparation des points miroirs. Une accélération peut également être induite par ce deuxième invariant. Si une particule dérive vers une région où l'intensité du champ est plus forte, ses points miroirs se situeront à une altitude plus haute et son trajet le long de la ligne de champ sera plus court. Ainsi $\oint dl$ diminue tandis que $\oint mv_{\parallel}dl$ est conservée. La vitesse $v_{\parallel}$ doit donc augmenter et la particule subit une accélération de Fermi. La variation de l'énergie associée au mouvement de la particule perpendiculairement à $\mathbf{B}$ est proportionnelle à $R^{-2}$.

Le troisième invariant adiabatique est lié au mouvement de dérive des particules dû à la variation du champ magnétique. Il exprime la conservation du flux magnétique entouré par la coquille tridimensionnelle décrite par la particule. La figure 13 schématise les différents mouvements décrits par les particules dans le champ magnétique terrestre lorsque celui-ci est représenté en première approximation par un champ dipolaire.

### Brisure des invariants adiabatiques dans la magnétosphère terrestre

La théorie des invariants adiabatiques est applicable lorsque les champs varient peu sur des distances équivalentes aux rayons de courbure des particules. Dans la réalité, les lignes

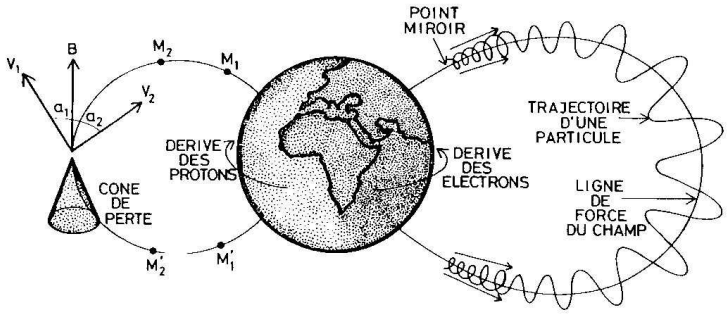


Figure 13: Schéma représentant les différents mouvements des particules chargées dans le champ géomagnétique (dans l'approximation dipolaire).

de champ de la queue de la magnétosphère sont très étirées, même à des distances de 8 ou 10 rayons terrestres. A la figure 14, on a représenté en pointillé la ligne neutre où la composante $B_z$ du champ magnétique s'inverse. Dans la queue au voisinage de la ligne neutre (zone en grisé), la valeur du champ magnétique est très faible et la courbure des lignes de champ est assez élevée. Les variations du champ ne peuvent plus être considérées comme faibles sur les distances équivalentes aux rayons de courbures des particules, même pour des particules de faible énergie. On ne peut donc pas supposer la conservation des invariants adiabatiques dans cette région. Cette région s'appelle la couche neutre, le champ magnétique y est plus faible et la densité de plasma plus importante que dans les lobes situés au nord et au sud de la couche neutre.

La limite entre les lignes de champ où la précipitation est adiabatique et celle où les particules subissent une accélération due à la morphologie étirée des lignes de champ s'appelle **limite isotrope** (*isotropic boundary*). Les observations *in situ* des flux de particules permettent de visualiser la position de cette limite isotrope : elle est la frontière abrupte entre la zone où la précipitation est isotrope (c'est-à-dire que le flux de particules précipitant $J_p$ est égale au flux de particules piégées $J_t$) et la zone où le taux de remplissage du cône de perte est faible ($J_p << J_t$) à toute heure locale. Les principales caractéristiques de la limite isotrope (limite IB) sont résumées par *Sergeev et al.* [1993]:

- Les limites pour les électrons et les protons sont séparées, vu leur différence de masse et donc de rayon de giration. La limite pour les protons est située à des latitudes plus équatoriales que celle des électrons.

- La position de la limite isotrope est différente en fonction de l'énergie des particules. Plus les particules sont énergétiques, plus équatoriale est la limite isotrope.

- Dans la région isotrope, le degré de remplissage du cône de perte ne dépend pas

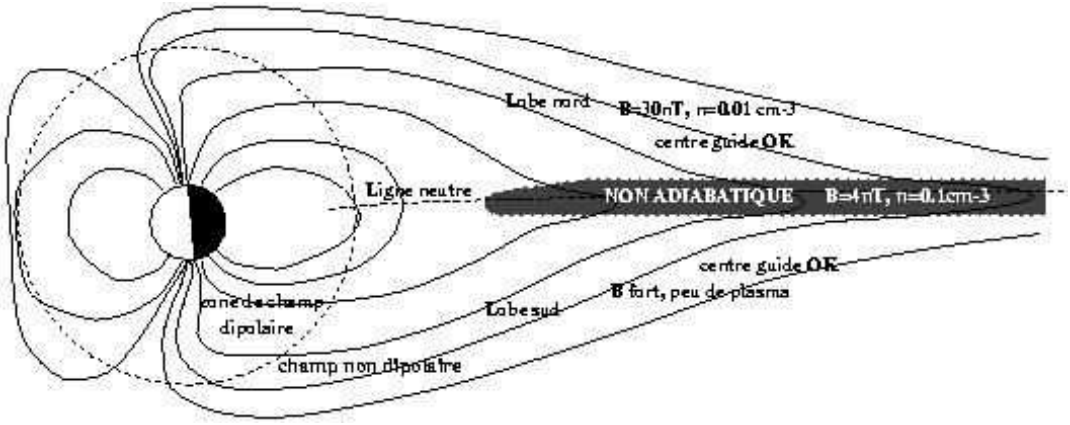


Figure 14: Schéma représentant la topologie de la queue de la magnétosphère et la région où le mouvements des particules ne respecte plus la conservation des invariants adiabatiques.

de façon importante de la valeur absolue du flux de particules (c'est-à-dire le rapport entre le flux de particules précipitées et le flux de particules piégées reste quasi constant).

- Une asymétrie midi-minuit est visible dans la limite isotrope. La position de la limite isotrope se situe à des latitudes plus polaires vers midi. La limite IB du coté jour n'est que rarement visible dans les observations *in situ*.
- Durant les périodes d'activité magnétique élevée, la position de la limite isotrope descend en latitude à toute heure locale (suite à l'étirement plus élevé de la queue de la magnétosphère).
- La limite équatoriale de l'ovale auroral de protons correspond à cette frontière IB [*Gérard et al.*, 2004].

### Modélisation du champ magnétosphérique

Comme expliqué dans le paragraphe précédent, à proximité de la Terre, le champ magnétique peut être, en première approximation, décrit par un champ dipolaire. Mais il existe des modèles prenant en considération les perturbations du champ par rapport au champ dipolaire. Dans le cadre de ce travail, nous utilisons un modèle IGRF. Les modèles IGRF (International Geomagnetic Reference Field) sont des modèles mathématiques décrivant le champ magnétique terrestre et ses variations. Le potentiel géomagnétique d'origine interne est développé en série sur la base des harmoniques sphériques et s'écrit :

$$V = a \sum_{n=1}^{N} \sum_{m=0}^{n} (\frac{a}{r})^{n+1} (g_n^m \cos m\phi + h_n^m \sin m\phi) P_n^m(\cos\theta) \tag{23}$$

où $a$ est le rayon moyen de la Terre (= 6371 km), $r$, $\theta$ et $\phi$ sont les coordonnées sphériques géocentriques (avec $r$ la distance mesurée à partir du centre de la Terre, $\theta$ la colatitude, et $\phi$ la longitude comptée à partir du méridien de Greenwich en direction de l'est), $g_n^m$, $h_n^m$ sont appelés coefficients de Gauss et $P_n^m$ sont les fonctions de Legendre associées. Le modèle IGRF pour la composante principale du champ tronque ce développement à N=10 (120 coefficients). Les coefficients sont arrondis au nanoTesla, correspondant à la limite de résolution du modèle. Le modèle IGRF décrivant les variations séculaires du champ tronque le développement à N=8 ( 80 coefficients arrondis à 0.1 nT/an ).

Le code GEO-CGM.for version 9.9. permet de passer des coordonnées géographiques aux coordonnées géomagnétiques corrigées calculées sur base du modèle IGRF, et inversement. Il fournit également un certain nombre de paramètres liés au champ géomagnétique : notamment, l'heure magnétique locale. Ce code peut être téléchargé sur le site Web du National Space Science Data Center (NSSDC) (http://nssdc.gsfc.nasa.gov/space/cgm/).

### Les champs électriques magnétosphériques

Deux types de champs électriques magnétosphériques à grande échelle sont remarquables: l'un dû au couplage avec le vent solaire, c'est le champ électrique de convection, l'autre dû à la rotation de la Terre, c'est le champ électrique de co-rotation. L'influence du champ de co-rotation est grande dans la région proche de la Terre, alors que celle du champ de convection se fait sentir dans les régions plus éloignées. La frontière entre les deux régimes est la plasmapause. La Figure 15 présente le flux de plasma lié à ces deux types de champ électrique magnétosphérique.

#### *Le champ électrique de convection*

*Dungey* [1961] a proposé un modèle de magnétosphère ouverte permettant d'expliquer la circulation à grande échelle dans la magnétosphère, causée par le vent solaire. Il propose que par le processus de reconnexion magnétique (dont la théorie sera développée plus loin), l'apparition d'un point neutre au front de la magnétosphère permette aux lignes de champ géomagnétique de se lier avec les lignes de champ interplanétaire, créant ainsi des lignes de champ ouvertes. Comme expliqué plus loin, pour que ce processus existe, les lignes de champ doivent être orientées en sens opposé : un champ magnétique interplanétaire orienté vers le sud est donc nécessaire pour ouvrir le champ magnétique terrestre du côté jour.

Le cycle de *Dungey* se décompose en plusieurs étapes, comme illustré à la Figure 16. La convection magnétosphérique opposée au Soleil se met en place lorsque les lignes de champs sont ouvertes. Celles-ci se dirigent vers la queue de la magnétosphère en traversant la calotte polaire à la vitesse du vent solaire. Le champ électrique du vent solaire, dirigé de l'aube vers le crépuscule, $\mathbf{E} = \mathbf{v}_{SW} \times \mathbf{B}_{SW}$, se projette le long des lignes de champ de la magnétosphère, puisque la grande conductivité électrique le long des lignes de champ magnétique permet de les considérer comme des équipotentielles. Une dérive

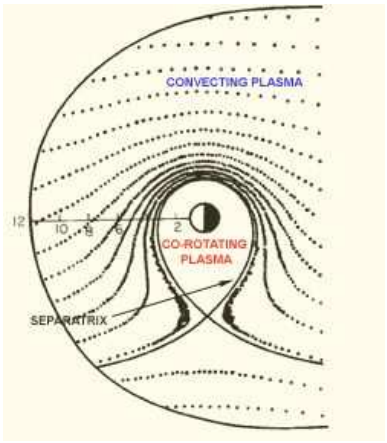


Figure 15: Schéma représentant le flux de plasma dans le plan équatorial de la magnétosphère. Dans la région proche de la Terre, le plasma est en co-rotation avec la Terre, alors qu'à distance plus élevé, c'est la convection qui domine.

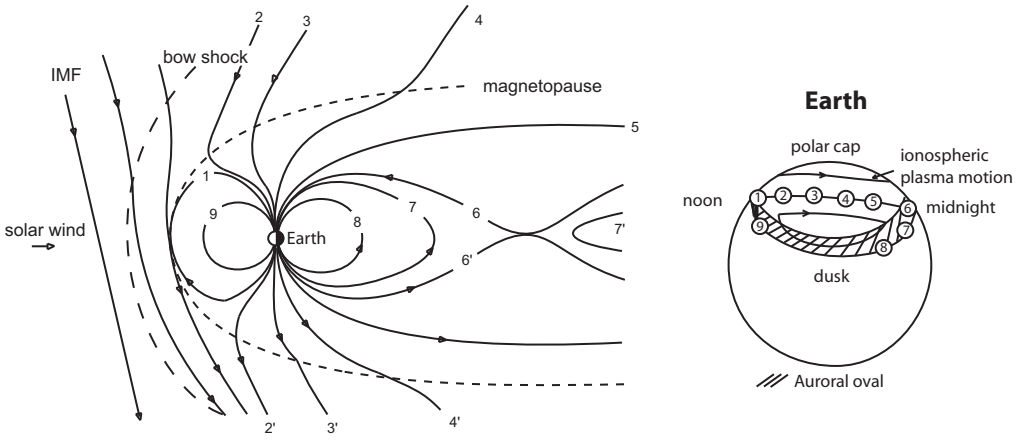


Figure 16: Convection du plasma dans la magnétosphère. Sur le schéma de gauche, les régions numérotées montrent la succession des configurations des lignes de champ géomagnétique. La reconnexion avec le champ IMF a d'abord lieu sur le front de la magnétosphère (1 et 1'). Ces lignes de champ dites "ouvertes" se dirigent ensuite vers la queue de la magnétosphère (2 à 5). Une seconde reconnexion a lieu dans la queue de la magnétosphère (6 et 6') après laquelle les lignes de champ retournent vers le côté jour par des latitudes plus basses. Sur le schéma de droite, la position du pied des lignes de champ est numérotées dans l'ionosphère de l'hémisphère nord. Les flux de plasma à haute altitude sont aussi représentés par des flèches : flux opposé au Soleil dans la calotte polaire.

opposé au Soleil $\mathbf{E} \times \mathbf{B}$ se forme dans la calotte polaire. En raison du mouvement du vent solaire, les lignes de champ des deux hémisphères nord et sud s'étirent vers la queue de la magnétosphère. Elles se reconnectent entre elles loin dans la queue de la magnétosphère.

Le potentiel magnétosphérique et le champ électrique peuvent être évalués approximativement en utilisant la distribution de potentiel de *Volland* [1973], avec le facteur multiplicatif $A(Kp)$ de *Maynard and Chen* [1975] :

$$\phi_{conv} = A(Kp)(\frac{r}{R_E}^2 \sin\varphi) \tag{24}$$

et

$$\mathbf{E}_{conv} = -\nabla\phi_{conv} \tag{25}$$

où $A(Kp) = \frac{0.045}{(1-0.159Kp+0.0093kp^2)}kV$ et $\varphi = 0^\circ$ à midi, $\varphi = 90^\circ$ à 06:00 MLT et $\varphi = 180^\circ$ à minuit.

### *Le champ électrique de co-rotation*

Le champ électrique de co-rotation est induit par la rotation du champ magnétique dipolaire terrestre et la présence de plasma conducteur en rotation avec le dipôle. L'expression de ce champ électrique s'écrit :

$$\phi_{cor} = \frac{-B_0\omega_E R_E^2}{\frac{r}{R_E}} \tag{26}$$

et

$$\mathbf{E}_{cor} = -\nabla\phi_{cor} \tag{27}$$

où $-B_0\omega_E R_E^2 = -3.1 \cdot 10^{-5}T \times \frac{2\pi}{24h} \times (6371.2km)^2 = -92kV$.

### Les courants magnétosphériques

La topologie du champ magnétique de la magnétosphère et les contraintes du vent solaire sur la magnétosphère font apparaître un système de régions diverses, dont nous avons parlé au début du chapitre, couplées à des systèmes de courants. On distingue plusieurs types de courants circulants dans la magnétosphère: le courant de la magnétopause, le courant de queue, le courant annulaire et les courants alignés. La Figure 17 en donne une représentation graphique.

Comme la magnétopause sépare une région où le champ magnétique est relativement intense (la magnétosphère) d'une autre où le champ est relativement faible (la magnétogaine), la frontière doit transporter un courant de surface pour maintenir un équilibre de

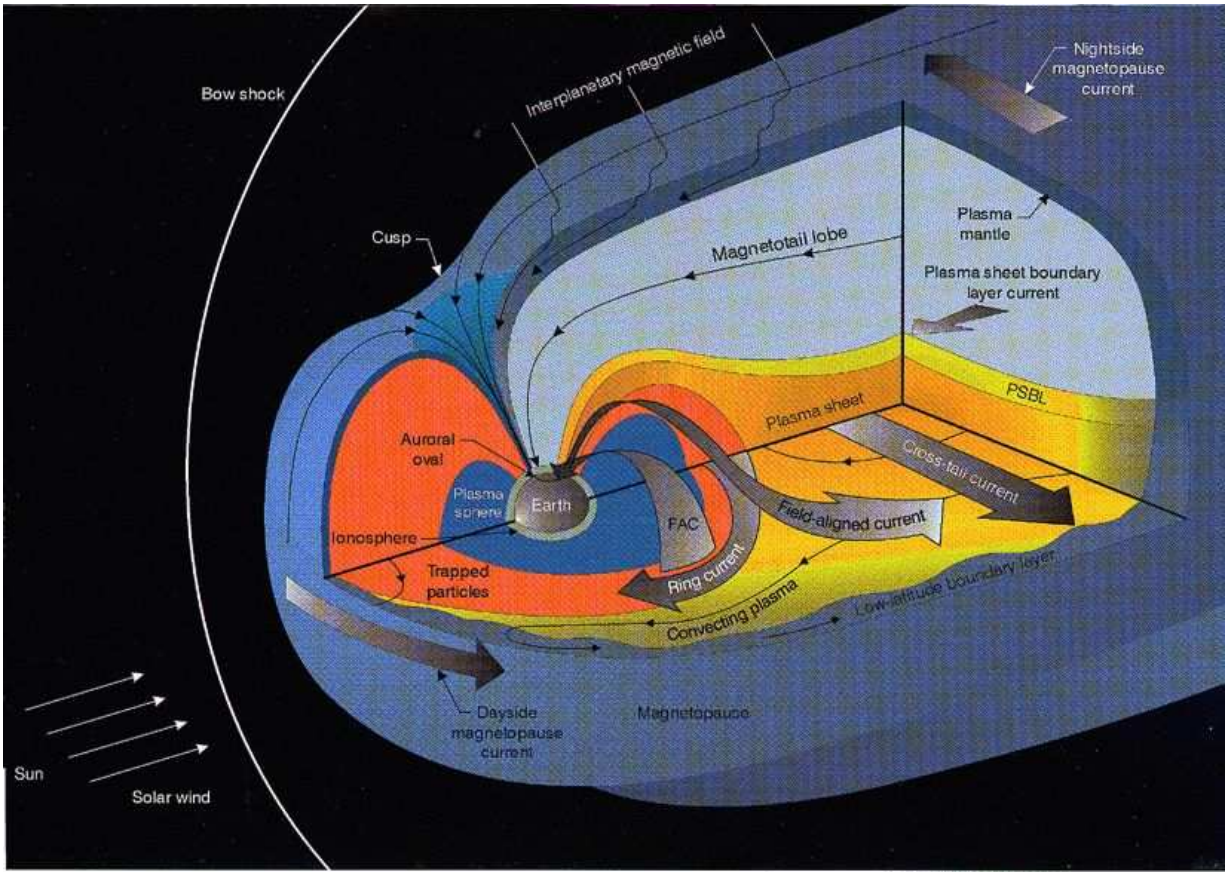


Figure 17: Schéma des différentes régions et courants magnétosphériques

force à travers la frontière. Ce **courant de la magnétopause** circule différemment du côté jour et du côté nuit de la Terre. Il encercle les deux lobes de la queue de la magnétosphère, comme le montre la figure 18. Le courant de la magnétopause se referme par un courant qui traverse la queue de la magnétosphère appelé "**courant de queue**". Il circule du côté soir (18h MLT) vers le côté matin (6h MLT) dans le plan de l'équateur.

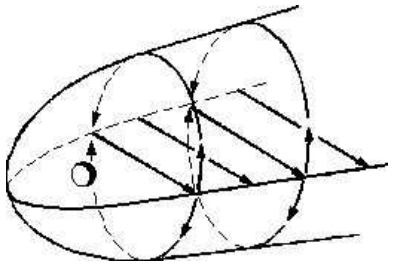

Figure 18: Schéma des courants de queue de la magnétosphère terrestre.

Comme décrit dans les sections précédentes, les particules chargées dans le champ magnétosphérique sont soumises à des forces et subissent une dérive. Comme les protons positifs et les électrons négatifs dérivent dans des directions opposées, leur mouvement est à l'origine d'un courant électrique qui circule autour de la Terre, dans le sens horlogique lorsque vue du pôle nord. Ce courant est le **courant annulaire**. Il consiste donc en des ions (principalement $H^+$, $He^+$ et $O^+$) et des électrons piégés, d'énergie entre 10 et 200 keV, qui dérivent autour de la Terre, à une distance d'environ 2 à 7 rayons terrestres. L'intensité du courant annulaire varie en fonction de l'activité magnétique terrestre. Il augmente en période de tempête. Deux processus sont suggérés pour expliquer cette augmentation : soit l'injection de particules nouvelles, soit le transport et l'énergisation des particules du feuillet de plasma dus à l'augmentation du champ électrique de convection.

Les **courants alignés** sont particuliers dans le sens où ils sont une combinaison du courant de queue et des courants ionosphériques. Une description détaillée de ce phénomène sera donc faite dans le chapitre relatif à l'ionosphère.

# L'activité géomagnétique

Comme le vent solaire provient du Soleil, la Terre est heurtée par du plasma chaud magnétisé, supersonique et non-collisionnel. Ce plasma transporte une grande quantité d'énergie cinétique et électrique. Une partie de cette énergie pénètre dans la magnétosphère et est à l'origine de l'activité géomagnétique, c'est-à-dire des tempêtes géomagnétiques, des sous-tempêtes et de leur signature dans l'ionosphère terrestre: les aurores. La pénétration

du plasma et de l'énergie du vent solaire est régie par une série de mécanismes allant de la frontière de la magnétosphère jusqu'à l'atmosphère terrestre.

## La reconnexion magnétique

Au front de la magnétosphère, le vent solaire intéragit avec le champ magnétique terrestre par un processus de reconnexion magnétique. L'idée de base du concept de reconnexion magnétique est que des lignes de champ magnétique anti-parallèles peuvent, en se rencontrant, fusionner et produire deux lignes de champ totalement différentes au point de vue de leur topologie magnétique. Ce processus est fortement discuté d'un point de vue théorique, principalement la notion de "point neutre", mais nous faisons ici état d'un point de vue qui permet d'expliquer beaucoup de phénomènes.

La reconnexion est supposée être le principal lien dans le processus de couplage entre le vent solaire et la magnétosphère. Elle se passe au niveau de la magnétopause du côté jour, entre le champ IMF dirigé vers le sud et le champ géomagnétique dirigé vers le nord. La figure 19b illustre la situation des lignes de champ lors de la reconnexion. Les modèles de reconnexion magnétique permettent d'expliquer le transport de masse et d'énergie du vent solaire vers la magnétosphère, ainsi que la convection magnétosphérique à grande échelle.

Dans le cas d'un champ magnétique interplanétaire dirigé vers le nord, un processus semblable peut avoir lieu, mais pas sur le front de la magnétosphère. La reconnexion a lieu à plus haute latitude (région proche du cusp - Figure 19a). L'orientaton de la composante $B_y$ joue alors un rôle prépondérant pour que le processus ait lieu. Il est alors beaucoup moins efficace, et l'échange d'énergie et de matière ne créent pas de conséquences aussi remarquables que lorsque la reconnexion à lieu sur le front de la magnétosphère. Finalement, un processus semblable peut aussi avoir lieu dans la queue de la magnétosphère.

La Figure 20 montre schématiquement les différentes configurations du champ magnétique durant le processus de reconnexion. Le graphique 20a représente la situation en $t<0$ lorsque les deux plasmas de champ magnétique orienté en sens opposés se dirigent l'un vers l'autre. Au temps $t=0$ (Figure 20 b), les deux plasmas se rencontrent et leur champs magnétiques fusionnent, formant une configuration en X. Au temps $t>0$, les lignes de champ reconnectées ont été créées et "s'échappent" dans la direction perpendiculaire à la direction d'origine (Figure 20 c). La topologie du champ magnétique est donc modifiée par rapport à la topologie initiale.

### Les courants dans la reconnexion magnétique

Pour expliquer la reconnexion magnétique, le concept de flux gelé est nécessaire. Ce concept montre que si la conductivité électrique d'un fluide est assez grande, le flux magnétique lié à un élément du fluide reste fixe, ce qui revient schématiquement à une ligne

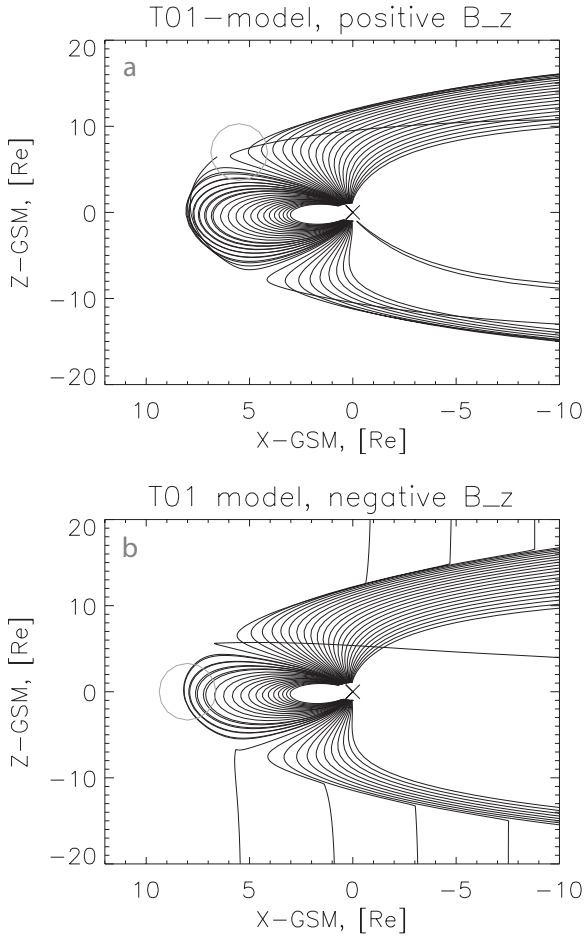


Figure 19: Lignes de champ magnétique lorsque le champ IMF est dirigé vers le nord avec $B_z$ = 5 nT (a) et vers le sud avec $B_z$ = -5 nT (b) et Dst = 20 nT, Pdyn = 7 nPa, $B_x$ = 2 nT, $B_y$ = 0 nT [*Tsyganenko*, 2002]. Les cercles indiquent la localisation des régions de reconnexion pour les conditions de champ IMF dirigé vers le nord et le sud [*Frey et al.*, 2003b].

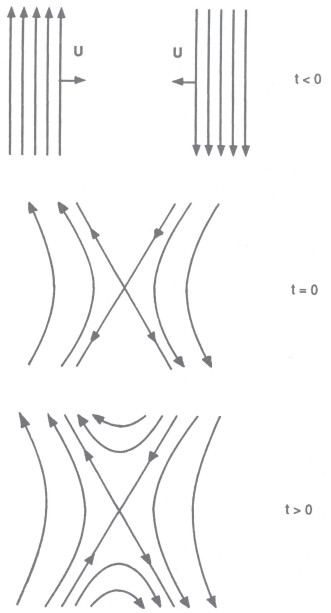


Figure 20: Schéma de la reconnexion des lignes de champ magnétique [*Parks*, 2004]

de champ magnétique se mouvant avec le fluide. La condition pour que le champ soit gelé est que le nombre magnétique de Reynolds [8] soit grand par rapport à 1, ce qui est généralement vrai dans la magnétosphère.

Si les conditions de champ gelé dans le flux sont d'application, le plasma ne peut se mélanger uniquement le long des tubes de flux [9] et jamais les traverser. Ainsi, les propriétés du plasma sont relativement uniformes le long d'un tube de flux, mais des changements abrupts dans ces conditions peuvent apparaître d'un tube de flux à son voisin. Si deux plasmas de régimes distincts, par exemple de sources disctinctes, se rencontrent, comme ils ne peuvent théoriquement pas se diffuser l'un dans l'autre, une fine frontière se crée entre

[8] le nombre de Reynolds magnétique est défini par le rapport entre le terme d'induction et le terme de dissipation ($R_m = rot(uxB)/\eta\Delta B \approx LU/\eta$ avec U et L les échelles caractéristiques de vitesse et de longueur et $\eta = 1/(\mu_0\sigma)$ la diffusivité magnétique, $\mu_0$ étant la perméabilité magnétique et $\sigma$ la conductivité électrique) de l'équation d'induction. On notera que si le nombre de Reynolds magnétique est faible, les effets dynamiques seront réduits: le champ magnétique sera dissipé rapidement. Si le nombre de Reynolds est élevé au contraire, le flux magnétique sera conservé plus longtemps, le champ magnétique pourra augmenter (et diminuer) selon la variation de la surface normale au champ local.

[9] Un tube de flux est un ensemble de lignes de champ défini par le flux magnétique qui traverse toute section de cet ensemble. Le flux magnétique est, par définition du tube de flux, constant tout au long du tube de flux. Ceci signifie que l'intensité du champ magnétique décroît lorsque la section du tube s'élargit et inversement.

eux, qui est en fait une couche de courant (**current sheet**). C'est dans cette couche de courant que le concept de champ gelé peut être transgressé. La région autour du point X (ou ligne neutre de type X si on visualise le problème à 3 dimensions) est une region où le nombre magnétique de Reynolds est inférieur à 1 et est appelée région de diffusion. Dans cette région, les lignes de champ sont coupées et reconnectées à des autres. Le plasma des différents tubes de flux provenant des différentes sources se retrouve alors sur un nouveau tube de flux, en totale violation du concept de champ gelé. Le flux magnétique traverse la couche de courant et le plasma traverse la frontière séparant les deux types de plasma initiaux en suivant les tubes de flux.

Des courants électriques sont associés aux configurations de la Figure 20 :
au temps t<0, les deux systèmes de plasma sont indépendants et comprennent des courants diamagnétiques [10] ($\mathbf{J} = \mathbf{B} \times \nabla p / B^2$ avec $\nabla p$ le gradient de pression) de même direction. Pour produire la configuration au temps t=0, les deux plasmas fusionnent au point X où B=0 et donc où les courants diamagnétiques disparaissent. Pourtant, le point X supporte tout de même un certain type de courant : comme la disparition du champ magnétique ne signifie pas que le champ électrique disparaisse, $\mathbf{E} = -\nabla\Phi - \partial\mathbf{A}/\partial t = -\nabla\Phi$. Ce champ électrique peut transporter des courants. L'existence de ce champ électrique est nécessaire pour le processus de reconnexion. A la Figure 20, le courant conduit par le champ électrique au point X est dirigé vers l'arrière de la page, dans la direction opposée aux courants diamagnétiques originaux. Chaque reconnexion de paire de lignes de champ crée une paire de nouvelles lignes de champ. Ainsi, au temps t>0, deux systèmes de courant prennent place : l'un induit sur les lignes de champ des deux plasmas arrivant l'un vers l'autre, l'autre sur les lignes de champ nouvellement créées. Le courant nouvellement créé est dissipatif puisque $\mathbf{E} \cdot \mathbf{J} \neq 0$ et on s'attend à un chauffage de Joule au point X.

## Les tempêtes et sous-tempêtes

### Les tempêtes

Les **tempêtes magnétiques** sont les événements les plus remarquables au point de vue de l'activité géomagnétique. Le terme "tempête magnétique" fut donné par Alexander

[10] Les plasmas ont des propriétés diamagnétiques, c'est-à-dire qu'ils se magnétisent dans le sens opposé du champ magnétique dans lequel ils sont placés. Dans les diamagnétiques, les électrons ajustent leurs trajectoires de façon à compenser l'influence du champ magnétique externe et ceci engendre un champ magnétique induit qui est dirigé dans le sens opposé. Ceci veut dire que le moment magnétique est anti-parallèle au champ extérieur. Dans l'espace, une région où règne un champ magnétique élevé tend à s'opposer à la venue des particules électriquement chargées. C'est l'effet diamagnétique. A titre d'exemple, certaines régions de la magnétosphère de la Terre, comme les lobes, ont un champ magnétique significativement plus élevé que dans le milieu interplanétaire. Bien que ces régions soient reliées à l'ionosphère (relativement dense) de la Terre, les lobes sont des régions plus vides (0.01 particule par centimètre cube) que l'espace interplanétaire (5 particules par centimètre cube). Les lobes sont peut-être les régions les plus vides que l'on ait jamais explorées. D'une façon générale, la magnétosphère est globalement moins dense que le milieu interplanétaire, c'est une conséquence de l'effet diamagnétique.

von Humboldt [11] à ce phénomène de perturbation du champ magnétique terreste à grande échelle. La définition suivante d'une tempête a été proposée par *Gonzales et al.* [1994] : "*Storm is an interval of time when a sufficiently intense and long-lasting interplanetary convection electric field leads, through a substantial energization in the magnetosphere-ionosphere system, to an intensified ring current strong enough to exceed some key threshold of the quantifying storm time Dst index.*".

La principale signature d'une tempête magnétique est un champ magnétique dirigé vers le sud, affaiblissant le champ dirigé vers le nord généralement observé dans les régions équatoriales, conséquence de l'intensification des ceintures de radiation et du courant annulaire. Durant les tempêtes magnétiques, les ceintures de radiation deviennent plus intenses par l'arrivée de protons provenant de la queue et d'ion $O^+$ provenant de l'ionosphère. Les tempêtes magnétiques ont généralement un déclencheur précis : souvent l'arrivée d'un choc interplanétaire. L'effet principal de cet événement sur la magnétosphère est l'injection d'ions et d'électrons énergétiques provenant de la queue vers les ceintures de radiation et causant l'intensification du courant annulaire. Ce processus a également lieu lors des sous-tempêtes mais à moindre échelle. Une autre signature des tempêtes est son influence sur la précipitation aurorale. L'ovale auroral est fortement perturbé, s'élargissant, principalement vers l'équateur et du côté nuit, ce qui a pour conséquence que des aurores soient visibles dans le ciel nocturne à des latitudes moyennes et basses, par exemple, sous nos latitudes.

Au début du $20^{ème}$ siècle, il a été montré qu'il existe un lien entre les tempêtes magnétiques et les taches solaires. En fait, l'interprétation de ce lien est la suivante : le champ magnétique intense des taches solaires entraine un soudain dégagement de l'énergie magnétique, manifesté par les protubérances et les éjections de masse coronale. Ces deux phénomènes éjectent des nuages de plasma chaud interplanétaire qui bouscule le vent solaire normal et induit un choc dans le vent solaire qui en rencontrant la magnétosphère terrestre provoque les tempêtes magnétiques.

Le phénomène de tempête magnétique peut être divisé en trois phases distinctes, selon la signature de l'indice [12], comme illusté à la figure 21:

***La phase initiale*** :

- Elle dure entre quelques minutes et quelques heures.
- L'indice Dst augmente jusqu'à des valeurs positives de quelques dizaines de nT.

[11] Alexander von Humboldt : Naturaliste et explorateur allemand (Berlin, 1769 - 1859). En 1829, le Ministre des finances russe offre l'opportunité à Humboldt de diriger une expédition dans les régions de l'Oural et de l'Altaï, afin d'y étudier le magnétisme terrestre et la géologie. Humboldt consacre les dernières années de sa vie à la rédaction d'une synthèse de ses travaux et connaissances scientifiques : il est l'auteur d'un ouvrage intitulé Kosmos, paru en 5 volumes.

[12] La définition de l'indice Dst est donnée dans la section suivante

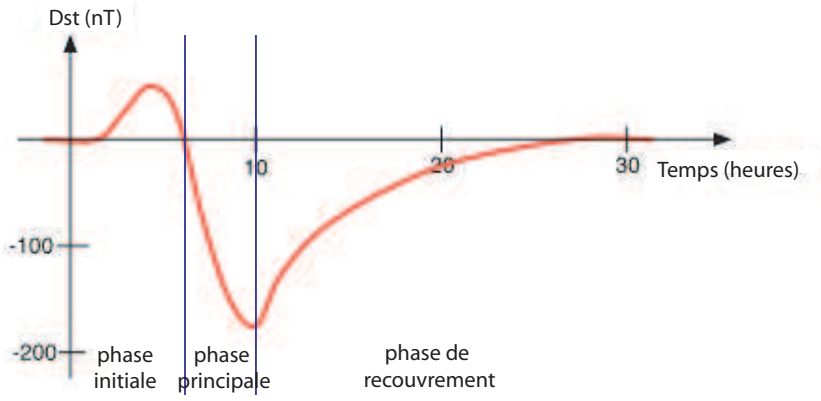


Figure 21: Illustration du comportement typique de l'indice Dst durant une tempête magnétique, composée de la phase initiale, la phase principale et la phase de recouvrement.

- Lorsque le vent solaire atteint la magnétosphère, la pression qu'il exerce sur le front est beaucoup plus important. La magnétopause du côté jour est alors fortement comprimée vers la Terre (parfois de plusieurs rayons terrestres), ce qui a pour conséquences l'augmentation de l'intensité du champ géomagnétique mais aussi la création et la propagation d'ondes magnétohydrodynamiques, ainsi que l'anisotropie des particules.

***La phase principale*** :

- D'une durée d'une demi-heure à plusieurs heures.
- L'indice Dst peut atteindre des valeurs negatives de quelques centaines de nT.
- La compression de la queue entraine un apport important de plasma dans les ceintures de radiation. Le courant annulaire se développe.
- Un fort champ électrique de queue rapporche la plasmapause de la Terre.
- Un champ électrique radial pointant vers l'extérieur dans le plan équatorial se développe au niveau du système courant annulaire-feuillet de plasma.

***La phase de recouvrement*** :

- Elle dure de quelques dizaines d'heures à une semaine.
- L'indice Dst retourne graduellement à une valeur normale (le champ géomagnétique revient à sa valeur d'équilibre).

- Les ions du courant annulaire sont graduellement perdus (L'expansion de la plasmasphère amène du plasma froid ionosphérique en interaction avec le courant annulaire. Les perturbations engendrées provoquent la diffusion en angles d'attaque des ions du courant annulaire et la redistribution dans le cone de perte. De plus, cette perte d'ions du courant annulaire est également due aux réactions d'échange de charges avec l'hydrogène neutre froid.)

### Les sous-tempêtes

Un autre phénomène dynamique est plus courant que celui de tempête magnétique, ce sont les **sous-tempêtes magnétiques**, qui fut décrit pour la première fois par *Akasofu* [1964]. Durant les sous-tempêtes, les aurores dans le ciel des régions polaires deviennent plus intenses, plus étendues et plus agitées. En plus de ces signatures optiques, les sous-tempêtes aurorales sont visibles dans les mesures des magnétomètres au sol et dans les valeurs de l'indice magnétique AE. Ce type d'événement peut apparaître plusieurs fois par jours.

Les perturbations magnétiques associées aux sous-tempêtes peuvent atteindre 1000 nT, c'est-à-dire environ 2% du champ magnétique total dans la région aurorale. Les courants électriques associés aux sous-tempêtes arrivent jusqu'à l'ionosphère, à une centaine de kilomètres de la surface terrestre. Ce sont les courants alignées dont nous reparlerons plus loin dans cette introduction.

Les sous-tempêtes se décomposent en trois phases [*McPherron et al.*, 1973] :

***La phase de croissance***:
La phase de croissance marque le début du phénomène de sous-tempête et est induite par des changements dans le vent solaire. Cette phase dure environ quarante minutes. Elle est initiée par une inversion de la direction de la composante nord-sud du champ magnétique interplanétaire vers le sud. Le phénomène de reconnexion entre le champ magnétique interplanétaire et le champ magnétosphérique prend place sur le front de la magnétosphère. La magnétosphère est dite "ouverte". Un transfert d'énergie provenant du vent solaire a lieu, ce qui augmente le champ électrique de convection.

D'autres phénomènes caractérisent cette phase :

- Le champ dans les lobes de la queue augmente, ce qui provoque un amincissement du feuillet de plasma.

- Le courant de queue augmente, ce qui implique un étirement des lignes de champ dans la queue de la magnétosphère. La conséquence visible de cette déformation de la queue de la magnétosphère est la descente en latitude (vers l'équateur) de l'ovale auroral.

- Le phénomène de "pseudobreakup" [13] peut avoir lieu durant cette phase.

***La phase d'expansion*** :
La phase d'expansion est le début de la phase active de la sous-tempête. Durant cette phase, la queue de la magnétosphère se décharge de l'énergie accumulée pendant la phase de croissance. Sa durée typique est d'environ une demi-heure (mais peut, dans certain cas, atteindre 2 heures).

Le début de la phase d'expansion est également ce qu'on appelle le déclenchement (*onset*) de la sous-tempête. Il est caractérisé visuellement par une intensification locale de l'ovale auroral. *Gérard et al.* [2004] ont montré que la position moyenne de l'*onset* se situait à $23.4 \pm 0.3$ heures MLT pour la précipitation aurorale des électrons et des protons. Dans certains cas, le déclenchement est clairement induit par des changements dans les caractéristiques du vents solaires ou du champ interplanétaire, dans d'autres cas la cause du déclenchement n'est pas remarquable.

La topologie de la magnétosphère est aussi modifiée au moment du déclenchement de la phase d'expansion. La théorie du déclenchement de la phase de croissance est toujours actuellement un sujet de débat. Toutefois, une explication plausible suggère comme événement critique pour le déclenchement l'apparition d'un point neutre de reconnexion dans la queue de la magnétosphère à une distance d'environ 15 à 30 rayons terrestres de la Terre, telle que le montre la Figure 22. La reconnexion magnétique a lieu entre les lignes de champ de sens opposés dans le plan équatoriale du feuillet de plasma. Les lignes de champ nouvellement reconnectées, situées vers la Terre par rapport au point X, reprennent une forme quasi dipolaires. D'autre part, les lignes du côté de la queue ne sont plus liées à la Terre. Elle forme un plasmoïde, c'est-à-dire une sorte de bulle de plasma qui s'éloigne de la Terre. Les satellites ISEE-3 et Geotail ont observé le passage de tels plasmoïdes loin dans la queue de la magnétosphère.

C'est au cours de la phase où les lignes de champ reprennent une forme quasi dipolaire, aussi appelée dipolarisation, que l'énergie de la queue est libérée. Les particules chargées du feuillet de plasma sont alors thermalisées et accélérées. Ces particules sont aussi "injectées" plus profondément dans la magnétosphère interne, proche de la Terre. Au fur et à mesure du développement de la phase d'expansion, l'aurore s'intensifie dans tout l'ovale auroral et sa limite polaire se rapproche des pôles.

***La phase de recouvrement***:
Durant la phase de recouvrement, la magnétosphère revient à son état d'équilibre. Elle peut durer environ une heure. Le feuillet de plasma se recharge petit à petit en particules chargées, venant de l'ionosphère et du vent solaire. L'ovale auroral reprend sa position

[13] événement de courte durée ressemblant à un commencement de sous-tempête mais qui ne se développe pas et n'atteint pas la puissance d'une sous-tempête

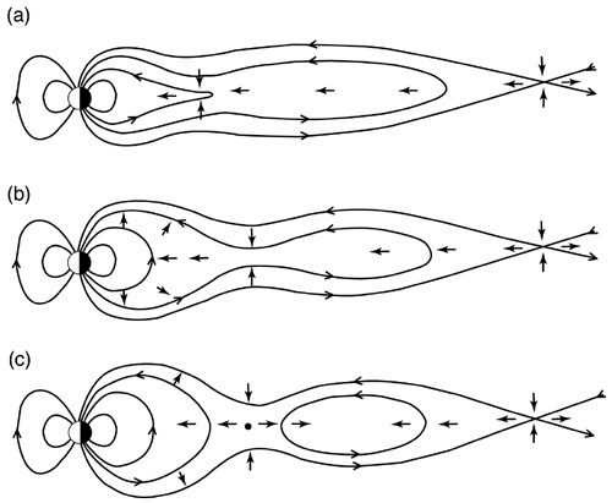


Figure 22: Topologie schématique de la magnétosphère (a) pendant le phase de croissance, (b) juste avant le déclenchement de la phase d'expansion et (c) au cours de la phase d'expansion. Sur le graphique (a), les lignes de champ sont étirées et la reconnexion du côté nuit à lieu très loin dans la queue. Juste avant le déclenchement, un point neutre (ou point X) se forme dans une région plus proche de la Terre. Lors du développement de la phase d'expansion (c), les lignes de champ reprennent une forme quasi dans le voisinage de la Terre, alors qu'un plasmoïde s'éloigne de la Terre. Les flèches visualisent la direction des flux de plasma.

moyenne et redevient relativement calme. Il arrive toutefois que, lors de la phase de recouvrement, la magnétosphère se prépare déjà au développement d'une nouvelle sous-tempête.

## La pluie polaire

Il arrive qu'au milieu de la calotte polaire, un flux incident de particules entraine une faible émission appelée pluie polaire (polar rain ou strahl). Les lignes de champ arrivant dans cette région sont les lignes de champ des lobes et du manteau de plasma, c'est-à-dire celles qui sont connectées aux lignes du champ magnétique interplanétaire. Les particules induisant ce phénomène sont des électrons rapides du vent solaire. Ces électrons sont capables de quitter le vent solaire et de se mouvoir le long des lignes de champ magnétiques dans n'importe quelle direction. La densité de ces particules est trop faible pour produire une émission visible, mais cette précipitation est observable *in situ* par des satellites.

## Les indices d'activité géomagnétique

Il existe une série d'indices, calculés à partir des mesures de magnétomètres au sol, dont le but est de qualifier l'activité géomagnétique. Je donne ici la définition de quelques indices que j'ai utilisés dans mes travaux ou que j'ai mentionnés dans cette introduction.

***Kp***

L'indice Kp est un indice planétaire d'activité magnétique caractérisant l'activité aux latitudes subaurorales. Il intègre à la fois les effets des électrojets auroraux et ceux du courant annulaire et fournit ainsi une bonne estimation du niveau planétaire moyen de l'activité magnétique d'origine magnétosphérique. Le nom "Kp" provient de l'expression "planetarische Kennziffer", qui signifie indice planétaire. L'indice Kp est établi à partir des mesures effectuées en plusieurs stations de latitudes moyennes, c'est-à-dire comprises entre $44^\circ$ à $60^\circ$ de latitude nord ou sud.

Lorsque les mesures faites dans les stations ne sont pas influencées par les courants électrojet auroraux, les conditions sont dites magnétiquement calmes. En périodes dites magnétiquement perturbées, la zone aurorale s'étend vers l'équateur et les stations enregistrent les effets du système de courant électrojet ainsi que du courant annulaire magnétosphérique et des courant alignés. L'indice Kp est calculé à partir des fluctuations des deux composantes horizontales du champ géomagnétique, sur un intervalle de trois heures. Les niveaux de perturbation locale sont déterminés en mesurant la différence entre les valeurs maximales et minimales, durant l'intervalle de trois heures, de la composante du champ horizontal la plus perturbée. L'indice Kp varie sur une échelle de valeurs de 0 à 9. Nous utilisons dans notre étude les indices Kp fournit pas le "GeoForschungsZentrum" (GFZ) à Potsdam, évalué à partir de 13 stations subaurorales.

***Ap***

L'indice tri-horaire Ap est, comme le Kp, un indice planétaire d'activité magnétique. Il est lié de l'indice Kp comme le montre le tableau 2.

| Kp | Ap | Kp | Ap |
|---|---|---|---|
| 0o | 0 | 5- | 39 |
| 0+ | 2 | 5o | 48 |
| 1- | 3 | 5+ | 56 |
| 1o | 4 | 6- | 67 |
| 1+ | 5 | 6o | 80 |
| 2- | 6 | 6+ | 94 |
| 2o | 7 | 7- | 111 |
| 2+ | 9 | 7o | 132 |
| 3- | 12 | 7+ | 154 |
| 3o | 15 | 8- | 179 |
| 3+ | 18 | 8o | 207 |
| 4- | 22 | 8+ | 236 |
| 4o | 27 | 9- | 300 |
| 4+ | 32 | 9o | 400 |

Table 2: Tableau de transformation Kp - Ap

***Dst***

L'indice Dst [14] caractérise l'activité du courant annulaire. Son calcul se fait à partir d'une moyenne horaire des perturbations magnétiques (de la composante H, nord-sud, du champ magnétique terrestre) mesurées par des magnétomètres localisés dans des stations de mesures proches de l'équateur terrestre. Cet indice est approximativement proportionnel à l'énergie de la tempête magnétique.

***$F_{10.7}$***

L'indice de *Flux Radio Solaire Décimétrique* $F_{10.7}$ représente l'intensité du flux émis par le Soleil en rayonnement radio à la longueur d'onde $\lambda$ = 10,7 cm, avec une résolution temporelle de 1 jour. Il est mesuré en unités de flux solaire, où chaque unité est égale à $10^{-22}$ Watts $m^{-2}$ $Hz^{-1}$. Cet indice n'est pas un indice d'activité magnétosphérique au sens propre, mais un indice d'activité solaire. L'activité du Soleil gouverne l'apport d'énergie dans l'environnement ionisé de la Terre : cet indice est indispensable comme paramètre d'entrée des modèles de thermosphère et d'ionosphère terrestres que nous utilisons.

**$\bar{F}_{10.7}$**

[14] "D" pour "disturbance" = perturbation, "st" pour "storm"= tempête

L'indice $\bar{F}_{10.7}$ est la valeur moyenne de $F_{10.7}$ sur une période de 90 jours centré sur le jour considéré. Cette période de temps correspond à environ trois révolutions du Soleil sur lui-même. L'indice représente donc l'état moyen du Soleil à la période considérée.

# L'ionosphère

L'atmosphère terrestre joue également un rôle dans la formation des aurores : les particules provenant de la magnétosphère, précipitent et interagissent avec les constituants atmosphériques pour produire l'émission aurorale. La composition atmosphérique est donc un facteur important dans l'émission aurorale.

La gravitation terrestre provoque une stratification horizontale du gaz atmosphérique. On peut donc définir plusieurs couches atmosphériques selon la densité et la température du gaz qui les composent. Dans le contexte auroral, seules les couches supérieures de l'atmosphère jouent un rôle, puisque la perte d'énergie subie par les particules aurorales précipitant ne leur permet pas d'atteindre des altitudes plus basses que 85 km environ. Nous décrirons donc ici principalement la couche où les réactions aurorales ont lieu, c'est-à-dire l'ionosphère. Cependant pour plus de clarté, nous replaçons d'abord cette couche dans son contexte.

## L'atmosphère terrestre

Plusieurs types de structures de l'atmosphère terrestre sont proposés selon qu'on analyse la température ou la composition de celle-ci. La Figure 23 représente la structure thermique de l'atmosphère, c'est-à-dire ses différentes couches et son profil moyen de température en fonction de l'altitude. A partir de la surface du sol, on rencontre :

- la **troposphère** où la température décroît jusqu'à environ 10 km d'altitude. La limite supérieure de la troposphère s'appelle la tropopause et correspond à un minimum de température.
- la **stratosphère** où la température augmente jusqu'à environ 50 km d'altitude. C'est dans cette couche que se situe la couche d'ozone et l'augmentation de température est due à l'absorption du rayonnement ultraviolet solaire par $O_3$. La stratosphère est limité en altitude par la stratopause, où la température est maximale.
- la **mésosphère** où la température décroît à cause du refroidissement radiatif. La mésopause, limite supérieure de la mésosphère est située vers 85 km d'altitude et la température y atteint le point le plus froid de l'atmosphère terrestre, environ -90°C.
- la **thermosphère** où la température augmente de nouveau rapidement. La température absolue dans la thermosphère dépend de l'activité solaire et varie entre 700 et

2500 K. Le rayonnement UV solaire responsable de l'augmentation de température est aussi responsable de l'ionisation de l'atmosphère neutre, créant l'**ionosphère**.

- L'**exosphère**, au-delà de 500 km d'altitude, est la zone où les collisions sont suffisamment rares pour que les particules suivent des trajectoires quasi balistiques. Si leur vitesse est suffisante et dépasse la vitesse de libération, les constituants les plus légers (H et He) s'échappent du champ gravitationnel de la Terre.

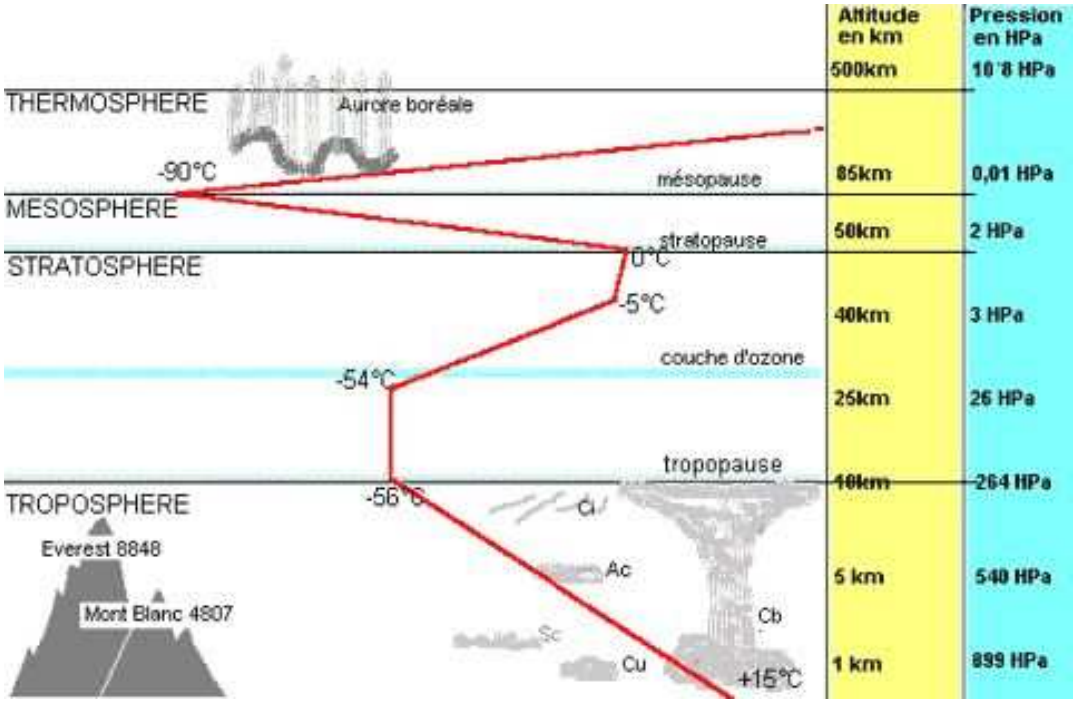


Figure 23: Structure thermique de l'atmosphère terrestre et profil de température

Une autre classification peut être proposée, relative à la composition de l'atmosphère.

- L'**homosphère**, entre 0 et 100 km d'altitude, est la zone où la composition chimique est uniforme en ce qui concerne la proportion des constituants inertes : on y trouve principalement de l'azote et de l'oxygène moléculaires ($N_2$ et $O_2$) en proportion respective de 78 et 21 %.

- L'**hétérosphère**, au delà de 100 km d'altitude, est la région de l'atmosphère de composition non uniforme. La composition varie en fonction de l'altitude. Vers 300 km d'altitude, l'oxygène atomique domine. Les constituants légers tels que l'hydrogène et l'hélium deviennent de plus en plus abondants au fur et à mesure que l'altitude augmente.

## Caractéristiques physiques de l'ionosphère terrestre

Dans cette introduction, nous présentons une description des caractéristiques physiques de l'ionosphère. L'aspect mathématique des processus de transport des particules dans l'ionosphère ainsi que les conductivités ionosphériques sont décrits dans l'introduction du chapitre 4 car c'est principalement dans ce chapitre que ces notions sont utilisées.

L'ionosphère est la région de l'atmosphère supérieure à 70 km d'altitude. Son épaisseur vaut environ 1000 km. Cette région est caractérisée par sa composition ionique : les atomes et molécules neutres de l'atmosphère subissent soit une photoionisation par le rayonnement solaire ou autre (par exemple le rayonnement auroral), soit des collisions avec des particules diverses (particules cosmiques, solaires, magnétosphériques ou ionosphériques). La Figure 24 représente la composition ionique et en atomes neutres de l'ionosphère du côté faisant face au Soleil. Remarquons que les processus du côté nuit ne sont pas identiques à celles du côté jour puisque le rayonnement solaire n'y joue pas de rôle.

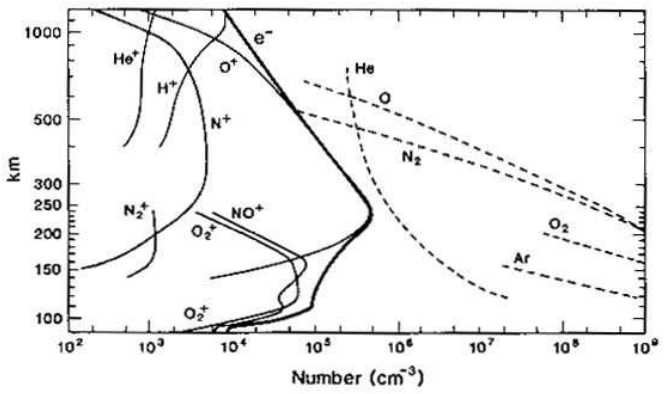


Figure 24: Composition de l'ionosphère du côté du Soleil. Densité volumique des composés neutres et ioniques ionosphériques en fonction de l'atitude. Ces valeurs sont basées sur des mesures de spectromètres de masse.

La composition de l'ionosphère permet de la décomposer en trois couches principales, identifiées par leur interaction différente avec les ondes radio :

- la couche D sous 90 km d'altitude,
- la couche E entre 90 et 130 km d'altitude, dont les composants principaux sont les ions $O_2^+$ et $NO^+$,
- la couche F au-dessus de 130 km d'altitude, dont le composant principal est l'ion $O^+$.

La densité du plasma ionosphérique varie selon certaines circonstances. En plus de la variation diurne déjà citée, les densités peuvent varier à cause des structures spatiales et temporelles dans la précipitation de particules ionisées. La densité de la couche E dans l'ovale auroral du côté nuit peut être très différente selon l'activité aurorale. Une variation dans les densités moyennes de plasma ionosphérique est aussi présente durant le cycle solaire. Les densités sont plus élevées pendant les années proches d'un maximum d'activité solaire que lors d'un minimum.

## La convection ionosphérique

La combinaison des processus de reconnexion et de processus visqueux au niveau de la magnétopause et dans la queue de la magnétosphère sont à la base de la création du champ électrique de convection magnétosphérique (voir convection magnétosphérique et cycle de Dungey (Figure 16)). Ce champ se projette au niveau de la haute ionosphère le long des lignes de champ magnétique, ce qui a pour conséquence la dérive du plasma ionosphérique dans la direction perpendiculaire au champ électrique et au champ magnétique. Le mouvement du plasma forme les cellules de convection.

La Figure 25 montre l'image de la convection magnétosphérique dans l'ionosphère, vue du pôle nord de la Terre. Elle consiste en deux cellules de lignes ouvertes qui se meuvent en direction opposée au Soleil au travers de la calotte polaire et de lignes de champ fermées qui se dirigent vers le Soleil aux latitudes plus basses. La vitesse moyenne de ce flux ionosphérique est de plusieurs centaines de mètres par seconde. Le cycle total a une durée d'environ 12 heures.

## Les courants ionosphériques

Trois types de courant circulent dans l'ionosphère :

- le courant parallèle (dans la direction $\parallel \mathbf{B}$ et $\parallel \mathbf{E}$)
- le courant de Pedersen (dans la direction $\parallel \mathbf{B}$ et $\perp \mathbf{E}$)
- le courant de Hall (dans la direction $\perp \mathbf{B}$ et $\perp \mathbf{E}$)

Les courants ionosphériques circulent tant en périodes calmes qu'en périodes actives. En période de forte activité magnétique, des courants sont associés à la précipitation aurorale.

La convection ionosphérique est à l'origine de **courants de Hall**. La convection donne un mouvement de dérive aux particules chargées dans la direction $\mathbf{E} \times \mathbf{B}$. Dans les plasmas où les collisions ne sont pas négligeables, les ions se meuvent beaucoup plus lentement que les électrons (les fréquences des collisions ions-espèces neutres sont beaucoup plus grandes

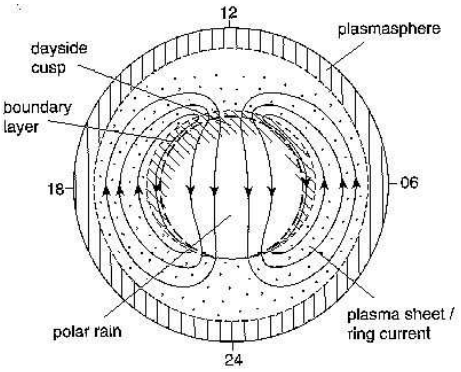


Figure 25: Vue polaire de l'ionosphère, montrant le flux de plasma associé au cycle de Dungey, ainsi que les zones principales où les particules de caracteristiques différentes se meuvent le long des lignes de champ magnétosphérique vers la haute atmosphère et l'ionosphère. Le cercle intérieur plus foncé montre la frontière entre les lignes de champ ouvertes à hautes latitudes et les lignes de champ fermées à plus basses latitudes.

que les fréquences de collisions électrons-espèces neutres vu leur taille respective). La différence de vitesses des ions et des électrons est à la base de la création de ces courants de Hall.

### L'électrojet auroral

Des courants horizontaux circulent dans les régions D et E de l'ionosphère aurorale et portent le nom d'**électrojet auroral**. Sa formation est due au champ électrique horizontal qui existe dans l'ionosphère aurorale, dont l'intensité est plus importante que sous les latitudes plus basses. Le cas de l'électrojet auroral est remarquable par la force et la persistence des courants. Son intensité peut dépasser le million d'Ampères. Durant les périodes d'activité magnétique calme, l'électrojet est confiné à l'ovale auroral. Alors que pendant les périodes perturbées, l'électrojet augmente en intensité et s'étend vers les latitudes plus hautes et plus basses. Cette expansion résulte de l'augmentation de la précipitation de particules et des champs électriques ionosphériques. L'électrojet est du type des courants de Hall. Selon le moment de la journée, les courants peuvent circuler de l'est vers l'ouest (*westward electrojet*) ou dans le sens contraire (*eastward electrojet*). La Figure 26 représente schématiquement l'électrojet auroral.

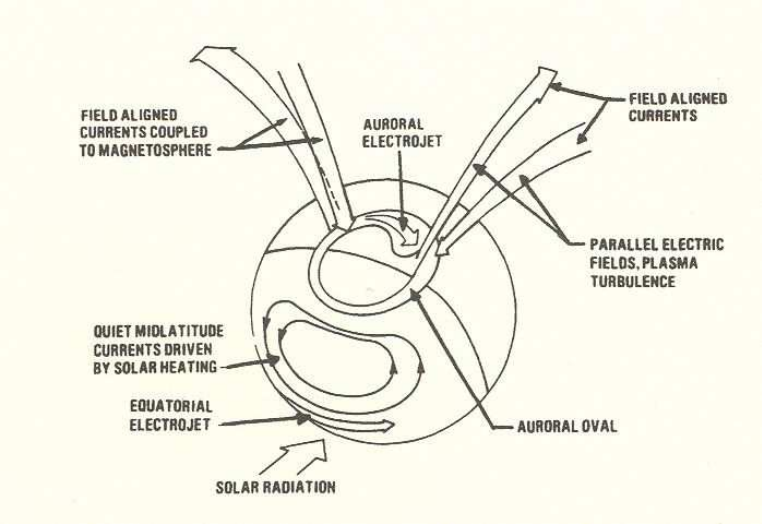


Figure 26: Schéma représentant les différents courants connectés à l'électrojet auroral.

### Les courants alignés

De par le couplage entre l'ionosphère et la magnétosphère, un autre type de courants prend place durant les périodes perturbées : les **courants alignés** au champ magnétique (*field-aligned currents*) aussi appelés "courants de Birkeland". De façon imagée, nous pouvons dire que les courants de queue magnétosphériques prennent un autre chemin et sont déviés vers l'ionosphère. Les courants circulent vers la Terre ou vers l'Espace selon les endroits. La Figure 27 présente la configuration des courants alignés ainsi que les régions où les courants alignés "entrent" et "sortent" de l'ovale auroral.

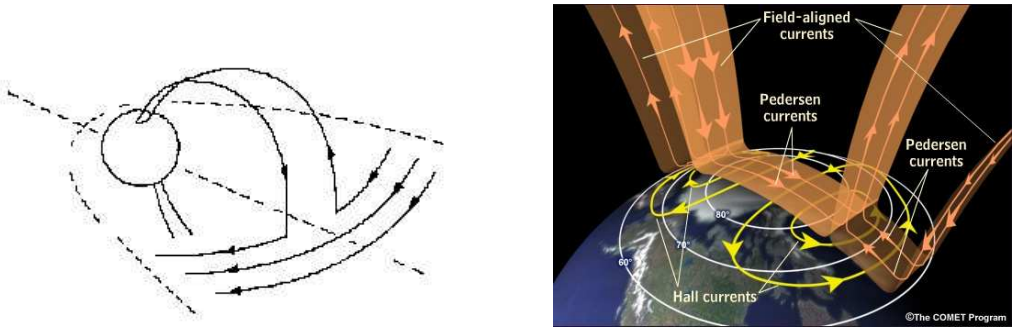


Figure 27: Courants alignés

Ces courants $J_{\parallel}$ alignés au champ magnétique sont associés à une divergence des courants de Pedersen $\mathbf{I}_P$ dans l'ionosphère. Les courants alignés peuvent s'écrire [*Lyons*, 1992]

$$J_{\parallel} = -\nabla_{\perp} \cdot \mathbf{I}_P \tag{28}$$

considérant le champ magnétique vertical dans l'ionosphère dans les régions polaires et négligeant la divergence du courant de Hall par rapport à la divergence du courant de Pedersen [*Lyons*, 1992]. Le courant de Pedersen $\mathbf{I}_P$ intégré sur la hauteur de l'ionosphère, considérant celle-ci comme une coquille conductrice, peut s'écrire

$$\mathbf{I}_P = \Sigma_P \mathbf{E} \tag{29}$$

où $\Sigma_P$ est la conductance de Pedersen et $\mathbf{E}$ le champ électrique. Le potentiel électrique couvrant la calotte polaire est illustré à la figure 28. Comme généralement les changements dans le champ électrique contribuent plus au gradient de $\mathbf{I}_P$ que les changements dans la conductivité de Pedersen, il est supposé que $J_{\parallel}$ dépend principalement de la divergence du champ électrique $\nabla \cdot \mathbf{E}$ . Ainsi, $J_{\parallel}$ devrait être dirigé vers le haut dans la région du renversement de convection du côté du crépuscule où $\nabla \cdot \mathbf{E} < 0$ et dirigé vers le bas dans la région du renversement de convection du côté du matin. Des courants alignés circulent donc le long des lignes de champ magnétique, vers le haut ou vers le bas. La convection du pied des lignes de champ magnétique forme deux cellules. La région de renversement de convection correspond à la région dans les cellules où les mouvements « midi vers minuit » et « minuit vers midi » s'inversent.

Le cône de perte est très petit le long des lignes de champ magnétique. Seule une faible fraction des électrons magnétosphériques (ceux qui sont principalement la cause du courant vers le haut et des aurores) contribue au courant ascendant. Cependant, si une différence de potentiel alignée au champ magnétique existe, elle va accélérer les particules vers l'atmosphère et augmenter la composante parallèle de la vitesse, ce qui aura pour effet que leur angle d'attaque sera mieux aligné au champ magnétique. Ce processus augmente le nombre de particules dans le cône de perte. Ainsi, l'intensité de $J_{\parallel}$ devrait augmenter avec la différence de potentiel.

A partir des équations 28 et 29, par un modèle simplifié d'ionosphère utilisant des valeurs plausibles pour les différentes grandeurs dans l'ionosphère, *Lyons* [1992] montre qu'une différence de potentiel de quelques kilovolts est nécessaire pour maintenir la continuité du courant dans l'ionosphère aux alentours du renversement de la convection du côté du crépuscule. Ainsi, pour produire les champs alignés parallèles, tout ce qui est nécessaire est un courant aligné au champ, dirigé vers le haut et uniforme, ainsi qu'une diminution de densité. L'accélération des particules est nécessaire pour conduire le courant imposé de sorte qu'il y ait continuité. La densité de courant aligné augmente lorsque l'altitude diminue à cause de la convergence du champ magnétique. Comme les électrons buttent sur leur point miroir et sont renvoyés vers le haut, il existe une altitude sous laquelle la densité de courant ne peut plus être transportée par le plasma existant à cette altitude et

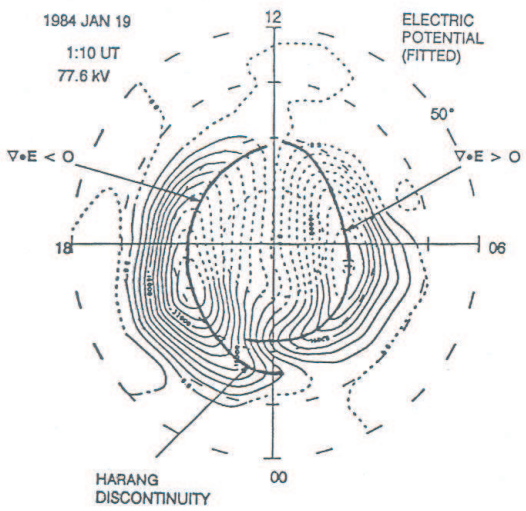


Figure 28: Potentiel électrique estimé sur l'ensemble de la calotte polaire, obtenu par *Richmond et al.* [1988] à partir de mesures au sol des champs électriques et courants ionosphériques. Les équipotentielles sont en pointillés lorsque les incertitudes sur le potentiel estimé sont supérieures à 50% [*Lyons*, 1992].

en dessous. Cette altitude est la limite supérieure de la région d'accélération des électrons auroraux. La densité de courant devant être transportée étant trop grande pour la densité de plasma existant, un champ électrique doit donc s'installer pour accélérer les électrons et permettre au courant de circuler [*Knight*, 1973]. Lors des sous-tempêtes, le courant aligné augmente fortement, la densité de courant est donc plus importante encore et la densité de plasma peut difficilement transporter ce courant. La conséquence est la création d'un champ électrique plus intense qui permet la continuité du courant et qui accélère de façon plus intense les électrons, provoquant ainsi des arcs auroraux intenses. La région d'accélération des électrons est comprise entre 1,5 et 2 rayons terrestres d'altitude [*Mozer and Hull*, 2001].

Pour obtenir l'expression du courant parallèle $j_{\parallel}$ en fonction du potentiel $\Phi_{\parallel}$, *Knight* [1973] a intégré le produit $-ev_{\parallel}f(\mathbf{v})$ sur tout l'espace des vitesses, où $e$ est la charge électronique, $v_{\parallel}$ la composante de la vitesse électronique parallèle au champ magnétique et $f(\mathbf{v})$ la fonction de distribution des vitesses. En supposant une distribution symétrique de $v_{\parallel}$ pour les électrons piégés [15], la seule contribution au courant vient des trajectoires de « traversée directe », provenant du feuillet de plasma (région S dans l'espace des vitesses) et de l'ionosphère (région E), ce qui correspond à l'expression homologue où $v_{\parallel}$ est négatif.

[15] les vitesses des électrons piègés sont distribuées de façon similaires pour les particules se mouvant en direction du pôle et celles s'éloignant.

L'intégrale s'écrit

$$j_{\parallel} = -e \int_S v_{\parallel}(f_S - f_E) d^3v \tag{30}$$

Si on suppose que les électrons magnétosphériques possèdent une distribution en énergie maxwellienne et une distribution en angle d'attaque isotrope, cette expression devient [*Knight*, 1973; *Lemaire and Scherer*, 1974] :

$$j_{\parallel} = en(\frac{K_{th}}{2\pi m_e})^{1/2} R\{1 - (1 - R^{-1}) \exp[\frac{-e\Phi_{\parallel}}{K_{th}(R-1)}]\} \tag{31}$$

où $K_{th}$ est l'énergie thermique des électrons, $m_e$ la masse de l'électron, $e$ la charge de l'électron et $n$ la densité électronique. Ici $R = \frac{B_E}{B_{\Phi_{\parallel}}}$ est le rapport du champ magnétique dans l'ionosphère ($B_E$) et du champ magnétique au sommet de la variation de potentiel aligné ($B_{\Phi_{\parallel}} = B_S$).

# Les mécanismes de précipitation aurorale

Nous avons décrit précédemment les mécanismes déclencheurs et les phases des sous-tempêtes magnétiques. Leur conséquence est de provoquer la précipitation des particules chargées du feuillet de plasma vers l'ionosphère. Nous allons, dans ce paragraphe, décrire les mécanismes de précipitation, c'est-à-dire les phénomènes induits dans la magnétosphère lors des sous-tempêtes qui ont pour conséquence d'accélérer les électrons et les ions magnétosphériques vers l'ionosphère.

## Les mécanismes spécifiques aux électrons

Les aurores produites par la précipitation d'électrons sont de deux types selon leur structure. La partie équatoriale de l'ovale auroral est la région où les **aurores diffuses** prennent place. Leur nom provient de l'absence de structure spatiale dans ce type d'aurore. Les **aurores discrètes** sont localisées dans la région polaire de l'ovale aurorale et sont les types d'aurores les plus intenses. Le terme "discrète" est donné par opposition au terme "diffuse" et est le terme générique des arcs auroraux. Ce type d'aurore est lié à l'accélération des électrons par des champs électriques alignés au champ magnétique.

### Les auroraux diffuses

Les aurores diffuses électroniques sont provoquées par une précipitation d'intensité plus faibles que les arcs auroraux et les particules sont distribuées sur un domaine d'énergie plus large [*Lyons*, 1992]. De telles précipitations aurorales résultent d'une précipitation directe des particules le long des lignes de champ magnétosphérique, sans accélération par

un champ électrique.

Comme nous l'avons décrit plus haut, les particules qui atteignent l'atmosphère sont celles dont le vecteur vitesse se trouve dans le cône de perte, c'est-à-dire celles dont l'angle d'attaque $\alpha_e$ est tel que $\sin\alpha_e < \sqrt{\frac{B_e}{B_i}}$ où $B_i$ est le champ magnétique à l'altitude de référence choisie et $B_e$ le champ à l'équateur. Seule une petite fraction des particules piégées pourrait précipiter si le premier invariant adiabatique était toujours conservé. En effet, vu les valeurs des champs $B_e$ et $B_i$ ($B_e \sim 50nT$ et $B_i \sim 50000nT$), le cône de perte est un angle solide relativement petit, soutendu par un angle de l'ordre de 5 degrés et se vide donc rapidement. Il existe un processus qui redistribue les angles d'attaque et qui par conséquent permet de remplir le cône de perte. Ce processus de **diffusion en angle d'attaque** est la conséquence d'interactions entre les ondes de plasma et les particules. Les ondes dans les plasmas sont principalement des ondes électromagnétiques. Les particules interagissent avec les ondes polarisées circulairement : les électrons avec les ondes circulaires droites et les protons avec les ondes circulaires gauches. Les particules entrent en résonance avec ces ondes par le phénomène de gyrorésonance. Ce type de résonance est associé au mouvement de giration des particules. Elle a lieu lorsque la fréquence de giration est semblable à la fréquence de l'onde et a pour conséquence d'augmenter l'amplitude des ondes et donc leur énergie. La diminution de l'angle d'attaque compense l'augmentation d'énergie des ondes.

### Les arcs auroraux

Les arcs auroraux sont produits par des particules chargées ayant subi une accélération par un champ électrique [*Lyons*, 1992], le même champ électrique que celui dont résultent les courants alignés au champ magnétique du type de ceux décrits ci-dessus.

La Figure 29 présente schématiquement les courants et les champs électriques à l'origine des arcs auroraux électroniques, dans le plan d'un méridien. Le courant circule le long des lignes rouges. Le courant ascendant est associé à des électrons descendants le long des lignes de champ magnétique. Les équipotentielles entourant les lignes de champ magnétique correspondent aux autres lignes de champ magnétique (vu leur grande conductivité). Elles sont considérées comme des équipotentielles jusqu'à ce qu'un phénomène limite leur conductivité. Dans la théorie de *Knight* [1973] (décrite dans le paragraphe sur les courants alignés), ce phénomène est dû à la convergence des lignes de champ magnétique. La densité de courant est alors trop importante pour être transportée par la densité de plasma. La solution est la création d'un champ électrique qui accélère les électrons. Cette région correspond à l'endroit de la Figure 29 où les équipotentielles se ferment. Les arcs auroraux sont produits à la base de la branche de courant montant (appelé « return current »), c'est-à-dire où les électrons entrent dans l'ionosphère. Le circuit de courant est fermé dans l'ionosphère grâce aux courants ionosphériques de Hall et de Pedersen.

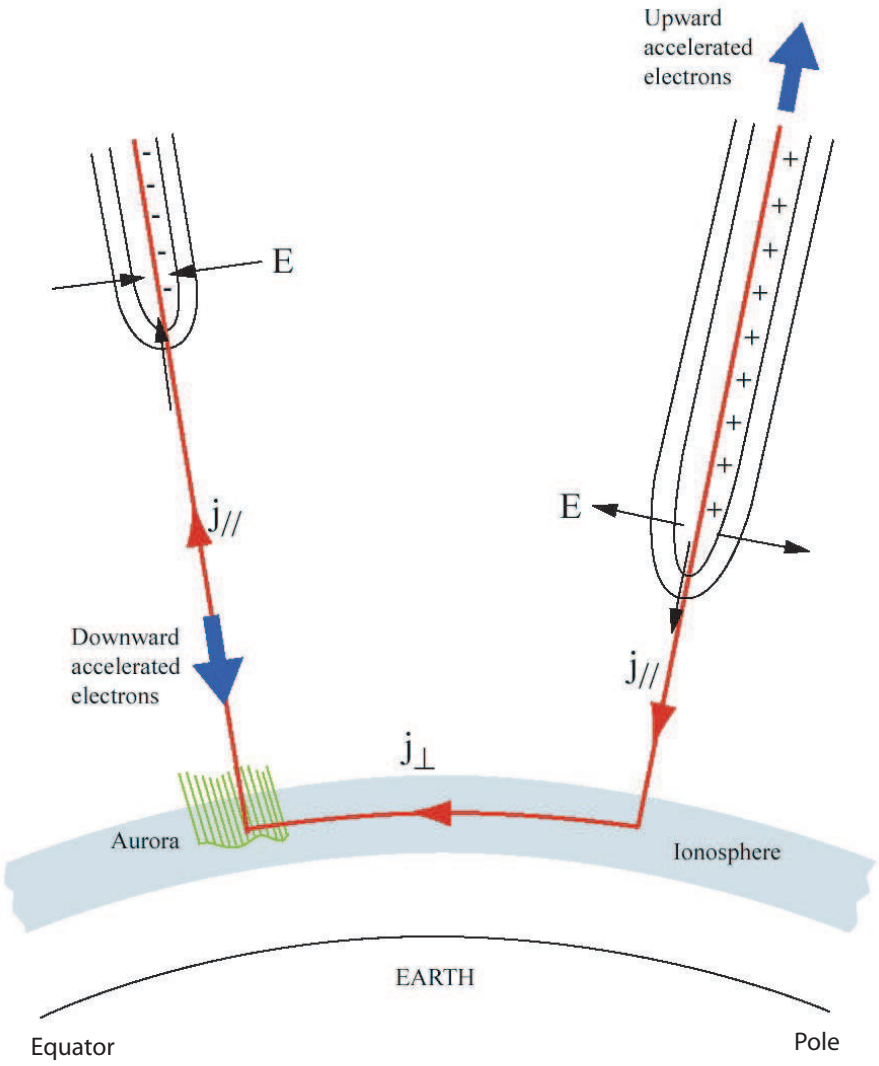


Figure 29: Structures d'accélération dans le circuit de courant auroral. Ce schéma montre une structure de potentiel chargée négativement représentative de l'aurore (à gauche) et une structure chargée positivement représentative de courant de retour auroral (à droite). Cette vue est dans le plan d'un méridien. Le courant descendant est situé du côté du pôle et le courant ascendant du côté de l'équateur. Les deux branches des contours des équipotentielles se ferment respectivement à des altitudes typiques de 5000 à 8000 km dans la région de courant ascendant au-dessus de l'aurore et vers 1500-3000 km dans la région du courant de retour. Au-delà, elles s'étendent vers de très hautes altitudes le long du champ géomagnétique, avec une forme en U caractéristique.

Notons que d'autres processus que ceux décrits par *Knight* [1973] interviennent probablement dans la création des champs alignés et dans l'accélération des électrons provoquant les arcs auroraux. *Lyons* [1992] accompagne le processus décrit ci-dessus de deux autres mécanismes, à plus basse altitude, qui permettent de rester cohérents avec la notion de neutralité du plasma. *Borovsky* [1993] propose 22 mécanismes théoriques permettant d'expliquer les arcs auroraux. Cependant, aucun modèle construit sur base de ces mécanismes ne permet de reproduire la faible épaisseur caractéristique des arcs auroraux.

## Les mécanismes spécifiques aux protons

Par la nature des protons, leur mouvement le long des lignes de champ est différent de celui des électrons. Le mouvement des particules aurorales le long des lignes de champ comprend une composante giratoire. Le mouvement circulaire se fait dans le sens direct pour les électrons et dans le sens horlogique pour les protons. Le rayon de giration (Equation 12) est directement proportionnel à la masse de la particule chargée. Comme la masse du proton est 1836 fois plus élevée que celle de l'électron, le rayon de giration du mouvement des protons est beaucoup plus grand que celui des électrons. De plus, les protons auroraux subissent des collisions avec les constituants neutres de l'atmosphère (voir chapitre I.2.1.). Durant une collision, un proton peut capturer un électron et devenir un atome d'hydrogène neutre. Comme sa charge est alors nulle, l'atome n'est plus soumis à l'influence du champ géomagnétique. Il peut alors dériver jusqu'à ce qu'à son tour, il entre en collision avec un constituant neutre atmosphérique. Il a alors une certaine probabilité de s'ioniser et de redevenir un proton qui continue son parcours en perdant son énergie au fur et à mesure des collisions successives. Ces deux mécanismes ont une influence importante sur la morphologie de l'aurore à protons. Ce type d'aurore est systématiquement diffuse et ne possède jamais les caractéristiques d'un arc auroral. De plus, la dérive des atomes neutres d'hydrogène ainsi que le fait que les protons et les électrons subissent un mouvement de dérive différent (les électrons dérivent vers l'Est et les protons vers l'Ouest sous l'influence principale du gradient du champ magnétique) permettent de comprendre pourquoi les régions de précipitation peuvent être différentes et la morphologie de l'aurore à protons peut être différente de celle de l'aurore électronique.

Il existe des mécanismes d'accélération des protons identiques à ceux des électrons. Lors des sous-tempêtes et tempêtes, certains mécanismes transmettent de l'énergie à l'ensemble du plasma et provoquent l'accélération autant des protons que des électrons. Cependant, d'autres mécanismes sont spécifiques aux protons et diffèrent de ceux qui accélérent les électrons. Nous donnons ci-après un exemple de processus d'accélération des protons auroraux, mais cette liste n'est pas exhaustive.

Un des principaux processus affectant les protons est dû à la brisure des invariants adiabatiques. Dans la région isotrope, là où les invariants adiabatiques ne sont plus conservés,

c'est le mécanisme de diffusion du feuillet de courant de queue (tail current sheet scattering - TCS) qui est la cause du remplissage du cône de perte, du moins du côté nuit (du côté jour, d'autres mécanismes entrent en jeu, également contrôlés par la forme du champ géomagnétique [*Sergeev et al.*, 1997]). Ce processus de diffusion en angle d'attaque des particules dans le feuillet de plasma dans la queue de la magnétosphère est dû à la non -adiabaticité (ou la stochastisation) du mouvement des particules dans cette région où le champ magnétique n'est pas du type dipolaire. Les déviations au mouvement adiabatique sont les plus importantes dans le plan de l'équateur où le phénomène d'accélération des protons a alors lieu efficacement. *Sergeev et al.* [1993] ont modélisé la position de la frontière IB dans le plan équatorial de la queue de la magnétosphère à environ 7 rayons terrestres ($R_E$) pour des protons de 80 keV. Le mécanisme d'accélération a donc lieu à des distances plus grandes que 7 $R_E$ de la Terre, dans le plan équatorial. *Zelenyi et al.* [1990] donnent une description analytique des trajectoires des ions. Selon leur modèle, le remplissage du cône de perte des protons est dû au renversement de la composante verticale du champ magnétique au niveau de l'équateur dans le feuillet de plasma. Comme cette précipitation 'stochastique' a lieu en absence de toute interaction onde-particule, elle peut avoir lieu même durant des conditions géomagnétiques calmes, expliquant ainsi pourquoi une précipitation de protons (et un signal dans la caméra SI12) est observée de manière quasi-permanente.

## Distribution énergétique des particules incidentes

La distribution des vitesses des particules en fonction de leur énergie est généralement représentée sous forme analytique pour en simplifier le traitement. Pour les électrons auroraux, nous considérons que cette distribution est maxwellienne [*Strickland et al.*, 1993]. En terme de flux, la fonction de distribution des particules en fonction de l'énergie peut s'écrire :

$$f(E) = \frac{Q_0}{2\pi E_0^2}\frac{E}{E_0}exp(-\frac{E}{E_0}) \tag{32}$$

où $E_0$ est l'énergie caractéristique des électrons et $Q_0$ est le flux total d'énergie transporté par la distribution (en $erg/cm^2.sec$). L'énergie caractéristique est relié à l'énergie moyenne par la formule $E_0 = \frac{<E>}{2}$.

Dans le cas des protons, nous utilisons l'approximation de la distribution par une fonction Kappa $\kappa$ [*Lyons and Evans*, 1984] s'écrivant :

$$f(E) = \frac{Q_0}{2\pi E_0^2}\frac{(\kappa-1)(\kappa-2)}{\kappa^2}\frac{E}{E_0}\frac{(\kappa E)^{\kappa+1}}{(E+\kappa E_0)^{\kappa+1}}) \tag{33}$$

où $\kappa$ est une constante dont la valeur influence la forme de la distribution. Il a été montré statistiquement que $\kappa = 3.5$ décrivait au mieux le cas des protons auroraux [*Hubert et al.*, 2001]. L'énergie caractéristique des protons est liée à leur énergie moyenne par la formule

$E_0 = (\frac{\kappa-2}{\kappa})\frac{<E>}{2}$.

# Les mécanismes d'émission aurorale

Les particules aurorales incidentes chargées positivement ou négativement entrent dans l'ionosphère où elles subissent des collisions élastiques et inélastiques avec les constituants neutres ionosphériques. Divers processus se déroulent : ionisation et excitation des constituants atmosphériques, dissociation des molécules, échauffement de l'atmosphère supérieure et production de rayons X par Bremsstrahlung. Au cours des collisions, l'énergie cinétique des particules incidentes sert soit à exciter les modes translationnel, vibrationnel et rotationnel des molécules atmosphériques, soit à exciter les électrons des couches extérieures, du niveau fondamental vers un niveau supérieur, soit à ioniser un constituant. Lorsque ces modes excités retombent dans leurs états fondamentaux, il y a émission d'un certain rayonnement caractéristique. Les émissions liées aux modes de vibration, de rotation et de translation ont des longueurs d'ondes dans l'infrarouge, celles liées aux transitions électroniques se situent dans les domaines visible et ultraviolet. Le spectre auroral contient donc les raies atomiques et les bandes d'émission moléculaires des constituants ionosphériques principaux, auxquelles s'ajoutent quelques émissions dues à des espèces minoritaires telles que NO, He et $CO_2$. Nous donnons ici quelques exemples d'émissions aurorales dans le domaine ultraviolet produites par collisions électroniques et protoniques. Ces exemples sont les principales émissions aurorales dans l'ultraviolet lointain observé par les instruments FUV à bord du satellite IMAGE.

## Les bandes LBH

La molécule $N_2$ est une molécule diatomique homonucléaire à plusieurs électrons. Connaissant la structure électronique des atomes N : $1s^2\ 2s^2\ 2p^3$, il est possible de construire la structure en orbitales moléculaires de ce type de molécules. Si A et B symbolisent les deux noyaux N, les orbitales moléculaires de cette molécule sont $1s_A$, $1s_B$, $1\sigma_g$, $1\sigma_u$, $2\sigma_u$, $1\pi_u$, $1\pi_g$, $2\pi_u$ sur lesquelles se répartissent les 14 électrons.

Dans le cas de l'état fondamental $N_2$ ($X\ ^1\Sigma_g^+$), les électrons se répartissent comme suit :

$$N_2(1s_A)^2(1s_B)^2(1\sigma_g)^2(1\sigma_u)^2(2\sigma_u)^2(1\pi_u)^4$$

Les électrons auroraux incidents peuvent, par collision, exciter la molécule $N_2$ dans l'état a $^1\Pi_g$ dont la répartition électronique est :

$$N_2(1s_A)^2(1s_B)^2(1\sigma_g)^2(1\sigma_u)^2(2\sigma_u)^2(1\pi_u)^3(1\pi_g)^1$$

La désexcitation électronique interdite $N_2(a^1\Pi_g) \longrightarrow N_2(X^1\Sigma_g^+)$ émet un rayonnement de longueur d'onde dans le domaine UV. Comme de nombreux sous-niveaux vibrationnels et

rotationnels sont également excités, une série de raies de longueur d'onde différentes sont visibles dans ce spectre de désexcitation, appelé LBH (Lyman-Birge-Hopfield). Ce spectre s'étend sur le domaine de longueur d'onde compris entre 120 et 190 nm.

## Les raies de l'oxygène neutre atomique OI

L'oxygène neutre peut être excité par collision électronique. La désexcitation émet une série de multiplets dont les raies les plus intenses ont pour longueur d'onde $\lambda$ =130.4 nm et $\lambda$ =135.6 nm. Le multiplet à $\lambda$ =130.4 nm est le résultat produit par la désexcitation des électrons du niveau $^3S_1^0$ vers les trois niveaux $^3P_2$ ,$^3P_1$ et $^3P_0$ . C'est en fait un triplet de longueur d'onde 130,21 nm, 130,48 nm et 130.60 nm. Le second multiplet à 135.6 nm est produite par un doublet électronique $^5S_1^0 \longrightarrow {}^3P_{2,1}$ dont les longueurs d'onde respectives sont $\lambda$ =135.56 nm et $\lambda$ =135.85 nm. Cette transition est dipolaire interdite.

## Les raies de l'azote neutre NI

L'azote neutre, excité par collision électronique, émet un multiplet à la longueur d'onde $\lambda$ =149.3 nm. Elle est due au doublet $(3s)^2P^0_{1/2,3/2} \longrightarrow (2p^3)^2D^0_{3/2,5/2}$ dont les longueurs d'onde respectives sont $\lambda$ =149.3 nm et $\lambda$ =149.5 nm [*Meier*, 1991].

## L'émission Lyman-$\alpha$

Les protons incidents échangent des charges avec les constituants ionosphériques. Les atomes d'hydrogène H énergétiques ainsi créés vont réagir à leur tour et se transformer en protons énergétiques $H_f^+$ qui interagissent avec les constituants ionosphériques selon les réactions 34. Ces processus correspondent à l'échange d'énergie cinétique par collisions élastiques et inélastiques (34a), à l'ionisation du constituant M (34b) et au transfert de charge (34c).

$$H_f^+ + M \rightarrow \begin{cases} H_{f'}^+ + M^{(*)} & \text{(34a)} \\ H_{f'}^+ + M^+ + e & \text{(34b)} \\ H_{f'}^{(*)} + M^+ & \text{(34c)} \end{cases} \tag{34}$$

où M représente les constituants $N_2$, $O_2$ et O.

Les atomes d'hydrogène chauds peuvent également se mouvoir dans l'atmosphère sans subir la contrainte du champ magnétique, pour ensuite interagir avec les constituants atmosphériques par transfert d'énergie cinétique lors de collisions élastiques et inélastiques

(35a), ou ionisation du constituant M (35b) ou de l'atome $H_f$ (35c).

$$H_f + M \rightarrow \begin{cases} H_{f'}^{(*)} + M & \text{(35a)} \\ H_{f'}^{(*)} + M^+ + e & \text{(35b)} \\ H_{f'}^{+} + M + e. & \text{(35c)} \end{cases} \tag{35}$$

Dans la réaction (35a), le constituant peut être dans un état excité. Une partie de l'hydrogène excité $H_{f'}^{(*)}$ est produit dans l'état H(2p) qui émet la raie Lyman-$\alpha$. De plus, les électrons secondaires produits lors de ces réactions vont participer aux collisions avec les constituants ionosphériques et produire les émissions décrites ci-dessus.

Remarquons qu'en conséquence de l'échange de charge des protons avec les constituants ionosphériques, l'aurore à protons est moins confinée que le flux de protons incidents, étant donné que le mouvement des atomes H n'est pas soumis à la contrainte des lignes de champ magnétique. Ces aurores se situent dans un ovale décalé vers le crépuscule par rapport à l'ovale électronique et ont un temps de réponse différent de celui lié aux aurores électroniques.

## L'absorption par $O_2$

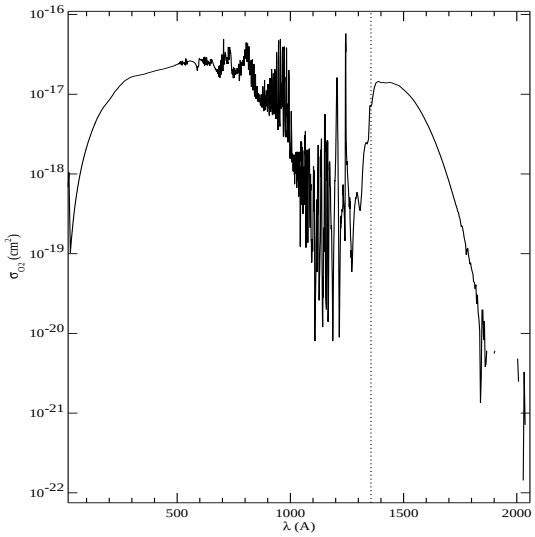


Figure 30: Section efficace d'absorption de la molécule $O_2$ en fonction de la longueur d'onde.

L'émission aurorale UV est produite dans la couche E de l'ionosphère, c'est-à-dire à une altitude d'environ 110 km. Comme cette émission est isotrope, une partie est émise vers

l'espace. Cette partie traverse l'atmosphère supérieure où elle est susceptible de produire des réactions d'excitations atomiques et moléculaires, de dissociations ou d'ionisations. L'émission est donc en partie absorbée par les constituants ionosphériques. C'est le cas pour la molécule d'oxygène $O_2$. La Figure 30 montre la section efficace d'absorption de la molécule $O_2$ en fonction de la longueur d'onde. Les photons ultraviolets de longueur d'onde comprise dans l'intervalle [100,150] nm ionisent $O_2$ en $O_2^+$. Ainsi, toutes les émissions ultraviolettes décrites ci-dessus sont en partie absorbées par $O_2$.

## Le satellite IMAGE et les instruments FUV

La mission IMAGE est un programme satellitaire conçu par la NASA pour donner une image de la magnétosphère terrestre [Burch, 2000]. Cette mission de sondage lointain observe toutes les régions de la magnétosphère simultanément. Elle a pour but de répondre aux questions suivantes :

- Quels sont les mécanismes dominants d'injection de plasma dans la magnétosphère aux échelles de temps des sous-tempêtes ?
- Quelle est la réponse directe de la magnétosphère aux variations du vent solaire ?
- Où et comment les plasmas magnétosphériques sont-ils énergétisés, transportés et ensuite perdus lors des tempêtes et sous-tempêtes magnétiques ?

En résumé : Comment la magnétosphère répond-elle globalement aux variations du vent solaire ? Pour répondre à ces questions, les instruments à bord du satellite observent trois régions de la magnétosphère : la magnétopause, la plasmasphère et le feuillet de plasma intérieur et cherchent à identifier les couplages entre ces régions ainsi que leurs réponses dynamiques aux changements de conditions dans le vent solaire.

Le satellite IMAGE (Figure 31) a été lancé le 25 mars 2000, sur une orbite polaire elliptique de 90° d'inclinaison, son apogée se situant à une distance géocentrique de 8.2 rayons terrestres et son périgée à environ 1000 km d'altitude. Le graphique de gauche de la Figure 32 schématise l'orbite initiale du satellite et son évolution au cours des deux premières années de la mission. Juste après le lancement, le demi grand axe de l'orbite elliptique était incliné de 40° par rapport au plan de l'écliptique. Le plan de l'orbite était quasi identique au plan du terminateur crépusculaire. Au cours des deux premières années de la mission, l'angle entre le grand axe et le plan de l'écliptique est passé de 40° à 90° puis de 90° à 40°. Au-delà des deux premières années de mission, l'évolution de l'orbite est schématisée sur le graphique de droite de la Figure 32.

La précession de l'orbite provoque l'évolution de la perspective d'observation de la Terre. Fin de l'année 2003, l'apogée se situait dans le plan de l'équateur. Ensuite, l'apogée du satellite se situait dans l'hémisphère sud. Ce changement d'angle de vue a permit de

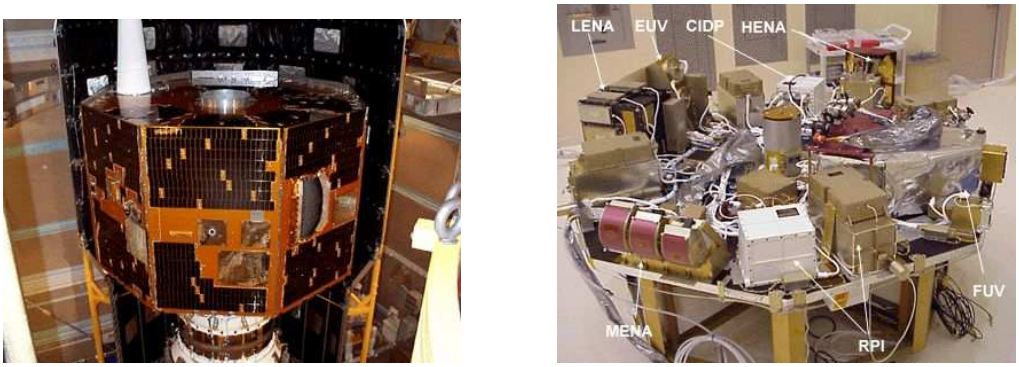


Figure 31: Satellite IMAGE. A gauche, lors de son installation dans la fusée. A droite, plateforme avec les différents instruments qu'il comprend.

faire évoluer les objectifs scientifiques de la mission : spécifiquement pour FUV, la phase d'apogée de faible latitude était idéale pour l'observation de l'aurore avec une meilleure résolution spatiale dans les deux hémisphères dans les parties ascendantes et descendantes de l'orbite, ainsi que l'observation conjuguée des aurores dans les deux hémisphères. Cependant, l'information globale des observations étaient perdues lors de cette phase. Ensuite, la phase d'apogée dans l'hémisphère sud avait pour intérêt de permettre des comparaisons avec les résultats obtenus lors de la première partie de la mission. Enfin, la prolongation de la mission initiale a fourni l'opportunité d'observer l'aurore globalement au fur et à mesure de la phase de déclin de l'activité solaire. Le satellite IMAGE a cessé de transmettre toute information fin décembre 2005. La mission a finalement duré 5.75 années, alors qu'elle était initialement prévue pour 2 ans. Elle constitue un succès scientifique remarquable.

Le satellite tournait sur lui-même avec une période de 2 minutes, ce qui signifie que le taux de rotation du satellite valait $3^{\circ}$/seconde. L'axe de rotation était perpendiculaire au plan de l'orbite.

## Description des instruments FUV

Les instruments d'imagerie FUV sont de trois types [*Mende et al.*, 2000a] :

- WIC (Wideband Imaging Camera) fournit une image deux dimensions dans la bande spectrale de LBH produite dans l'ovale auroral par les impacts électroniques sur $N_2$.
- SI (Spectrographic Imager) fournit une image monochromatique en deux dimensions.
- GEO observe la distribution de l'émission géocoronale Lyman-$\alpha$.

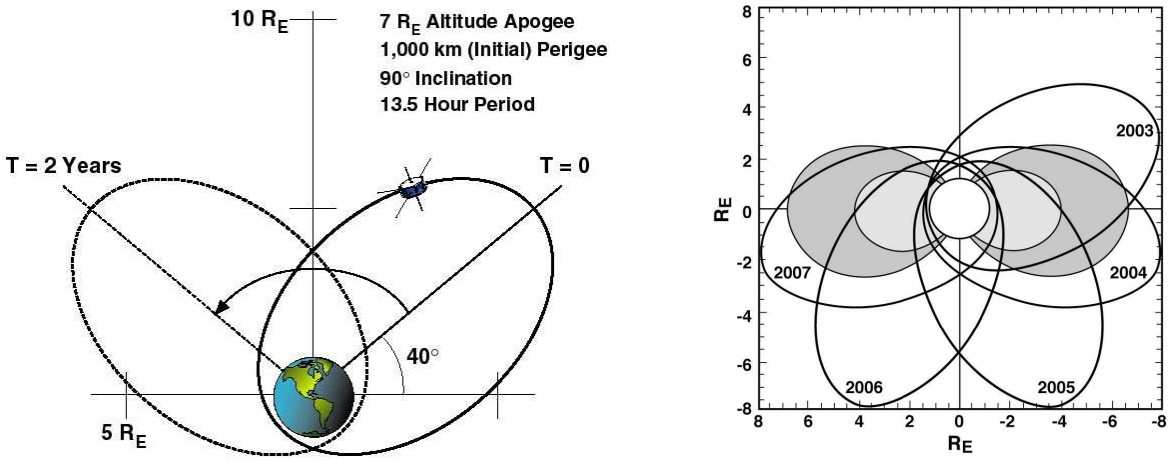


Figure 32: Orbite du satellite IMAGE. A gauche, évolution de l'orbite lors des deux premières années de la mission. A droite, évolution de l'orbite pour la mission prolongée jusqu'en 2007. Les orbites sont représentées pour le 25 mars de chaque année. Notons que le point de vue des deux figures est opposé.

Nous nous intéressons ici uniquement aux instruments WIC et SI.

### WIC

WIC a pour but de mesurer l'intensité totale de l'aurore dans les régions de longueur d'onde les plus représentatives des sources aurorales et les moins contaminées par la planète éclairée et d'autres sources indésirables. La bande passante de l'instrument est comprise entre 140 et 190 nm, avec une faible contribution sous 140 nm (Figure 33). WIC mesure donc principalement l'intensité de l'émission LBH due à l'excitation des atomes $N_2$ par les électrons et la raie d'émission à 149.3 nm due à NI atomique. L'émission due aux collisions des électrons sur les atomes d'oxygène contribue également au taux de comptage. L'influence de l'émission OI à 130.4 nm est minime tandis que l'émission OI à 135.6 nm est en partie observée. Enfin, une contribution due à la lumière solaire réfléchie influence aussi la mesure. En fait, la bande passante de WIC n'est pas tout à fait nulle au-dessus de 190 nm. Or le spectre d'émission du Soleil se comporte comme le spectre d'un corps noir de température égale à 5700 K. L'émission devient non négligeable pour les longueurs d'ondes supérieures à 170 nm et elle est maximale pour une longueur d'onde d'environ 500 nm. Ainsi, la lumière solaire diffusée par l'atmosphère de longueur d'onde supérieure à 170 nm est également observée par WIC.

Le détecteur WIC est une camera CCD. Son champ de vue est de 17.2°x17.2°. A

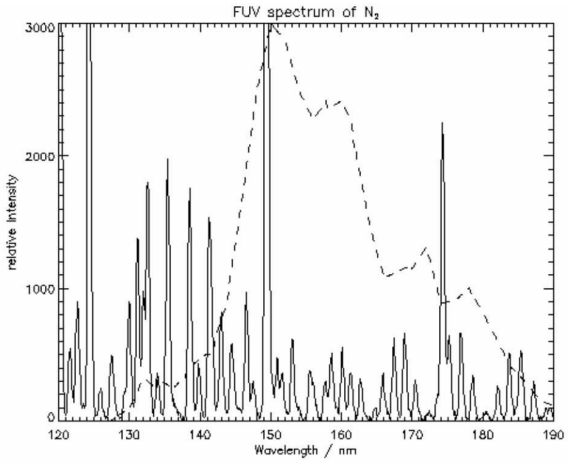


Figure 33: Spectre $N_2$ LBH sur lequel est tracée la bande passante du détecteur WIC (en traits pointillés).

l'altitude du point d'apogée ( 7 $R_E$ ), WIC permet d'observer une zone de 13300 km x 13300 km. L'ovale auroral est visible entièrement lorsque le satellite se situe à 4 à 5 $R_E$ d'altitude au moins.

La résolution du détecteur a été étudiée afin de pouvoir observer des phénomènes à des échelles spatiales de l'ordre de la centaine de kilomètres. Pour ce faire, il faut que le détecteur ait une capacité minimale de 128 x 128 pixels pour couvrir la totalité du champ de vision. Le détecteur WIC fournit en fait des images de 256 x 256 pixels. Par conséquent, à l'apogée, un pixel couvre une région de 52 km x 52 km. La résolution du détecteur vaut donc environ 1 à 2° de latitude. Il est à noter que le champ de vue de WIC vaut en fait 17.2° dans la direction parallèle à l'axe de rotation du satellite et 30° dans la direction perpendiculaire à l'axe de rotation. Cependant, seule une image de 17.2° x 17.2° est enregistrée.

WIC est monté à bord d'IMAGE de telle manière qu'il offre une vue radiale par rapport à l'axe de rotation du satellite. Attendu que WIC a un champ de 30° dans la direction de rotation et que le taux de rotation vaut 3°/sec, chaque point observé passe 10 secondes dans le champ de WIC. Cette considération définit le temps d'exposition, afin de tirer avantage de la période entière lors de laquelle l'instrument observe la zone aurorale.

**SI**

Le Spectrographic Imager, fabriqué par le Centre Spatial de Liège, est un instrument d'imagerie monochromatique. Par une série d'éléments optiques, deux longueurs d'ondes

différentes sont sélectionnées et ces photons sont comptés par deux détecteurs différents. Son champ de vue est de 16.3°x16.3°. La résolution du détecteur SI est 128 x 128 pixels. Ainsi, à 7 $R_E$, un pixel couvre une région de 100 km x 100 km.

Un des deux détecteurs (SI12) est sensible à la raie Lyman $\alpha$ de l'hydrogène. En fait, l'émission Ly-$\alpha$ pour l'hydrogène a deux origines :

- l'émission géocoronale donne une raie à 121.56 nm, appelée « Ly-$\alpha$ froide ».
- l'émission Ly-$\alpha$ aurorale produite par les protons entrant dans l'atmosphère. Elle donne une raie élargie, appelée « Ly-$\alpha$ chaude ». Pour rappel, un proton incident peut arracher un électron lors d'une collision avec un atome ou une molécule de gaz de l'atmosphère et se combiner pour donner un atome d'hydrogène excité. La probabilité est grande que cet atome H excité se trouve dans un état de transition Ly-$\alpha$. La désexcitation spontanée produit un photon dont la longueur d'onde vaut 121.56 nm. Cette émission est déplacée par effet Doppler puisque les protons incidents et par conséquent les atomes H produits, se déplacent par rapport au détecteur.

L'imageur spectral SI12 a été conçu de sorte que la raie Ly-$\alpha$ froide ne soit pas transmise. Les tests de laboratoire ont montré que l'émission géocoronale apporte une contribution inférieure à 2%. La Figure 34 montre la transmission du détecteur SI 12 en fonction de la longueur d'onde.

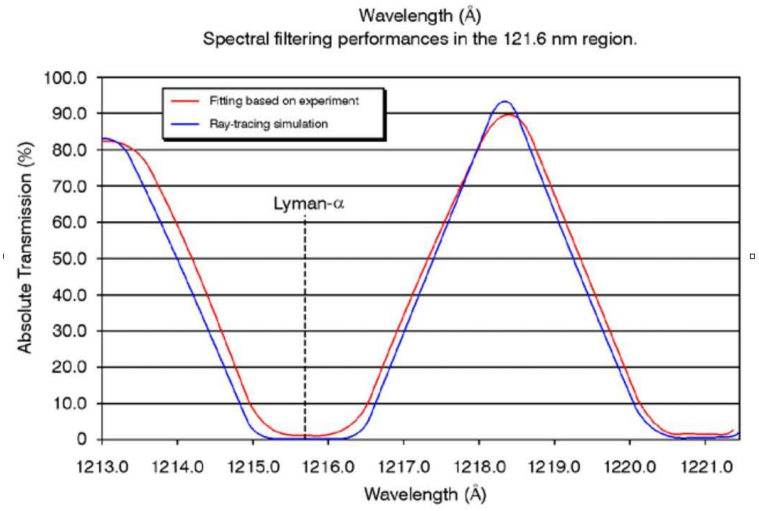


Figure 34: Transmission du détecteur SI12 en fonction de la longueur d'onde, sur laquelle est indiquée la position du pic d'émission Lyman-$\alpha$ froide. La courbe de transmission expérimentale est représentée en rouge et une courbe de transmission simulée, en bleu.

Le deuxième détecteur (SI13) est sensible à la longueur d'onde de l'émission OI due à la collision des électrons avec les atomes d'oxygène de la haute atmosphère. En fait, ces collisions produisent, entre autres, deux raies relativement intenses. La plus intense est la raie à $\lambda$=130.4 nm mais elle subit des diffusions multiples dans l'atmosphère. Elle ne permet pas d'obtenir une distribution correcte en deux dimensions de la densité des sources aurorales. La raie à 135.6 nm est moins intense, mais également beaucoup moins diffusée. Elle donne donc une meilleur image de l'émission aurorale. Le détecteur SI13 est sensible à l'émission de longueur d'onde $\lambda$=135.6 nm ainsi qu'aux raies de $N_2$ LBH présentes dans sa bande passante (le canal de sa bande passante se situe autour de 135.6 $\pm$ 4.0 nm). Les mesures de calibration ont montré que la contribution de l'émission à 130.4 nm était inférieure à 1%.

## La calibration des instruments FUV

La sensibilité des détecteurs WIC et SI a été calibrée en vol à partir d'observations stellaires [*Gladstone et al.*, 2000; *Frey et al.*, 2003a]. Quatorze étoiles dont les spectres sont connus par les observations du satellite IUE (International Ultraviolet Explorer) ont été choisies sur base de la variété de leur spectre. La Figure 35 montre les courbes et les paramètres de calibration de WIC et de SI12. L'orbite d'IMAGE restant fixe dans l'espace, les mêmes étoiles ont été observées de manière continue au cours de la mission. Cette caractéristique a été utilisée pour réétalonner quotidiennement les caméras FUV [*Frey et al.*, 2003a].

Après la mise en fonctionnement des instruments en orbite, une seconde calibration a été faite. Elle consistait à effectuer des comparaisons avec des mesures *in situ* de flux de particules. Deux approches ont été traitées. D'un part, les observations IMAGE-FUV ont été transformées en flux énergétique des particules précipitées pour comparer les flux calculés au pied des lignes de champs sur lequelles se meuvent le satellite avec les flux mesurés *in situ* par ce satellite. La transformation des observations FUV en flux énergétique repose sur des courbes d'efficacités des instruments FUV évaluées à partir de modèle de transport et de dégradation de l'énergie des particules. Des telles comparaisons ont été effectuées à l'aide des mesures *in situ* des satellites FAST [*Bisikalo et al.*, 2003], NOAA [*Hubert et al.*, 2002; *Meurant et al.*, 2003b] et DMSP [*Bisikalo et al.*, 2003; *Coumans et al.*, 2004b].

La seconde approche consiste en la méthode opposée, c'est-à-dire à simuler les taux de comptages des instruments FUV à partir des flux mesurés par les satellites *in situ* et à les comparer avec les taux de comptage FUV réellement mesurés le long de la trace du satellite *in situ*. Cette méthode fut utilisée par *Frey et al.* [2001] avec des mesures du satellite FAST. C'est également la méthode que nous avons choisi lors de la première partie de notre travail et dont la méthode complète et les résultats sont décrits au chapitre 1.3. Ces comparaisons ont été effectuées avec les mesures *in situ* des satellites NOAA.

Nos résultats ont montré que l'accord entre la simulation et l'observation est satisfaisant

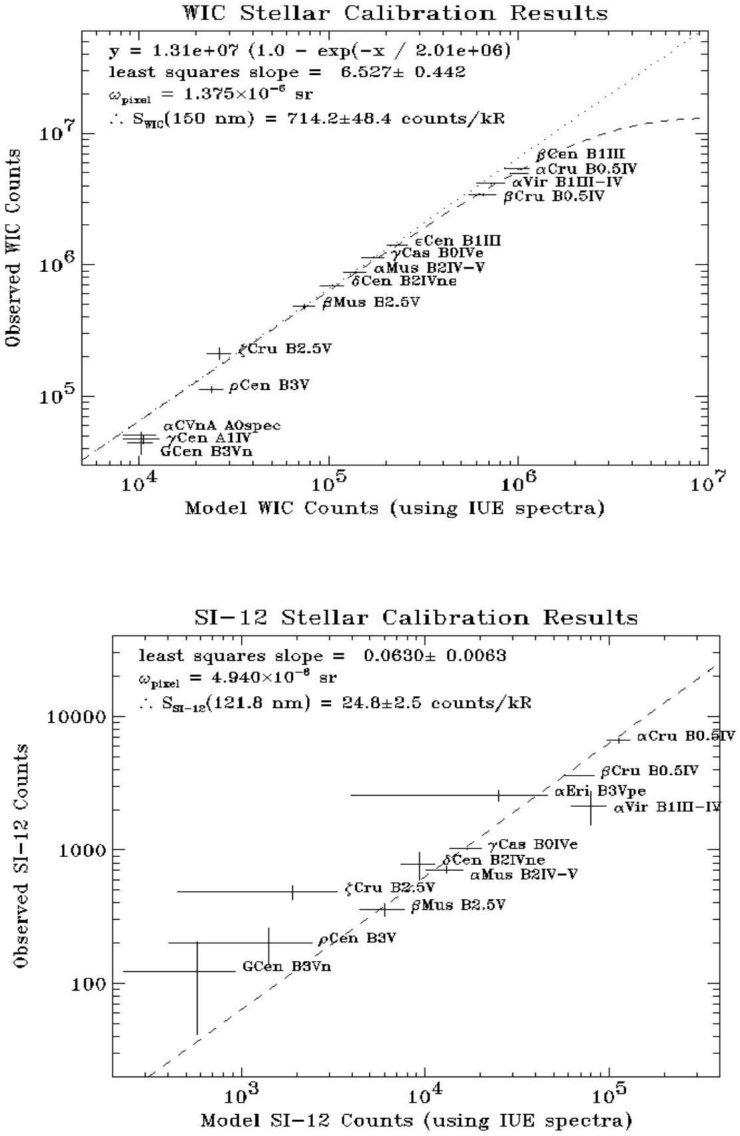


Figure 35: Résultats de la calibration stellaire des détecteurs WIC (en haut) et SI12 (en bas), utilisant 14 étoiles ayant des spectres IUE variés. Les observations ont été effectuées par les instruments FUV le 19 juin 2000 [*Gladstone et al.*, 2000].

tant en morphologie qu'en intensité pour la plupart des comparaisons effectuées [16]. Dans le cas de WIC, l'accord moyen est de 70%, alors que dans le cas de SI12, le nombre de coups observé semble systématiquement 2 fois plus élevé que le nombre de coup calculé. Si on inverse la démarche, on obtient pour un nombre de coups calculé, un flux énergétique deux fois trop grand par rapport au flux énergétique réel. Pour cette raison, nous avons décidé de systématiquement diviser par un facteur 2 les flux de protons que nous évaluons à partir des observations SI12 à l'aide du modèle de Monte Carlo [*Gérard et al.*, 2000].

[16] En tenant compte des différences de résolution spatiale et temporelle des instruments, nous avons comparé les observations simulées et les observations réelles le long du pied des lignes de champ suivant 12 trajectoires des satellites NOAA.

# Objectifs de nos recherches

## Pourquoi s'intéresser à la précipitation aurorale de protons?

Comme nous l'avons expliqué précédemment, les mécanismes d'accélération et de précipitation des électrons et des protons auroraux sont différents et peuvent se situer dans des régions de l'espace différentes. Les mécanismes de précipitation d'électrons sont assez bien connus car beaucoup de ces mécanismes ont lieu dans des régions assez proches de la Terre et parce que beaucoup de mesures et d'observations diverses de la précipitation électronique sont disponibles : mesures *in situ*, observations radar du sol mais aussi observations globales. Certains mécanismes accélérant les protons sont quant à eux localisés assez loin dans la queue de la magnétosphère et sont encore assez mal connus, notamment par le manque d'observation globale.

Il est important d'analyser la précipitation de protons auroraux pour mieux connaître notre environnement géomagnétique. En effet, jusqu'au lancement du satellite IMAGE, la précipitation aurorale de protons ne pouvait être observée qu'à partir de mesures *in situ* ou d'observations au sol. Aucune observation globale de l'ensemble de la précipitation de protons dans l'hémisphère Nord n'était accessible alors que la précipitation d'électrons était, quant à elle observée. Par exemple, l'instrument UVI (ultraviolet imager) à bord du satellite POLAR a donné une image de l'ensemble de l'hémisphère Nord dans le domaine de longueur d'onde ultraviolet allant de 160 à 180 nm. Il observait les raies LBH (Lyman-Birge-Hopfield) induites par l'excitation de l'azote moléculaire par la précipitation électronique aurorale ainsi que par les électrons secondaires produits par la précipitation aurorale de protons. Ces observations contiennent donc une composante due aux protons, mais aucun moyen ne permet de discriminer les effets des deux types de particules. Ainsi, les travaux analysant la précipitation aurorale ignorent les protons en les assimilant à des électrons.

L'instrument SI12 à bord du satellite IMAGE, décrit ci-dessus, permet de visualiser et d'analyser la précipitation instantanée de protons auroraux. Comme nous le montrons au chapitre 1, les protons peuvent localement contribuer à plus de 50 % au flux énergétique total et les négliger pourrait entraîner localement une erreur relativement importante.

Nos recherches s'intègrent donc dans l'étude générale de l'influence des protons auroraux sur notre environnement. Mais le but à long terme de ce type d'étude est la "prédiction". Le souhait général est de pouvoir prédire l'apparition et l'intensité des aurores. Ces phénomènes ont une influence pratique sur notre environnement car ils impliquent des perturbations électriques notamment sur les communications radio dans la haute atmosphère. De plus, une meilleure connaissance de l'environnement magnétique terrestre et du couplage entre celui-ci et le vent solaire permettrait de développer une "météorologie spatiale" fiable.

# Chapter 1

# Electron and proton excitation of the FUV aurora : Simultaneous IMAGE and NOAA observations

## 1.1 Introduction : Les modèles de transport et de dégradation d'énergie des particules aurorales

Afin de transformer les coups observés par les instruments FUV en flux énergétique de particules précipitées, des modèles de transport et de dégradation des particules aurorales sont utilisés. Il existe divers modèles d'interaction des électrons et des protons auroraux avec l'atmosphère. Ils permettent de calculer les taux d'ionisation, de désexcitation, d'échauffement et les processus d'émission. Ils fournissent également les intensités aurorales pour différentes longueurs d'ondes.

Les modèles ont été utilisés pour calculer les courbes d'efficacité des instruments FUV, c'est-à-dire le rapport du nombre de photons détectés au flux de photons incidents en fonction de la longueur d'onde. Ainsi, à partir des coups observés par les instruments FUV, il est possible d'obtenir directement les flux énergétiques précipités connaissant l'énergie des particules qui précipitent.

### Modèle d'interaction des électrons auroraux avec l'atmosphère

Le modèle utilisé est le modèle GLOW [*Solomon et al.*, 1988]. Il se base sur un modèle de transport des électrons [*Banks and Nagy*, 1970; *Stolarski*, 1972; *Banks et al.*, 1974] qui prend en considération les collisions élastiques et inélastiques entre les électrons et les particules neutres et ionisées de l'atmosphère supérieure.

Le flux d'électrons est calculé en se basant sur une approximation à deux faisceaux, ce

qui signifie que la distribution des angles d'attaque est décrite approximativement par un faisceau ascendant et un faisceau descendant d'électrons. La méthode résout les équations de transport pour les deux flux hémisphériques le long d'une ligne de champ géomagnétique, en fonction de l'énergie. Elle prend en considération les collisions élastiques et inélastiques avec les trois espèces neutres majoritaires (O, $O_2$, $N_2$) et avec les particules ionisées de l'atmosphère supérieure, ainsi que la production d'électrons secondaires. Les effets de la gravité, des champs électriques parallèles et de la convergence des lignes de champ sont négligés.

Lorsque la dégradation de l'énergie dans ces flux d'électrons est calculée en fonction de l'altitude, les intensités d'émissions aurorales pour différentes longueurs d'ondes peuvent être déterminées en utilisant les sections efficaces d'excitation et d'ionisation. Une étude [*Solomon*, 2001] a montré que, lorsque les pas en énergie et en altitude sont adéquats, la méthode à deux faisceaux fournit des distributions verticales identiques aux méthodes plus sophistiquées (multi-faisceaux, Monte-Carlo).

### Le modèle de transport

Comme indiqué précédemment, ce modèle se base sur une approximation à deux faisceaux. Le flux d'électrons dans un domaine d'énergie cinétique ($\varepsilon$,$\varepsilon$ +d$\varepsilon$) [1], le long d'une ligne de champ géomagnétique (coordonnées $s$), est décomposé en deux : $\phi^+(\varepsilon, s)$ est le flux dirigé vers le haut, par lequel les électrons s'éloignent de la Terre et $\phi^-(\varepsilon, s)$ est le flux dirigé vers le bas, c'est-à-dire en direction de la Terre.

Des électrons sont également produits au sein de l'atmosphère lors de réactions d'ionisation. Le taux de production de ces électrons secondaires par unité d'énergie et de volume est représenté par $q(\varepsilon, s)$. La répartition est supposée égale entre les deux faisceaux et une contribution de $q/2$ intervient dans les deux composantes du flux : $\phi^+$ et $\phi^-$.

Les électrons se mouvant dans l'atmosphère interagissent avec les particules neutres et chargées, lors de collisions élastiques de section efficace $\sigma_e(\varepsilon)$ et de collisions inélastiques de section efficace $\sigma_a(\varepsilon)$. Les collisions élastiques modifient le nombre d'électrons participant aux flux hémisphériques. En effet, au cours d'une collision élastique, un électron se dirigeant vers le bas peut être rétrodiffusé et ainsi prendre part au flux ascendant et vice et versa. Les collisions inélastiques modifient l'énergie des électrons, ce qui provoque un effet de cascade entre les différents groupes d'électrons d'énergies différentes. Des électrons de haute énergie peuvent céder une partie de celle-ci aux particules cibles et ainsi se retrouver avec une énergie plus faible. Les collisions inélastiques peuvent également provoquer une

[1] Le modèle de transport utilise une grille en énergie composée de 190 intervalles de largeur variable. A basse énergie, les intervalles sont petits (largeur $\sim$ 0.5 eV pour E =10 eV). La largeur augmente graduellement avec l'énergie (largeur $\sim$25 keV pour E $\sim$ 1 MeV).

rétrodiffusion.

Ainsi, les équations de continuité pour les flux hémisphériques s'écrivent :

$$\frac{d\phi^+}{ds} = -\frac{1}{<\cos\theta>}\sum_k n_k(\sigma_a^k + p_e^k\sigma_e^k)\phi^+ + \frac{1}{<\cos\theta>}\sum_k n_k p_e^k \sigma_e^k \phi^- + \frac{q}{2<\cos\theta>} + \frac{q^+}{<\cos\theta>} \tag{1.1}$$

$$-\frac{d\phi^-}{ds} = -\frac{1}{<\cos\theta>}\sum_k n_k(\sigma_a^k + p_e^k\sigma_e^k)\phi^- + \frac{1}{<\cos\theta>}\sum_k n_k p_e^k \sigma_e^k \phi^+ + \frac{q}{2<\cos\theta>} + \frac{q^-}{<\cos\theta>} \tag{1.2}$$

avec

$$q^{\pm}(\varepsilon, s) = \sum_k n_k(s) \sum_i \{p_{ai}^k(E)\sigma_{ai}^k(E \to \varepsilon)\phi^{\mp}(E, s) + [1 - p_{ai}^k(E)]\sigma_{ai}^k(E \to \varepsilon)\phi^{\pm}(E, s)\}$$

et
$s$, la distance le long d'une ligne de champ (+ en s'éloignant de la Terre),
$\phi^+(\varepsilon, s)$, le flux dirigé vers le haut, le long de s,
$\phi^-(\varepsilon, s)$, le flux dirigé vers le bas, le long de s,
$k$, l'indice correspondant aux différentes espèces neutres,
$n_k(s)$, la densité de la k$^{ème}$ espèce,
$p_e^k(\varepsilon)$, la probabilité que les électrons soient rétrodiffusés au cours d'une collision élastique avec la k$^{ème}$ espèce,
$q(\varepsilon, s)$, le taux de production d'électrons secondaires dans le domaine d'énergie ($\varepsilon$,$\varepsilon + d\varepsilon$), dû aux processus d'ionisation,
$q^{\pm}$, le taux de production d'électrons dans le domaine d'énergie ($\varepsilon$,$\varepsilon + d\varepsilon$) dû à la cascade d'électrons de haute énergie vers des énergies plus basses, provenant des processus inélastiques avec la k$^{ème}$ espèce,
$p_{ai}^k$, la probabilité que les électrons soient rétrodiffusés au cours d'une collision inélastique avec la k$^{ème}$ espèce,
$\sigma_{ai}^k$, la section efficace du i$^{ème}$ processus d'excitation de la k$^{ème}$ espèce, tel que $\sigma_a^k = \sum_i \sigma_{ai}^k$,
$\theta$, l'angle d'attaque des électrons.
Le signe négatif devant la variation du flux descendant $\frac{d\phi^-}{ds}$ est dû au fait que $ds$ est dirigé vers le haut tandis que $\phi^-$ est dirigé vers le bas.

Pour rappel, l'angle d'attaque d'une particule est l'angle entre son vecteur vitesse et la tangente à la ligne de champ magnétique sur laquelle elle se meut. L'angle d'attaque est compris dans l'intervalle [0°,90°] pour le flux descendant $\phi^-$ et dans l'intervalle [90°,180°] pour le flux ascendant $\phi^+$. La division par le cosinus moyen de l'angle d'attaque vise à prendre en considération la distribution angulaire des particules précipitées dans une modélisation à deux faisceaux. En effet, les électrons ayant un grand angle d'attaque vont subir un plus grand nombre de collisions dans la portion $ds$. Nous avons considéré que la

distribution des angles d'attaque est isotrope. Dans ce cas, $< \cos\theta >= \frac{1}{2}$ [2].

On peut écrire

$$T_1 = \frac{1}{< \cos\theta >} \sum_k n_k p_e^k \sigma_e^k \tag{1.3}$$

$$T_2 = \frac{1}{< \cos\theta >} \sum_k n_k (\sigma_a^k + p_e^k \sigma_e^k) \tag{1.4}$$

$$p^{\pm} = -\frac{q}{2 < \cos\theta >} + \frac{q^{\pm}}{< \cos\theta >} \tag{1.5}$$

où $T_1$ est le terme de production par rétrodiffusion, qui contrôle le flux d'électrons quittant le faisceau opposé, $T_2$ le terme de perte dû aux collisions élastiques et inélastiques et $p^{\pm}$ le terme de cascade des électrons ayant perdu leur énergie par collision inélastique.

Si l'on suppose que les lignes de champ sont parallèles et verticales (hypothèse par laquelle on néglige la convergence des lignes de champ), $ds \approx dz$ et on obtient le système d'équations couplées suivant :

$$\frac{d\phi^+}{dz} = -T_2\phi^+ + T_1\phi^- + p^+ \tag{1.6}$$

$$-\frac{d\phi^-}{dz} = -T_2\phi^+ + T_1\phi^- + p^- \tag{1.7}$$

Il suffit de sortir $\phi^+$ de l'équation 1.6 et de l'injecter dans l'équation 1.7 pour obtenir l'équation différentielle du deuxième ordre suivante :

$$\frac{d^2\phi^+}{dz^2} + \alpha\frac{d\phi^-}{dz} + \beta\phi^- + \gamma = 0 \tag{1.8}$$

où

$$\alpha = T_1 \frac{d}{dz}(\frac{1}{T_1}) = -\frac{1}{T_1}\frac{dT_1}{dz} \tag{1.9}$$

$$\beta = T_1^2 - T_2^2 - T_1 \frac{d}{dz}(\frac{T_2}{T_1}) \tag{1.10}$$

$$\gamma = T_1 p^+ + T_2 p^- + \frac{dp^-}{dz} - \frac{p^-}{T_1}\frac{dT_1}{dz} \tag{1.11}$$

Remarquons que les termes $T_{1,2}$ dépendent des flux $\phi$ par le biais des $q^{\pm}$.

Le code FORTRAN utilisé résout cette équation différentielle (équation 1.8) par la méthode de Cranck-Nicholson (méthode numérique d'intégration implicite) en considérant les conditions aux limites décrites ci-dessous.

[2] Il existe d'autres conventions pour la valeur moyenne du cosinus de l'angle d'attaque. L'une d'elles est de considérer $< \cos\theta >= \frac{1}{\sqrt{3}}$ [*Grodent*, 2000].

### Le modèle d'atmosphère

Pour obtenir les densités en particules neutres dans l'atmosphère, nous avons fait appel au modèle MSIS-86 (Mass Spectrometer and Incoherent Scatter) [*Hedin*, 1987]. C'est un modèle semi-empirique développé principalement sur base de mesures de spectrométrie de masse par satellites et de sondeurs ionosphériques à diffusion incohérente. Il approche les profils verticaux de température et de densité par des fonctions analytiques théoriques, compatibles avec la loi d'équilibre hydrostatique. L'ajustement se fait sur base de données d'activité solaire, d'activité magnétique, ainsi que sur l'heure universelle et la position géographique.

### Conditions aux limites

Afin de résoudre l'équation différentielle 1.8, il a été nécessaire d'imposer des conditions aux limites.

Pour la limite inférieure :

$$\phi^+(E, z \to 0) = \phi^-(E, z \to 0) = 0 \tag{1.12}$$

ce qui signifie que les flux d'électrons au niveau du sol sont nuls.

Pour la limite supérieure :
$\phi^-(E, z = a)$ est donné par une distribution énergétique maxwellienne du flux incident connaissant l'énergie des électrons incidents.

### Modélisation des taux d'émission

Lorsque la dégradation de l'énergie dans les flux d'électrons est calculée en fonction de l'altitude, les taux d'émission aurorale pour différentes longueurs d'ondes peuvent être déterminés. Le calcul des taux d'émission volumique s'effectue sur base des sections efficaces d'excitation et d'ionisation. Celles-ci ont été mesurées en laboratoire sous conditions les plus similaires possibles à celles régnant dans la haute atmosphère.

Le calcul du taux d'émission volumique résoud les intégrales suivantes :

$$\eta_i^k(z) = n_i \int_S^\infty \phi(E)\sigma_i^k(E)dE \tag{1.13}$$

où
$\eta_i^k$ est le taux d'émission volumique dans la transition $k$ à l'altitude $z$,
$n_i$ est la densité de la i$^{ème}$ espèce à l'altitude $z$,
$\phi(E)$ est la fonction de distribution des électrons. La forme de $\phi(E) = \phi^+ + \phi^-$ est donnée par les solutions des équations 1.1 et 1.2,

$\sigma_i^k$ est la section efficace d'émission dans la transition $k$ de la i$^{ème}$ espèce à l'altitude $z$, $S$ est le seuil d'excitation de la transition $k$.

### Résultats du modèle

Le code FORTRAN fournit le taux volumique d'émission aurorale en fonction de l'altitude, pour toute une série de longueurs d'ondes ; entre autres, l'émission OI à 130,4 nm, celle à 135,6 nm et l'émission LBH.

Les taux d'émission volumique aurorale pour les diverses longueurs d'ondes en fonction de l'altitude ainsi calculés sont intégrés sur l'altitude, le long de diverses lignes de visée [3], pour pouvoir directement être utilisés avec les données FUV. De plus, connaissant la section efficace d'absorption par $O_2$ (voir Figure 30), ainsi que la densité de ce constituant dans toute l'atmosphère (fournie par le modèle MSIS-86), l'intégration a pris en considération l'absorption de l'émission par $O_2$.

## Modèle d'interaction des protons auroraux avec l'atmosphère

Comme expliqué précédemment, lors de collisions inélastiques avec les constituants ionosphériques, les protons incidents peuvent subir un échange de charge et devenir des atomes d'hydrogène excités (voir Equations 34). La désexcitation de ceux-ci produit l'émission Lyman-$\alpha$.

Le modèle de transport des protons auroraux présenté par *Gérard et al.* [2000] résout les équations de Boltzmann pour un faisceau $H^+$-H par une méthode de Monte Carlo. Pour un faisceau de protons ayant une certaine énergie et un certain flux énergétique entrant au sommet de l'atmosphère, ce modèle suppose que les collisions de ce faisceau avec les constituants de l'atmosphère provoquent, entre autres, des processus d'échange de charge. Ces collisions vont générer une population d'atomes d'hydrogène rapides, qui à leur tour, vont être convertis en ions $H^+$. Le code calcule toutes les collisions élastiques et inélastiques (résumées par les Equations 34 et 35) que subissent ces deux espèces.

Ce modèle a permis de calculer les taux d'émission de Ly-$\alpha$ en fonction de l'énergie des particules incidentes. La Figure 1.1 présente le taux d'émission pour un flux de protons de 1 $erg/cm^2.s$ en fonction de l'énergie cinétique des particules précipitées. Ce taux est exprimé en $kR$ (kiloRayleigh) [4] par unité de flux incident.

[3] les taux sont intégrés sur plusieurs lignes de visée différentes, dont les angles varient par pas de 10° entre 0° et 90°

[4] Un Rayleigh est égal à un taux d'émission intégré de $10^6$ photons par $cm^2$ et par seconde : $1[R] = \frac{10^6}{[cm^2]\cdot[sec]}$. Cette définition suppose que la source est étendue et permet ainsi de ne pas prendre en considération l'éloignement de celle-ci par rapport à l'observateur. En effet, la brillance d'une source est inversement proportionnelle au carré de sa distance à l'observateur. Mais, la région vue par l'observateur

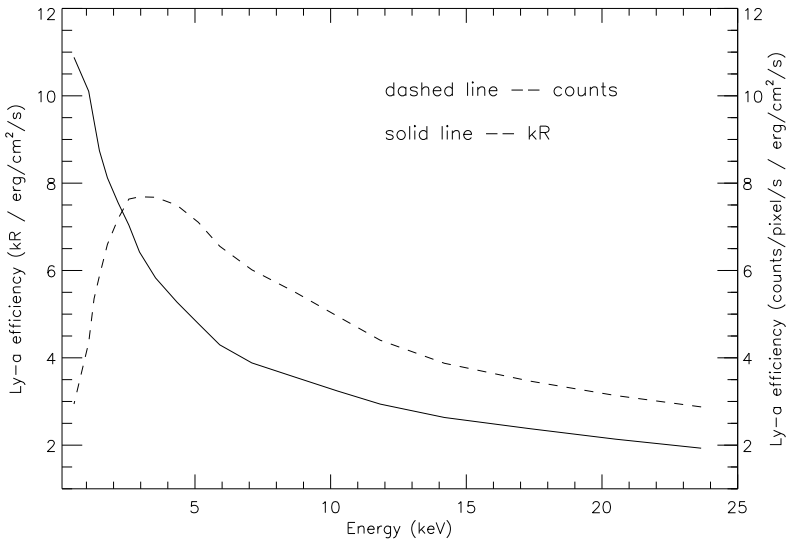


FIG. 1.1 – Taux d'émission total calculé pour un flux de protons de 1 $erg/cm^2.s$ en fonction de l'énergie cinétique des particules (trait continu). La courbe en traits pointillés représente le taux de comptage SI12 correspondant pour une observation verticale.

Pour la modélisation des taux de comptage WIC dus aux protons, le procédé est le suivant : la méthode de Monte Carlo a permis de calculer le taux de réactions entre les protons et les constituants ionosphériques et donc le nombre d'électrons secondaires produits. Connaissant les taux de production des électrons et leur énergie (liée à l'énergie des protons incidents), les émissions dues à ces électrons ont été modélisées comme expliqué dans le paragraphe précédent. Ainsi, la contribution des protons dans les observations WIC peut être soustraite avant d'évaluer les flux énergétiques des électrons précipités à partir des observations WIC.

est proportionnelle au carré de la distance entre celui-ci et la source. Ainsi, dans la cas d'une source étendue, l'augmentation de la brillance liée à l'augmentation de l'angle de vue et la diminution de celle-ci liée à l'éloignement se compensent.

## 1.2 Résumé introductif

Peu après le lancement du satellite IMAGE, j'ai commencé mes travaux par une étape de validation et de calibration des observations FUV. J'ai comparé les observations des instruments WIC et SI12 avec des prédictions de modèles couplées à des mesures de particules des satellites NOAA-15 et 16. La situation des satellites lors de ces comparaisons est schématisée à la Figure 1.2. Les modèles d'interaction des particules aurorales avec l'atmosphère (décrits au paragraphe précédent) sont utilisés avec les flux de protons et d'électrons mesurés *in situ* et les énergies charactéristiques des particules afin de calculer l'émission aurorale au pied des lignes de champ magnétique le long des trajectoires des satellites NOAA. Ces satellites sont équipés de 2 types de détecteurs : l'un mesurant les particules dont l'énergie est comprise entre 50 eV et 20 keV et l'autre, celles dont l'énergie est supérieure à 30 keV, de sorte que ces comparaisons incluent toute la gamme des énergies aurorales. En considérant les résolutions spatiales différentes pour les deux détecteurs et le lissage correct des mesures *in situ*, le signal observé par WIC est bien modélisé. La comparaison du signal SI12 observé et du signal modélisé montre un (dés)accord de 50% : résultat important puisqu'il aura des répercutions pratiques pour la suite du travail. Les comparaisons ont montré les principaux résultats suivants :

- on observe un accord satisfaisant tant en morphologie qu'en intensité pour la plupart des survols des satellites,
- la contribution des protons dans le signal WIC peut localement être significative et ne peut donc pas être systématiquement négligée,
- dans certains secteurs, les protons de haute énergie dominent le flux énergétique de protons et comptent pour une fraction importante de l'émission Ly-$\alpha$,
- au point de vue de la morphologie, on observe le décalage en latitude entre l'ovale de protons et l'ovale des électrons dans le secteurs du crépuscule.

Tous ces résultats sont décrits explicitement dans l'article repris dans les pages suivantes (publié dans la revue *Journal of Geophysical Research* en 2002.)

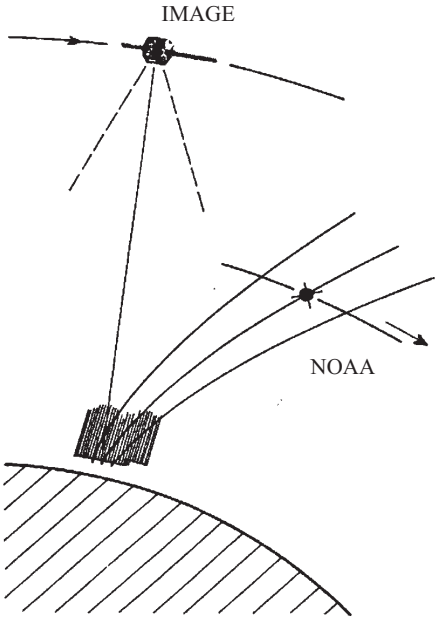


FIG. 1.2 – Schéma résumant la situation des satelittes IMAGE et NOAA lors de leurs mesures respectives.

# 1.3 Electron and proton excitation of the FUV aurora : Simultaneous IMAGE and NOAA observations

V. Coumans, J.-C. Gérard, B. Hubert
Laboratoire de Physique Atmosphérique et Planétaire, Université de Liège

D.S. Evans
NOAA Space Environment Center, Boulder

*Published in Journal of Geophysical Research - Space Physics (November 6, 2002).*

## Abstract

[1] *The Far Ultraviolet (FUV) imaging system on board the IMAGE satellite provides a global view of the north auroral region in different spectral channels. The Wideband Imaging Camera (WIC) is sensitive to the $N_2$ LBH emission and NI emissions produced by both electron and proton precipitations. The SI12 camera images the Lyman-$\alpha$ emission due to incident protons only. We compare WIC and SI12 observations with model predictions based on particle measurements from the TED and the MEPED detectors on board NOAA-TIROS spacecraft. Models of the interaction of auroral particles with the atmosphere are used together with the in situ proton and electron flux and characteristic energy data to calculate the auroral brightness at the magnetic footprint of the NOAA-15 and NOAA-16 orbital tracks. The MEPED experiment measures the precipitating particles with energy higher than 30 keV, so that these comparisons include all auroral energies, in contrast to previous comparisons. A satisfactory agreement in morphology and in magnitude is obtained for most satellite overflights. The observed FUV-WIC signal is well modeled if the different spatial resolution of the two sensors is considered and the in situ measurements properly smoothed. The calculated count rate includes contributions from LBH emission, the NI 149.3 nm line and the OI 135.6 nm line excited by electrons and protons. The proton contribution in WIC can locally dominate the electrons. The comparisons indicate that protons can significantly contribute to the FUV aurora at specific times and places and cannot be systematically neglected. The results confirm the shift of the proton auroral oval equatorward of the electron oval in the dusk sector. We also show that in some regions, especially in the dusk sector, high-energy protons dominate the proton energy flux and account for a large fraction of the Lyman-$\alpha$ and other FUV emissions.*

### 1.3.1 Introduction

[2] The IMAGE (Imager for Magnetopause-to-Aurora Global Exploration) satellite, launched in March 2000, is a mission for remote sensing simultaneously of all regions of the Earth's magnetosphere. Its main objective is to determine how the magnetosphere responds globally to the changing conditions in the solar wind [*Burch*, 2000]. On board the IMAGE satellite, the FUV imaging system globally observes the north auroral region in the far ultraviolet [*Mende et al.*, 2000a]. The imagers are designed to monitor the electron and proton precipitation and discriminate between the two types of particles. The experiment is composed of three different instruments: the Wideband Imaging Camera (WIC) and two Spectrographic Imagers (SI12 and SI13). One characteristic of the FUV imager is its capability to simultaneously observe in all three spectral regions. SI12 is the first FUV imager able to detect incident proton flux without contribution from electrons. The WIC passband covers a spectral region including emissions excited by both protons and electrons.

[3] *Senior et al.* [1987] used simultaneous data obtained with the Chatanika incoherent scatter radar and the Dynamics Explorer 2 (DE 2) and NOAA 6 satellites to relate the locations of the precipitating particles in the evening-sector auroral oval. Auroral luminosities observed with the Dynamics Explorer 1 (DE 1) imager were compared with simultaneous Chatanika radar observations [*Robinson et al.*, 1989] to determine an empirical relationship between the luminosities measured at FUV wavelengths and the Hall and Pedersen conductances. *Østgaard et al.* [1999] and *Østgaard et al.* [2000] made a similar analysis from POLAR UVI satellite data. Comparisons were made between the precipitation patterns of the high-energy (PIXIE) and low-energy (UVI) electron populations, correlated with ground-based observations and geosynchronous satellite data. *Liou et al.* [1999] compared auroral images from the Polar UVI and simultaneous particle observations from the Defense Meteorological Satellite Program (DMSP) in the afternoon (1300-1600 MLT) sector along the oval in the northern hemisphere to determine the magnetospheric source region of postnoon auroral bright spots. Similarly when in situ measurements of charged particle flux and energy are available, one can model the responses of the FUV imagers from models of the interaction of auroral particles with atmospheric constituents. *Frey et al.* [2001] used in situ particle data from the FAST satellite along two orbits on June 24 and 25, 2000 to model the WIC imager response. A comparison between the modeled WIC response and the observations showed good agreement. It was also demonstrated that in one case protons contributed significantly to the observed signal. *Gérard et al.* [2001] presented a comparison with SI12 observations for one of the two FAST overflights where the simulated SI12 response underestimated the latitudinally integrated brightness. This discrepancy was possibly attributed to high-energy protons above the 30 keV upper limit of the FAST detector, suggesting that higher energy protons could be important in producing this emission. In the present work, we use in situ particle measurements from NOAA-15 and NOAA-16 satellites to verify this possibility and assess the role of proton excitation of FUV emissions. The NOAA measurements offer the advantage of observing electrons in the energy range 50 eV-1000 keV and protons from 50 eV to 800 keV, including all relevant

auroral energies. We are thus able to analyze separately the contribution of protons and electrons in the WIC signal and to assess the importance of the high-energy protons.

[4] The statistical study by *Hardy et al.* [1989] using the DMSP satellite data set indicated that the highest average proton energies are found in the evening sector of the oval, with average energies close to or exceeding 30 keV. Even though energetic protons are not an overall dominant energy source in the high-latitude region, they can be important at given locations and times, particularly near the equatorward boundary of the auroral oval in the afternoon and premidnight sectors as suggested by *Hubert et al.* [2001]. The NOAA-15 orbit is well suited to study the region around 1800 MLT and the evening sector.

[5] In section 1.3.2, we first describe the instrumentation characteristics on board IMAGE and NOAA satellites, and the in situ data from which we model the emission rates to be compared with the FUV observations. In a second part we describe the models used to calculate the auroral brightness from the particle flux and average energy. Section 1.3.2 summarizes the methodology of all the comparisons, including the procedure used to extract FUV information along the NOAA satellite track and the comparison of the modeled emission rate based on NOAA data with the FUV observations. In section 1.3.3 we present some of the results obtained for WIC and SI12. Section 1.3.4 analyzes the role played by high-energy protons in the energy flux and in FUV signals. We finally discuss possible sources of expected errors and model uncertainties.

## 1.3.2 Instrumentation and models

[6] For this work we used two of the FUV instruments on board the IMAGE satellite : WIC and SI12. Data from the two different particle detectors on board the NOAA satellites were used as well. We first describe those instruments and second the numerical models that calculate the FUV auroral brightness from particle measurements.

### FUV experiment

[7] The IMAGE satellite is in a highly elliptical orbit with an initial perigee altitude of 1000 km and an apogee of about 7 Re. The WIC imager has a passband between 140-180 nm with a low sensitivity below 140 nm. It is mostly sensitive to the LBH bands and the 149.3 nm NI line excited by electron impact on $N_2$ and N with a small contribution of the NI 174.3 nm doublet. The WIC response also includes a small contribution from the OI 135.6 nm line. NI and OI excitations are produced by incident primary electrons and protons and secondary electrons colliding with neutral atoms. The LBH emission can also be produced by protons and secondary electrons those protons produce. The WIC CCD camera outputs the information digitally in the form of AD converted 8-bit bytes (AD units). The Spectrographic Imager is a narrow-band imager of far ultraviolet auroral emissions at

121.8 nm and 135.6 nm. In this study, we only consider the SI12 imager, which measures the brightness of the Doppler shifted Lyman-$\alpha$ auroral emission. Precipitating protons colliding with neutral atmospheric constituents can capture an electron and become fast hydrogens. A fraction of fast atoms is produced in the H(2p) state and radiates the Ly-$\alpha$ line. The observed line is shifted owing to the relative motion between the emitting atoms and the detector. SI12 efficiently rejects the geocoronal Ly-$\alpha$ emission at 121.56 nm and only images proton precipitation [*Mende et al.*, 2001].

### NOAA/MEPED-TED instruments

[8] The Space Environment Monitor on board the NOAA-TIROS satellites includes two instruments used for this study. The Total Energy Detector (TED) measures the directional energy flux carried towards the atmosphere by electrons and positive ions in the energy range from 50 eV to 20 keV. The measurements are made at two pitch angles within the atmospheric loss cone. These pitch angles are transformed along the magnetic field to 120 km altitude, and an integration of the directional energy fluxes over pitch angle is made to obtain the downward energy flux carried by electrons and protons. The energy fluxes carried by these particles are calculated along the satellite trajectory every 2 seconds. The TED instrument also identifies the energy band in which the maximum sensor response occurred during the energy sweep. Modeling of the instrument response shows that this energy band generally contains the maximum in the differential energy flux spectrum. This energy band, together with the downward energy flux, is also telemetered every 2 seconds for both types of particle. No significant difference between the characteristic energies associated with the two pitch angles is usually found [*Fuller-Rowell and Evans*, 1987]. Table 1.1 lists the energy bins from each detector. The combination of the characteristic particle energy and the total energy flux, assuming a particular energy spectral distribution, may be used to define the initial particle energy distribution above the atmosphere. Additionally, the sensors' responses in four energy channels are telemetered every 16 seconds for electrons and protons. These data have been used to check the validity of the Maxwellian (electrons) or kappa (protons) distributions assumed for the higher time-resolution, but less spectral information, data provided every 2 seconds.

[9] The Medium Energy Proton and Electron Detector (MEPED) instrument is a set of solid-state particle detectors sensitive to electrons in three integral energy bands, >30 keV, > 100 keV, and >300 keV, and to protons in the three differential energy bands 30-80 keV, 80-250 keV, and 250-800 keV. The measurements are made with a 2-s resolution at one particle pitch angle within the atmospheric loss cone and at a second pitch angle near 90°. The MEPED 2-s average proton and electron counts are telemetered separately for each energy channel. The characteristics of both detectors are summarized in Table 1.1.

[10] The low-energy observations may be combined with the measurements of the more energetic particles from the solid-state detectors to reconstruct the particle energy spectrum

| Channel Number | Energy range, eV | Proton Energy, keV | Electron Energy keV |
|---|---|---|---|
| | | *TED* | |
| 1 | 50-73 | | |
| 2 | 73-106 | | |
| 3 | 106-154 | | |
| 4 | 154-224 | | |
| 5 | 224-325 | | |
| 6 | 325-473 | | |
| 7 | 473-688 | | |
| 8 | 688-1000 | | |
| 9 | 1000-1454 | | |
| 10 | 1454-2115 | | |
| 11 | 2115-3075 | | |
| 12 | 3075-4472 | | |
| 13 | 4472-6503 | | |
| 14 | 6503-9457 | | |
| 15 | 9457-13753 | | |
| 16 | 13753-20000 | | |
| | | *MEPED* | |
| 1 | | 30-80 | >30 |
| 2 | | 80-240 | >100 |
| 3 | | 204-800 | >300 |

Table 1.1: Characteristic energies of the TED and MEPED detectors

over an energy range extending from 50 eV to more than 100 keV. The energy spectrum is reconstructed providing that (1) the energy flux in the 50 eV - 20 keV interval matches the TED measurements and (2) the peak energy flux is reached at an energy corresponding to the characteristic energy identified in the TED measurements. For the electron flux, we use a Maxwellian approximation as recommended by *Strickland et al.* [1993]:

$$f(E) = \frac{Q_0}{2\pi E_0^2}\frac{E}{E_0}\, exp\,(-\frac{E}{E_0}), \tag{1.14}$$

where $E_0$ is the characteristic energy of the electrons and $Q_0$ the total energy flux (in $mW/m^2$). Equation (1.14) represents the form of the differential flux we used. The Maxwellian flux peaks at the energy $E_p = 2E_0 = \langle E \rangle$.

[11] In the case of protons, measurements suggest that a kappa distribution provides a better fit to the observed proton energy spectrum. The shape of the kappa function is represented by equation (1.15)

$$f(E) = \frac{Q_0}{2\pi E_0^2}\frac{(\kappa-1)(\kappa-2)}{\kappa^2}\frac{E}{E_0}\frac{(\kappa E_0)^{\kappa+1}}{(E+\kappa E_0)^{\kappa+1}}, \tag{1.15}$$

where $E_0$ is the characteristic energy of the protons, $Q_0$ the total energy flux. This flux is maximal at the energy $E_p$ given by:

$$E_p = 2E_0\frac{\kappa}{\kappa-1} = \langle E \rangle \frac{\kappa-2}{\kappa-1}. \tag{1.16}$$

The kappa index was determined by fitting the average proton energy spectra given by *Hardy et al.* [1989]'s Figure 7 for Kp=3 at four different local times [*Hubert et al.*, 2001]. A value of 3.5 was adopted as it provides a reasonably good fit to the data.

[12] Using these approximations, the combination of the measured energy flux between 50 eV and 20 keV and the TED peak energy allows one to extrapolate the total energy flux up to 30 keV. The total energy flux is then calculated by integrating the energy distributions (1.14) and (1.15).

$$\phi(E) = \int_0^\infty f(E)EdE \tag{1.17}$$

[13] As shown in equations (1.14) and (1.15), the function $f(E)$ can be estimated from the total flux between 50 eV and 20 keV and the TED characteristic energy. The total energy flux was calculated with equation (1.17), assuming that the peak energy in the range 50 eV - 30 keV is similar to the one in the range 50 eV - 20 keV. The high-energy component of the energy flux is obtained by multiplying the particle flux measured by the MEPED by the mean energy of each channel and summing up the contributions.

[14] For the reconstruction of the electron energy spectrum the Maxwellian flux is truncated at 30 keV and the high-energy tail is replaced by the flux measurements from MEPED. In the case of protons, a kappa distribution is used over the full energy spectrum. The difference between the kappa flux and the MEPED measurements in high-energy channels is added to the kappa flux. In so doing, we obtain a full energy spectrum of precipitating particles every 2 seconds. Figure 1.3 presents the proton energy spectrum for August 12, 2000 at 1013:10 UT (case c in Table 1.2). We compare the kappa distribution we used with a Maxwellian one with the same peak energy. Figure 1.3 also shows the values measured in channels 4, 8, 11 and 14, which are telemetered every 16 seconds. We note that the high-energy tail is better reproduced by the kappa flux than by the Maxwellian one. The measured flux for low energy protons is strongly underestimated by the kappa function. However, the relative importance of channel 4 whose energy band width is only 70 eV is quite small in comparison with, for example, channel 14 whose width is 2954 eV. The energy flux in the channel 4 is only about $5 \times 10^{-4} mW/m^2$ while it is approximately 0.05 $mW/m^2$ in channel 14. However, the H(2p) excitation cross section is significantly larger at low than higher energy.

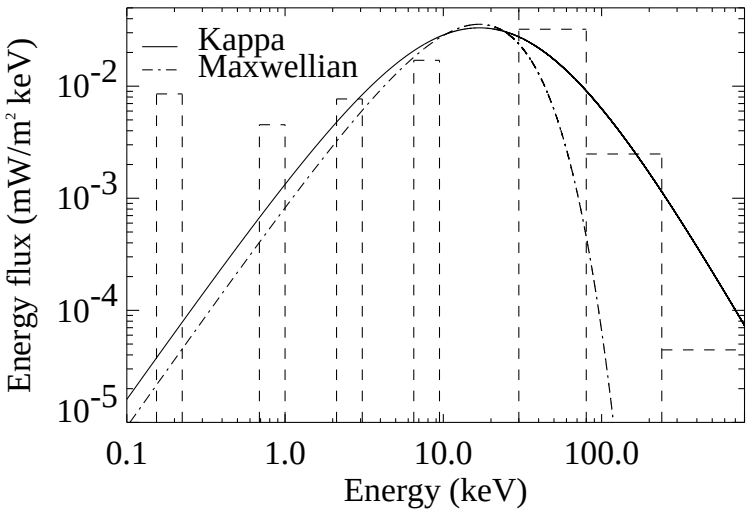


Figure 1.3: The proton energy flux distribution over the energy range 0.1 - 800 keV for August 12, 2000 at 1013:10 UT. The solid line shows the kappa ($\kappa$=3.5) function used in the emission model. The dashed line shows a Maxwellian function with same peak energy and integral flux as the NOAA measurements. Also shown are the energy flux measured in the 3 high-energy channels and in TED low-energy channels 4, 8, 11 and 14.

**Calculation of emission and count rates**

[15] NOAA data are used to reconstruct the electron and proton energy distribution incident at the top of the atmosphere. This distribution serves as an input to auroral emission models to calculate the emission rate profiles. These theoretical profiles are integrated along a line of sight consistent with the viewing geometry of the observations. The instrument response is then used to compute the theoretical count rates which can be compared with the FUV count rates extracted from the observations.

[16] The calculation of the volume excitation rates of the FUV emissions for comparison with the FUV observations is based on two transport models describing respectively the interaction of an electron and a proton beam with the atmosphere. The calculation of auroral electron energy degradation and excitation by electron-induced processes is based on the GLOW model [*Solomon et al.*, 1988] extended to higher energies for auroral calculations [*Hubert et al.*, 2001]. The initial electron energy distribution is assumed to be Maxwellian below 30 keV with a possible high-energy tail derived from the MEPED measurements as described in section 1.3.2. The error resulting from the use of a single Maxwellian distribution over the full range of electron energies was discussed by *Hubert et al.* [2001]. An estimation of the error based on the electron spectral shape measured with the DMSP detector shows that when using a Maxwellian approximation for electron distribution instead of the sum of two Maxwellian distributions the error varies with the emission wavelength. For example, the calculated LBH emission is 6% higher using the single Maxwellian and can reach up to 30% for OI 135.6 nm emission.

[17] The proton energy transport code was described in detail by *Gérard et al.* [2000]. It is based on the direct Monte Carlo method [*Marov et al.*, 1997] which is a stochastic implementation of the solution of the Boltzmann equations for the $H^+$ - H beam. Charge exchange collisions of protons with ambient constituents generate a population of fast H atoms which, in turn, may be converted back to energetic protons. The Monte Carlo proton aurora code includes a detailed calculation of all elastic and inelastic processes for both species. A detailed treatment of the momentum transfer in all collisions makes it possible to follow the pitch angle distribution of the simulated particles. Ionization of the major constituents by collisions with energetic $H^+$ and H particles generates secondary electrons which are treated similarly to the electron-generated secondary population. Many of the proton excitation cross sections for FUV emission are still poorly known or undetermined. Although its volume emission rate is isotropic, the Ly-$\alpha$ line profile depends on the relative angle between the magnetic field line and the direction of observation. This effect is accounted for in calculation of the SI12 expected count rate [*Gérard et al.*, 2001].

[18] The temperature profile and the O, $O_2$ and $N_2$ densities are calculated from the MSIS-90 model atmosphere [*Hedin*, 1991]. The MSIS input parameters are adapted to the geophysical and geographic conditions of each observation. The ionospheric electron temperature and density used in the calculation of the electron cooling term are taken from

the International Reference Atmosphere-1990 (IRI-90) model [*Bilitza*, 1990].

[19] The volume excitation rates for Ly-$\alpha$, $N_2$ LBH-bands, OI-135.6 nm and NI in the FUV passbands are integrated with the appropriate view angle to simulate observations by the two FUV imagers. We ignore multiple scattering for the $N_2$ LBH bands but each line is individually attenuated by $O_2$ for the appropriate view angle to provide the emergent emission rate. These emerging intensities are folded with the absolute spectral response of the cameras to calculate the expected count rate associated with each auroral pixel. For this purpose, the view angle of the pixel is determined from the orientation of the optical axes of the imagers. The corresponding Ly-$\alpha$ line profile is integrated over the SI12 complex transmission function [*Gérard et al.*, 2001].

[20] We use the Monte Carlo model to calculate the efficiency of the high-energy proton channels in SI12 signal. We only consider channels in the energy ranges 30-80 keV and 80-240 keV since higher energy protons make negligible contribution to SI12 for two reasons. First, they produce most of the Ly-$\alpha$ photon at very low altitude where the auroral emission is totally absorbed by $O_2$. Second, the efficiency of the Ly-$\alpha$ production drops significantly at high proton energy. The calculation was made with a fixed mean energy in each channel taken as the central value for different view angles. For example, for a vertical observation, the efficiency expressed in count $pix^{-1}$ $s^{-1}$ per incident $mW/m^2$ in the energy ranges 30-80 keV is 1.75 and in the energy ranges 80-240 keV, the calculated efficiency is 1.06. The efficiency calculation was also made with a random energy in each channel. We used the efficiencies calculated by the second method for this study. For a vertical observation, the calculated efficiency in the energy ranges 30-80 keV with a random energy is 1.5 count $pix^{-1}$ $s^{-1}$ per incident $mW/m^2$.

## FUV-in situ comparisons

[21] The instrumental count rate was extracted for the FUV pixel corresponding to the footprint at 120 km of the magnetic field line at the instantaneous NOAA spacecraft position. An FUV image is obtained every 2 minutes. During this period, the NOAA spacecraft moves about 850 km along its orbit. To account for this, the count rate from each individual FUV image was extracted along the footprint track of NOAA from the position one minute before to one minute after the central snapshot time. Before extraction of FUV pixels, data were filtered by smoothing by the point spread function (PSF) of the imagers. The width of the PSF was evaluated from the observation of hot stars crossing the field of view: about 3.5 WIC pixels and 2 SI12 pixels. The appropriate FUV pixel from the snapshot was chosen to minimize the difference of the geographic coordinates of the magnetic field line mapped from the NOAA satellite to 120 km and the position of the FUV pixel.

[22] The spatial resolution of the in situ data is much higher than the FUV instrumental resolution. To account for this difference it is necessary to smooth the NOAA data before

comparing the modeled intensity with the FUV observation. The NOAA measurements were averaged over a time period corresponding to the combination of the PSF of the FUV instruments with the displacement of the IMAGE satellite along its orbit during the observation. A 1.5 FMHW (6 WIC pixels, 3 SI12 pixels) smoothing width was chosen in consideration of a 66% decrease of the peak of a Gaussian PSF. In a second step, we empirically estimated the smoothing function from comparisons between NOAA and WIC data from one case where the electron incident flux measured by NOAA was very narrow and intense. This comparison provided an upper limit of 120 seconds of NOAA observation for the smoothing resolution. The NOAA satellites fly over 6 WIC pixels (i.e. 1.5 FMHW) in about 66 seconds. We thus estimate that the appropriate time period for smoothing the NOAA data is between 66 and 120 seconds for comparisons with the WIC data. The difference between the theoretical and effective value may stem from the fact that NOAA measurements are made along the orbital track, while FUV globally observes the auroral region. Each FUV pixel includes contributions from emissions adjacent to the NOAA track due to its PSF.

[23] A set of 12 NOAA north polar crossings was selected including 7 NOAA-15 and 5 NOAA-16 orbits. Table 1.2 lists the dates, UT, MLT and geomagnetic latitudes of the observed first and second peak of electron precipitation. Figure 1.4 shows the WIC images with the track of the NOAA-15 or NOAA-16 satellites mapped at 120 km. The direction of the spacecraft motion is indicated by an arrow on each image.

| | Date | Satellite | Kp | First peak | | | Second peak | | |
|---|---|---|---|---|---|---|---|---|---|
| Case | Year | | | UT | GEOLAT | MLT | UT | GEOLAT | MLT |
| Number | 2000 | | | | deg. | hr-min | | deg. | hr-min |
| a | Jul. 15 | NOAA-15 | 6 | 1227:52 | 72.80 | 1805 | 1241:42 | 57.09 | 0835 |
| b | Jul. 15 | NOAA-15 | 6 | 1409:12 | 73.29 | 1836 | 1423:24 | 55.41 | 0802 |
| c | Aug. 12 | NOAA-15 | 7 | 1014:36 | 66.68 | 1746 | 1030:06 | 58.65 | 0910 |
| d | Aug. 12 | NOAA-15 | 7 | 1158:50 | 75.66 | 1739 | 1211:42 | 57.02 | 0843 |
| e | Sep. 19 | NOAA-15 | 5 | 0921:44 | 77.07 | 1627 | 0927:52 | 76.68 | 1155 |
| f | Sep. 30 | NOAA-15 | 3 | 0142:42 | 59.63 | 1753 | 0154:04 | 77.39 | 0926 |
| g | Oct. 03 | NOAA-15 | 4 | 0033:54 | 58.45 | 1817 | 0046:54 | 73.92 | 0842 |
| h | Dec. 07 | NOAA-16 | 3 | 0519:46 | 75.23 | 1144 | 0531:50 | 60.65 | 0343 |
| i | Dec. 07 | NOAA-16 | 2 | 1854:30 | 68.47 | 1151 | 1906:06 | 68.81 | 0253 |
| j | Dec. 23 | NOAA-16 | 4 | 0558:57 | 79.73 | 1117 | 0609:33 | 59.48 | 0329 |
| k | Dec. 23 | NOAA-16 | 4 | 0740:15 | 78.05 | 1220 | 0753:43 | 52.54 | 0242 |
| l | Dec. 25 | NOAA-16 | 3 | 1405:51 | 72.64 | 1347 | 1416:31 | 68.39 | 0156 |

Table 1.2: Characteristics of the NOAA-TIROS auroral oval crossings.

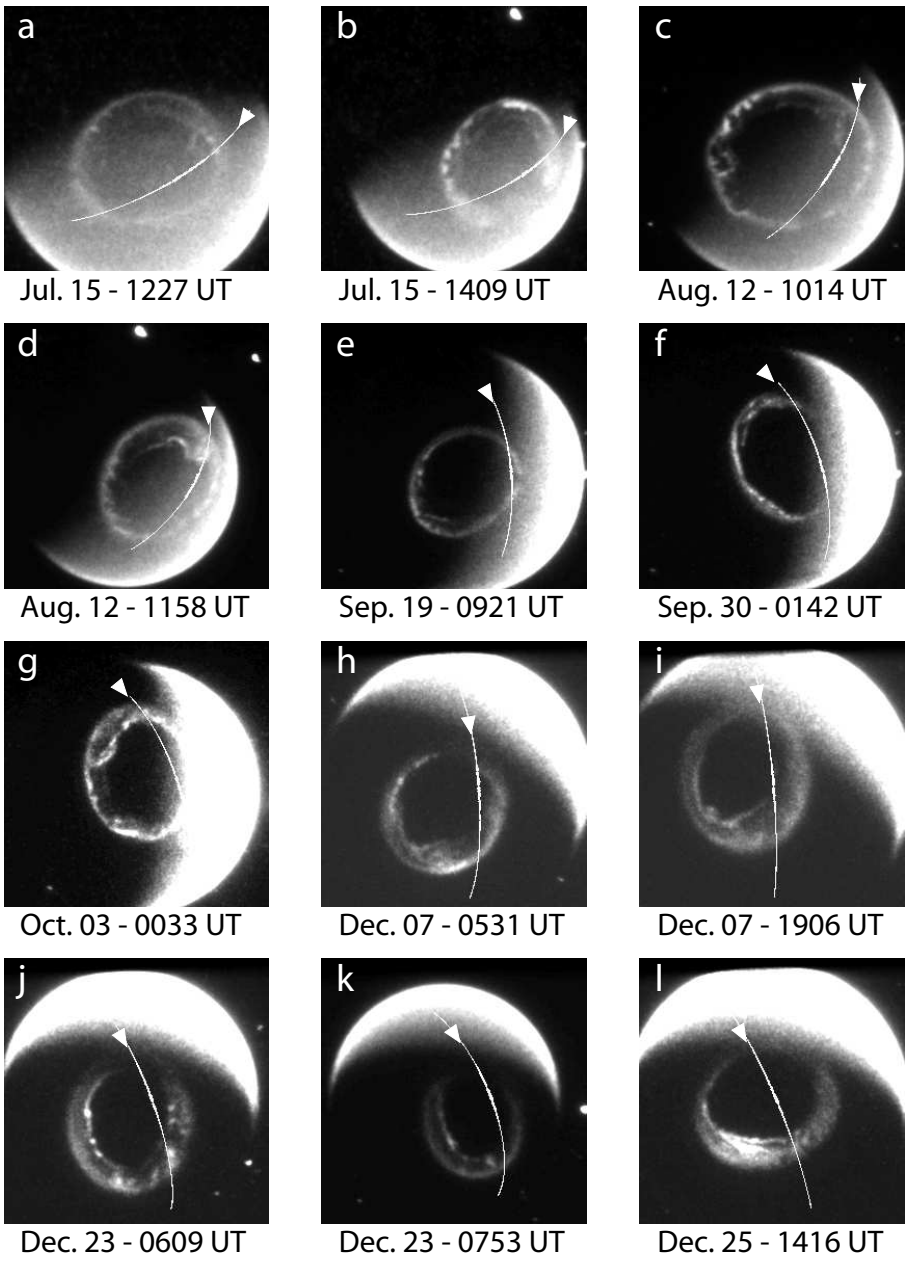


Figure 1.4: Images taken by the WIC imager. The footprint of the NOAA-TIROS track at 120 km is plotted on each image. For each track the WIC snapshot time was selected to be closest to the time of the electron precipitating energy flux main peak. The arrows show the direction of the NOAA spacecraft motion.

### 1.3.3 NOAA-FUV comparisons

[24] We now present the results of the comparisons, separately for WIC and for SI12.

#### WIC data

[25] Figures 1.5 and 1.6 show examples of comparisons between the observed WIC signal and the WIC signal expected from simulation using NOAA in situ measurements. The global form of the observed signal is well reproduced by the model calculation, both in morphology and in intensity. The comparisons have been made after removal of the dayglow background emission by fitting a third degree polynomial to the WIC signal along the NOAA track. The fit is made using WIC data from the region outside the auroral oval, that is inside the polar caps and outside the equatorward boundary of the auroral oval.

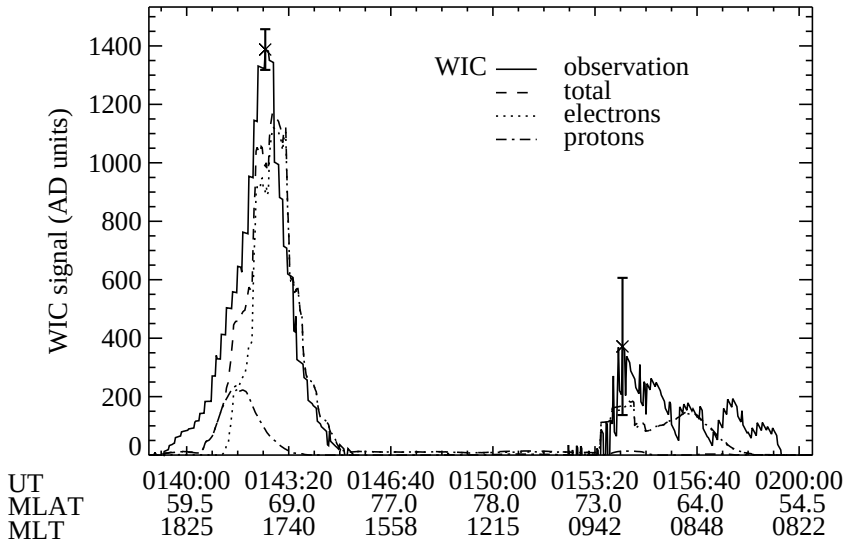


Figure 1.5: Comparison between the WIC observations (solid line) and a simulated WIC signal based on NOAA particle measurements (dashed line) for case f - September 30, 2000. The modeled contribution of electrons (dotted line) and protons (dotted-dashed line) to the simulated signal are also shown. The error bars represent ± one standard deviation on typical observations.

[26] Figure 1.5 shows the observed and the modeled WIC signals illustrated by Figure 1.4-f and whose characteristics are summarized in Table 1.2-case f. The first oval crossing occurred around 1800 MLT (between 0140 and 0145 UT) and the second oval crossing around 0900 MLT (between 0153 and 0200 UT). The polar cap between 0145 and 0153 UT is characterized by the absence of precipitating particles. The WIC signal corresponding

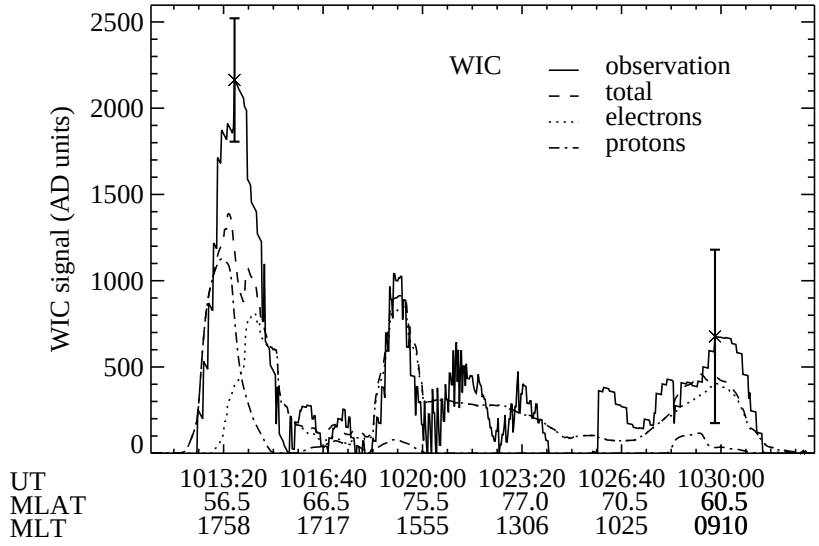


Figure 1.6: Same as Figure 1.5 for case c - August 12, 2000.

to the oval around 0900 MLT was affected by an important contribution from the dayglow. The difficulty in removing this contribution can explain the somewhat poor agreement with simulated signal in the dayside auroral region and the importance of the error bar. The evaluation of the error on each observation was made in considering the statistical error on the count rates, taking the smoothing of the FUV observation before the pixel extraction into account, and the error induced by the background removal. In Figures 1.5 and 1.6 two representative error bars are illustrated. Figure 1.6 present the comparison illustrated by Figure 1.4-c. In Figure 1.6, the NOAA spacecraft does not seem to cross any region corresponding to the polar cap because of the great extend of the auroral oval and the orbit of the NOAA satellite footprint reached only 78° magnetic latitude and barely entered the polar cap. This example from August 12, 2000 was characterized by a very intense magnetic activity (Kp = 7), which explains the great width of the auroral oval. After 1555 MLT, the observed signal shows oscillations not present in the calculated signal. These variations may also be attributed to the insufficient removal of the background dayglows contribution to the WIC signal in the dayside auroral region. Moreover, Figure 1.6 shows that the modeled signal around 1800 MLT underestimates the observed WIC signal. The disagreement can locally reach a factor 2. In some other cases (not shown) the simulated WIC signal locally overestimates the observation.

[27] We now statistically compare predicted and observed WIC signal. To avoid uncertainties due to possible inadequate smoothing, we integrate the observed and predicted count rates over the width of the auroral oval crossings. Figure 1.7 shows the individual data points. All the polar crossing illustrated in Figure 1.4 were used for this analysis,

except case b which was removed from the analysis because it was apparently aberrant. The observed count rate was three times larger than the calculated one. A linear least squares fit to these data gives a slope of 0.71± 0.06, implying that the calculation slightly underestimates the observation. We estimated the horizontal error bars on each point, i.e. the error on the observation. They are found to be comparable to the width of the plot symbols. The dashed line represents the bisecting line corresponding to perfect agreement between simulated and observed signals. Most of the points characterized by a moderate count rate are in quite good agreement with the model. The small discrepancy is principally caused by crossings with large count rates. Possible causes of this difference are discussed in section 4. When removing the NOAA-15 data point of 2.25x105 AD units corresponding to case d in Figure 1.4, the slope becomes 0.89± 0.08 (thin solid line in Figure 1.7), that is quite close to the perfect match.

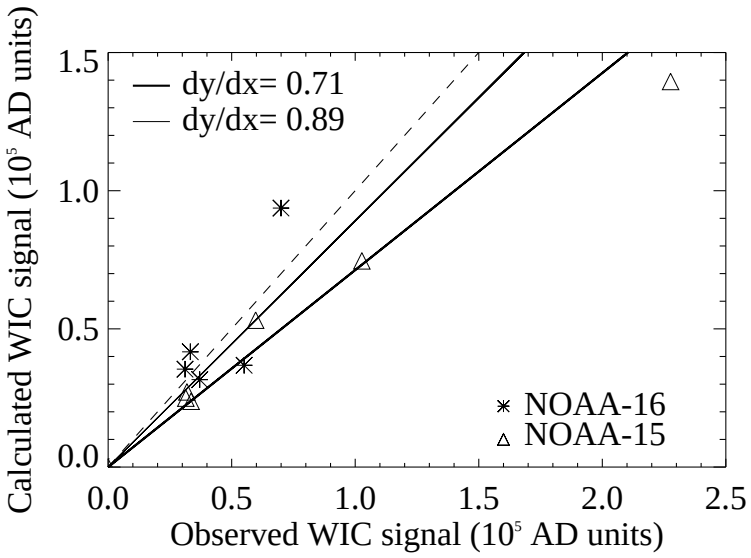


Figure 1.7: Observed and simulated WIC AD units summed over oval crossing. A least-squares regression (bold solid line) gives a slope of 0.71±0.05. The thin solid line shows the least-square regression line when removing the data point at $2.25 \times 10^5$ AD units. The slope is then 0.89±0.08. The dashed line corresponds to a perfect agreement between observations and simulations. The size of the horizontal error bars is comparable to the size of the symbol.

[28] We now test to what extent thermospheric composition can influence the results of this study. The semi-empirical MSIS-90 model [*Hedin*, 1991] is used in the transport models to calculate the temperature and neutral density profiles. This model reproduces the mean thermospheric behavior and does not represent local auroral variations in details. Auroral precipitation produces local heating of the atmosphere causing enhancement of

molecular-rich gas in the upper thermosphere. The result of this upwelling is an increase in the $N_2/O$ ratio as confirmed by a large number of observations in the auroral region [*Hecht et al.*, 2000]. As a sensitivity test, we modeled the WIC response assuming the $N_2$ density was a factor of 2 greater that the MSIS model, in the same time of a doubling of the $O_2$ density, and compared these results with the outputs using the MSIS model. Figure 1.8 shows that change corresponding to case i in Table 1.2. Doubling of the $N_2$ and $O_2$ density resulted in an increase in the calculated WIC signal, owing to an increase in the $N_2$ LBH emission. The increase of $O_2$ enhances the absorption of the emission and moderate the increase in the calculated signal. In a second test, we reduced the atomic oxygen density by a factor of 2. This decrease in O density had little consequence on the WIC signal. The final case illustrated in Figure 1.8 shows the results obtained when combining the two perturbations. The result is very close to the doubling $N_2$ and $O_2$ result.

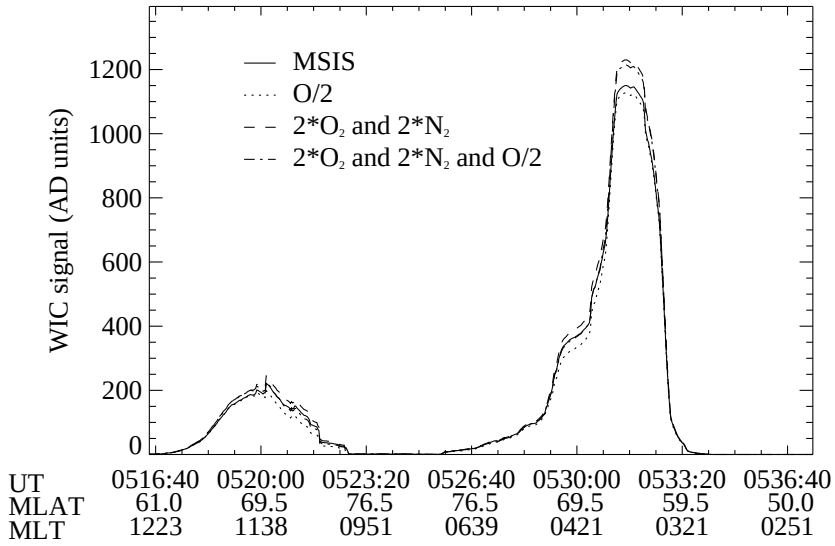


Figure 1.8: Sensitivity test of the influence of the atmospheric composition for case i - December 7, 2000. The solid line is the model integrated result using the MSIS-90 atmosphere. Halving the O density produces no noticeable effect (dotted line). Doubling the $N_2$ and the $O_2$ density (dashed line) increases the LBH emission The addition of both previous perturbations (dashed-dotted line) leads to an increased of the observed signal.

[29] This study also provides an opportunity to quantify the role of precipitating protons on $N_2$ LBH emission. Secondary electrons generated from colliding incident protons contribute to the excitation of $N_2$ and therefore to the WIC signal. The FUV-in situ comparisons indicate that WIC observations can be dominated by proton contribution. In Figure 1.6, corresponding to the case c in Table 1.2, around 1013 UT the contribution of protons locally dominates the contribution of electrons. This feature was also pointed out

by *Frey et al.* [2001]. The orientation of the NOAA-15 orbit is well adapted to study the characteristics of the particle precipitation in the dusk sector. As expected from statistical precipitation patterns, the proton oval is generally displaced equatorward of the electron oval in this sector. The proton contribution often explains, in part, the width of the observed WIC oval in the region around 1800 MLT. Model calculations that consider only the electron contribution usually underestimate the WIC signal. A study of the proton contribution to the WIC signal was made by calculating the ratio of simulated WIC counts due to protons to the total WIC counts for the 12 NOAA orbits. The ratios were calculated using 20 seconds-averaged simulated WIC observations, and neglecting the in situ measurements whenever the total incident energy flux was lower then 0.05 $mW/m^2$. The study shows the importance of protons in the dusk sector in the equatorward region of the oval: below 65°N, 57% of ratios exceed 0.8 and 82% of the ratios are over 0.1. Above 65°N, only 1% of cases have ratios greater than 0.8 but more than 55% of cases reach 10% of the total contribution. Neglecting the proton contribution in the dusk sector to latitudes under 65°N would introduce errors of over 80% in most cases. In other sectors, the proton contribution would not be so important but it can reach more than 10% in 50% of the cases. We thus conclude that protons cannot be systematically neglected if the WIC signal is to be reliably interpreted in terms of precipitated particle energy flux.

### SI12 data

[30] Figures 1.9 and 1.10 show comparisons between the simulated SI12 signal based on the NOAA data and the actual SI12 observations. In general, the agreement between observations and modeled SI12 responses is quite good. As for the WIC signal, the shape of the SI12 signal is also characterized by first a crossing of the auroral oval, followed by the polar cap and then a second oval crossing. In Figure 1.9, corresponding to the case b in Table 1.2 and illustrated in Figure 1.4-b, the polar cap crossing between 1410 and 1420 UT presents a weak continuous emission. This is probably the signature of the polar rain which are low-energy solar-wind particles precipitating into the atmosphere along the opened magnetospheric field lines poleward of the auroral zone. *Fairfield and Scudder* [1985] demonstrated that the more energetic component of the polar rain is composed of charged particles from the solar wind "strahl", a field-aligned component of the solar wind. In this case b, the intensity and the width of the oval crossing around 0810 MLT are well reproduced by the simulated signal. However, around 1850 MLT the calculated signal does not correctly reproduce the width of the peak even though the intensity of both signals seems to be quite well matched. This discrepancy was also present in the comparisons with the FAST measurements [*Frey et al.*, 2001; *Gérard et al.*, 2001]. Figure 1.10 presents a second example of comparison between SI12 calculated and observed signal, illustrated by Figure 1.4-f and whose characteristics are summarized in Table 1.2-case f. In Figure 8, the agreement around the secondary peaks (between 0151 and 0157 UT) is not good. However, the maximum observed count rates are only about 3 while the simulated one reaches 1 count. Those count rates are very small and cannot be considered as significant

as may be seen from the size of the error bars. The standart deviation on the count rate of these observations is about 1 count.

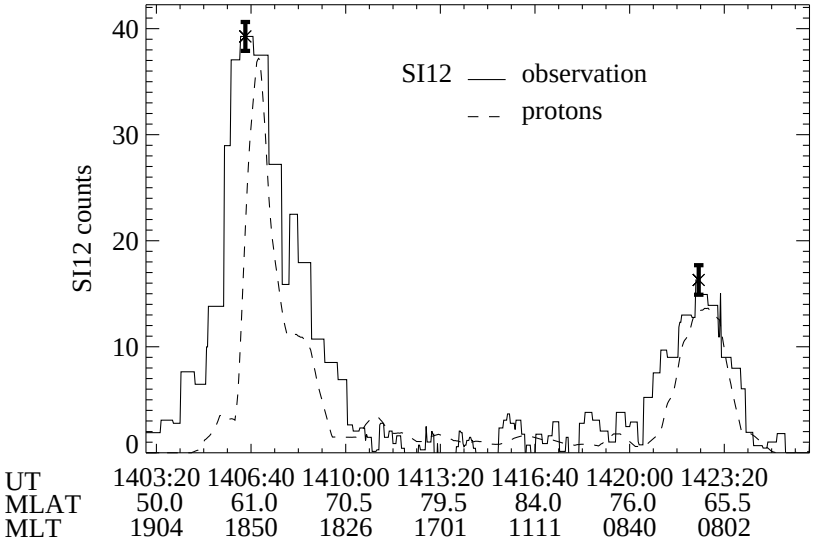


Figure 1.9: Comparison of the observed SI12 (solid line) and the expected SI12 signals from simulations using NOAA in situ measurements (dashed line) for case b - July 15, 2000. The error bars represent ± one standard deviation on typical observations.

[31] The integration of both the actual and simulated SI12 counts over the oval a number of crossings is displayed in Figure 1.11 which shows all the individual data points. All the cases illustrated in Figure 1.4 were used for this analysis, except case b which was removed from the analysis because it was apparently aberrant. The slope of the regression line is 0.55± 0.04. This result is consistent with the disagreements between the width of observed and simulated auroral oval as illustrated in Figure 1.9. The agreement is not as good as for WIC (see Figure 1.7), but we consider it is still quite acceptable in view of all the uncertainties as discussed in section 1.3.4.

[32] In this case varying the ratio $O/N_2$ from the MSIS model does not significantly influence the calculated emission rate because the Ly-$\alpha$ emission is directly produced by precipitating protons. The calculated Ly-$\alpha$ efficiencies are expected to remain virtually unchanged when altering the density of O and $N_2$ in comparison with MSIS. Simulations with the Monte Carlo model show that the SI12 count rate responds only very moderately to composition changes. For example, for proton with a kappa distribution with $E_0 = 1$ keV, an incident flux of 1 $mW/m^2$ gives an estimated Ly-$\alpha$ brightness of 5.94 kR with the MSIS-atmosphere for a vertical view, implying about 36 SI12 counts per pixels. In dividing the neutral oxygen density by a factor of 2, which is an extreme case, the evaluated SI12

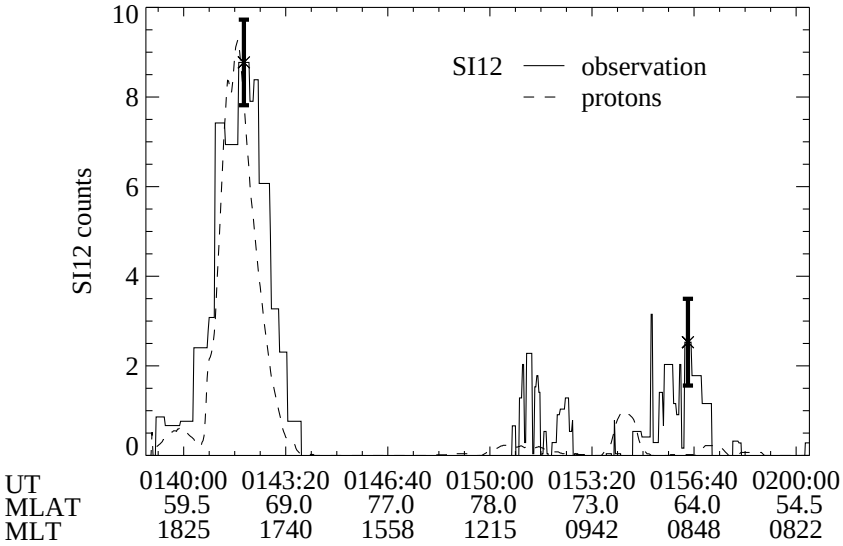


Figure 1.10: Same as Figure 1.9 for case f - August 12, 2000.

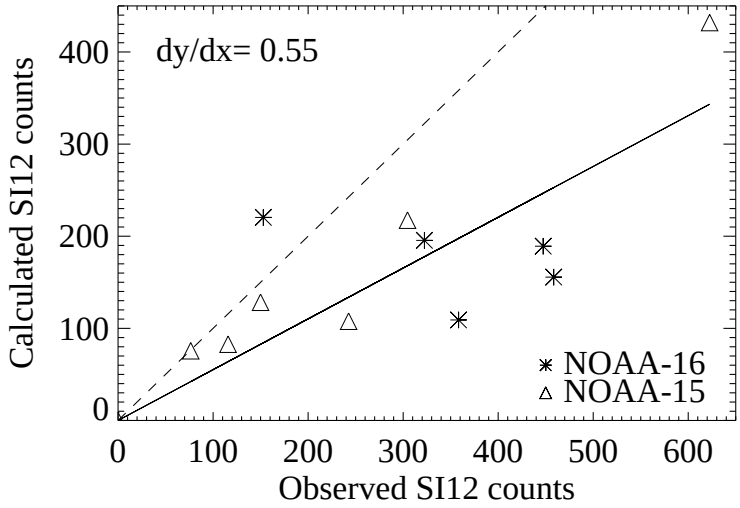


Figure 1.11: Observed and simulated SI12 counts summed over oval crossings. A least-squares regression (solid line) gives a slope of $0.55 \pm 0.04$. The dashed line corresponds to a perfect agreement between observations and simulations. The size of the horizontal error bars is similar to the size of the symbol.

count rate becomes 33.2. The reduction of O density by a factor of 2 and the doubling of the $N_2$ density result in a count rate of 32.6.

### 1.3.4 Contribution of high-energy particles

[33] Some previous similar studies [*Liou et al.*, 1999] did not take high-energy particles in consideration because most low altitude satellites have only particle detectors sensitive to less than 30 keV particles. The MEPED experiment provides the possibility to analyze the importance of protons of energy higher than 30 keV in the FUV auroral brightness. Figure 1.12 shows the contributions of protons with energies less and higher than 30 keV in the total energy flux for a NOAA-15 transit of the polar region on August 12, 2000 (case c in Table 1.2). In this example, the high-energy proton contribution locally dominates the low energy one: the mean contribution of low energy protons along this oval crossing is 24 %. The contribution of high-energy protons in the total energy flux as a function of the MLT sector may be statistically analyzed. In order to perform this analysis we calculate the ratio between energy fluxes carried by high (>30 keV) and low (<30 keV) energy protons averaged over 20 seconds of NOAA data. In so doing, we neglect the in situ measurements where the proton incident energy flux was lower then 0.05 $mW/m^2$. Figure 1.13 displays the calculated ratios for all cases illustrated in Figure 1.4 as a function of the magnetic latitude in three local time sectors. The results in Figure 1.13 encompass all levels of magnetic activity. A ratio higher than 1.0 means that the contribution of high-energy protons to the total flux is over 50%. The three different local time sectors were determined from the magnetic footprint crossed by the NOAA satellites. One region extends on the dusk sector between 1600 and 2100 MLT, another sector includes the post-midnight aurora and the last one covers the dayside sector between 0600 and 1600 MLT. In the dusk sector, high-energy protons significantly dominate the precipitating proton flux near the equatorward boundary of the auroral oval. Below 65° N the mean contribution in energy flux of high-energy protons is 8.2 times larger than the contribution of low energy protons. Near the polar boundary the mean ratio is 0.93 so the mean energy flux due to high-energy protons is around 50% of the total energy flux. In the sector between 0600 and 1600 MLT, the major portion of energy flux is carried by low energy protons, as indicated by the mean ratio of 0.43. In the postmidnight sector, the relative contribution of the high-energy component is higher than 50% only for the NOAA-16 crossing around 0609 UT on December 23, 2000. This is probably an isolated injection event as the Kp index over the previous 3-hours was 6. These results are in agreement with the statistical model of ion precipitation by *Hardy et al.* [1989] based on DMSP data. The particle detectors on board the DMSP satellites covered the energy range 30 eV to 30 keV. When the derived mean energy is close to 30 keV, it is likely that the real mean energy exceeds this limit as the Maxwellian extrapolation probably underestimated the actual value. The study from *Hardy et al.* [1989] also shows that in the dusk sector the proton mean energy increases for decreasing latitudes. Moreover, the average proton energy is the lowest in the dayside sector between 0600 and 1200 MLT.

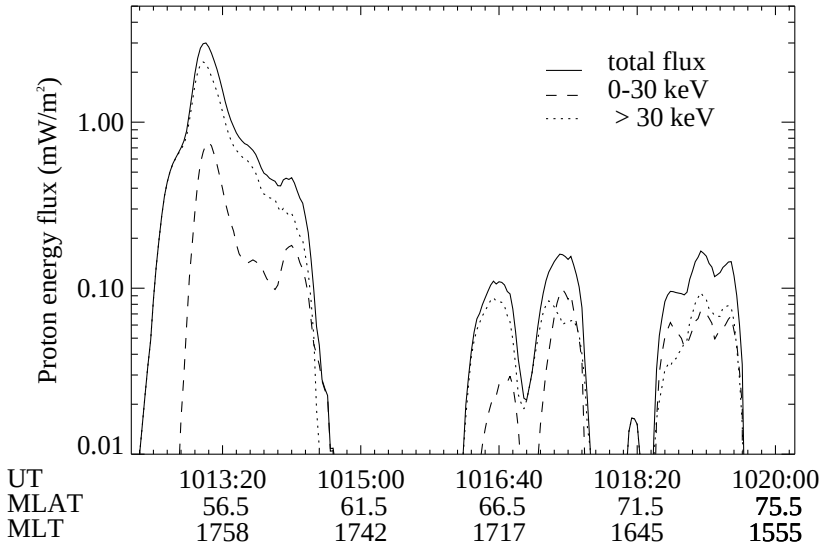


Figure 1.12: Variation of the proton energy flux measured along the NOAA-TIROS orbit during the first auroral oval crossing on case c - August 12, 2000. The solid line shows the total energy flux. The dashed line represents the contribution of low-energy protons from the TED measurements using an extrapolation up to 30 keV. The dotted line shows the MEPED measurements.

[34] We analyzed the contribution of protons of energy greater than 30 keV and less than 30 keV to the simulated WIC signal by calculating the relative contributions of high and low energy proton to the modeled WIC counts (Figure 1.14). They are quite similar to those of Figure 1.13 obtained for the energy flux, but a smaller fraction of the WIC ratios are above the limit of 1.0. This means that the relative contribution of high-energy protons in the WIC signal is less important than in the energy flux. WIC efficiencies due to incident protons vary with proton mean energy but no substantial variation occurs near or above 30 keV. However the amount of $O_2$ absorption increases for increasing energy so that high-energy protons produce emission that is more efficiently absorbed by $O_2$. For electrons, the proportion above 30 keV is insignificant to the WIC signal. Even under very intense events when the contribution of high-energy electrons to the total energy flux can reach 30%, the resulting LBH emission is negligible. This is because high-energy electrons reach lower altitudes so that the emission they produce is strongly absorbed by $O_2$.

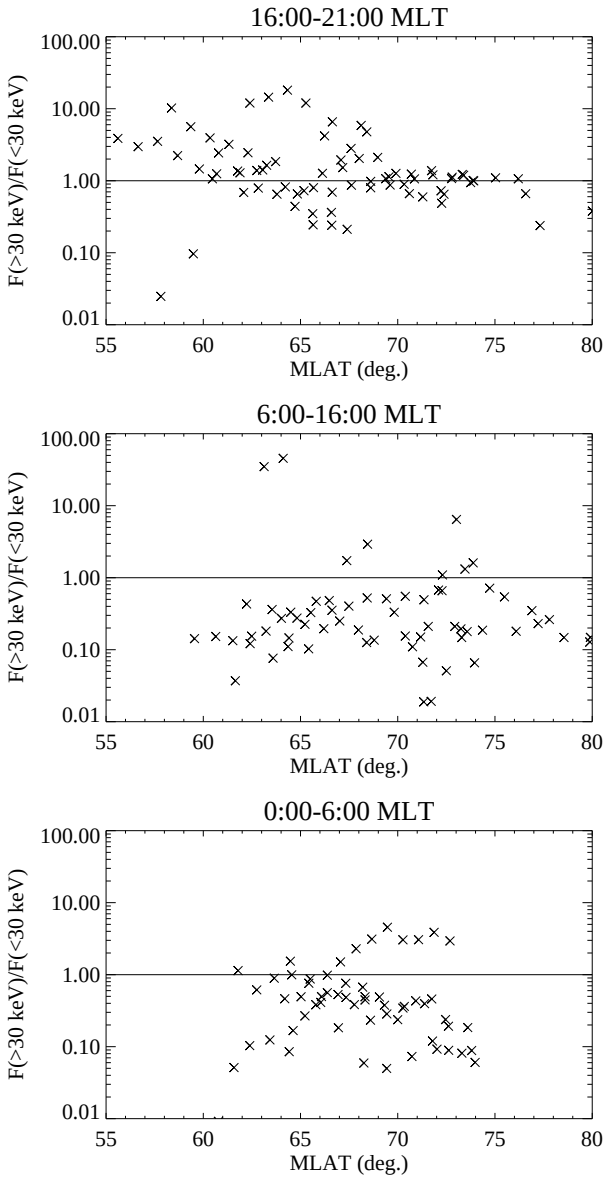


Figure 1.13: Ratio of the high-energy to the low-energy proton energy flux for all cases listed in Table 1.2 as a function of the latitude for three different magnetic local time sectors. The solid line indicates where the contributions of high-energy and low-energy protons are equal.

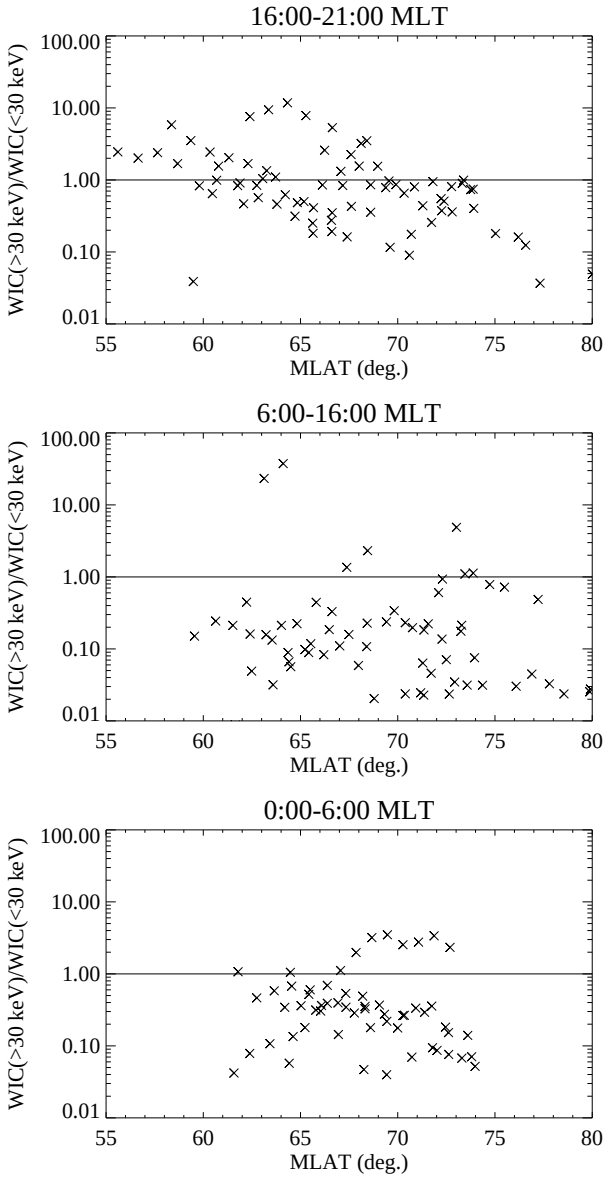


Figure 1.14: Ratio of high-energy and low-energy proton contribution to the WIC signal for all cases listed in Table 1.2. The solid line indicates where the contributions of high-energy and low-energy protons are equal.

### 1.3.5 Discussion and conclusions

[35] The results of the comparison described in the preceding sections (Figures 5 and 9) show statistical agreements between observations and model calculations of about 70% for the WIC signal and about 55% for the SI12 signal, both of which we consider as very satisfactory. For WIC - in situ comparisons several different explanations for the remaining discrepancy can be suggested. First, there are uncertainties associated with the calibration of the MEPED and TED instruments. On the basis of pre-flight calibrations and comparisons between NOAA-15 and NOAA-16 observations at nearly the same locations and times, the uncertainty in the TED energy flux measurements is estimated to about +/- 25% for energy fluxes of above 1 $mW/m^2$ while the error in the mean energy can be approximately one channel. Second, a part of the disagreement can be assigned to the assumptions about the precipitating particles. The TED instrument measures particles less than 20 keV at two pitch angles, both within the loss cone. In contrast, we used only the MEPED measurements at the pitch angle within the loss cone and calculated the total flux incident on the atmosphere assuming isotropy over the loss cone. If the incident energetic particles were not isotropic, this assumption could lead to an underestimate of the actual incident fluxes. When proton fluxes are significant, their angular distribution is generally isotropic and so probably cannot fully explain the disagreements. Radiation damage to the MEPED proton solid state detectors is another potential source of error especially for data from the NOAA-15 satellite that had been in operation for over two years. The effect of radiation damage is to increase the proton energy thresholds over their original values and, if not taken into account, leads to an underestimate of the >30 keV energy flux to the atmosphere. Because comparisons with NOAA-16 observations also lead to underestimates of the SI12 signal (Figure 1.11), radiation damage is unlikely to fully account for the discrepancies.

[36] The models we use can also introduce some error. As described in section 1.3.3, the MSIS model that calculates the atmospheric composition profile can introduce errors in the WIC-in situ comparisons. It is probable that local density variations are not reproduced by the model and so the calculation may underestimate the real emission brightness. In addition, errors can stem from the cross sections used in models [*Kanik et al.*, 2000]. For example, previous studies [*Eastes and Dentamaro*, 1996; *Eastes*, 2000] indicate that *Ajello and Shemansky* [1985]'s LBH cross section used in the GLOW model for electrons may be underestimated owing to the presence of three close-lying states ($a^1\Pi_g$, $a'^1\Sigma_u^-$ and $w^1\Delta_u$) of $N_2$. The $a'^1\Sigma_u^-$ and $w^1\Delta_u$ states are long-lived and optically forbidden to the ground state but are optically allowed to the $a^1\Pi_g$ state. Cascading from these two states can induce in the upper atmosphere a 30% additional contribution to the direct LBH cross section. In the case of SI12, the uncertainties in instrument calibration, in cross section values used in models all contribute to the disagreement. Moreover, space and time averaging, dayglow subtraction, IMAGE detector calibration and limited resolution are also potential sources of uncertainties.

[37] Considering all sources of errors, we conclude that the observed FUV intensities are in accordance with intensities predicted from in situ NOAA measurements. The FUV observations from the WIC and SI12 instruments can thus be used for quantitative analyses and determination of auroral particle precipitation. We have shown that auroral particle energy flux information may be extracted from global observations of the auroral region separately for protons and for electrons. The WIC and SI12 instruments are shown capable of observing the temporal evolution of auroral particle injection to the ionosphere on a spatially global basis.

[38] Characterization of proton precipitation using NOAA in situ measurements and FUV observations gives results in agreement with the *Hardy et al.* [1989] precipitation model. The results confirm that in the dusk sector the proton auroral oval is shifted equatorward of the electron one and high-energy protons contribution is more important at low latitudes. In the other local time sectors the high-energy proton contribution does not play such an important role. We have shown that auroral protons locally contribute substantially to ionosphere characteristics, in particular ionization and heating at high latitudes.

# Chapitre 2

# The average proton aurora

## 2.1 Introduction : la morphologie de l'ovale auroral protonique

Très peu de moyens existent jusqu'à présent pour qualifier de façon globale l'aurore à protons, puisque aucun instrument ne permettait l'observation globale de l'ovale protonique, avant le lancement du satellite IMAGE ; cependant, quelques études existent. La principale est l'étude statistique de *Hardy et al.* [1989]. Les auteurs ont utilisé 27 000 survols des pôles par les satellites DMSP F6 et F7. Des cartes statistiques de l'énergie moyenne, du flux de particules et du flux énergétique ont été produites pour les électrons et les protons, selon le niveau d'activité magnétique mesuré par l'indice Kp. Avant ces études, il était déjà connu que la précipitation des protons et des électrons se produit dans une région annulaire situé plus ou moins aux mêmes latitudes pour les deux types de particules. Les études précédentes basées sur des mesures au sol [*Vallance-Jones et al.* [1982], et références incluses] avaient également déjà montré que l'ovale auroral protonique s'intensifie et se meut vers l'équateur lorsque l'activité géomagnétique et aurorale augmente.

*Hardy et al.* [1989] ont montré la présence d'un minimum dans le flux énergétique de protons dans le secteur avant-midi, alors que la valeur maximale est observée dans le secteur avant-minuit pour tous les niveaux d'activité. Ainsi, la précipitation de protons a plutôt la forme d'un "C". Le même type de comportement a été observé pour les électrons [*Hardy et al.*, 1985]. Ce motif en forme de "C" pour les protons est globalement la réflexion par rapport au méridien midi-minuit du motif de l'ovale électronique. Le minimum pour le flux électronique se présente dans le secteur de l'après-midi, alors qu'il est situé dans le secteur du matin pour les protons. Cette caractéristique est expliquée par les dérives dues au gradient de $\mathbf{B}$ et à la courbure des lignes de champ magnétique (voir Introduction générale) subie par ces particules. Les protons de haute énergie provenant du feuillet de plasma dérivent préférentiellement vers l'ouest, c'est-à-dire via le secteur du crépuscule vers le secteur de l'après-midi et ensuite le secteur juste avant midi. Ils sont donc absents d'une grande partie de l'ovale dans le secteur du matin [*Hardy et al.*, 1989]. Puisque pour

les électrons, la dérive à lieu préférentiellement vers l'est, ils sont absents dans le secteur de l'après-midi. Je montre dans ce chapitre que cette symétrie par rapport au méridien "midi-minuit" entre les électrons et les protons n'est pas parfaite, puisque le maximum du flux énergétique pour les deux types de particules est situé dans le même quadrant de l'ovale. Comme c'est la région où les sous-tempêtes débutent, ce résultat est expliqué par l'injection directe de plasma chaud provenant de la queue de la magnétosphère. Finalement, *Hardy et al.* [1989] ont aussi montré que, dans le secteur du crépuscule, la précipitation moyenne de protons se localise à des latitudes plus basses que la précipitation des électrons. Ce résultat a également été vérifié au chapitre 1 sur base de données instantanées. De plus, d'un point de vue quantitatif et statistique, *Hardy et al.* [1989] ont montré que le flux énergétique auroral est principalement transporté par les électrons, qui contribuent à 85% ou 90% de l'apport total. Les ions, principalement des protons, transportent le reste de l'énergie [1].

Plusieurs études ont tenté de qualifier la précipitation aurorale globale d'un point de vue quantitatif. La notion de puissance hémisphérique a donc été introduite. La puissance hémisphérique totale (hemispheric power HP) est une mesure du taux instantané d'injection d'énergie aurorale dans l'atmosphère d'un hémisphère. Elle a été calculée à partir de mesures au sol [*Ahn et al.*, 1983; *Richmond et al.*, 1990; *Lu et al.*, 1998], ainsi que de mesures de particules *in situ* [*Fuller-Rowell and Evans*, 1987]. Mais toutes ces études sont limitées par l'aspect local des mesures. Par exemple, les instruments TED (Total Energy Detector) à bord des satellites NOAA-TIROS fournissent des estimations des puissances hémisphériques pour les deux hémisphères. Ces instruments intègrent les flux d'énergie mesuré séparément pour les électrons et les protons qui précipitent, dont l'energie est comprise entre 50 eV et 20 keV. L'estimation est basée sur une comparaison entre les intégrations pondérées sur la latitude des flux d'énergie mesurés le long de la trajectoire du satellite NOAA et les cartes climatologiques statistiques des flux d'énergie obtenus par la base de données NOAA. Ces cartes sont basées sur 10 niveaux de puissance hémisphériques. L'intensité des flux d'énergie qui précipitent mesurée le long de l'orbite NOAA est mise en accord avec une des 10 cartes pour estimer la puissance hémisphérique totale [*Fuller-Rowell and Evans*, 1987]. Cette méthode suppose que les apports d'énergie des particules aurorales suivent les caractéristiques des cartes climatologiques. Cette hypothèse n'est pas valable durant les périodes dynamiques, telles que les sous-tempêtes, lorsqu'il y a de fortes différences locales de flux énergétique. L'estimation des puissances hémisphériques durant de telles périodes peut donc être erronée.

Avec la disponibilité des observations de l'instrument SI12, les puissances hémisphériques instantanées peuvent être obtenues en intégrant la luminosité auroral observée, à condition de connaître la relation entre le taux de comptage de l'instrument et le flux incident de particules aurorales. Cette estimation est possible puisque cette relation a été modélisée,

[1] C'est pourquoi dans l'ensemble de mon travail, je ne fais allusion qu'aux protons auroraux et non aux ions.

comme expliqué au chapitre 1.1.

## 2.2 Résumé introductif

Tous les résultats décrits ci-dessus relatifs à la morphologie de l'ovale de protons ont été découverts à partir de mesures locales. Ils donnent donc une image statistique de l'ovale basée sur des données locales non simultanées. Pour la première fois, j'ai pu vérifier toutes ces connaissances à partir d'observations globales de l'ovale auroral de protons. J'ai utilisé les observations FUV pour construire des cartes statistiques du flux énergétique des protons auroraux. Les observations qui ont servi à cette statistique se répartissent sur les périodes proches des solstices d'été 2000 et 2001 et des solstices d'hiver 2000-2001 et 2001-2002. Au total, plus de 69000 observations SI12 ont été utilisées. J'ai montré que la morphologie de l'ovale protonique moyen observé par SI12 ressemble fortement à la vue statistique déduite des données DMSP [*Hardy et al.*, 1989]. Elle présente un ovale en forme de "C" avec un minimum dans le secteur du matin. La puissance hémisphérique moyenne de la précipitation de protons est de l'ordre de 2.2 GW pour une valeur moyenne de Kp égale à 2, ce qui est également en accord avec les valeurs du modèle empirique de *Hardy et al.* [1989]. De plus, j'ai comparé pour chaque valeur de Kp, la puissance hémisphérique moyenne des protons avec les valeurs de l'étude statistique de *Hardy et al.* [1989]. L'accord entre les deux est très satisfaisant, ce qui démontre la validité de la méthode utilisée pour évaluer les flux de protons à partir du taux de comptage de SI12. Finalement, mon étude a également permis de mettre en évidence un effet saisonnier dans la précipitation de protons : globalement, la puissance hémisphérique est plus grande en été qu'en hiver. Cet effet saisonnier est en opposition avec celui observé pour les électrons.

La base de données construite pour cette étude statistique a également été utilisée pour mettre en évidence les relations entre la précipitation de protons, le vent solaire et le champ magnétique interplanétaire (IMF). J'ai cherché l'existence de corrélations entre l'émission aurorale produite par les protons et la vitesse, la densité et la pression dynamique du vent solaire ainsi que l'orientation du champ IMF. En effet, on sait que les caractéristiques du vent solaire influencent la reconnexion entre les champs IMF et magnétosphérique et a ainsi un impact sur l'activité aurorale. Cependant, l'effet de cette reconnexion sur les processus de précipitation ne sont pas encore totalement compris, principalement pour les protons. J'ai montré que les deux facteurs qui influencent fortement la précipitation de protons sont l'orientation de la composante verticale de champ IMF ainsi que la pression dynamique du vent solaire. Ces deux facteurs jouent un rôle prédominant sur l'efficacité de la reconnexion sur le front de la magnétosphère et sur l'étirement de la queue de la magnétosphère.

Tous ces résultats sont décrits explicitement dans les deux articles repris dans les pages suivantes (publiés dans la revue *Journal of Geophysical Research* en 2004 et en 2006).

## 2.3 Morphology and seasonal variations of global auroral proton precipitation observed by IMAGE-FUV

V. Coumans, J.-C. Gérard, B. Hubert
Laboratoire de Physique Atmosphérique et Planétaire, Université de Liège

S. B. Mende
Space Science Laboratory, University of California

S. W. H. Cowley
Department of Physics and Astronomy, University of Leicester

*Published in Journal of Geophysical Research - Space Physics (December 10, 2004).*

## Abstract

[1] *Observations with the FUV imagers on board the IMAGE satellite have been used to map the auroral electron and proton energy fluxes during the summer and winter solstices of 2000, in order to construct a statistical view of the global auroral proton precipitation. The distribution for electrons compare well both in morphology and in magnitude, with those obtained previously with the Polar-UVI instruments, and with an empirical auroral precipitation model based on DMSP data. The proton morphology also closely resembles the statistical ion oval derived from DMSP data, showing a 'C-shaped' morphology with a minimum located in the morning sector. The precipitation proton auroral power is on the order of 2.2 GW for an average Kp value of 2, also in close agreement with the values of the DMSP empirical model. The FUV data also reveal the presence of seasonal effects in the proton precipitation. Specifically, the latitudinal width of the proton oval is larger in summer than in winter, so that the globally precipitated proton power is 1.5 times higher in summer than in winter. The occurrence probability of intense proton auroras (with energy flux* $> 0.5\,mW/m^2$*) is also shown to be nearly three times higher in summer than in winter. This seasonal effect in the proton precipitation contrasts with those observed for electrons, where intense electron events occur more often in winter than in summer. We discuss a mechanism which may account for these results, based on the presence of field-aligned potential drops which accelerate auroral electrons downward in regions of upward-directed field-aligned current, while suppressing the precipitating magnetospheric proton flux. The presence of such field-aligned potentials is dependent on the differing solar illumination in winter and summer.*

### 2.3.1 Introduction

[2] The proton auroral region is located at the feet of magnetic field lines where protons precipitate downward into the atmosphere and interact with neutral atmospheric constituents to produce auroral hydrogen emission. The poleward limit of this region corresponds to the boundary between open and closed magnetic field lines. The equatorward limit is generally coincident with the isotropic boundary, which is the boundary between regions of adiabatic and stochastic proton motion in the equatorial tail current sheet [*Sergeev et al.*, 1983]. The field lines closer to the Earth are dipole-like, where trapped protons experience little pitch angle scattering or other processes that populate the loss cone under quiet conditions. Protons in this region are stably trapped. *Mende et al.* [2002] have discussed four processes that may produce significant precipitation. First, proton aurora can be produced by precipitation from an isotropic proton population injected into a region of closed field lines, for example by dayside reconnection or nightside substorm processes. Secondly, under some active circumstances, significant precipitation from a stably trapped population can also be produced by pitch angle diffusion due to particle interactions with electric fields (dc or wave). The loss cone is then populated, and trapped particles will move down into the atmosphere. Thirdly, precipitation can also be produced when a magnetic reconfiguration compresses the region occupied by the particles, for example, following a solar wind-induced compression of the magnetosphere. Fourthly, proton precipitation also occurs when particles are scattered in a stretched field line configuration, such that the proton motion is no longer adiabatic. Some of these processes occur only during substorms, but because of the magnetic configuration of the magnetosphere, weak precipitation at latitudes exceeding the isotropic boundary takes place continuously.

[3] To date, the global morphology of auroral precipitation has been analyzed using two different methods. First, a statistical approach was used by *Hardy et al.* [1985, 1989], who employed in situ data obtained from ∼27000 polar passes by DMSP spacecraft. Statistical maps of the mean particle energy, number flux, and energy flux were provided for electrons and protons for 7 different magnetic activity levels measured by the Kp index. It was already known prior to these studies that both proton and electron precipitation occur within annular regions which are roughly co-located. Ground based measurements had also shown that the auroral proton pattern intensifies and moves equatorward with increasing geomagnetic and substorm activity [*Vallance-Jones et al.*, 1982], and references therein]. *Hardy et al.* [1989] emphasized the fact that a minimum in the ion energy flux occurs in the pre-noon sector, while the maximum value is observed pre-midnight at all levels of activity. Comparison with results for electrons of *Hardy et al.* [1985] also showed that the peak ion energy flux is located equatorward of the peak electron energy flux in the dusk sector. The second approach was initiated by the Dynamics Explorer 1 mission [*Frank and Craven*, 1988], which provided global FUV images of the auroral region. Similar global images from the Polar UVI instrument have been analyzed by *Liou et al.* [2001] to determine the statistical characteristics of global auroral precipitation and its seasonal variations. However, no detailed comparisons have yet been made with the statistical studies based

on DMSP data. In addition, no study has been made of proton precipitation using global FUV images, since the above imagers could not discriminate between proton and electron precipitation. A new era started with the launch of the IMAGE satellite in March 2000, which carries a multi-spectral FUV imaging system including the SI12 camera sensitive to Doppler-shifted Lyman-$\alpha$ emission providing snapshots of the global proton precipitation. We emphasize that statistical maps obtained from in situ measurements and from IMAGE-FUV global images are based on two very different approaches. Particles studies build statistical maps from a large set of measurements made along the satellite track, and since satellite orbits drift slowly in local time it is often difficult to decouple local time and seasonal dependences. By contrast, the IMAGE-FUV study discussed here is based on global images which cover the entire auroral oval simultaneously. Therefore, the results of these two methods do not necessarily lead to the same global picture of the auroral morphology.

[4] Seasonal effects in the auroral electron precipitation have been observed in data from both the DMSP satellites [*Newell et al.*, 1996b] and the Polar images [*Liou et al.*, 2001]. *Liou et al.* [2001] found that the dayside auroral power is enhanced in the summer, while nightside emission is suppressed. They found that the summer nightside suppression is due to a decrease in the average electron energies, while the summer dayside enhancement is due to an increase in the electron number flux. *Newell et al.* [1996b] showed that intense electron events are suppressed under sunlit conditions. Such events, with energy fluxes higher than 5 $mW/m^2$, were found to be associated with discrete auroral arcs, based on an examination of electron energy spectra. The 'sunlight' effect is also clearly related to the seasonal effect, since the time of year determines the amount of sunlight present. Indeed, *Newell et al.* [2001] found that the same 3:1 ratio in the frequency of occurrence of intense aurora was obtained whether the data were divided by season into winter and summer solstice conditions, or by solar zenith angle into cases with angles $>110^\circ$ and $<85^\circ$. These observations were explained in terms of an ionospheric conductivity feedback mechanism. In this conceptual model, the precipitating auroral electrons create an enhanced ionospheric Pedersen conductivity, the response to which depends on whether the background ionospheric conductivity is high or low. If the background ionospheric conductivity is high, a polarization electric field is produced, which reduces the convection electric field and limits the growth of the current. On the other hand, if the background ionospheric conductivity is low, the enhanced ionospheric Pedersen conductivity induces an enhanced Pedersen current. Through ionosphere-magnetosphere coupling, the enhanced currents create a field aligned potential drop which accelerates the auroral electrons downward, which ultimately creates the auroral arcs. Due to EUV solar radiation the background ionospheric conductivity on the dayside is higher than on the nightside, thus explaining the suppression of nightside electron auroral arcs during the summer. In this picture, the seasonality is due to the seasonal variation of the ionospheric illumination by the Sun.

[5] Here we first describe a statistical study based on IMAGE-FUV observations that provides maps of the auroral particle energy flux, which can be compared with related results

obtained from in situ measurements [*Hardy et al.*, 1985, 1989]. Results obtained for electron precipitation are compared with those from earlier studies. The electron energy flux maps are used to determine the averaged morphology of the electron precipitation separately for winter and summer, from which the probability of occurrence of intense electron aurora is determined. The same procedure is applied for proton precipitation. Second, we examine the statistical proton energy flux maps to determine possible seasonal dependences. The results for protons are compared to those for the electrons.

### 2.3.2 Data analysis

[6] The analysis presented here is based on imaging data from the IMAGE satellite, which has an eccentric orbit with a ∼7 Earth radii apogee and a 1000-km perigee. The IMAGE FUV imaging system provides a snapshot of the global northern auroral region every 2 minutes. The Wideband Imaging Camera (WIC) is mostly sensitive to the LBH bands of molecular nitrogen, and the 149.3 nm NI line. The SI12 Spectrographic Imager images the Doppler-shifted Lyman-$\alpha$ emission (121.8 nm) produced by auroral protons, while the SI13 camera isolates the OI 135.6 nm emission [*Mende et al.*, 2000a] with some contributions of the $N_2$ LBH bands. The WIC and SI13 images are contaminated by a dayglow on the dayside, which is subtracted using the method described by *Hubert et al.* [2002]. The SI12 images also contain a weak background contribution that has also been removed from each individual image. This background signal is mainly due to the geocoronal H Lyman-$\alpha$ emission at 121.56 nm, and depends on the illumination and view angles. A very small contribution also originates from the N 120 nm emission and from some weak $N_2$ LBH emission lines. Moreover, dark counts in the detector are also present over the SI12 images. This background contribution is small and may be efficiently removed by a mathematical method, consisting in a polynomial least squares regression. The regression is applied to each SI12 image over the region void of auroral emission and the function so determined is then subtracted over the full observed disk.

[7] For this study, we selected a period of 12 days in summer 2000 (14-17 June plus 21-28 June), and 15 days in winter 2000 (15-29 December). This database includes 10,602 WIC images and the same number of SI12 and SI13 images, corresponding to a total of $6.95 \times 10^8$ WIC pixels and $1.73 \times 10^8$ SI12 and SI13 pixels. Thus, although the time period is restricted to intervals close to the solstices, the statistical study is based on a large number of individual FUV samples in the north hemisphere. The two time intervals selected for this study correspond to very similar values of the mean solar flux, so that the study is not biased by the level of solar activity. The mean $F_{10.7}$ index was 184 in the summer interval, and 191 during the winter interval. The corresponding mean Kp index was 2.6 in summer, compared with 1.5 in the winter. Similarly, the mean hemispheric power derived from NOAA POES satellite measurements [*Lummerzheim et al.*, 1997] was 25.3 GW in the summer, and 20.2 GW in winter. Both indices thus show that the activity level was quite close during the two intervals, though being slightly higher in the summer interval than in

the winter interval.

[8] For each set of three simultaneous FUV images, global maps of the electron average energy, the electron energy flux, and the proton energy flux were calculated. The method and associated uncertainties were described previously by *Hubert et al.* [2002] and *Meurant et al.* [2003b]. The determination of the electron mean energy is based on the ratio between simultaneous WIC and SI13 images [*Meurant et al.*, 2003b; *Coumans et al.*, 2004b]. The precipitating electron energy flux is calculated from the WIC images using the estimated mean energy and the WIC efficiency function. The method used to obtain the proton energy flux [*Gérard et al.*, 2001] is also based on the SI12 efficiency function. An assumption is required concerning the proton energy, since it cannot be determined from the observations. The *Hardy et al.* [1989] empirical mean energy model, which was constructed from in situ DMSP measurements, was therefore used for this purpose. For each FUV pixel, the mean proton energy was evaluated from the model, using its geomagnetic location and the concurrent Kp value. The proton energy fluxes are then obtained from the SI12 count rate using the relationship between the SI12 signal and the NOAA in situ measurements of proton precipitation [*Coumans et al.*, 2002]. The proton flux so derived is also used to remove the proton contribution from the WIC and the SI13 images. This method was validated by comparisons with in situ measurements of the auroral particle energy flux obtained from the FAST [*Frey et al.*, 2001; *Bisikalo et al.*, 2003], NOAA [*Hubert et al.*, 2002; *Coumans et al.*, 2002; *Meurant et al.*, 2003b], and DMSP [*Bisikalo et al.*, 2003; *Coumans et al.*, 2004b] satellites.

[9] The determination of the statistical particle energy flux patterns requires the FUV observations to be mapped into geomagnetic coordinates. The mapping technique is based on the classical Delaunay triangulation method, constructed in a manner to avoid information loss. The magnetic latitude system employed is the modified apex coordinate system defined by *Richmond* [1995]. The statistical models derived by *Hardy et al.* [1985, 1989], on the other hand, are defined in corrected geomagnetic coordinates. However, *Richmond* [1995] emphasized the fact that magnetic apex coordinates are very similar to corrected geomagnetic coordinates for magnetic field lines intersecting the ionosphere at high latitudes. Specifically, *Gasda and Richmond* [1998] noticed that at auroral latitude ($\sim 68^\circ$ MLAT), the maximum difference between the apex magnetic latitude at 110 km and corrected geomagnetic latitude at ground level is $0.17^\circ$, which is smaller than the IMAGE-FUV resolution. Therefore, in this paper, we thus use the term 'magnetic latitude' to mean either apex or corrected magnetic latitude.

### 2.3.3 Electron fluxes and probability of intense electron aurora

[10] The averaged precipitating electron energy flux was calculated for the summer and winter intervals given above using the method outlined. As mentioned before, the dayside sector of the WIC and SI13 images is contaminated by dayglow, mainly in the summer.

The dayglow subtraction method in these imagers, however, is not sufficiently accurate for our purposes, so that reliable statistics on summer electron precipitation cannot be obtained. At winter solstice, a large part of the northern hemisphere is in darkness, thus allowing electron precipitation parameters to be derived free of dayglow contamination. Figure 2.1a thus shows results for the nightside winter data only, where the region around noon up to 77° MLAT has been omitted since contamination is still present following background subtraction. The maximum value of the mean winter electron energy flux pattern is located in the pre-midnight sector, between 2100 and 2400 MLT, at around 70° MLAT, and reaches 1.6 $mW/m^2$. The auroral oval is seen to extend between 65° and 75° MLAT in the pre-midnight sector, between 60° and 75° MLAT in the post-midnight sector, and between 65° and 80° MLAT in the morning sector. The energy flux decreases with decreasing MLTs in the dusk sector and reaches a value below 0.5 $mW/m^2$ in the afternoon sector around ~1730 and 73° MLAT.

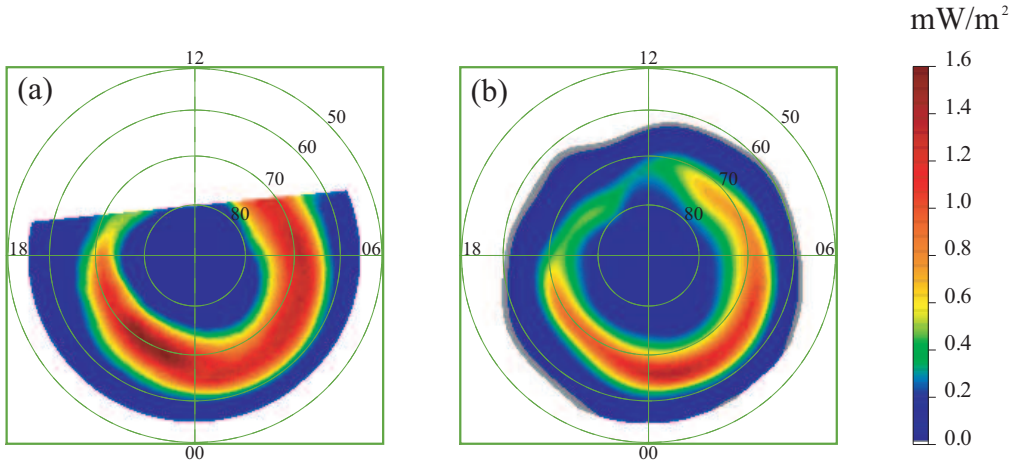


Figure 2.1: Maps of the mean electron energy flux (a) from our statistical study using IMAGE-FUV data in winter 2000 for all Kp values, and (b) from the *Hardy et al.* [1985] model with a weighted Kp index but without seasonal discrimination.

[11] We now compare our winter electron energy flux map with the *Hardy et al.* [1985] statistical model, which was derived from DMSP measurements and binned by Kp level. Figure 2.1b shows the *Hardy et al.* [1985] energy flux map using a weighted Kp index evaluated for our winter 2000 interval. A weighting factor was calculated for each Kp value from the ratio of the number of images obtained for that Kp value and the total number of images obtained during the interval. Each DMSP precipitation pattern was then multiplied by the associated weighting factor and added together to obtain Figure 2.1b. It can be seen that the shape of the pattern and the range of electron energy flux values are quite similar to those found here, in the region without dayglow contamination.

The pattern is characterized by a C-shaped morphology with a minimum in the afternoon sector. The maximum is located in the post-midnight sector and reaches ∼1.4 $mW/m^2$. A difference is that the precipitation region determined from the in situ particle data is somewhat narrower than the FUV oval. This is possibly a seasonal difference and/or due to the difference of the spatial resolution of the DMSP and IMAGE instruments. It should also be borne in mind that the *Hardy et al.* [1985] statistical model does not differentiate between seasons, while the IMAGE-FUV map in Figure 2.1a was derived specifically from winter observations. Overall, however, the general agreement between these two sets of results is quite satisfactory, considering the different resolution and approach used to build the statistical SI12 and DMSP global map.

[12] Related results were also obtained by *Liou et al.* [2001] using Polar-UVI measurements. The averaged precipitating electron energy flux derived for winter conditions from Polar-UVI images also exhibits a C-shaped pattern, with a minimum in the afternoon and a maximum pre-midnight, similar to Figure 2.1a. The magnitude of the pre-midnight maximum was 25% higher than in Figure 2.1a, reaching 2 $mW/m^2$. This small difference is within the uncertainties in the calibration of the instruments. In addition, part of the difference may also stem from the different level of solar activity in the two databases. We also note that the Polar UVI images include a contribution due to proton precipitation which could not be removed, which also plays a role in the energy flux difference noted above.

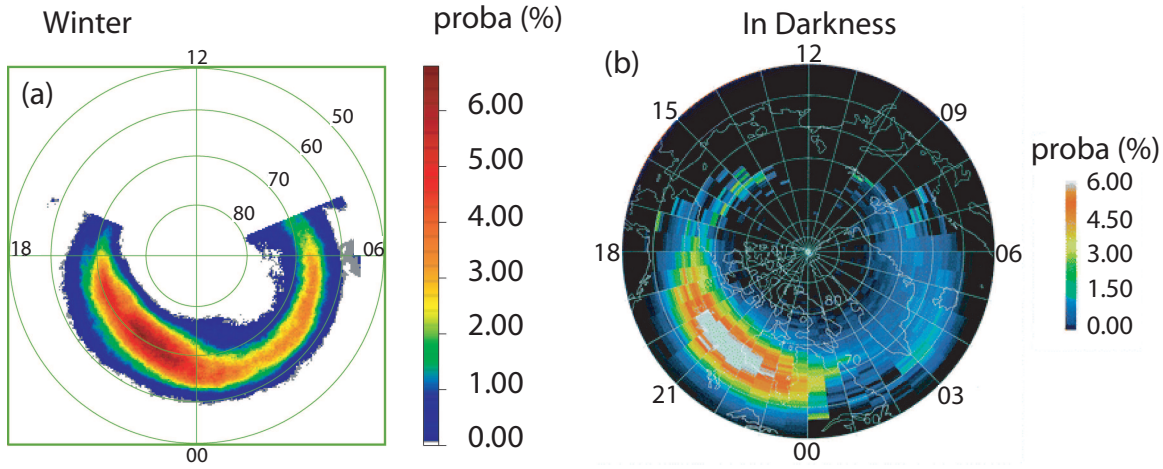


Figure 2.2: (a) Probability of occurrence of intense electron aurora in winter 2000 as a function of magnetic latitude and local time, determined from IMAGE-FUV observations, and (b) related DMSP observations from *Newell et al.* [1996b].

[13] In Figure 2.2a we also show the occurrence probability distribution for observing intense electron aurora in the IMAGE data. For each pixel we have calculated the ratio between the number of cases where the energy flux is higher than 5 $mW/m^2$ and the total number of cases. The region between 0730 and 1630 MLT has been masked out to avoid dayglow contamination. Within the region shown, the probability pattern is C-shaped, with a maximum of about 7% in the 2100-2400 MLT sector at around 70° MLAT. The probability decreases on sectors going to the dayside, around 1700 MLT and 70° MLAT and around 0430 MLT and 68° MLAT. In the post-midnight sector between 0230 and 0600 MLT and 60°-70° MLAT the probability reaches ∼3.5%. At around 0200 MLT and 65° MLAT, however, the probability locally drops to 3%. In Figure 2.2b we show related results obtained by *Newell et al.* [1996b] from DMSP data, specifically the probability of observing accelerated electron distributions associated with the discrete aurora. The comparison shows very good agreement with our results, both in morphology and in magnitude. The maximum probability is around 6% in the 2000-2300 MLT sector, while the minimum probability is located near noon, with a secondary local minimum in the post-midnight sector. We note, however, that the peak value in the post-midnight sector between 0230 and 0600 MLT is 1.5% in the DMSP study, which is lower than that in Figure 2.2a. This difference may be related to the fact that the DMSP study used 9 years of measurements, almost encompassing a complete solar cycle, while we have only included FUV observations obtained in a period close to solar maximum. In addition, the DMSP methodology used to obtain this map also employed additional criteria based on the evolution of the electron energy spectra along the orbit.

[14] Overall, we conclude from the results shown in this section that our winter electron statistical precipitation pattern is in adequate agreement with earlier in situ and remote sensing observations. We now apply the same procedure to the proton precipitation, using SI12 images.

### 2.3.4 Proton energy flux

[15] Since the SI12 images are only minimally contaminated by dayglow which may be efficiently removed, the method described above may be used to obtain statistical maps of the precipitating proton energy flux during both summer and winter. The maps derived for the summer and winter intervals employed here are shown in Figures 2.3a and 2.3b respectively, showing C-shaped morphologies during both seasons. The minimum is located in the morning sector near 1000-1100 MLT, while the maximum is observed in the midnight region. In summer the statistical maximum flux is 0.28 $mW/m^2$ located in the post-midnight sector, while in winter the maximum is 0.24 $mW/m^2$ located just before midnight. The magnitude of the proton energy flux is seen to be quite similar in summer and winter, while the latitudinal extent of the precipitation is greater in summer than in winter.

[16] For comparison, Figure 2.4 shows the Kp-weighted statistical proton energy flux pat-

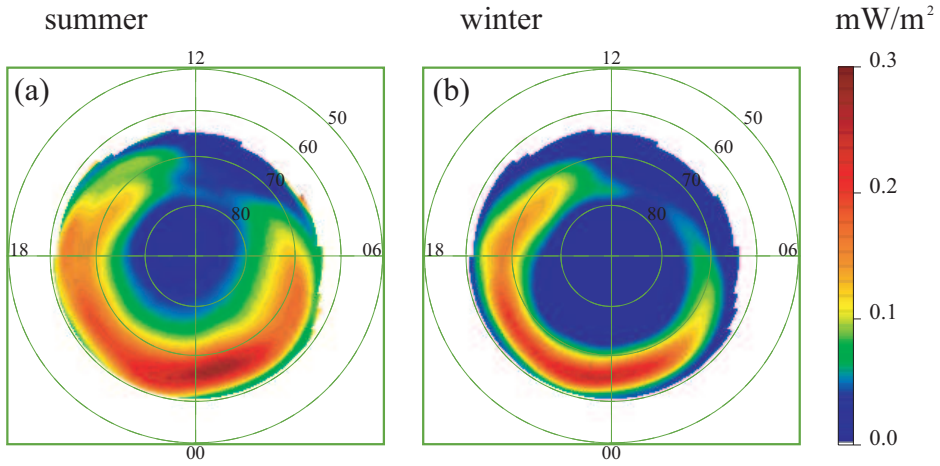


Figure 2.3: Averaged energy flux maps for protons evaluated from IMAGE-FUV observations, for (a) our summer, and (b) our winter intervals, displayed in geomagnetic coordinates.

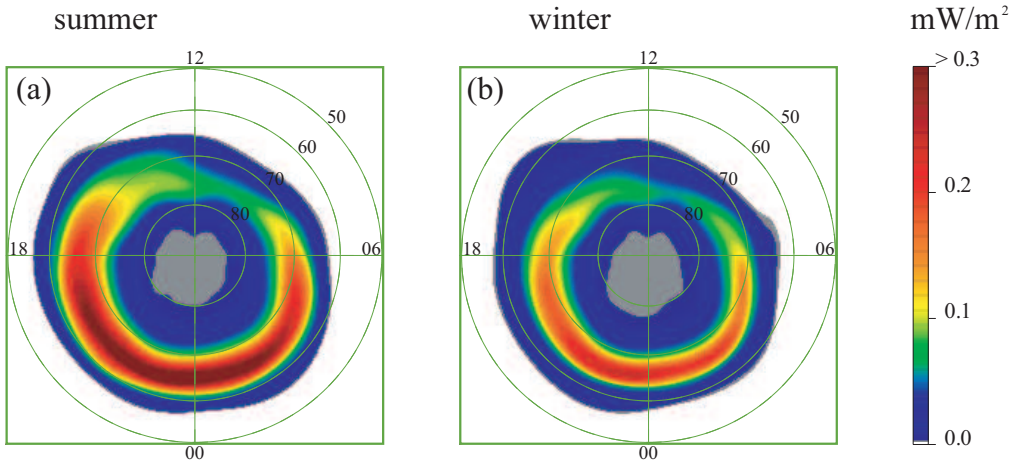


Figure 2.4: Proton energy flux from the *Hardy et al.* [1989] empirical model, using a Kp weighting evaluated for (a) our summer 2000 interval, and (b) our winter 2000 interval.

terns obtained from DMSP data by *Hardy et al.* [1989], using the method outlined above. Figures 2.4a and 2.4b show results for the summer and winter intervals, respectively, where we note that the difference arises solely from the different Kp values which occurred during the intervals, and not from seasonal differences in the empirical model input. The C-shaped pattern is similar to that found here, with a minimum in the pre-noon sector, and a maximum located in the 2300-2400 MLT sector reaching 0.35 $mW/m^2$ for the summer interval and 0.24 $mW/m^2$ for winter.

[17] To verify that our statistical results are not unduly influenced by the difference in the Kp values between the two seasons, we analyzed the seasonal variation in the proton energy flux separately for two ranges of Kp, namely Kp $\leq 3$ and Kp $\geq 4$. Results are summarized in Table 2.1. The energy fluxes were integrated over the complete auroral region (between $60^\circ$ and $80^\circ$ MLAT) for both ranges of Kp, and the ratio of the summer to the winter powers were evaluated. As can be seen in Table 2.1, the ratios are found to be 1.2 for both Kp ranges, indicating that overall, the area integrated proton energy flux in summer is $\sim$20% larger than in winter. The seasonal difference thus exists independent of the Kp value. When all Kp values are taken together, the summer-winter total proton power ratio is found to be 1.5, this higher value being due to the distribution of samples with Kp in the two intervals. This value can also be obtained by weighting the averaged energy flux maps divided into the two Kp ranges for summer and winter (not shown) by the ratio between the number of cases in those Kp ranges and the total number of cases. Overall, the results for both ranges of Kp suggest that the difference in the magnetic activity during the two seasons is not the cause of the observed seasonal difference in the proton energy flux.

| Kp | $N_{summer}$ | $N_{winter}$ | $\phi_{summer}$ | $\phi_{winter}$ |
|---|---|---|---|---|
| $\leq 3$ | 3526 | 5423 | 2.00 | 1.65 |
| $\geq 4$ | 1400 | 253 | 4.32 | 3.73 |

Table 2.1: Summary of the characteristics of the summer and winter samples for two ranges of Kp. The first column gives the Kp range, while the second and third columns indicate the number of cases in each range over the summer and winter periods respectively. The fourth and fifth columns then give (in GW) the proton power integrated over the whole auroral oval for both seasons.

[18] Observation of Figures 2.3a and 2.3b indicates that the seasonal difference in the proton energy flux comes mainly from the latitudinal extent of the precipitation. A confirmation of these findings was obtained through a parallel study consisting in studying the width of the proton oval observed by SI12 in two specific MLT sectors: 2200 $\pm$ 0.5 and 0200 $\pm$ 0.5 MLT. The poleward and the equatorward boundaries were defined by taking the $1/10^{th}$ of the total count number of the emission peak in the sector considered. This study was made in both MLT sectors separately for November 2000 and June 2001. It shows that the equatorward boundary of the oval is globally located at lower latitude in summer than

in winter, while the poleward boundary is located at higher latitude in summer than in winter. The average latitudinal width in June 2001 is $13.5^{\circ} \pm 2.9^{\circ}$, while it is $8.3^{\circ} \pm 1.9^{\circ}$ in November 2000. These results, obtained over another time period, are in agreement with those described before. We also used boundaries determined from DMSP spectrograms [*Newell et al.*, 1996a], to verify whether the seasonal difference in the width of the proton oval is also present. The B5i boundary is defined as the poleward boundary of the auroral oval, determined by an abrupt drop in the ion energy flux, and B1i as the "zero-energy" ion boundary. We evaluated the latitudinal difference between those two boundaries and analyzed their seasonal variations. The DMSP oval crossings were selected in the 1630 and 2200 MLT sectors, where the proton oval is wider in summer according to our results. We first use the same time period as in this study, that is 12 days in summer 2000 and 15 days in winter 2000, corresponding to 181 and 317 DMSP oval crossings respectively. The average latitudinal difference is $9.4^{\circ} \pm 3.0^{\circ}$ in summer and $6.9^{\circ} \pm 1.5^{\circ}$ in winter. In a second test, to extend the time period and confirm our results, we evaluated the averaged latitudinal difference between B5i and B1i over the months of June and July 2000 and over December 2000 and January 2001. The values are $8.8^{\circ} \pm 2.9^{\circ}$ and $7.3^{\circ} \pm 1.6^{\circ}$ respectively. This result shows that the proton auroral oval is 19% wider in summer than in winter.

[19] To analyze the influence of the assumed proton energy on the seasonal effect, a test was made where the proton mean energy was set to 8 keV rather then using the statistical values from *Hardy et al.* [1989]. The 8-keV energy value is the mean energy of the midnight number flux maximum for a Kp value between 0 and 1 and is approximately half the value of the highest average energy of the entire auroral region in the same Kp range [*Hardy et al.*, 1989]. Results show that the morphology of the proton average energy flux pattern is very similar to Figure 2.3 for both seasons. The maximum in the proton energy flux is consistently located in the night sector and the minimum in the pre-noon sector in winter and summer. The proton power, evaluated on the region between $60^{\circ}$ and $80^{\circ}$ MLAT, is $\sim$3.2 GW in summer and $\sim$1.7 GW in winter, while it was $\sim$2.6 GW and $\sim$1.7 GW respectively when using the *Hardy et al.* [1989]'s mean energy. The seasonal difference is still present with a higher ratio of 1.9 between the summer and winter powers. Since parallel electric fields that accelerate electrons downward and produce discrete arcs are weaker in summer than in winter, it is expected that protons would be more energetic during this season. We test the influence of an increase in the summer proton mean energy by evaluating the average energy flux pattern using a fixed energy of 15 keV and comparing with the calculation with the 8-keV energy. The 15-keV energy is the average energy characteristic of the midnight number flux maximum and around half the value of the average energy maximum for Kp $\sim$ 3 [*Hardy et al.*, 1989]. The morphology of the high latitude summer average energy flux is similar to the one showed in Figure 2.3a, with a maximum value of 0.43 $mW/m^2$ and a total auroral power of 4.4 GW. The ratio between summer power with $<E_{pr}>$=15 keV and winter power with $<E_{pr}>$=8 keV is 2.6. This result shows that the seasonal difference is enhanced if the proton mean energy is also influenced by season. This trend may be expected since the Lyman-$\alpha$ efficiency function decreases with increasing proton mean energy [*Gérard et al.*, 2001]. The energy flux

producing a given Lyman-$\alpha$ emission rate is consequently higher for higher proton energies.

[20] Comparing the winter energy fluxes for protons and electrons shown in Figures 2.3b and 2.1a, respectively, we find that the maximum proton energy flux is $\sim$0.3 $mW/m^2$ compared with 1.6 $mW/m^2$ for electrons. The electron power over the uncontaminated sector between 60° and 80° MLAT is 19.4 GW and the proton power over the same region is 1.6 GW. Protons thus provide $\sim$8% of the total precipitating particle energy flux. The C-shaped pattern for protons is roughly the mirror reflection in the noon-midnight meridian of the pattern for electrons. The minimum in electron flux is expected in the afternoon sector from Figure 2.1b, while for protons it is located in the morning sector, as previously noted by *Hardy et al.* [1989]. This feature can be explained by the grad-B and curvature drifts experienced by these particles. High-energy ions from the nightside plasma sheet drift preferentially westward via dusk into the afternoon and the late morning sectors, and are thus excluded from much of the morning-side oval [*Hardy et al.*, 1989]. On the other hand the plasma sheet electrons drift eastward, and are hence excluded from much of the afternoon-side oval. The noon-midnight reflection symmetry between the electron and proton ovals is not perfect, however, since the maximum energy flux for both species is located in the same quadrant, around 2100 MLT for electrons and 2300 MLT for protons. This is the region where substorms are usually initiated, resulting in the direct injection of heated auroral plasma from the magnetotail. It can also be seen that in the dusk sector, the proton precipitation is located equatorward of the electron precipitation, as observed in previous studies [e.g., [*Hardy et al.*, 1989; *Coumans et al.*, 2002]. Comparison of Figures 2.1a and 2.3b also shows that the winter electron oval is narrower than the proton oval in the sector between 1500 and 1800 MLT, while it is wider at later magnetic local times.

### 2.3.5 Probability of intense proton aurora

[21] We next calculate the occurrence probability of intense proton aurora, defined by the occurrence of a proton energy flux higher than 0.5 $mW/m^2$. This value corresponds to 10% of the limit used for intense electron aurora, in approximate proportion to the fractional contribution of protons to the total particle energy flux. Results are shown in Figures 2.5a and 2.5b for our summer and winter intervals, respectively. The patterns again show a C-shaped morphology, with a minimum consistently in the morning sector between 0600 and 1200 MLT. The maximum probability in summer is located just after midnight with a value of $\sim$15%, while in winter it is located just before midnight with a value of $\sim$9%. When the probability distributions are integrated over the whole auroral region, the summer to winter ratio is found to be 2.9, implying that the global probability of occurrence of intense proton auroras is nearly 3 times higher in summer than in winter.

[22] We have also calculated the ratio of summer to winter mean probabilities in individual 1-hr sectors of MLT, shown (as inverse winter to summer ratios) in Figure 2.6. It can be seen that values are less than one in each sector, meaning that the probability of occurrence

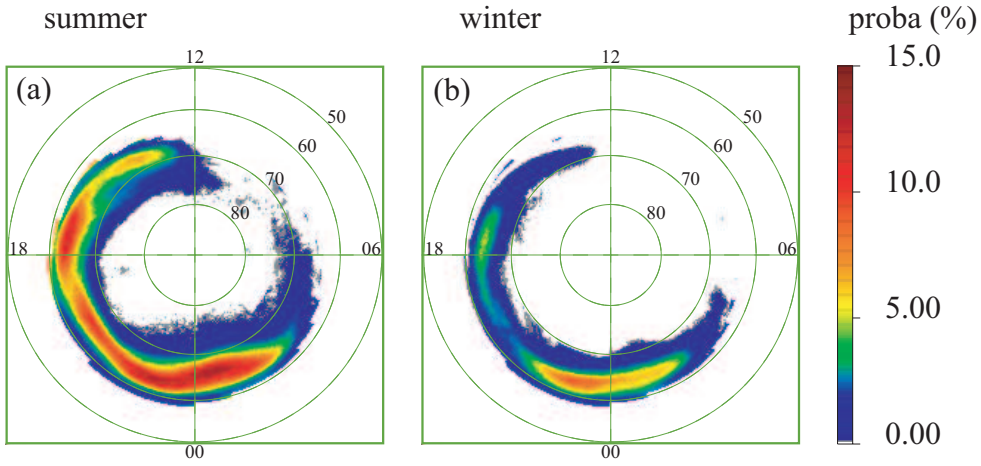


Figure 2.5: Probability of occurrence of intense proton aurora in (a) our summer, and (b) our winter intervals, plotted in geomagnetic coordinates. An intense proton aurora is defined by a precipitating energy flux exceeding 0.5 $mW/m^2$.

of intense proton events is higher in summer than in winter at all local times. Ratios are lower than 0.1 from 0500 to 1500 MLT, and are essentially zero from 0800 to 1200 MLT, where no intense events were observed in winter. Ratios between 0.1 and 0.3 are observed from 1500 to 2100 MLT and from 0300 to 0500 MLT, while values are between 0.4 and 0.6 in the midnight sector from 2200 to 0200 MLT. We thus find that the probability is nearly twice as high in summer than in winter even in the sector where the winter probability is a maximum.

### 2.3.6 Discussion

[23] In this paper we have used IMAGE-FUV data to derive maps of the mean precipitating energy flux for electrons in winter and for protons in both summer and winter. Our results for electrons show good agreement with previous results derived from in situ DMSP particle data and from Polar-UVI observations, both in morphology and in magnitude. For protons, the agreement with previous results obtained from in situ DMSP data is very good. Thus we find that statistical maps based on DMSP overpass data that are not collected simultaneously at each MLT, and those from global images of the auroral region are in fact comparable. The results obtained here on auroral proton precipitation have then been compared with previous electron observations obtained from DMSP and Polar UVI data.

[24] Our proton results show that the total precipitating power integrated over the com-

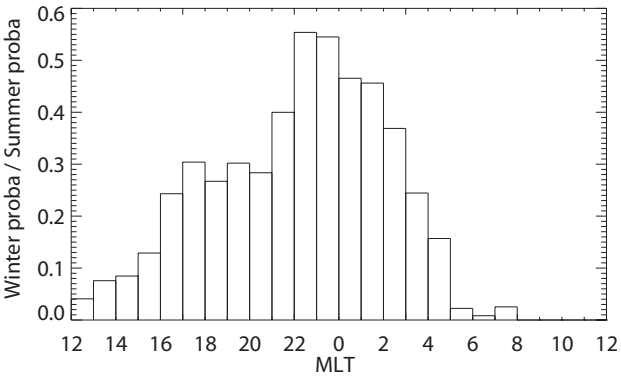


Figure 2.6: Histogram of the ratio between the integrated probabilities of occurrence of intense protons events in winter and summer evaluated for each 1-hour MLT sector. A ratio lower than one, as observed, means that the probability is higher in summer than in winter. The average ratio for all MLT sectors is 0.35.

plete auroral oval is higher in summer than in winter. This is a consequence of the larger latitudinal extent of the proton oval in summer than in winter, while the peak value of the energy flux is quite similar for the two seasons. The occurrence probability of intense proton auroras, whose energy flux is higher than 0.5 $mW/m^2$, is also higher in summer than in winter, while intense electron precipitation is enhanced in the winter, as found in previous studies.

[25] In the following section, we first discuss the origins of auroral protons and what acceleration process is associated with the intense events where the protons energy flux is higher than 0.5 $mW/m^2$. To address to this question we have examined in situ particle measurements obtained by the ion and electron electrostatic analyzers on board the FAST spacecraft [*Carlson et al.*, 1998], during simultaneous crosses of such events observed by SI12. Protons producing emission observed by SI12 can either originate from the magnetospheric tail, or from the ionosphere. Secondly, we consider several possible explanations for the seasonal difference emphasized in the proton precipitation: a seasonal variation in the geometry of the geomagnetic tail or seasonality in the modulation of electric fields accelerating protons downward into the atmosphere or retarding proton access to the atmosphere.

[26] The analysis of in situ particle measurements gives information about the energy spectra of proton during intense proton events. Instruments on board the FAST spacecraft [*Carlson et al.*, 1998] provide ion and electron energy-time spectrograms measured in the pitch angle range $0^\circ$ - $30^\circ$, and pitch angle-time distributions for particles with energies higher than 1 keV. We selected cases where FUV observations showed a proton flux higher

than 0.5 $mW/m^2$ and simultaneous FAST measurements were available. Seven cases were found in winter 2000, when the FAST orbit was ideally located, crossing the auroral region in the 2200 MLT sector. The FAST data show that the intense proton aurora corresponds to precipitation of high-energy protons with energies above 1 keV, often up to at least 25 keV, which is the detector limit. The pitch-angle distribution of the precipitating ion during such events is isotropic. We also observed that, as expected, the ion flux decreases during electron inverted-V events. The empirical proton precipitation model derived by *Hardy et al.* [1989] also shows that in the sector where intense proton aurora are more frequent, in the midnight sector around 63° MLAT, the mean proton energies lie between 5 and 30 keV for all Kp values.

[27] In a recent study, *Hultqvist* [2002] has analyzed Freja observations of downward nightside ion acceleration events at auroral latitudes, in ion spectra at energies up to 3.5 keV. He showed, among other things, that the ion pitch-angle distributions are generally somewhat field aligned but not far from isotropic, that all ion species ($H^+$, $O^+$, and $He^+$) are accelerated to the same energy, and that such ion precipitation is generally not observed in regions with primary auroral Birkeland currents associated with electron inverted-V distributions. He concluded that a potential drop along the magnetic field lines can provide the observed kinetic energies, and that the accelerated particles originated in the ionosphere. However, if such accelerated particles are limited to energies less than ∼3 keV, this mechanism will produce only a small contribution in the overall proton energy flux. Moreover the results of the comparison with the FAST spectrograms have shown that the intense proton events are usually due to precipitation of protons with higher energy. The ionospheric origin of the protons can thus be rejected.

[28] Possible mechanism of the observed seasonality may be due to variations in the geometry of the Earth magnetic environment. A seasonal variation of the magnetotail stretching may explain the seasonal variation in the proton precipitation. It has been shown that the main mechanism for proton precipitation is related to the nightside geometry of stretched magnetic field lines and its non-adiabatic effects on the ion motions[*Sergeev et al.*, 1983]. The auroral region can be subdivided into different zones whose boundaries may be determined from DMSP spectrograms [*Newell et al.*, 1996a]. The proton isotropy boundary described by *Sergeev et al.* [1983] is a good approximation to the earthward edge of the tail current sheet. In the DMSP automated classification, a proxy (b2i) for the ion isotropy boundary is defined as the precipitating energy flux maximum of high-energy (3 keV) ions [*Newell et al.*, 1996a]. Proton isotropy poleward of this boundary is a consequence of pitch angle scattering in the current sheet where the gyroradius is comparable to the magnetic field line curvature. The region located just poleward of the isotropy boundary is the main sector where intense proton aurora should occur. The level of stretching of magnetic field lines thus influences the degree to which ions are scattered. It is well known that the magnetotail configuration depends on the dipole tilt towards and away from the Sun, and is thus partly controlled by the seasons. However, ion scattering within the current sheet under any given conditions will produce the same isotropic population on both sides of

the equatorial plane, and hence the same 'source' ion population on both 'summer' and 'winter' hemisphere field lines during solstice conditions. Therefore the magnetotail effects themselves will not produce a seasonal effect on the ion precipitation.

[29] Another possible mechanism explaining the seasonal variations of the proton precipitation is a variation in parallel electric fields. Downward electric field would increase the proton energy flux into the atmosphere and produce downward-directed ion beams. This type of events has been observed in the auroral zone by the FAST satellite [*Klumpar et al.*, 2000]. Individual events are narrowly confined in latitude and display a latitude profile similar to electron inverted-Vs. The acceleration process occurs at altitude above the FAST satellite (∼4000 km), and is thought to be a quasistatic, downward-directed, parallel potential structure. *Klumpar et al.* [2000] showed that these downward-directed ion beams occur predominantly in the post-midnight sector, close to the region of the summer maxima in the proton energy flux and occurrence probability of intense proton aurora found in this work (Figures 2.3a and 2.5a). Such events may thus contribute to the intense events observed here in the summer data but would not be dominant as *Klumpar et al.* [2000]'s description of the spectral distribution does not agree with the results of the comparisons with FAST measurements described before. Peak characteristic energies of those downward-directed ion beams often reach only 1 keV and the pitch angle distribution is not isotropic.

[30] Variations of the upward electric fields which downward accelerate auroral electrons, creating inverted-V events, and which would also influence the proton precipitation is also a possible cause of the seasonality of proton aurora. Based on measurements from the DMSP satellites, *Newell et al.* [1996b] has emphasized the suppression of discrete electron aurora in sunlit regions. As mentioned above, they interpreted the observations in terms of an ionospheric conductivity feedback mechanism [*Lysak*, 1986]. We suggest that this mechanism may also play an important role in the seasonal control of proton precipitation. In this picture the ionospheric 'background conductance', the approximately constant ionospheric conductance due largely to solar ionization, plays a role in the formation of the aurora. A large-scale electric field is present in the ionosphere associated with magnetospheric plasma convection, which drives a large-scale system of electric current. The Pedersen component of these currents will close in the magnetosphere via large-scale field-aligned (Birkeland) currents. Precipitating particles create a density perturbation, and thus increase the Pedersen conductivity. As mentioned in the introduction, the reaction of the ionosphere then depends upon its state. If the background conductivity is too high (i.e. on the dayside), the ionosphere responds by producing a polarization electric field which reduces the large-scale convection electric field and limit the current. If the background conductivity is low (i.e. on the nightside), the ionosphere responds with an increase in the Pedersen current, which must be closed by field-aligned currents flowing at the conductivity gradient. A larger current then flows between the magnetosphere and ionosphere, requiring a larger field-aligned potential drop to accelerate electrons downward from the low-density magnetosphere. A consequence of the positive feedback, which couples the enhanced current with

the magnetosphere through field-aligned currents, is the formation of high-energy electron precipitation and intense electron auroral arcs. In addition to the downward acceleration of magnetospheric electrons, the field-aligned electric fields will also accelerate ionospheric ions upward into the magnetosphere, while down-coming magnetospheric ions will be decelerated. Observations of seasonal variations in the upward ion beams which correspond to the electron results of *Newell et al.* [1996b] were found by *Collin et al.* [1998] using data from the TIMAS instrument onboard the Polar satellite *Shelley et al.* [1995]. FAST observations have also been used to study the upward-directed ion beams accelerated by the field-aligned potential difference [*McFadden et al.*, 1999]. Since these field-aligned potentials will also suppress proton precipitation from the magnetosphere, less intense proton auroras may be expected in winter.

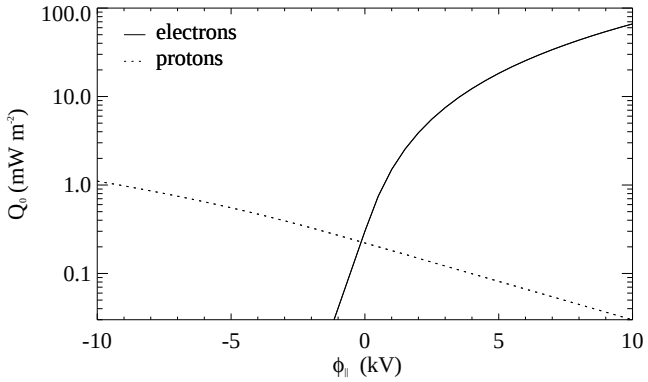


Figure 2.7: Variation of the precipitating electron and proton energy fluxes ($Q_0(\varphi_\parallel)$) with the field-aligned voltage ($\varphi_\parallel$), for a plasma sheet 'source' population with a number density of 0.5 cm$^{-3}$ and proton and electron thermal energies (equal to $kT$) of 5 and 0.5 keV, respectively. A positive voltage implies an upward-directed electric field. The solid line shows the electron energy flux, while the dashed line shows the proton energy flux.

[31] We now quantitatively examine how proton and electron precipitation from the magnetosphere is affected by the presence of a field-aligned electric field. We use the kinetic theory due to *Knight* [1973], which has been employed in numerous studies of terrestrial auroral electron precipitation [e.g. [*Lyons et al.*, 1979], and has been applied more recently to jovian conditions as well [e.g. [*Cowley and Bunce*, 2001]. We consider the electrons first, and assume that the magnetospheric plasma sheet 'source' population is an isotropic Maxwellian of number density N and thermal energy $W_{th} = kT$. If these electrons are accelerated downward by an upward-directed parallel electric field through a (positive) voltage $\varphi_\parallel$ , their precipitating energy flux $Q_0(\varphi_\parallel)$ is

$$Q_0(\varphi_\parallel) = Q_0(0)[1 + \frac{e\varphi_\parallel}{W_{th}} + \frac{1}{2}(\frac{e\varphi_\parallel}{W_{th}})^2], \tag{2.1}$$

where e is the electron charge, and $Q_0(0)$ is the precipitating electron energy flux for zero field-aligned voltage, given by

$$Q_0(0) = 2NW_{th}(\frac{W_{th}}{2\pi m_e})^{1/2}. \tag{2.2}$$

This expression for $Q_0(\varphi_\parallel)$ was first derived by *Lundin and Sandahl* [1978]. It is based on two simple assumptions, the first being that the acceleration region is sufficiently compact along the field lines that no particles mirror before experiencing the full field-aligned potential. The second is that the acceleration region lies at a sufficient altitude that $(B_i/B_{\varphi_\parallel}) > (e\varphi_\parallel/W_{th})$ , where $B_i$ is the magnetic field strength in the ionosphere and $B_{\varphi_\parallel}$ is the field strength in the acceleration region. For the case of plasma sheet electrons decelerated by a downward-directed electric field through a (negative) potential $\varphi_\parallel$ , the expression becomes modified to

$$Q_0(\varphi_\parallel) = Q_0(0)\exp(\frac{e\varphi_\parallel}{W_{th}}). \tag{2.3}$$

With a change in the sign of the charge, similar expressions also apply to proton precipitation from the plasma sheet, where the upper expression for $Q_0(\varphi_\parallel)$ then becomes valid for negative voltages which accelerate protons downward into the ionosphere, while the lower expression is valid for positive voltages which decelerate the precipitating protons. Figure 2.7 then shows the variation of the electron (solid line) and proton (dashed line) energy fluxes as function of the field-aligned voltage $\varphi_\parallel$, using realistic values for the plasma sheet number density and particle thermal energies. Specifically we have used $N = 0.5$ cm$^{-3}$, and $W_{th} = 0.5$ keV for electrons and 5 keV for protons [*Baumjohann et al.*, 1989]. It can be seen that for positive voltages corresponding to upward-directed electric fields, the precipitating electron energy flux increases rapidly with the voltage, while the energy flux of the hotter magnetospheric protons more gradually declines. For example, if the potential difference doubles from 5 to 10 kV, then with these plasma sheet parameters the accelerated electron flux increases from 20 to 66 $mW/m^2$, while the proton energy flux decreases from 0.08 to less than 0.03 $mW/m^2$. For negative voltages corresponding to downward-directed electric fields, however, the electrons are decelerated and the energy flux rapidly falls to very small values, while the proton energy flux steadily increases. It can thus be seen that if the above ionospheric conductivity feedback process seasonally modulates the electron-accelerating voltage as explained above, then a seasonal effect of the opposite sense will also occur in precipitating protons, as observed here.

[32] In view of the different points discussed above, the results of this study suggest that seasonal variation in proton precipitation probably originates mainly from seasonal variations in the field-aligned electric fields that accelerate particles from the magnetospheric tail, in each hemisphere, as a consequence of the variation of solar illumination.

## 2.4 Global auroral proton precipitation observed by IMAGE-FUV : Noon and midnight brightness dependence on solar wind characteristics and IMF orientation

V. Coumans, J.-C. Gérard, B. Hubert
Laboratoire de Physique Atmosphérique et Planétaire, Université de Liège

M. Meurant
Institute for Space Research,University of Calgary, Canada

*Published in Journal of Geophysical Research - Space Physics (May 26, 2006).*

## Abstract

[1] *The brightness of proton aurora observed near solar maximum at summer and winter solstices with the FUV-SI12 global imager on board the IMAGE satellite has been correlated with the solar wind and the interplanetary magnetic field characteristics measured by ACE satellite instruments. By contrast to the electron aurora, we find a strong correlation both on night- and day-sides between the proton precipitated power and the solar wind dynamic pressure calculated with one hour averaged solar wind data. For both southward and northward IMF, the proton power increases with $|B_z|$, but much more rapidly on the nightside for southward IMF orientation. Correlations for the nightside aurora were also calculated with a series of solar wind-magnetosphere coupling functions. We find highest correlation coefficients for expressions containing the dynamic pressure or involving the solar wind electric field in the Y-Z plane. The influence of the solar wind dynamic pressure on the proton aurora is tentitatively explained by the effect of the pressure on the shape of the magnetosphere, generating stretching of the magnetotail and proton precipitation, but also by other coupling processes between the solar wind and the magnetosphere. Adding FUV-WIC and SI13 electron aurora images in the study, we determine how proton and electron precipitations simultaneously react to solar wind and IMF characteristics and Kp. Results shows that protons are more reactive to dynamic pressure variations than electrons when $B_z$ is positive, while the influence on of both types of particles is similar for negative $B_z$. The precipitating proton flux is found proportionally larger compared to the electron flux when the total auroral flux increases for low activity level. Instead, for high activity level, the proportion of the proton and the electron powers are similar when auroral power increases. Consequently, it is suggested that similar mechanisms cause proton and electron auroral precipitation for high activity levels, while they appear somewhat decoupled for lower activity conditions.*

### 2.4.1 Introduction

[2] Variations in the solar wind have an important influence on the magnetosphere and on the characteristics of the aurora. It is well known that abrupt solar wind variations such as pressure pulses associated with CMEs can induce significant auroral precipitation [*Zhou and Tsurutani*, 1999; *Chua et al.*, 2001; *Hubert et al.*, 2003; *Meurant et al.*, 2003a]. The morphology of the aurora has also been extensively studied as a function of the IMF orientation. For example, *Lasen and Danielsen* [1978] studied quiet time arcs observed from the Greenland all-sky camera network. They showed that the oval arc pattern is prominent for southward IMF, and practically vanished as steady IMF is shifted toward a northward direction. They also showed a contraction of the oval pattern depending the sign of $B_y$: for positive $B_y$, the contraction takes place in essentially the evening sector of the oval, while for negative $B_y$, the morning sector is more affected. The location of the electron auroral oval had also been studied in different MLT sectors in relation with the IMF and the solar wind characteristics. *Kamide and Winningham* [1977] made a statistical study of the 'instantaneous' nightside auroral oval, using measurements from the ISIS 1 and 2 satellites. They showed that the north-south component of the IMF plays a dominant role in controlling the motion of the equatorward boundary of the nightside oval. *Makita et al.* [1983] studied the shift of the auroral electron boundaries in the dawn-dusk sector in association with the IMF, from measurements of DMSP-F2 satellite. They showed that the locations of the poleward and the equatorward boundaries are both controlled by the $B_z$ orientation. The dayside aurora is also influenced by changes in the solar wind as shown by *Jacobsen et al.* [1995]. Using ground-based observations, they found that the pre-noon aurorae morphology is dependent on the IMF $B_z$ and the solar wind density.

[3] The brightness of the aurora and its control by the solar wind parameters and the IMF have been investigated by *Liou et al.* [1998], using global UVI images from Polar and the solar wind measurements from the Wind satellite. They showed that the afternoon aurora is more active for large IMF cone angle and large solar wind electric field. The nightside auroral brightness is moderately correlated with the orientation of the $B_z$ components of the IMF and the solar wind velocity, while no effects are induced on the nightside aurora by the solar wind dynamic pressure. They explained the dayside results by a partial penetration of the IMF into the dayside closed magnetic field and the solar wind electric field entering into the magnetosphere via field line reconnections in different locations. The nightside processes controlling the aurora are due to reconnection and viscous-like interactions mechanisms. Using similar data, *Shue et al.* [2002] examined the relationship between auroral brightness and solar wind and IMF characteristics, on the basis of the IMF $B_z$ orientation and the season. They found that both winter and summer precipitation powers are mostly controlled by solar wind density and velocity for southward IMF on the nightside. Globally, these studies indicate that the electron aurora morphology and brightness are strongly influenced by the IMF orientation but also by the solar wind conditions.

[4] The transfer of energy from the solar wind to the magnetosphere, which is the ultimate source of the nightside auroral precipitation, has been the object of extensive studies. *Arnoldy* [1971] used the north-south component of the IMF as a signature in the interplanetary medium for substorms. *Gonzales and Mozer* [1974] suggested that the energy transfer through the reconnection depends on the magnetospheric electric field in the transverse plane. *Akasofu* [1981] suggested a first approximation expression for the solar wind-magnetosphere energy coupling function $\varepsilon$. This expression, already described by *Perreault and Akasofu* [1978], correlates well with the total energy consumption rate of the magnetosphere. They showed that $\varepsilon$ is the primary factor controlling the time development of the magnetospheric substorms and storms. This expression indicates that the solar wind and the magnetosphere work together as a dynamo, by which the solar wind couples its energy with the magnetosphere. Other empirical functions were suggested to describe the strength of the solar wind-magnetosphere coupling. Vasyliunas et al. [1982] searched for a functional dependence on solar wind parameters of the rate of energy transfer from dimensional analysis constraints. They found that the energy transfer depends on the solar wind dynamic pressure, velocity, and transverse IMF orientation. *Wygant et al.* [1983] used S3-3 measurements of the polar cross polar cap electric potential, and compared them with the reconnection electric fields predicted by several theoretical and experimental models. They found best agreement for a dependence on $\theta_c$, the angle between the transverse component of the IMF and the Earth's magnetic field at the magnetopause, with a fourth power of $sin\theta_c$ . Other factors influencing the reconnection efficiency are the solar wind velocity and the absolute value of the transverse component of the IMF. *Liou et al.* [1998] made a correlative study of the auroral power derived from Polar UVI observations with the concurrent solar wind and IMF observations from the Wind satellite. Their conclusion was that the response function for nightside aurora is best represented by $VB_t sin^4(\theta_c/2)$ or $P^{1/6}VB_t sin^4(\theta_c/2)$ transfer functions.

[5] Processes leading to the proton aurora are much less known than for electron precipitation. *Mende et al.* [2002] listed four processes identified as the cause of the proton precipitation. First, proton aurora can be produced by precipitation from an isotropic proton population injected into a region of closed field lines, for example by dayside reconnection or nightside substorm processes. Secondly, under some active circumstances, significant precipitation from a stably trapped population can also be produced by pitch angle diffusion due to particle interactions with electric fields (dc or wave). The loss cone is then populated, and particles that were previously trapped then precipitate. Thirdly, precipitation can also be produced when a magnetic reconfiguration compresses the region occupied by protons, for example, following an abrupt solar wind-induced compression of the magnetosphere. Finally, proton precipitation also occurs when particles are scattered in a stretched field line configuration, such that the proton motion violates the adiabatic invariants.

[6] Morphological and quantitative characteristics of the proton aurora have been the subject of several studies, based on ground-based or in situ measurements, but never on

global observations as no global imager of proton aurora was available before FUV-SI12. *Hardy et al.* [1989] employed in situ data obtained from ∼27000 polar passes by DMSP spacecraft to build statistical maps of the mean particle energy, number flux, and energy flux that were provided for protons for 7 different magnetic activity levels measured by the Kp index. They emphasized the fact that a minimum in the ion energy flux occurs in the pre-noon sector, while the maximum value is observed pre-midnight at all levels of activity. *Coumans et al.* [2004a] used IMAGE-FUV observations to map the auroral electron and proton energy fluxes during the summer and winter solstices of year 2000, and to construct a statistical view of the global auroral proton precipitation. They confirmed the 'C-shaped' distribution of the proton precipitation with a minimum located in the morning sector, already described by *Hardy et al.* [1989]. They also found that the latitudinal width of the proton oval is larger in summer than in winter, so that the globally precipitated proton power is 1.5 times higher in summer than in winter. Moreover, the occurrence probability of intense proton aurora (with energy flux $> 0.5 mW m^{-2}$) was also shown to be nearly three times as high in summer as in winter. By contrast, *Newell et al.* [2005] investigated the seasonality of the ion aurora using one solar cycle of DMSP satellite particle data. One of the results of their study was that the ion aurora is approximately equal in the summer and winter hemispheres in the dusk-midnight sector, while in the sectors from midnight to dawn, the ion precipitating energy flux is higher in winter than in summer.

[7] Using the set of IMAGE-FUV instruments, *Frey et al.* [2002] studied the signature of the proton aurora in the cusp and its control by the solar wind magnetic field and plasma parameters. They showed that a cusp signature separated from the auroral oval appears in the Lyman-a images only when the IMF has a northward $B_z$ component, but the intensity of the precipitation is not controlled by the magnitude of $B_z$. Strong correlations between the UV intensity and the dynamic pressure were found, likewise between the location in local time and the IMF $B_y$ component. However, this study concentrated on a localized and specific proton auroral precipitation, characterized by the direct connection between the ionosphere and the interplanetary medium through magnetic reconnection at the high-latitude magnetopause.

[8] The purpose of this study is to determine how the global proton aurora is influenced by variations in the solar wind and to analyze possible correlations between the auroral proton precipitation power and the characteristics of the solar wind and the IMF orientation. We use observations of proton aurora from IMAGE-SI12 and measurements of the solar wind parameters from the ACE satellite. Section 2.4.2 explains how the data from both satellites were selected and processed for correlation studies. The solar wind measurements were averaged over the preceding hour, considering the solar wind - magnetosphere coupling as a loading-unloading system. The choice of the time averaging is explained in Section 2.4.2. Section 2.4.3 describes results of correlation between the precipitating proton flux and the solar wind characteristics. Since both proton and electron aurora are observed simultaneously, we analyze the simultaneous behavior of both types of precipitation with variations in the solar wind and present results in Section 2.4.4. Section 2.4.5 discusses the

results and suggests how the response of proton aurora to changing activity levels may be understood. Finally, Section 2.4.6 summarizes the results and the discussion.

## 2.4.2 Data analysis

### Precipitating proton power

[9] The IMAGE satellite has an eccentric orbit with a ∼7 Earth radii apogee and a 1000-km perigee. The IMAGE FUV imaging system includes three instruments which provide snapshots of the global northern auroral region every 2 minutes. The Wideband Imaging Camera (WIC) is mostly sensitive to the LBH bands of molecular nitrogen, and the 149.3 nm NI line. The SI12 Spectrographic Imager images the Doppler-shifted Lyman-a emission (121.8 nm) produced by auroral protons, while the SI13 camera isolates the OI 135.6 nm emission [*Mende et al.*, 2000a] with some contributions from the N2 LBH bands. The WIC and SI13 images are contaminated by dayglow on the dayside, which is subtracted using the method described by *Hubert et al.* [2002]. The SI12 images also contain a weak background contribution that is also removed from each individual image. This background signal is mainly due to the geocoronal H Lyman-$\alpha$ emission at 121.56 nm, and depends on the illumination and view angles. A very small contribution also originates from the N 120 nm emission and from some weak $N_2$ LBH emission lines. Moreover, dark counts in the detector are also present in the SI12 images. This background contribution is small and may be efficiently removed by a mathematical method, consisting of a polynomial least squares fit [*Hubert et al.*, 2002]. The fit is applied to each SI12 image over the region void of auroral emission and the function so determined is then subtracted over the full-observed disk.

[10] For each northern hemisphere observations with IMAGE-FUV, the electron energy and energy flux can be calculated from WIC and SI13 images. The proton energy flux can be evaluated from SI12 depending on an assumption on the proton energy, which cannot be determined from the observations. In this study, the proton energy is taken from the *Hardy et al.* [1989]'s empirical model. The method used to calculate the particle energy flux and associated uncertainties were fully described by *Hubert et al.* [2002], *Meurant et al.* [2003b] and *Coumans et al.* [2004b]. It is based on FUV instrument efficiency function, evaluated from transport and energy degradation models of particles in the Earth atmosphere [*Solomon et al.*, 1988; *Gérard et al.*, 2000]. The proton energy fluxes are obtained from the SI12 count rate using the relationship between the SI12 signal and NOAA in situ measurements of proton precipitation fluxes [*Coumans et al.*, 2002].

[11] This work is a statistical study extending the morphology and seasonal variation study of global auroral proton precipitation by *Coumans et al.* [2004a]. The statistical proton energy flux is studied in connection with the solar wind characteristics and the IMF orientation. The time period of the study is extended over summer June 1 to July 10, 2000 and winter December 3, 2000 to January 8, 2001, which time periods are very close to the solar activity maximum. This corresponds to a total of 30,184 FUV snapshots,

including 15,878 summer cases and 14,306 winter cases. The two selected time intervals correspond to very similar values of the mean solar flux, so that the study is not biased by the level of solar activity. The mean F10.7 index was 178 in the summer interval, and 171 during the winter interval. Table 2.2 shows the distribution of the number of cases sorted by Kp value. The corresponding mean Kp index was 2.4 in summer, compared with 1.7 in the winter. The difference is not important and, as it is shown hereinafter, does not have a major influence on the seasonality. The power associated with each FUV image is actually dependent on the previous observations because of the integrated time response of the magnetosphere in relation with the solar wind. Therefore, the statistical analysis is not based on 30,184 independent data point. This suggests that the individual images should be in some way time-averaged. In our treatment, this time averaging is replaced by binning the auroral powers into intervals of hourly averaged solar wind characteristics values. Since one hour of observations corresponds to ∼30 FUV snapshots, the statistics in this work are thus based on about 1000 independent hourly averaged samples.

| Kp | 0 | 1 | 2 | 3 | 4 | 5 | 6 |
|---|---|---|---|---|---|---|---|
| Summer | 374 | 4443 | 4529 | 3559 | 1769 | 937 | 267 |
| Winter | 1265 | 5623 | 3976 | 2734 | 628 | 0 | 80 |
| Total | 1639 | 10066 | 8505 | 6293 | 2397 | 937 | 347 |

Table 2.2: Kp distribution of data (used in this study) of summer 2000 and winter 2000-2001 observations.

[12] Using the data base built for this present work, a comparison between the averaged proton auroral power from SI12, evaluated from the 30,184 FUV snapshots, and the one evaluated from the *Hardy et al.* [1991] model of proton flux and energy is presented in Figure 2.8. The power was calculated between 60° and 80° MLAT over all MLT sectors. Moreover, to test the importance of the assumption on the proton energy, the proton power was also deduced from SI12 observations using a fixed averaged mean energy (8 keV) for all geographic locations. The results are plotted in Figure 2.8 with triangle symbols. The agreement between the power derived from SI12 and from the empirical model is, at worst, within 20% for Kp = 1. It is within 5% for Kp = 2 or 3 and 10% for higher Kp. The agreement assuming a fixed proton energy is within 15% except for Kp = 0 where it is ∼2% and for Kp ≥ 6 where it is ∼22%. Remembering that the empirical model was built over 9 years of data while we use observations near the solar activity maximum, and all other sources of uncertainties, as discussed by *Coumans et al.* [2004a], we consider the agreement as very satisfactory. It demonstrates the validity of the methodology applied to derive proton fluxes from the SI12 count rate. The global calibration of the method uses the relationship between the SI12 signal and NOAA in situ measurements of proton precipitation from *Coumans et al.* [2002]. Moreover, changing the assumption over the proton energy induces a mean difference of 15%, that is the same order of magnitude as the model uncertainties.

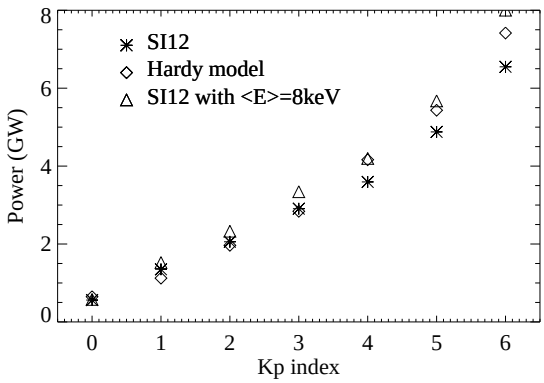


Figure 2.8: The averaged proton auroral power from SI12 (stars) and evaluated from the *Hardy et al.* [1991] proton flux model (diamonds) as a function of the Kp index. The power was calculated between 60 and 80 MLAT over all MLT sectors. The proton power was also deduced from SI12 observations using a fixed averaged energy (8 keV) whatever the geographic location of the precipitation(triangles).

[13] The study by *Coumans et al.* [2004a] was based on observations covering a period of 12 days in summer 2000 and 15 days in winter 2000. This database included 10,602 FUV snapshots. This study in contrast to in situ satellite measurements gives a global picture of the aurora and are equivalent to many orbits of in situ satellite data. In the present study, the database was extended over 40 days in summer 2000 (1 June to 10 July) and 37 days in winter 2000-2001 (3 December to 8 January), corresponding to a total of 30,184 FUV snapshots. As a first step, we verified the seasonal variation of the proton precipitation using IMAGE-FUV observations in summer 2001 and winter 2001-2002. We used 39,129 FUV snapshots, with 20,004 over the period between 1 June and 12 July 2001 and 19,125 between 1 December 2001 and 9 January 2002 respectively. This new database is totally independent of that used in our previous work and, in the way the data were used, FUV snapshots are considered as independent from one another. The averaged Kp index over the summer period is 1.79, while it is 1.77 over the winter period. The averaged Kp index over the full observation period is 1.78, indicating that the magnetic activity in both periods was very similar. Panels in Figure 2.9 show maps of the winter and the summer averaged proton precipitating fluxes. Figures 2.9a and 2.9b are the statistical precipitating flux over summer 2000 and winter 2000-2001, which is the sample of the present work. Figures 2.9c and d show results for the summer 2001 and winter 2001-2002 seasons. A seasonal difference is seen in both panels. The averaged proton oval is wider in latitude in summer than in winter. The flux maximum around 0100 MLT is also higher in summer than in winter, reaching 0.27 $mWm^{-2}$ and 0.30 $mWm^{-2}$ in summer 2000 and 2001 respectively, compared to 0.23 $mWm^{-2}$ and 0.22 $mWm^{-2}$ in winter 2000-2001 and 2001-2002

respectively. Unlike *Newell et al.* [2005], the IMAGE data show a peak in energy flux in the post-midnight sector in summer, rather than in winter. The precipitated proton power integrated between 60° and 80° MLAT over the entire oval still shows seasonal differences, reaching 2.6 GW and 3.0 GW in summer 2000 and 2001 respectively, and 1.4 GW and 1.3 GW in winter 2000-2001 and 2001-2002 respectively. Therefore, the summer averaged power is respectively 1.9 and 2.3 times as high as the winter one. These results thus confirm our previous study based on a smaller database over the year 2000.

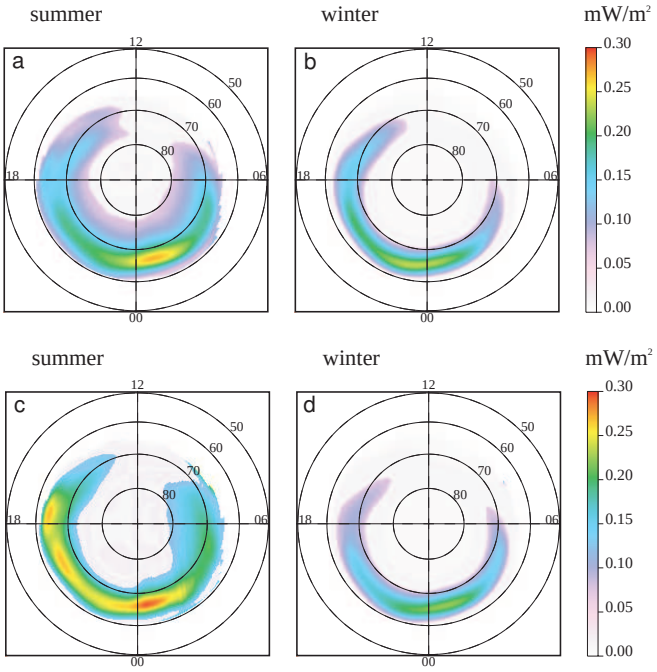


Figure 2.9: Maps of the (a and c) winter and the (b and d) summer averaged proton precipitating flux. In Figures 2.9a and 2.9b the statistical precipitating flux was calculated with data from the summer 2000 and winter 2000-2001 solstices, corresponding to 30,184 IMAGE-FUV snapshots. In Figures 2.9c and 2.9d, 39,129 IMAGE-FUV snapshots around summer 2001 and winter 2001-2002 seasons solstices were used.

[14] We also analyze our database to characterize the proportion of proton energy flux in the region of the cusp compared with the entire oval. The cusp is not apparent on the averaged energy flux map (Figure 2.9 ). As it will be discussed more extensively in section 2.4.5, the relatively low energy of proton cusp precipitation causes the cusp to be observable by SI12 only under specific conditions. The *Hardy et al.* [1989] spectrograms of the averaged integral number flux shows that the cusp region is located in a sector around noon, 1 to 2 MLT hours wide, and varying in latitude with the Kp index. The cusp is centered on ∼80° MLAT for Kp = 0 and ∼72° for Kp = 5. However, because of the low

energy of precipitating protons in the cusp, the spectrograms of the proton integral energy flux do not show any dayside cusp signature. From the *Hardy et al.* [1989] maps of the average integral number flux, we defined an averaged region for the cusp (between 72° and 82° MLAT and between 1115 and 1245 MLT), and calculated from our data base the fraction ratio of the energy flux in this region relative to the entire oval. We find that the proton energy flux in this sector represents ∼1.3% of the entire oval. However, the cusp is not always detected by SI12 because of the low proton average energy.

### Solar wind data

[15] The IMF and solar wind measurements from the Advanced Composition Explorer (ACE) satellite have been used to investigate the solar wind control of the proton auroral precipitation. ACE orbits the L1 libration point about 1.5 million km from Earth and 148.5 million km from the Sun. The propagation time of the solar wind between the ACE satellite and the Earth was taken into consideration using the ACE-Earth distance and the measured bulk velocity. The time of the solar wind characteristics measured by ACE was delayed by adding the propagation time evaluated from the solar wind speed measurement. Each FUV image was thus related to the characteristics of the solar wind reaching the magnetosphere when the image was taken. The solar wind-magnetosphere system may be viewed as a loading-unloading system. The magnetosphere has a memory of past events and reacts according to this background history as suggested by *Liou et al.* [1998]. We compared the correlation coefficient between the auroral power and $B_z$, using various delay time: instantaneous characteristics (averaged over 1 minute), delayed by 5, 10, 20, 30, 45, 60 or 90 minutes, and averaged over 60 or 90 minutes before the FUV observations. For the electron aurora, the correlation coefficient between the power and $B_z > 0$ was -0.10, -0.23 and -0.17 respectively for instantaneous $B_z$ values, for 60 minutes time-lag and for 60 minute averaged, while the values are -0.28, -0.35 and -0.37 for correlation with $B_z < 0$. A negative correlation coefficient implies a negative slope of the linear regression. For protons, the values of the correlation coefficient are 0.24, 0.20 and 0.15 for $B_z > 0$ and -0.41, -0.43 and -0.43 for $B_z < 0$ respectively for the same time delay. These results indicate that using solar wind data with a time lag of 60 minutes or averaging over 60 minutes present similar correlations. Therefore, we present only correlation studies on solar wind and IMF characteristics averaged over 60 minutes prior to each observation, with the appropriate time shifting for solar wind propagation between the ACE satellite and the Earth. This point will be discussed further in Section 2.4.3.

[16] Intercorrelation between solar wind and the IMF characteristics may affect the correlation between the auroral power and these parameters and influence the interpretation of the results. Table 2.3 shows the cross-correlation matrix between the 3 components of the IMF and the solar wind velocity, density and dynamic pressure for the time period of our sample. The coefficients were calculated for $B_z > 0$ (below the main diagonal in Table 2.3) and $B_z < 0$ (above the main diagonal in Table 2) separately. A total of 15,322

cases correspond to positive $B_z$ and 14,862 to negative $B_z$. The density and the dynamic pressure appear as highly correlated, with r = 0.78 for $B_z < 0$ and 0.84 for $B_z > 0$ respectively. This result is not unexpected since the dynamic pressure depends linearly on the solar wind density. The transverse IMF components, $B_x$x and $B_y$, are correlated at ∼50% (r = -0.50 for $B_z < 0$ and r = -0.43 for $B_z > 0$). This result is the signature of the solar wind 'garden hose' configuration. The density is also moderately correlated (r = 0.48) with $B_z > 0$, but weakly correlated with $B_z < 0$ (r = 0.21). A weak negative correlation is obtained between the solar wind velocity and its density (r = -0.28 / -0.32 for $B_z <$ 0 / $B_z > 0$). The correlation between $B_x$ and $B_z$ for southward condition and between $B_y$ and the velocity for northward condition are not significantly different of zero. Except between $B_x$ and $B_y$, between positive $B_z$ and the density, and between the velocity and the dynamic pressure, the correlations between the IMF and the solar wind characteristics are weak and should not affect the correlation with the auroral power. Finally, the averaged Kp index was evaluated for both signs of $B_z$. For positive $B_z$, the averaged Kp is 1.9 and 2.2 for negative $B_z$. This indicates that there is a small difference in the magnetic activity for the two north-south orientations of the IMF. This is expected since a southward IMF orientation is itself frequently associated with enhanced substorm activity.

| | $B_x$ | $B_y$ | $B_z$ | V3 | N | P dyn |
|---|---|---|---|---|---|---|
| $B_x$ | . | -0.495 ± 0.006 | -0.001 ± 0.008 | -0.048 ± 0.008 | 0.138 ± 0.008 | 0.141 ± 0.008 |
| $B_y$ | -0.427 ± 0.007 | . | -0.032 ± 0.008 | -0.086 ± 0.008 | -0.045 ± 0.008 | -0.089 ± 0.008 |
| $B_z$ | 0.068 ± 0.008 | 0.026 ± 0.008 | . | -0.045 ± 0.008 | -0.212 ± 0.008 | -0.210 ± 0.008 |
| V | -0.035 ± 0.008 | -0.018 ± 0.008 | -0.129 ± 0.008 | . | -0.285 ± 0.007 | 0.251 ± 0.008 |
| N | 0.179 ± 0.008 | -0.107 ± 0.008 | 0.481 ± 0.006 | -0.321 ± 0.007 | . | 0.780 ± 0.003 |
| P dyn | 0.188 ± 0.008 | -0.098 ± 0.008 | 0.367 ± 0.008 | 0.128 ± 0.008 | 0.838 ± 0.002 | . |

Table 2.3: Intercorrelation coefficients of the solar wind and IMF characteristics for $B_z>0$ (15322 cases below the principal diagonal) and for $B_z<0$ (14862 cases - above the principal diagonal).

### 2.4.3 Control of proton precipitation by the solar wind and IMF

[17] The dependence of the proton auroral power, calculated from IMAGE-SI12 observations, with the solar wind characteristics and the IMF components is now analyzed. Figures 2.10 and 2.11 summarize the proton power versus the IMF and the solar wind characteristics for the 2200 - 0200 MLT nightside sector and the 1000 - 1400 MLT dayside sector respectively. The power data were binned by the three components of the IMF, solar wind density, speed and dynamic pressure and averaged. Bins for the B components are 2 nT wide between -8 nT and +8 nT, and the extreme ones include all data points for $B_z <$ -8 nT and $B_z >$ 8 nT. The solar wind density bins are 2 $cm^{-3}$ between 0 and

16 $cm^{-3}$, the velocity bins are 50 km $s^{-1}$ between 350 and 700 km $s^{-1}$ and the dynamic pressure bins range between 0 and 8 nPa in 1 nPa bins. The vertical error bars show one standard deviation of the proton precipitation power associated with the averaged value in each bin. Figure 2.10 shows that on the nightside, the power is independent of $B_x$between -5 and 5 nT. For $B_x$ less than -5 nT, it is difficult to discriminate between the scatter of the data and a low and non linear increase of the power with $B_x$ intensity. Finally, the power increases with positive values of the X component of the IMF higher than 5 nT. A quasi similar behavior is observed for $B_y$. The power does not vary with $B_y$ between -7 and 7 nT, while it increases for extreme values. The nightside proton power positively responds to an increase of the $B_z$ magnitude, but much more rapidly for southward IMF than for northward IMF. The minimum is for $B_z$ between 0 and 2 nT, where the statistical power reaches 0.50 GW. For southward IMF, it reaches a maximum of 1.37 GW, while for northward IMF the maximum is 0.73 GW. The power shows a moderate increase with the solar wind density. The maximum power is in the density range between 12 and 14 cm-3 and reaches twice the minimum value. The solar wind velocity does not appear to control the proton power, while a dynamic pressure increase produces a nearly linear increase of the power. The slope of the regression is 0.15 GW/nPa or $150\times10^{15}$ W/Pa. The plot for the dynamic pressure is not a mix of the density and the velocity curves, even though the dynamic pressure is $NV^2$. The product of the two quantities is calculated for each individual case, before binning in dynamic pressure range. On the dayside, the trends are globally similar to the nightside. Figure 2.11 shows that the power is only controlled by extreme values of $B_x$ and $B_y$. The dayside proton power increases slightly with the solar wind density, while the velocity does not exert any real influence. The major difference with nightside is for $B_z$. The power increases for both positive and negative $B_z$ values. The trend is more symmetric about $B_z = 0$, so that the regression slopes for $B_z>0$ and for $B_z<0$ are both 0.01 GW/nT. Moreover, the power increases quasi linearly with the dynamic pressure but shows a more moderate dependence (0.054 GW/nPa or $54\times10^{15}$ W/Pa) than on the nightside.

[18] Because of the quasi linearity between the proton power and the dynamic pressure or $B_z$ observed in Figures 3 and 4, the correlation coefficients were calculated. They were calculated over the full sample of data (not binned) for both seasons, i.e. over a 30,184 sample data set. The correlation coefficients are summarized in Table 3. These were obtained separately for nightside, between 2200 and 0200 MLT, and dayside, between 1000 and 1400 MLT, with solar wind characteristics averaged over 1 hour. For northward IMF, the correlation is fair on both sides, while for southward IMF, the correlation is negative and fairly low on the dayside (r = -0.18) but high on the nightside (-0.43). For the dynamic pressure, the correlation coefficients are high and are slightly higher on the nightside than on the dayside. In the light of these results, one would suspect that the solar wind kinetic energy flux $\frac{NV^3}{2}$ (or $\frac{PV}{2}$ ) would influence the proton precipitation processes. The correlation coefficients of the solar wind kinetic energy flux with the proton auroral precipitation are 0.50 and 0.46 respectively for nightside and dayside aurora. The same calculation

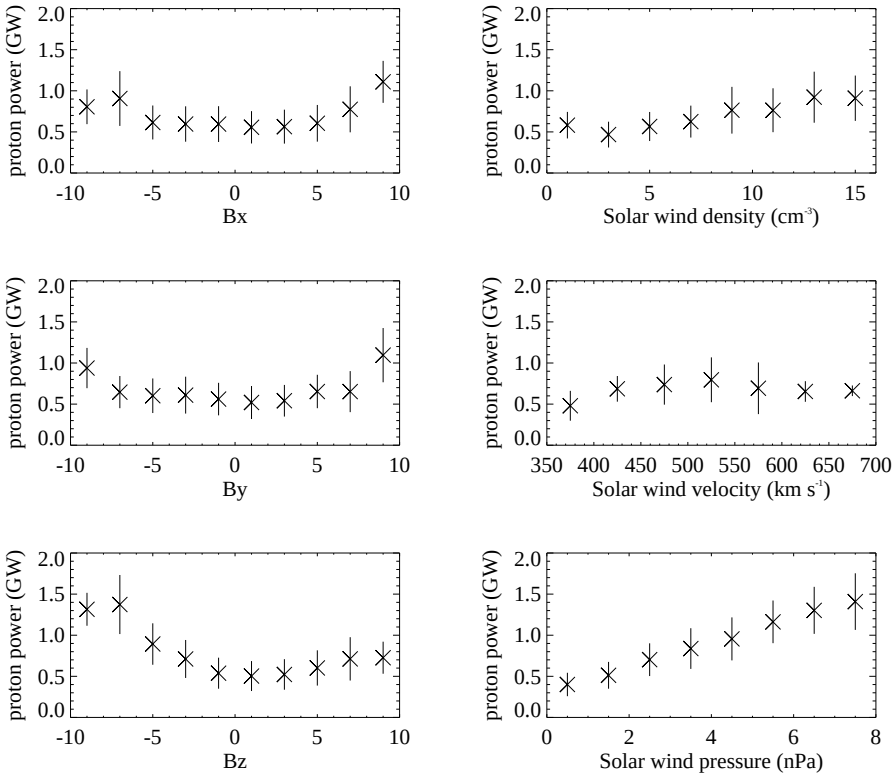


Figure 2.10: Precipitated proton power versus IMF and SW characteristics on the nightside for both seasons. The power was averaged in SW ranges fixed in width. The proton power was evaluated in the sector between 2200 and 0200 MLT and between 60 and 80 MLAT. The left column panels show the dependence with the IMF orientation ($B_x$, $B_y$, and $B_z$), and the right panels are the dependence with the solar wind density, velocity, and dynamic pressure, respectively.

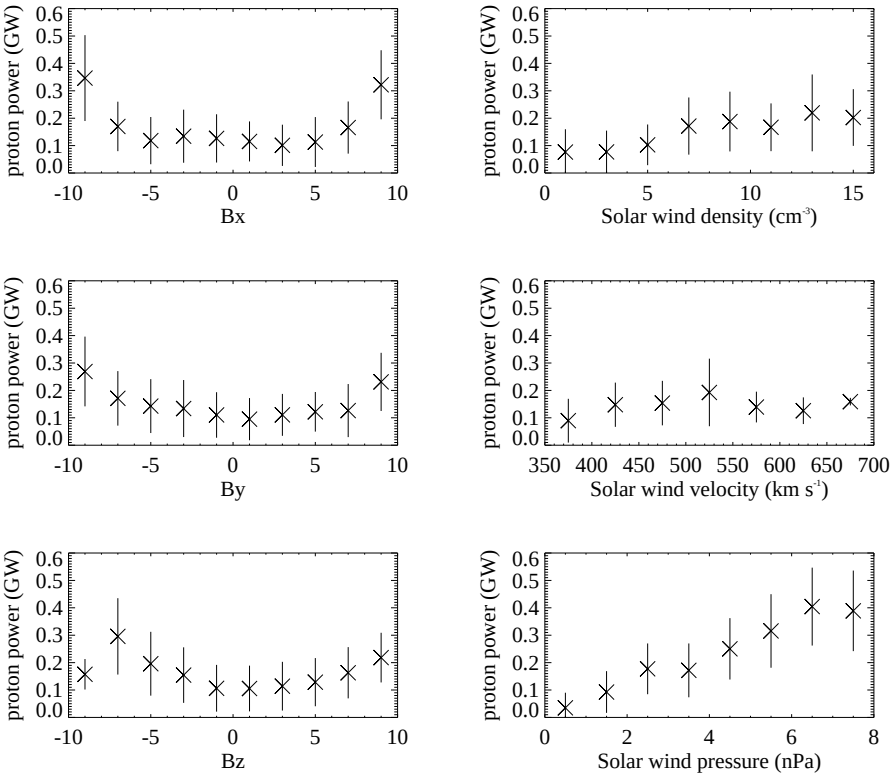


Figure 2.11: Precipitated proton power versus IMF and SW characteristics on the dayside for both seasons. The power was averaged in SW ranges fixed in width. The proton power was evaluated in the sector between 1000 and 1400 MLT and between 60 and 80 MLAT. The left column panels show the dependence with the IMF orientation ($B_x$, $B_y$, and $B_z$), and the right panels are the dependence with the solar wind density, velocity, and dynamic pressure, respectively.

was made with the IMF magnetic energy flux, $\frac{(VB^2)}{8\pi}$ . Correlation coefficients are slightly less than for the kinetic energy flux: 0.39 and 0.42 on nightside and on dayside respectively.

| | Nightside | Dayside |
|---|---|---|
| $B_z > 0$ | 0.147 ± 0.006 | 0.141 ± 0.006 |
| $B_z < 0$ | -0.430 ± 0.005 | -0.178 ± 0.006 |
| P | 0.483 ± 0.004 | 0.435 ± 0.005 |

Table 2.4: Correlation Coefficients Between the Proton Power and the IMF North-South Component and the Solar Wind Dynamic Pressure for Nightside (Between 2200 and 0200 MLT) and Dayside (Between 1000 and 1400 MLT)

[19] It was also shown that the nightside proton power increases for extreme values of positive and negative $B_x$. This influence of $B_x$ is a priori difficult to understand as this component has no influence on the reconnection process, nor on the magnetosphere stretching. However, we have shown in section 2.4.2 that the $B_x$ component is fairly strongly correlated with $B_y$ (r = -0.50/-0.43 for $B_z < 0/B_z > 0$) owing to the solar wind 'garden hose' configuration. Moreover, values of $B_x <$ -6 nT are strongly correlated with the solar wind velocity (r = -0.83) and fairly highly with the $B_y$ component of the IMF (r = 0.54). The values of $B_x > 6$ nT are weakly correlated with $B_y$ (r = -0.25), and moderately with the solar wind density (r = 0.35) and dynamic pressure (r = 0.40). These correlations probably explain the apparent influence of extreme $B_x$ values on the proton and the electron power.

### Solar wind dynamic pressure control

[20] The apparent linearity and the strong correlation found with the solar wind dynamic pressure suggest to analyze this relation in more detail. Figure 2.12 shows the slope of the linear regression between these two quantities in each 2-hour MLT sector. The regression was calculated separately by season and orientation of $B_z$, as it is known that these two parameters have an effect on the proton power *Coumans et al.* [2004a]. The slope was determined for proton power between 60° and 80° MLAT in all MLT sectors. The error bars plotted in the panel show the confidence interval of the linear regression. Figure 2.12 shows that the linear fit slope is globally higher in summer than in winter whatever the sign of $B_z$. This implies that the dynamic pressure influence is more active in summer. In both seasons, the regression slope is highest for southward IMF conditions on nightside. We note a local time dependence of the slope: a limited slope in the morning sector and a steeper slope over the dusk and the midnight sectors, indicating that the power increase with the dynamic pressure is largest in the night and dusk sectors. For all cases, a local minimum in the slope is observed in the evening sector. The lower slope values in this sector stem from the lower value of the proton power in the dynamic pressure range between 7 and 8 nPa. In this domain, the number of observations is substantially less than in the

other bins. The error bars in this sector are thus larger, at least in winter.

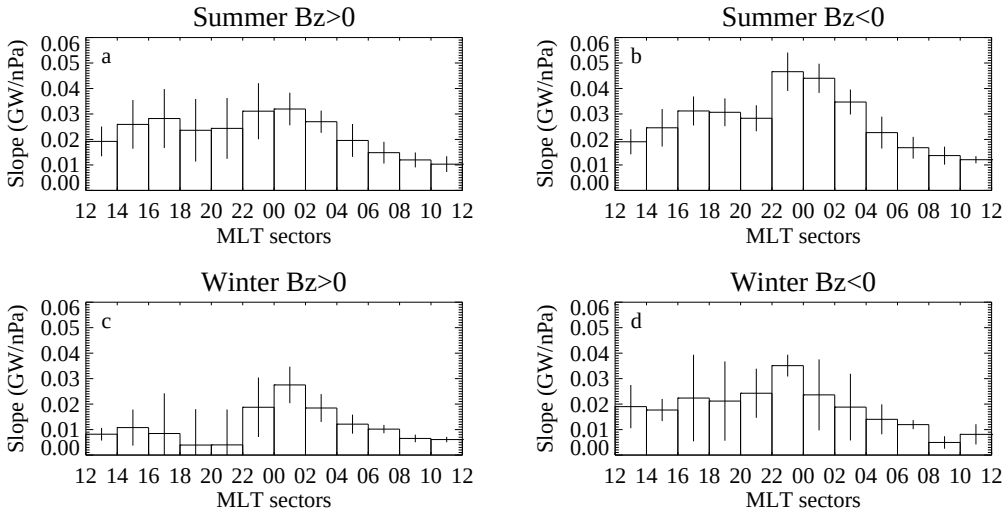


Figure 2.12: Slope (GW/nPa) of the linear regression between the proton power and the solar wind dynamic pressure, in summer (upper panels) and in winter (lower panels), for northward IMF (left panels) and for southward IMF (right panels). The slope was evaluated with the proton power separately in each 2-hours MLT sector.

**Solar wind - magnetosphere coupling**

[21] We now analyze the energy coupling relation between the solar wind and the magnetosphere to understand how the interaction between them control the proton precipitation. A list of coupling functions was summarized by *Liou et al.* [1998] together with their physical interpretation. Such empirical solar wind-magnetosphere energy coupling functions have been used as proxies of the energy input into the magnetosphere. Table 2.5 summarizes the correlation coefficient between the proton power and the value of the coupling function. $B_t$ is the transverse component of the IMF and is equal to $\sqrt{B_y^2 + B_z^2}$; $\theta_c$ is the clock angle, i.e. the angle of the component of B in the Y-Z plane given by $\theta_c = \arccos \frac{B_z}{B_t}$. The correlations were calculated over the full database, for the nightside. The highest correlations are for $P^{1/3} V B_t^2 \sin^4(\theta_c/2)$ [*Vasyliunas et al.*, 1982] and $P^{1/6} V B_t \sin^4(\theta_c/2)$ [*Vasyliunas et al.*, 1982], but large values are also found with $V B_t \sin(\theta_c/2)$ [*Gonzales and Mozer*, 1974] and $V B_t \sin^2(\theta_c/2)$ [*Kan and Lee*, 1979]. The first two functions assume that the amount of energy which is transferred from the solar wind to the magnetosphere is proportional to the amount of solar wind kinetic energy intercepted by an energy 'collection' region on the magnetopause [*Vasyliunas et al.*, 1982]. The two others involve the

magnetospheric electric field in the Y-Z plane.

| | Nightside |
|---|---|
| $VB_z$ | -0.210 ± 0.005 |
| $VB_t$ | 0.417 ± 0.005 |
| $V^2B_z$ | -0.225 ± 0.005 |
| $VB_z^2$ | 0.246 ± 0.005 |
| $VB_t \sin(\theta_c/2)$ | 0.465 ± 0.005 |
| $VB_t sin^2(\theta_c/2)$ | 0.457 ± 0.005 |
| $VB_t sin^4(\theta_c/2)$ | 0.434 ± 0.005 |
| $VB^2 sin^4(\theta_c/2)$ | 0.397 ± 0.005 |
| $P^{1/2}VB_z$ | -0.187 ± 0.006 |
| $P^{1/3}VB_t^2 sin^4(\theta_c/2)$ | 0.486 ± 0.004 |
| $P^{1/6}VB_t sin^4(\theta_c/2)$ | 0.477 ± 0.005 |

Table 2.5: Correlation Coefficient Between Proton Power and 11 Coupling Functions on Nightside. The solar wind characteristics were averaged over 60 min before the IMGE-FUV snapshot.

### Solar wind data delay

[22] As mentioned in Section 2.4.1, the solar wind measurements from ACE satellite were first delayed by the propagation time between the satellite and the Earth using the velocity measurement. They were subsequently averaged over 1 hour before the IMAGE observation to consider the magnetosphere as a loading system. This 1-hour averaging was selected following a correlation analysis between the proton power and $B_z$. For their study of the solar wind control of the electron auroral precipitation, *Liou et al.* [1998] used solar wind data delayed by 1-hour. As a check, we calculated correlations between proton power on nightside and solar wind data or coupling functions separately with solar wind data averaged over one hour and delayed by one hour. The correlation coefficients for hourly averaged solar wind characteristics are higher or, at the most, 1% lower (except for $B_z > 0$, where the difference is ∼35%). In the case of the coupling functions, the correlation coefficients are also larger, except for $VB_z^2$, where the difference is about 20% but the coefficient is moderate (0.30 / 0.25). Figure 2.13 shows the 2200-0200 MLT nightside proton power versus dynamic pressure for 3 different treatments : the triangles show the 1-hour average dynamic pressure dependence, the diamonds the 1-hour delayed pressure and the crosses the instantaneous pressure (in fact, one minute averaged). The error bars shows the statistical scatter of the powers by one standard deviation, for the 1-hour averaged dynamic pressure. The scatter is not shown for the other delayed pressures for clarity of the figure. The standard deviation is of the same order of magnitude for the other points. Figure 2.13 shows that the choice is not critical for dynamic pressure bins up to 5-6 nPa.

Using the instantaneous, or 1-hour delayed or 1-hour averaged dynamic pressure yields similar results. In the 6-7 nPa bin, the difference is less than 10% and about 30% in the 7+ nPa bin. The small difference between the results for the 3 delay times probably stems from the low statistical probability of high dynamic pressure events. Thus the probability for a same order of magnitude pressure 1 hour later or for the 1-hour averaging is high. The behavior for the 3 delay times is thus quite similar, except for high dynamic pressures where the differences are maximum.

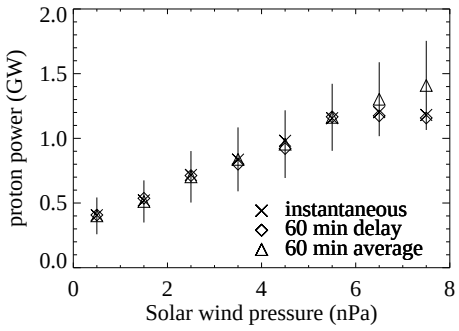


Figure 2.13: Precipitated proton power versus the solar wind dynamic pressure for three different delay times. The triangles show the 1-hour average dynamic pressure dependence, the diamonds show the 1-hour delayed pressure, and the crosses show the instantaneous pressure (in fact, 1-min averaged). The error bars show the statistical 1-s scatter of the power, for the 1-hour averaged dynamic pressure. The standard deviation for the other two cases (not shown for clarity) is on the same order of magnitude.

### 2.4.4 Fractional electron and proton power

[23] The IMAGE-FUV instruments allow the study of the electron and proton auroral precipitation globally, simultaneously and distinctly. It is thus possible to compare the simultaneous reaction of the precipitation of the two types of particles with changes in the solar wind and determine if this dependence is similar for both particles.

[24] First, a study of the solar wind control of the nightside and winter electron precipitation power, made in parallel of the proton precipitation one, has shown that the strongest correlations are for the north-south component of the IMF and for the solar wind velocity. The behavior of the electron power with $B_z$ is nearly linear. The power is maximum for large negative Bz and decreases with increasing $B_z$. The orientation of $B_z$ exerts the main control on the nightside precipitating electron power. Moreover, the power slowly increases with the velocity, but the scatter is high. The analysis of the coupling function response of the nightside electron power has shown that the strongest correlation is found

for $P^{1/6}VB_t\sin^4(\theta_c/2)$ [*Vasyliunas et al.*, 1982] and $VB_t\sin^4(\theta_c/2)$ [*Wygant et al.*, 1983]. These two functions were also found by *Liou et al.* [1998] to be best correlated with the auroral brightness.

[25] The ratio between the proton and the electron power was evaluated and averaged over solar wind density, velocity and dynamic pressure ranges. Figure 2.14 shows the binned ratio as a function of the solar wind characteristics in winter, on nightside (between 2200 and 0200 MLT) and separately for positive and negative $B_z$. A ratio increase implies that the proton power increases more than the electron power with the solar wind parameters. Results show that the proton power is more dependent on the solar wind density than the electron power, whatever the sign of $B_z$. The regression slope values are quite close (within 10%). The velocity control of the particle precipitation shows a negative slope, for both signs of $B_z$, meaning that electrons are more reactive to variations of the velocity than protons. For negative $B_z$, the slope is lower than for positive $B_z$. In fact, the regression slopes for both particles separately are lower for negative $B_z$ than for positive $B_z$. Finally, the most contrasted result is for dynamic pressure. The slope of the regression is much higher for positive $B_z$ than for negative $B_z$. Moreover, the slope is close to zero for southward IMF. These results show that the protons are more influenced by a dynamic pressure increase than the electrons when $B_z$ is positive while the effect is similar for both particles for negative $B_z$ values.

[26] Finally, we investigate the slope of the regression between the proton and the electron power. Figure 2.15 shows the slope evolution as a function of the Kp index. A regression was calculated between the proton and the electron powers in the night sectors, over the full range of data, separately for each range of Kp values. A high slope value implies that the precipitating proton flux is proportionally larger compared to the electron flux when the total auroral flux increases. A nearly null slope shows that the proton proportion in the total flux is similar when the flux increases. Figure 2.15 shows that the slope is higher for $Kp < 4$. This result was expected since, for low activity, the proton contribution in the total flux is higher, for example before substorms [*Hubert et al.*, 2002; *Coumans et al.*, 2004b]. The black column for $Kp = 5$ corresponds to the absence of data for this Kp value.

### 2.4.5 Discussion

#### Proton precipitation processes

[27] As described earlier, one of the mechanisms of nightside proton precipitation is linked to the magnetic field line stretching in the magnetotail. The ions traveling through the magnetotail magnetic field reversal are submitted to scattering of their magnetic moment, which can be viewed as an impulsive centrifugal force perturbing the particle gyromotion [*Delcourt et al.*, 1996]. As a result of magnetic damping in the field reversal, the loss cone can be filled. This stochastic pitch angle distribution appears when the magnitude of the

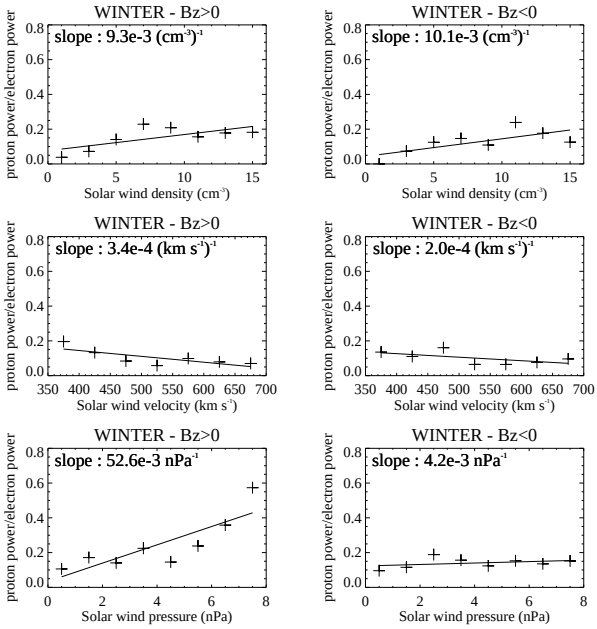


Figure 2.14: Variation of the ratio of proton to the electron powers with the solar wind density (upper panels), velocity (medium panels) and dynamic pressure (lower panels). The ratios were calculated in winter, on the nightside (between 2200 and 0200 MLT) and separately for positive $B_z$ (left panels) and negative $B_z$ (right panels). A linear fit is added and the slope is indicated for each case.

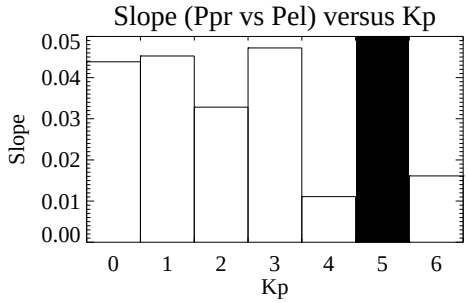


Figure 2.15: Slope of the linear regression between the proton and the electron power as a function of the Kp ranges. The powers were evaluated in the night sector (2200-0200 MLT), with winter data. No data are available for Kp = 5.

centrifugal force is on the order of the Lorentz force of the magnetic field. This condition is especially fulfilled in regions where the magnetic field varies significantly within a cyclotron radius, in the near-Earth tail, and forms an associated sharp transition from dipole-like to tail-like magnetic field. For weakly curved field lines (dipole approximation), the ion motion in the magnetic field is adiabatic (with the conservation of the magnetic moment as a first-order invariant of motion). When the curvature is on the order of magnitude of the gyromotion radius, chaos becomes strong, leading to the injection of the ions into the loss cone, hence their precipitation into the ionosphere. *Sergeev et al.* [1983] found from magnetospheric magnetic field model simulations that the stochastization process of protons is limited for stretched field lines where $R_c/\rho > 8$, where $R_c$ is the field line curvature radius at the equator and $\rho$ the Larmor gyroradius. Since this stochastic precipitation takes place in the absence of wave-particle interactions, it occurs even during very quiet geomagnetic conditions. A change in the shape of the magnetosphere, e.g. due to a change in the solar wind conditions, will modify the source region of the precipitating ions. An increase in the dynamic pressure produces a modification of the topology of the magnetosphere, compressing the field lines of the dayside magnetosphere and stretching the field lines on the opposite side, leading to variations of the intensity of the precipitation proton flux on the nightside [*Tsyganenko*]. Particles that were trapped on dipolar field lines are now on stretched field lines and can precipitate into the ionosphere. Thus, variations of the amount of stretching affect of the nightside proton precipitation characteristics with the dynamic pressure variations.

[28] The mechanisms causing proton precipitation on the dayside are different from the nightside. A modification in the dynamic pressure and in the compression level of the dayside field lines was shown to influence proton precipitation. On the dayside, the dependence of the proton power on the dynamic pressure is not so high as on the nightside. The less pronounced effect on the dayside supports the idea that the mechanisms are different from the nightside. The dayside auroral precipitation originates from different plasma sources, which can be of solar wind/magnetosheath or of inner magnetosphere origin. The dayside cusp is the area where magnetosheath plasma can most easily access the ionosphere. Statistical studies confirmed the localized nature of the cusp near local noon [*Newell and Meng*, 1994]. However, magnetosheath protons that precipitate in the cusp have typical energies of ∼1 keV. The FUV-SI12 camera is mostly sensitive to precipitating protons with initial energies of 2-8 keV [*Gérard et al.*, 2000]. Consequently, only energetic protons observed during periods of enhanced solar wind dynamic pressure produce emissions measured by SI12 [*Fuselier et al.*, 2001]. Observability of cusp proton precipitation by SI12 is thus expected to be strongly influenced by variations of dynamic pressure. Consequently, in this statistical study, cusp precipitation is not the main component on the dayside over the time period we analyzed. Other mechanisms for dayside proton precipitation have been proposed by *Sergeev et al.* [1997]. They showed, using magnetospheric models, that a weak magnetic field in the outer cusp inevitably contributes to regular scattering of energetic protons on closed field lines in a ∼2-3 hour wide MLT sector centered on noon. They also emphasized a second zone of dayside proton precipitation, formed by scattering on

closed field lines crossing the nightside equatorial region near the magnetopause. Such field lines have their footprint in the dayside sector and are curled toward the nightside where they cross the equatorial plane. This mechanism provides isotropic precipitation in a sector located ∼1.5-2 hours MLT from noon, which smoothly connects with the precipitation originating from the tail current sheet. Their model computations showed that, moving away from noon in magnetic local time, the outermost closed field line remain approximately in the meridian plane until they reach the outer cusp latitude, where they sharply turn tailward and cross the equatorial region near the magnetopause. Central plasmasheet protons injected in the night sector, which subsequently drift to the dayside also contribute to proton dayside precipitation. Finally, proton precipitation on the dayside may also be caused by plasma turbulence [*Sergeev et al.*, 1997; *Clemmons et al.*, 2000].

**Role of solar wind dynamic pressure**

[29] We previously discussed how solar pressure controls the nightside proton precipitation through the stretched magnetotail. Our results suggest that compression due to a dynamic pressure increase also influence proton precipitation on the dayside. It is likely that the shape of the closed field lines crossing the nightside equatorial region near the magnetopause [*Sergeev et al.*, 1997] is not so stretched as the tail ones when the dynamic pressure increases. But other mechanisms also operate. The dynamic pressure plays an important role for aurora generated by a sudden increase of dynamic pressure. Fast and high dynamic pressure jumps generate Alfvén waves and pitch angle scattering inducing dayside auroral enhancements, respectively at high and low latitudes. The role of these mechanisms was confirmed by in situ measurements [*Zhou et al.*, 2003; *Meurant et al.*, 2003a]. In addition to the above processes, strong compressions of the magnetopause and the outer magnetosphere also lead to particle precipitation due to lowering of the mirror points of trapped particles to altitudes below 100 km [*Spann et al.*, 1998]. Adiabatic compression leads to loss cone instability, wave growth and enhanced pitch angle scattering [*Zhou and Tsurutani*, 1999; *Tsurutani et al.*, 2001]. These mechanisms may also be present for high dynamic pressure not resulting from shocks.

[30] Complementary analysis shows that the increase in the power with $P_{dyn}$ is due to an increase of the latitudinal width of the precipitation region and to an enhanced brightness of the proton aurora. For different classes of solar wind dynamic pressures, we calculated maps of the average precipitating proton flux. The result was that the power increase is due to both a widening and an intensification of the proton auroral region. The question is then whether field line stretching can be the cause of both types of increase. It is easy to explain the widening of the precipitation region. If the magnetotail is more stretched, more magnetic field lines fulfill the criterion of the proton scattering. The stochastization area becomes larger, extending closer to the Earth, and the footprints of these field lines spread over a larger ionospheric region. Stretching of the magnetotail may also influence the brightness of the proton emission and thus the intensity of precipitating flux. The field

lines which are more stretched following an increase of the solar wind dynamic pressure cross the equatorial plane of the magnetotail in a region different than before the increase of stretching. If the plasma sheet density of this region is higher or if the plasma is hotter, the proton precipitating flux would increase. This plasma sheet proton density or temperature change may be either intrinsic to the plasmasheet distribution, or due to a simultaneous increase of the density or variation of the temperature caused by new plasma injection for example. This second explanation would imply that more complex dynamical processes than a simple increase of the stretching take place in the magnetosphere, involving the transfer from the solar wind to the magnetosphere and the transfer to the tail. The correlation coefficients are larger using coupling functions than for solar wind parameters alone. This result is one additional clue suggesting that a number of different mechanisms control particle precipitation. Auroral precipitation is not the effect of one isolated change in the solar wind dynamic pressure or in the velocity. A collection of parameters acts together to control particle precipitation and the aurora. The fact that the correlation coefficients are globally quite low, always below 0.55, is another evidence showing the multiplicity of the processes controlling the particle precipitation.

**Solar wind-magnetosphere coupling**

[31] Reconnection between the IMF and the magnetospheric field lines also plays a role on proton precipitation. Our results have shown that the dynamic pressure has more influence on the proton precipitation for southward IMF than for northward IMF, especially on the nightside. It is established that reconnection takes place at the front of the magnetopause for antiparallel configuration, i.e. for southward IMF, while the merging region is located at higher latitude for northward IMF. The antiparrallel reconnection induces a large fresh plasma injection from the solar wind to the magnetosphere. This plasma reaches the plasmasheet through magnetospheric convection. The dynamic pressure control on the tail stretching is then more efficient since more plasma is pre-conditioned to be accelerated. It is possible that the different dependence of the proton power on the dynamic pressure according to the IMF north-south orientation is due to an influence of the dynamic pressure on the reconnection efficiency. It was shown in Section 2.4.2 and Table 2.3 that the correlation between the dynamic pressure and the intensity of $B_z$ according its sign was weak, but stronger for $B_z > 0.1$. The effects on the reconnection efficiency of the orientation of the $B_z$ component and the pressure intensity may be coupled.

[32] Our coupling function study shows that the proton power mostly responds to the solar wind kinetic energy that is intercepted by the magnetopause. This kinetic energy depends on the dynamic pressure which controls the magnetotail stretching as described above. The correlation with the coupling function in this case may not be characteristic of the energy transferred from the solar wind to the magnetosphere via the magnetopause. The influence could also result from the modification of the magnetospheric shape due to changes in the solar wind kinetic energy. The stretching rate of the magnetosphere may be de-

pendent of the energy transfer between the solar wind and the magnetosphere. However, magnetospheric stretching is probably the main cause of proton nightside precipitation during quiet activity level. In this case, the solar wind influence on the auroral proton precipitation is indirect and mainly due to the solar wind control of the magnetospheric shape.

**Response of electrons and protons to solar wind characteristics**

[33] Our study of the ratio of the nightside proton and electron simultaneous precipitation showed that the regression slope is lower for high Kp values, meaning that for high activity level, the proportion of the proton power remains unchanged when total auroral power increases. For low activity levels, the precipitating proton flux proportionally increases in relation to the electron flux. The similar behavior of protons and electrons for high activity levels may be a consequence of identical mechanisms of energization for both types of particles, especially during substorms. Fresh plasma is injected from the solar wind to the plasma sheet by reconnection mechanisms. During quiet activity periods, the precipitation mechanisms are probably different and bear different signatures of the solar wind influence. As explained before, during quiet periods, proton aurora is dominated by chaotization of the proton distribution on the stretched field line, a mechanism which is not efficient for electrons. By contrast, during active periods, precipitation of both particles is due to new plasma injection into the plasmasheet or to a compressed magnetic reconfiguration. In this last case, particles which were stably trapped, are precipitated following compression of the magnetosphere and reconfiguration of the shape of the guiding lines.

[34] In addition, we have also shown that an increase in the solar wind density increases the proton power proportion in the total auroral precipitation while an increase in the solar wind velocity increases the electron proportion, whatever the $B_z$ orientation. Morevover, the nightside protons are more influenced by a dynamic pressure increase than electrons when $B_z$ is positive while the effect is similar for both types of particles for negative $B_z$. This last result reinforces the above-described mechanisms, since a southward IMF orientation is favorable to substorm development. The precipitation mechanisms are similar and the effect of the dynamic pressure is then attenuated. For northward IMF, the protons are more influenced by the dynamic pressure controlling the levels of magnetospheric stretching and the efficiency of proton precipitation via the chaotization mechanism in the magnetotail.

### 2.4.6 Summary

[35] The main result of the correlation study between the proton auroral power and the solar wind characteristics is that the power of the precipitated protons is mainly controlled by the solar wind dynamic pressure, at least during periods of solar activity maximum. The main cause of this control on the nightside appears related to dynamic pressure effect

on the shape of the magnetosphere and thus the amount of magnetotail stretching. On the dayside, the dynamic pressure also plays a role, although the precipitation mechanisms are different from those on the nighside. We have shown that the magnitude of the southward IMF component has more control on the nightside proton power than on the dayside. Moreover, the orientation of the IMF has an influence on the dynamic pressure effect mainly on the nightside power. These results confirm the multiplicity of the processes controlling auroral proton precipitation.

[36] The correlation is higher between the nightside proton power and the coupling functions $P^{1/3}VB_t^2\sin^4(\theta_c/2)$ and $P^{1/6}VB_t\sin^4(\theta_c/2)$ [*Vasyliunas et al.*, 1982] than with other proposed solar wind coupling formulae. These assume that the amount of energy transferred from the solar wind to the magnetosphere is proportional to the solar wind kinetic energy intercepted by the magnetopause. The presence of the dynamic pressure factor in these functions suggests that the changes in the solar wind kinetic energy exerts some control on the shape of the magnetotail and thus on the proton stochastization process. We have also shown that significant correlations are found with $VB_t\sin(\theta_c/2)$ [*Gonzales and Mozer*, 1974] and $VB_t\sin^2(\theta_c/2)$ [*Kan and Lee*, 1979], two alternative proxies for the magnetospheric electric field in the Y-Z plane.

[37] Results described above were obtained with 1-hour averaged solar wind data, which precludes analysis of short-term correlations. Nevertheless, we also showed that correlations between proton power and instantaneous, 1-hour averaged or 1-hour delayed dynamic pressure yields very similar results. This indicates that the choice of the averaging time is not critical, a result explained by the rather rare occurrence of high dynamic pressure events.

## 2.5 Discussion sur la saisonnalité de la précipitation de protons

Nos recherches ont montré que la précipitation des protons auroraux présente des différences saisonnières. La puissance hémisphérique moyenne est plus élevée en été qu'en hiver. Cette différence est principalement due au fait que la largeur en latitude de l'ovale auroral de proton est plus grande en été qu'en hiver. Ces résultats ont été mis en évidence sur un échantillon de 69313 observations SI12, réparties sur un total de 159 jours durant les mois de juin et juillet 2000 et 2001 et les mois de décembre 2000 et 2001 et janvier 2001 et 2002.

En parallèle, *Newell et al.* [2005] mettaient en évidence des résultats contradictoires. Leur étude utilise des mesures de particules par le satellite DMSP réparties sur un cycle solaire. Ils montrent que le flux énergétique des ions précipités est 15 à 40 % plus grand en hiver qu'en été dans les secteurs entre minuit et 6h local. Pour eux, ce comportement saisonnier est la conséquence de champ éléctriques divergents [2], accélérant les ions vers la Terre, sont plus intenses en hiver.

Il est légitime de se demander qui a raison. Il pourrait sembler logique de donner le plus de poids à l'étude basée sur une période plus longue, et donc de supposer que les résultats de *Newell et al.* [2005] sont plus crédibles. Pourtant, bien que notre étude porte sur une plus courte période d'observation, par la nature des observations, l'information contenue dans chaque carte statistique est plus importante. En effet, chaque passage DMSP permet de connaître le flux de proton sur une très faible portion de l'oval auroral, alors que chaque observation SI12 fournit le flux sur la totalité de l'oval. Ainsi, l'information apportée par chaque passage DMSP ne couvre que quelques pixels d'une image SI12 et l'ensemble de toutes les mesures DMSP ne permet pas de faire une moyenne de plus de 30000 informations pour chaque pixel. D'autre part, notre étude porte sur une période proche du maximum d'un cycle solaire. Cette donnée peut influencer les résultats. Il faut donc être conscient que les différences saisonnières mises en évidence dans nos recherches sont valables pour cette période du cycle solaire.

Une étude supplémentaire étaie nos résultats. *Emery et al.* [2007] (l'article soumis au mois de juin 2003 est joint en annexe) comparent les données de plusieurs satellites in situ sur plusieurs années. Ils analysent le rapport de la puissance hémisphérique des ions de l'hémisphère sud et de l'hémisphère nord et montrent que la puissance en été est entre 20 et 50% plus élevée en été qu'en hiver. Plus précisément, pour Kp 1 et 2, la puissance hémisphérique due aux ions est 30% plus élevée en été qu'en hiver, et pour Kp 4, elle est 10% plus élevée en été. Rappelons que nos résultats montrent une augmentation saison-

[2]Les champs électriques divergents ou champs électriques dirigés vers le bas sont fréquemment situés dans la région "après minuit" de l'oval auroral, alors que les champs électriques convergents ou dirigés vers le haut dominent dans le secteur avant minuit [*Marklund et al.*, 1994, 1997; *Ergun et al.*, 1998].

nière de 16% à 131%.

# Chapitre 3

# Proton precipitation during substorm growth phase

## 3.1 Résumé introductif

Le travail décrit ci-dessous a été réalisé en collaboration avec Caroline Blockx. Nous avons ensemble sélectionné les cas que nous avons analysés. J'ai développé et analysé personnellement principalement deux parties :

- l'analyse de la relation entre la descente en latitude de l'ovale auroral et les caractéristiques du vent solaire et du champ magnétique interplanétaire. Ce travail comprend également l'étude de la correlation entre le mouvement en latitude de l'ovale et les fonctions de couplage avec le vent solaire. Il s'inscrit dans la continuité de la section 2.4 : je vérifie si les résultats obtenus lors de l'étude de la dépendance de la précipitation aurorale de protons avec les caractéristiques du vent solaire et l'orientation du champ IMF s'appliquent également pour le cas particulier des phases de croissance.

- l'étude de l'aspect local ou global du mouvement des frontières de l'ovale auroral de protons. Pour chaque cas sélectionné, le mouvement des frontières dans chaque secteur nocturne a été lissé à l'aide d'une régression linéaire, ce qui a permis de classer chaque cas selon la nature du mouvement : global (c'est-à-dire avec un taux de mouvement identique dans tous les secteurs), local (c'est-à-dire avec un taux de mouvement nul dans tous les secteurs, excepté dans 4 secteurs contigus au plus). J'ai mis en évidence un autre type de comportement : une superposition des deux autres comportements (c'est-à-dire un mouvement dans tous les secteurs nocturnes avec des taux de descente différents).

Ces résulats sont décrits dans un article que nous avons soumis à la revue *Journal of Geophysical Research* le 7 février 2007 et qui a été accepté pour publication en juillet 2007. La version qui est sous presse est jointe ci-après.

## 3.2 Global morphology of substorm growth phases observed by the IMAGE-SI12 imager

V. Coumans, C. Blockx, J.-C. Gérard, B. Hubert
Laboratoire de Physique Atmosphérique et Planétaire, Université de Liège

M. Connors
AUGO, Athabasca University, Canada

*Journal of Geophysical Research - Space Physics (in press).*

## Abstract

[1] *We present case studies and a statistical summary of optical observations of proton precipitation made during substorm growth phases. Our analysis is based on observations of the Doppler shifted Lyman-$\alpha$ auroral emission obtained with the SI12 Spectrographic Imager on board the IMAGE satellite. These images are used to determine the morphology and dynamics of the auroral oval and of the polar cap boundary on a global scale, as well as the total open magnetic flux and its time evolution. We also investigate the relationship with the solar wind and the IMF characteristics measured by the ACE satellite, and with the magnetic elevation angle measured by GOES-8. The statistical study shows that the sector of maximum proton precipitation during the growth phase is on average centered around 2200 MLT, and rapidly shifts in local time by about 1.2 hours toward midnight at the time of the onset. The open magnetic flux increases by 33% on average during the growth phase. The mean value of the open flux immediately before the substorm onset is about 0.66 GWb for substorms triggered by a northward turning of Bz and 0.74 GWb for non-triggered substorms. The averaged open flux at the substorm onset is smallest when the substorm is triggered by a sudden reversal of Bz, suggesting that the accumulation of energy by the magnetosphere is perturbed by changes in $B_z$. The open magnetic flux continues to increase during the 20 minutes following the onset, for a large number of events. The rate of equatorward displacement of the auroral oval boundaries during growth phase is typically $\sim$3 deg/hour. It is statistically correlated ($r = 0.40$) with the magnitude of the $B_z$ component of the IMF measured by the ACE satellite. It is also correlated, with higher coefficient ($r = 0.54$), with functions describing the efficiency of solar wind energy transfer involving the transverse electric field carried by the solar wind. The equatorward motion may be global, restricted to local time sectors or a combination of both. At no nightside local time sector does the motion of the equatorial boundary appear more pronounced than at others, but the maximum displacement of the polar boundary is statistically located around midnight MLT.*

### 3.2.1 Introduction

[2] According to *Akasofu* [1964]'s definition, the substorm development was divided into two main phases: an explosive expansion phase whose beginning defines the onset of the substorm, and a more gradual recovery phase. A third stage, the growth phase, usually lasting between 30 and 60 minutes, was first described by *McPherron* [1970]. This is the initial phase of many substorms, which starts following a southward turning of the interplanetary magnetic field (IMF). The main characteristics of growth phases are (1) merging of geomagnetic and interplanetary magnetic field lines on the dayside, creating new open magnetic flux, (2) an increase of the size of the polar cap, (3) an increase of the cross-tail electric field, causing energization of the particles of the plasma sheet and earthward acceleration, (4) an increase of the cross-tail current in the equatorial plane of the magnetosphere, (5) tailward stretching of the magnetic field lines and thinning of the plasma sheet [*Kaufmann*, 1987; *Sergeev et al.*, 1990], and (6) an equatorward motion of the auroral oval.

[3] Since the energy stored in the magnetotail originates from the solar wind through reconnection between the magnetospheric field and the IMF, the orientation of the north-south component of the IMF is a key factor influencing the efficiency of this energy transfer [*Arnoldy*, 1971]. However, several studies show that other factors also control reconnection. *Perreault and Akasofu* [1978] and *Akasofu* [1981] suggested a first approximation expression for the solar wind-magnetosphere energy coupling function $\varepsilon$, involving the solar wind speed, magnetic field strength and orientation, which correlates well with the total energy accumulation rate of the magnetosphere. This coupling being the primary factor controlling the time development of magnetospheric substorms and storms indicates that the solar wind and the magnetosphere work together as a dynamo, by means of which the solar wind exchanges its energy with the magnetosphere. Other empirical functions were subsequently suggested to describe the strength of solar wind-magnetosphere coupling, and some are examined below.

[4] During the last three decades, growth phase characteristics have been studied using ground based or space observations. Ground based studies of growth phases are based on data from sets of meridian scanning photometers and magnetometers such as the CANOPUS network or radar measurements such as SuperDARN [*Voronkov et al.*, 1999; *Jayachandran et al.*, 2005]. Such studies made it possible to determine characteristics of growth phases such as, for example, that the proton aurora intensifies during the growth phase toward the onset of the substorm intensification [*Voronkov et al.*, 1999]. *Jayachandran et al.* [2005] used ground-based instruments to follow the temporal evolution of the equatorial boundary of the ion auroral oval during growth phases across several hours in local time. They analyzed 68 growth phases with the SuperDARN radar network over the Canadian sector to explore whether magnetotail stretching is a local or a global phenomenon. They noticed two types of latitudinal motion of this boundary on the nightside: a global motion such that the boundary retained its shape throughout the growth phase, and

a local motion limited to a few hours of local time bracketing the onset region. They interpreted these results by dividing the substorms into two classes. In the first one, the growth phase involves stretching in the inner magnetosphere that is most pronounced around the onset meridian. In the second one, the stretching extends many hours in local time away from the onset meridian. However, these studies were based on data covering only a limited sector of the auroral oval and did not provide a global view of growth phase dynamics. The SI12 auroral imager is the first instrument allowing global observation of the proton aurora and further investigation of these intriguing results.

[5] Some previous studies analyzed the relations between what happened in the solar wind and the growth phase characteristics. *Brittnacher et al.* [1999] determined the boundaries of the auroral oval and area of the polar cap as a function of local time and substorm phase using images from the Polar UVI for different IMF orientations during three substorms in January 1997. They observed that the polar cap region clears of precipitation during the substorm growth phase, which expands the size of the polar cap but is not necessarily related to an expansion of the open flux region. They also found that the increase in polar cap area prior to onset can be independent of the strength of the southward IMF component. The region designed as the 'polar cap' in the study of *Brittnacher et al.* [1999] is not equivalent to the region of open flux tubes that usually defines the polar cap. It is instead the region contained within the boundaries of auroral luminosity, determined by a statistically significant threshold of auroral luminosity measured in terms of a photon flux at the camera of 4 photons $cm^{-2}$ $s^{-1}$ (the minimum instrument sensitivity is about 0.5 photons $cm^{-2}$ $s^{-1}$). All regions poleward of the auroral oval that are below this threshold are included in the polar cap region but oval-aligned arcs or theta auroral structures are not. *Newell et al.* [2007] used the OVATION system [*Newell et al.*, 2002] to identify the equatorward and poleward boundaries of the auroral oval. This system uses DMSP particle boundaries as a starting point and calibrates other measurements, particularly the SuperDARN radar measurements, to these boundaries, using a different statistically determined offset at each 1 hour MLT. The polar cap size was one of the ten variables which characterize the state of the magnetosphere, which were correlated with more than 20 candidate solar wind coupling functions. *Shukhtina et al.* [2004, 2005] analyzed the magnetotail magnetic flux at substorm onset as a function of solar wind parameters. They show that the tail magnetic flux, stored during the growth phase, mainly depends (CC = 0.95) on the merging electric field $E_m = V_{SW} B_t sin^3(\theta/2)$ ($V_{SW}$ is the solar wind velocity, $B_t = \sqrt{B_y^2 + B_z^2}$, $\theta$ is the clock angle). It implies the lack of a threshold magnetic flux at substorm onset. We cannot completely substantiate this latter result as is discussed in more detail below.

[6] The present study improves on these previous attempts since the SI12 images used allow global determination of ion auroral boundaries with good time resolution and minimal dayglow contamination. We first examine in detail two examples of growth phase. We then do a statistical study of the morphology of the auroral oval and thus of the polar cap boundary (the open/closed field line boundary) on the global scale as described by *Hubert*

*et al.* [2006]. We calculate the total open magnetic flux and its time evolution, the time evolution of the brightest MLT sector, the relation between the latitudinal motion and the IMF and SW characteristics, and the differences between global or local equatorward motion during growth phases.

### 3.2.2 Instrumentation and methodology

[7] Until the availability of the IMAGE satellite, no capability existed for global remote sensing of the proton aurora. Since its launch in March 2000, its FUV spectrographic proton imager (SI12) provides snapshots of proton precipitation with a 2-min resolution. This imager detects Doppler shifted Ly-$\alpha$ auroral emission by isolating a narrow (0.2 nm) spectral region near 121.8 nm, allowing imaging of global-scale proton precipitation. It includes a grill system to reject the intense (>10 kR) geocoronal Ly-$\alpha$ emission at 121.6 nm, which would otherwise appear as a bright diffuse glow [*Mende et al.*, 2000a]. Numerous factors influence the Ly-$\alpha$ line profile, on which the response of the SI12 instrument depends [*Gérard et al.*, 2001]. For present purposes, this response is well understood, and was validated by laboratory and daily in-flight calibrations using hot stars [*Frey et al.*, 2003a]. The sensitivity threshold of SI12 is estimated to be on the order of $\sim$ 100 R.

[8] We considered all 2437 substorms listed by *Frey et al.* [2004], selecting those which occurred at least 2 hours after the previous listed onset, and whose auroral oval is entirely visible with IMAGE-FUV from at least 1 hour before the onset to 20 min. after. Based on these criteria, we selected 1118 events between June 2000 and December 2002. The FUV SI12 images were used to determine the equatorial and polar boundaries of the proton auroral oval follow their evolution during the growth phase. A threshold was determined on a statistical basis to discriminate between the auroral signal and the image background. This threshold had to be accurately determined, as the boundary sought corresponds to the limit where the auroral emission drops to zero as was described by *Hubert et al.* [2006]. As mentioned before, the advantage of using the SI12 images of the proton aurora to estimate the location of the proton oval equatorial limit and the open/closed field line boundary is the absence of dayglow contamination (despite limitations described by *Hubert et al.* [2006]). Then the open magnetic flux is given by

$$\Phi = \int_S \vec{B} \cdot \vec{n} ds \tag{3.1}$$

where $\vec{n}$ is the vector normal to the area S inside this boundary, and $\vec{B}$ the Earth's magnetic field. The poleward boundary estimated from the SI12 images is taken to be the open/closed field line boundary and the integral is calculated over the area delimited by it.

[9] Since the aim of this study is to characterize the slow stretching of the magnetic field lines during the growth phases, we only selected events exhibiting a significant equatorward

motion of at least one of the boundaries during the growth phase in the midnight sector. A total of 55 growth phase intervals between June 2000 and December 2002 were selected on based of this criterion, but this selection is not exhaustive. Many other substorm growth phases exhibited some equatorward motion of one or both boundaries, but this motion was not regarded as obvious, thus they were not included in this study. The length of the growth phases exceeds 60 minutes in 36 cases, between 40 and 60 minutes in 12 cases, and less than 40 minutes for the last 7 cases. The onset of 26 substorms took place in the midnight sector, 13 in the 2230-2330 MLT sector, 7 in the 2030-2230 MLT sector, and 8 between 0030 and 0330 MLT.

[10] The IMF data used in this study were obtained by the Magnetic Field Experiment (MAG) on the Advanced Composition Explorer (ACE) satellite [*Smith et al.*, 1998] with a time resolutions of 16 s. Plasma data were collected by the Solar Wind Electron Proton Alpha Monitor (SWEPAM) on ACE [*McComas et al.*, 1998] with time resolutions of 64 s (these data are courtesy of the NASA CDAWeb site). ACE measures far from the Earth, at the L1 libration point ($\sim$220 $R_E$ upstream of Earth). ACE data are propagated to the bow shock using the *Weimer et al.* [2002, 2003] and *Weimer* [2004] pseudo-minimum variance technique. A delay of 4 minutes was added to consider the propagation to the ionosphere. Each FUV image was thus related to the characteristics of the solar wind reaching the magnetosphere at the time the image was taken.

[11] The selected substorm onsets were separated into two categories: those for which we could identify a trigger in the solar wind parameters and/or IMF components, according to the criteria given below (called 'triggered' events later in this paper), and those for which we could not (called 'non-triggered' events). The concept of external triggers of auroral substorms has been extensively discussed [*Lyons*, 1996; *Henderson et al.*, 1996; *Hsu and McPherron*, 2003]. In this study we consider as triggers:

- a sudden reversal of the $B_z$ component to positive values,
- a sudden increase of the density, velocity, and/or dynamic pressure (by 1 nPa or more),
- a sudden reversal of $B_y$ from positive to negative values (see *Henderson et al.* [1996]),
- a sudden reduction in the magnitude of $B_y$ as described by *Lyons* [1995, 1996]. A minimum decrease of 2 nT was considered to be significant.

To be considered as triggers, these changes must take place during the few minutes ($\leq$ 6 min) before the onset time observed by SI12. In this way, from the 55 selected events, we identified 22 substorms as triggered by a solar wind changes. The other cases do not appear to show any evidence of a solar wind trigger.

[12] The magnetospheric magnetic field measurements are from GOES (Geostationary Operational Environmental Satellite). These satellites are on geostationary orbits and are

equipped with magnetometers measuring the 3 components of the Earth's magnetic field. We concentrate on GOES 8 and 10 measurements since one or the other of these satellites was favorably located in the midnight sector at the time of the onset.

### 3.2.3 Case studies

[13] The methodology described above is illustrated by two examples. The first is typical of most cases included in this study. It occurred on 28 August 2000 while the $B_z$ IMF component measured by the ACE satellite was continuously oriented southward. In the second one, which occurred on 26 November 2000, the growth phase started while $B_z$ turned southward. After ∼10 minutes, Bz became positive until the substorm onset, while the open flux still increased and the boundaries continued their equatorward motion.

#### First case: 2000, day 241 (2000/08/28)

[14] We present here an example of a substorm onset preceded by a growth phase, that occurred on August 28, 2000. The onset is observed on SI12 images at 0936 UT and 2230 MLT. We consider the time period of one hour preceding the onset. During this interval, the SI12 images showed a clear latitudinal motion of the equatorial and polar boundaries of the auroral oval. Figure 3.1 shows the keogram of the SI12 count rate in the MLT sector of the substorm onset (figure 3.1a, between 2130 and 2230 MLT in this case) and in the midnight sector (figure 3.1b, between 2330 and 0030 MLT) versus magnetic latitude and UT. The equatorward motion of both boundaries is clearly visible, as well as the motion of the maximum of Lyman-$\alpha$ emission. Figure 3.2 shows the trace of the oval boundaries and of the emission maximum in the onset sector. The linear regression fits to the boundaries' motion are also plotted to show the average equatorward motion during the growth phase period. The slopes in this case are respectively -2.5 deg/hour for the polar boundary and -3.8 deg/hour for the equatorial boundary in the onset sector, and -3.6 and -2.3 deg/hour in the midnight sector (not shown). Figure 3.3 shows that the open flux increases during the whole growth phase, meaning that magnetic reconnection opens magnetic flux on the dayside of the magnetosphere. The number of magnetospheric field lines connected to the IMF increases during the entire growth phase time. After the onset, the open flux decreases, as a consequence of field line reconnection in the magnetotail. The reconnection rate in the tail at that time exceeds the reconnection rate on the dayside.

[15] Growth phase stretching is generally agreed to be a consequence of the loading of magnetic flux into the tail, which in turn is a consequence of energy entering the magnetospheric system through dayside merging at a rate greater than it can be transported through the nightside magnetotail via the standard convection cycle (see, e.g., *Baker et al.* [1999], and references therein). This stretching has been observed by magnetometers on board satellites crossing the magnetotail such as GOES. Figure 3.4 shows the elevation

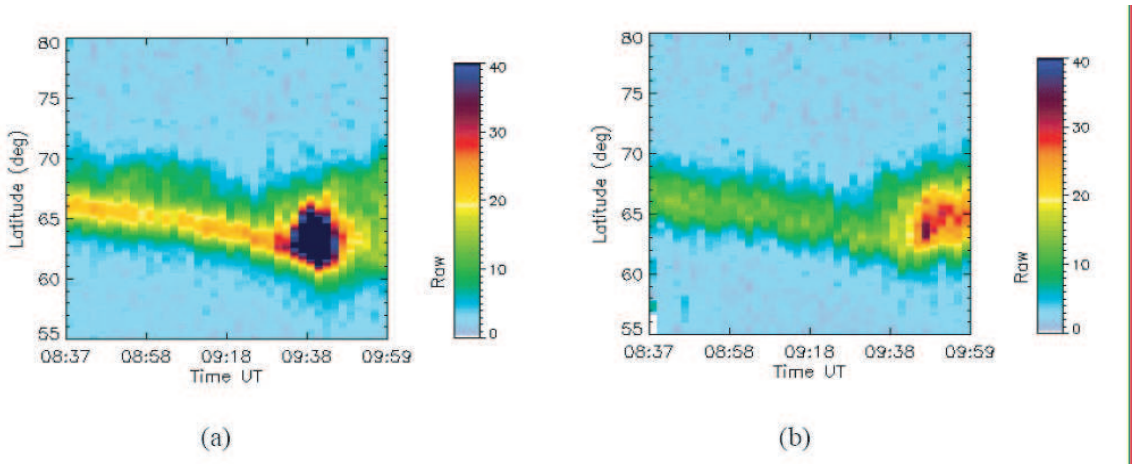


Figure 3.1: Keogram of SI12 count rate for the substorm growth phase preceding the onset of August 28, 2000 at 0936 UT (case study 1). Figure 3.1a is the keogram in the onset sector (between 2130 and 2230 MLT in this case) and figure 3.1b in the midnight sector (between 2330 and 0030 MLT).

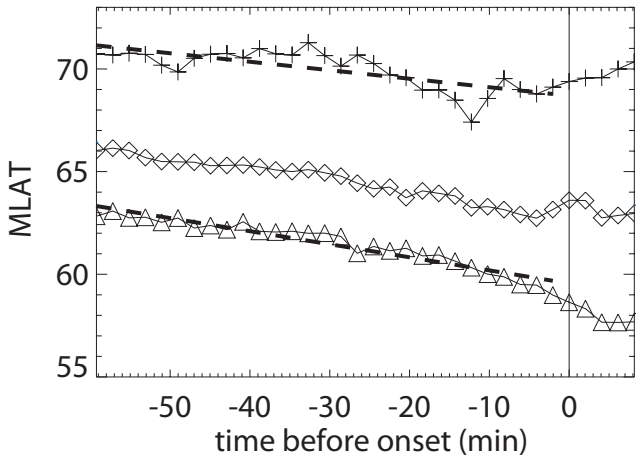


Figure 3.2: Equatorward motion of the polar boundary (+), the equatorial boundary (△) and the maximum of emission (◇) in the onset sector for the growth phase of case study 1. The abscissa axis is the time before the onset expressed in minutes. Dashed lines show best fits to the motion of the polar and equatorial boundaries before onset.

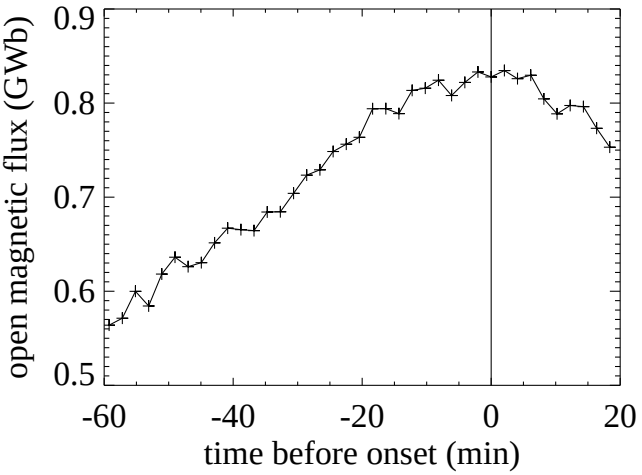


Figure 3.3: Open magnetic flux calculated from SI12 images obtained during the growth phase of case study 1.

angle, which is defined here as the angle between the geographic equatorial plane and the geomagnetic field direction. Consequently, Figure 3.4 shows that the elevation angle decreases during the growth phase, indicating that the tail field line stretching increases during this period. Following the onset, the observed increase of the elevation angle shows that the tail field lines progressively retrieve their original morphology. The dashed line in Figure 3.4 at 66° represents the value of the average elevation angle calculated from the complete set of GOES 8 and GOES 10 orbits during the time period between October 2000 and July 2001.

[16] *McPherron* [1970] showed that the beginning of the growth phase is in most cases controlled by the IMF $B_z$ orientation. One goal of the present study is to determine in which way the solar wind characteristics and the IMF conditions determine the growth phase. Figure 3.5 presents the evolution of the IMF components and the solar wind density, velocity and dynamic pressure measured by ACE during the hour before the onset of the substorm on August 28, 2000. This is an example of a triggered onset where the solar wind conditions changed during the minutes preceding the onset. A 2 to 6 minute uncertainty around the onset time is a possible error due to the propagation time of the solar wind between the satellite and the ionosphere. Figure 3.5 shows that the velocity increased from 500 km/s to more than 520 km/s while the dynamic pressure also increased from ∼5 to ∼7 nPa. Simultaneous changes are also observed in the IMF. The magnitude of the (negative) $B_z$ decreased from -4 to -2nT. As expected, $B_z$ was negative during the time of the growth phase, a favorable situation for dayside reconnection and growth phase development. During this period, $B_x$ was negative while $B_y$ was positive (except during the 10 minutes before the onset). Solar wind density, velocity and dynamic pressure varied

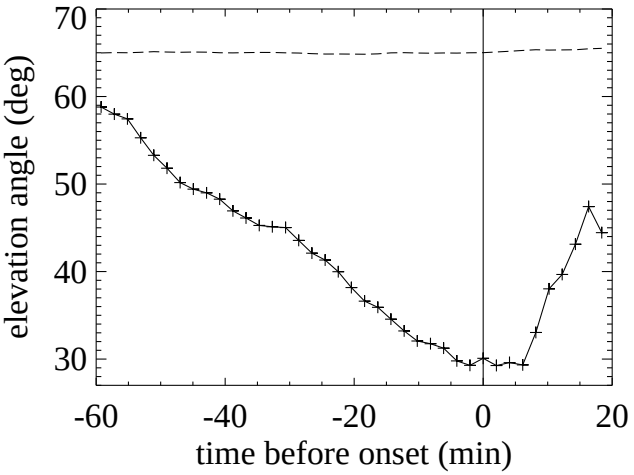


Figure 3.4: Elevation angle (+) measured in the 2300-0020 MLT sector by the GOES10 satellite during the growth phase of case study 1. The dashed line represents the mean elevation angle at the corresponding MLT measured by GOES10 on all the orbits (1 per day) from October 2000 to July 2001.

only slowly until the last few minutes prior to the onset.

**Second case: 2000, day 331 (2000/11/26)**

[17] The growth phase described here after took place on 26 November 2000. The onset is observed on SI12 images at 1548 UT and 0000 MLT. The growth phase started around 1522 UT as was identified from the polar boundary equatorward motion (Figure 3.6) and from open flux increase (Figure 3.7). ACE measurements show that $B_z$ turned southward 5 minutes before this time, as shown by Figure 3.8. We consider this change of orientation as the trigger of the growth phase. The 5 minute delay is considered as the reaction time of the magnetosphere, to which uncertainties of the propagation time could be added. Five minutes later, when $B_z$ was most negative, $B_y$ also turned negative. About 15 minutes before the substorm onset, $B_z$ became positive again, while the open flux continued to increase and the boundaries continue to move equatorward. This example shows a case of a growth phase occurring with a mainly northward $B_z$. Finally, 5 minutes before the onset time, ACE measurements showed that $|B_y|$ decreased in magnitude by 2 nT, which is a triggering factor according to our criteria.

[18] *Petrukovich et al.* [2000] studied properties of substorms occurring during northward IMF $B_z$. They showed that the rate of the solar wind energy accumulation in the magnetosphere was low due to azimuthal IMF orientation with dominating IMF $B_y$ and small

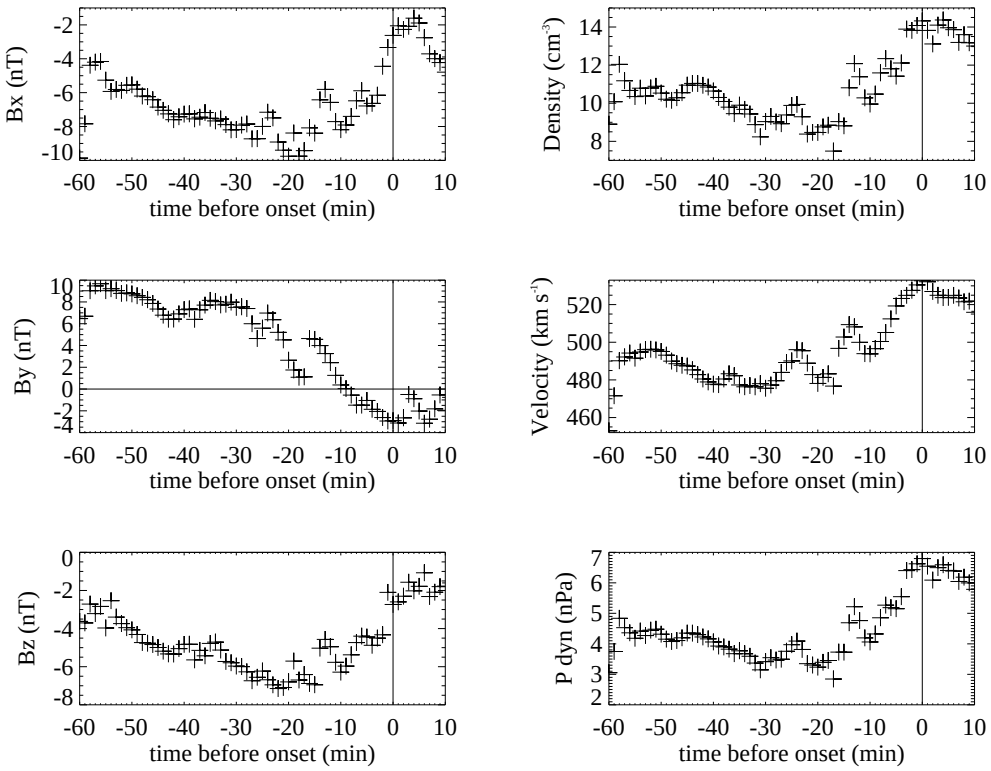


Figure 3.5: Solar wind and IMF characteristics measured by the ACE satellite during case study 1.

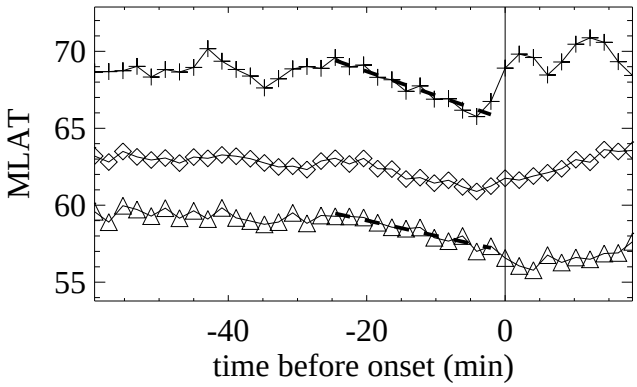


Figure 3.6: Equatorward motion of the polar boundary (+), the equatorial boundary (△) and the maximum of emission (◇) in the onset sector for the growth phase of case study 2 happening on 26 November 2000. The abscissa axis is the time before the onset expressed in minutes. Dashed lines show best fits to the motion of the polar and equatorial boundaries before onset.

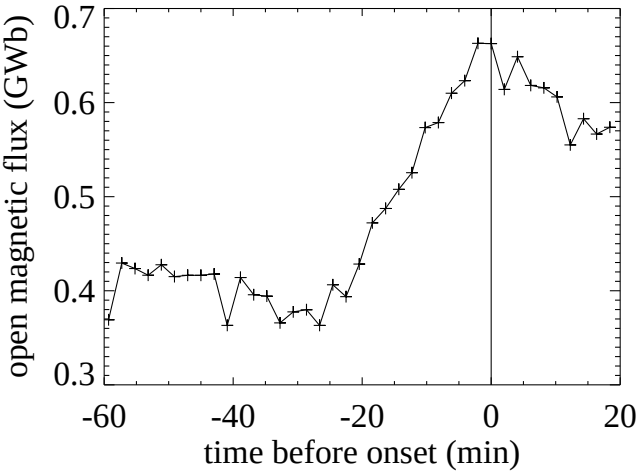


Figure 3.7: Open magnetic flux calculated from SI12 images obtained during the growth phase of case study 2.

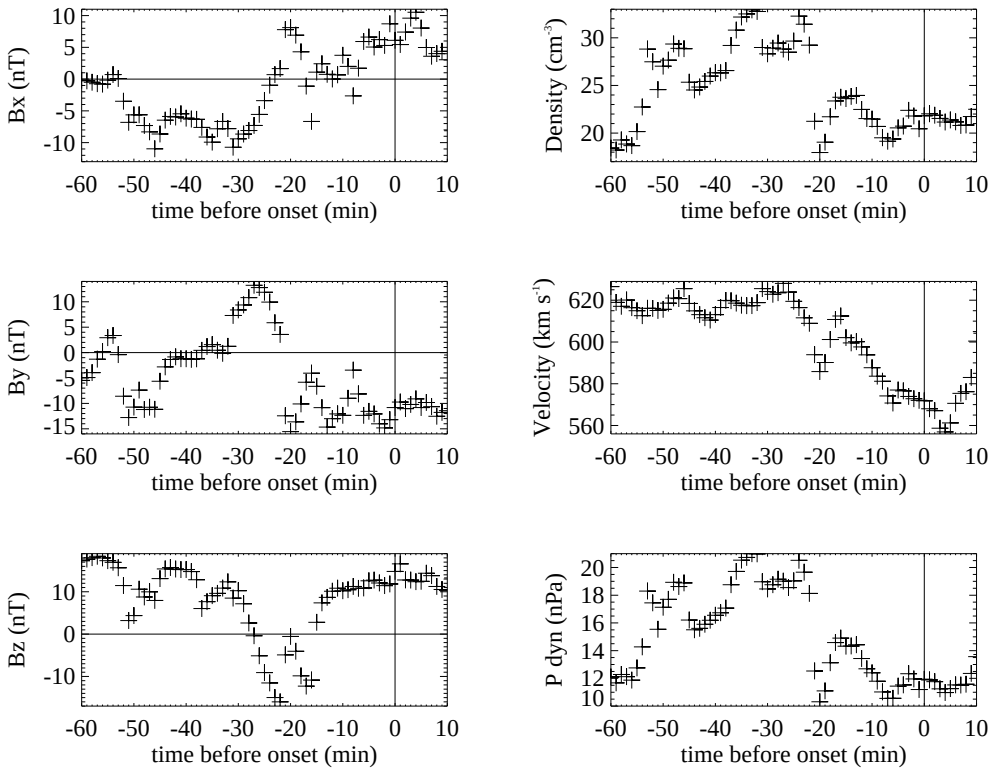


Figure 3.8: Solar wind and IMF characteristics measured by the ACE satellite during case study 2.

fluctuating IMF $B_z$. In their sample of 43 substorms with northward $B_z$, they analyzed the average values of IMF and found that either the magnitude of $B_y$ was larger than that of $B_z$ or both $B_y$ and negative $B_z$ were small, except in two cases where positive $B_z$ was very large, with $B_y$ also very large. Here, $B_z$ has a positive value over the growth phase of 2.4 nT. The average value of $B_y$ is negative but the magnitude is much higher (-7.9 nT). This example is thus in agreement with *Petrukovich et al.* [2000]'s work.

[19] We now proceed to examine the ensemble properties of the growth phases studied.

### 3.2.4 Statistical study

**Evolution of the maximum brightness MLT sector during growth phases.**

[20] Figure 3.9 shows the MLT sector where the SI12 count rate is largest, when averaged over the growth phases (1 hour UT before the onset until 20 min after) for the 55 events. The vertical line indicates the time of the synchronized onsets. Statistically, the most intense MLT sector is located at ∼2200 MLT during the growth phase period and rapidly moves towards midnight (*sim*23.2 MLT) following the onset development. On average, the substorm expansion remains close to midnight (∼23.5 MLT) at least ∼15 minutes after the onset. This is consistent with previous studies showing that the local time distribution of the onsets observed with the WIC camera on board IMAGE is concentrated between 2000 and 0200 MLT with a median at 23.4 MLT [*Gérard et al.*, 2004; *Frey et al.*, 2004]. During the 10 minutes preceding the onset, the largest observed change in the location of the most intense MLT sector was 6.2 MLT hours (from 19.6 to 1.8 MLT in this case). We also observed a displacement of 5.9 MLT hours in the opposite direction (from 2.7 to 20.8 MLT). On average, the most intense MLT sector is shifted by 1.2 MLT hour during the 10 minutes before the onset (from 22.0 to 23.2 MLT). The distribution of the location of the brightest MLT sector at the time of the onset is quasi Gaussian with a peak at 23.2 MLT, a median at 23.3 MLT and a standard deviation of 1.3 MLT.

**Evolution of the open magnetic flux during the growth phase.**

[21] The opening of magnetic flux at the dayside creates the necessary conditions to produce substorms via an accumulation of open magnetic flux and hence field energy in the magnetic tail. The growth phase is thus characterized by an increase in radius of the auroral oval. During subsequent substorm expansions, magnetic field lines that have previously been opened on the dayside and convected downtail by the solar wind reconnect within the tail plasma sheet, causing a substantial flux closure which releases accumulated field energy to the plasma particles. This reconfiguration of the tail magnetic field takes place together with poleward expanding auroral particle precipitation, and modification of the electric field, plasma flow, and currents flowing in the coupled magnetosphere-ionosphere

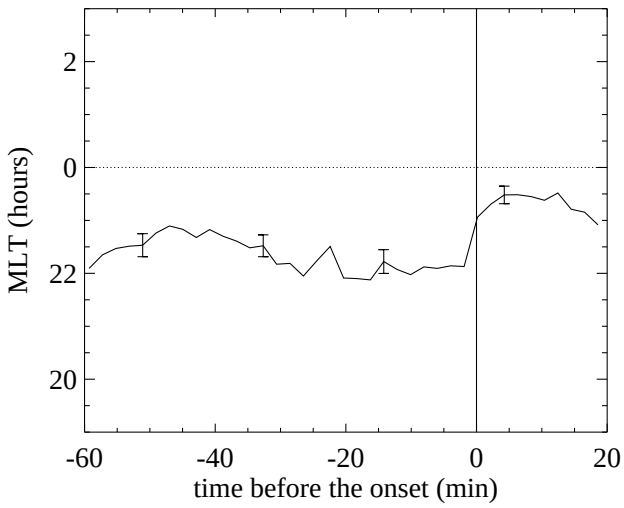


Figure 3.9: MLT sector of the maximum SI12 brightness averaged on the growth phases of the 55 selected events. The vertical line is the time of the onsets, the events have been synchronized on their onset time. The abscissa axis is the time before the onset expressed in minutes. The vertical bars indicate the estimation of the standard error of the mean (1-$\sigma$ dispersion / sqrt(n)) every 18 minutes.

system.

[22] The poleward and equatorward boundary locations have been determined from all SI12 images available in the 55 growth phase dataset described before. Their time variation has been determined every 2 minutes for all selected time sequences during and following the growth phases. We then applied a superposed epoch analysis where all substorm onsets have been synchronized at t = 0 to analyze the statistical properties of the open magnetic flux and its time evolution. Figure 3.10 shows the time evolution of the open magnetic flux averaged over the growth phases (from 1 hour UT before the onset until 20 min after) of the 33 non-triggered substorms. Also shown are the evolution of the 9 substorms triggered by a sudden reversal of $B_z$ towards positive values, the 6 substorms triggered by a sudden reduction in the magnitude of $B_y$, and the 5 substorms triggered by a sudden reversal of $B_y$ from a positive towards a negative value. In our selection of 55 events, the two remaining substorms were triggered by a dynamic pressure increase, but they are not shown in this figure. The vertical black line indicates the time of the onsets. On the average, the open flux continuously increases during the growth phase for all categories of events as the magnetosphere accumulates open magnetic flux. This is consistent with expectations and with the events discussed in Section 3.2.3. As in those events, immediately following the substorm onset, during the expansion phase, the open flux is expected to decrease as a consequence of the field line closure in the magnetotail. However, on average during the 20 minutes after the onset, this decrease is not significant, and sometimes the open flux keeps increasing. The mean open flux at onset is smallest for events triggered by a sudden reversal of $B_z$ towards positive values (0.66 GWb). It is essentially the same for non-triggered events (0.74 GWb) and events triggered by $B_y$, i.e., it is 0.75 GWb for substorms triggered by a sudden reduction in the magnitude of $B_y$, and 0.77 GWb for substorms triggered by a sudden reversal of $B_y$ from a positive towards a negative value. The maximum increase over 60 min. or less of the open magnetic flux of the non-triggered events is 0.34 GWb, and the highest rate of increase is 0.29 GWb during 25 min (0.7 GWb/hour). On average, the increase of the magnetic flux is 0.16 GWb (0.19 GWb/hour). At the onset time, the maximum and the minimum open flux observed were respectively 1.01 GWb and 0.53 GWb, whereas at the beginning of the growth phase the open flux was between 0.82 GWb (max) and 0.36 GWb (min). The distribution of the open flux value of the non-triggered events at the time of the onset is quasi Gaussian with a peak at 0.74 GWb, a median at 0.73 GWb and a standard deviation of 0.09 GWb (full width at half maximum of 0.19 GWb).

**Relation between the latitudinal motion and the IMF and SW characteristics.**

[23] The growth phase is the phase of substorm during which the magnetosphere stores magnetic energy in the tail. This energy originates from the solar wind through reconnection at the front of the magnetosphere and a signature of the storage is the increase in the tail stretching. The orientation of the IMF $B_z$ component is expected to control this

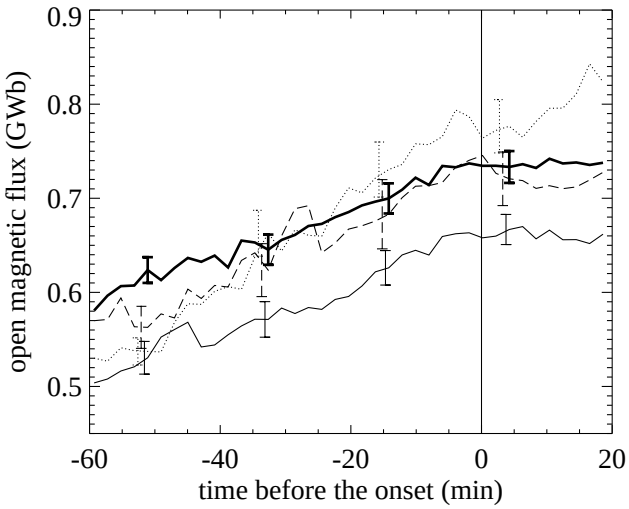


Figure 3.10: Superimposed epoch analysis of the evolution of the open magnetic flux averaged over the growth phases of the 33 non-triggered substorms (thick solid line), of the 9 substorms triggered by $B_z$ changes (thin solid line), of the 6 substorms triggered by a sudden reduction in the magnitude of $B_y$ (dashed line), and of the 5 substorms triggered by a sudden reversal of $B_y$ from positive towards negative value (dotted line). The vertical black line is the time of the onsets, the events having been synchronized compared to the onset. The horizontal axis is the time from the onset in minutes. The vertical bars indicate the estimation of the standard error of the mean (1-s / sqrt(n)) at 18 minute intervals.

energy storage and its time evolution. We thus now analyze the relation between the latitudinal motion of the proton oval polar boundary and the vertical orientation of the IMF. Figure 3.11 shows the slope of the linear regression of the equatorward motion of the polar boundary versus $B_z$ integrated over the growth phase time period. For the majority of the substorms analyzed, the time integrated $B_z$ is between 10000 and -20000 nT.s (Figure 3.11). A linear regression (correlation coefficient r = 0.4) on the sample shows that the equatorward motion tends to increase for low negative values of $B_z$, confirming that the intensity of $B_z$ controls the energy storage. A similar result was previously pointed out by *Kullen and Karlson* [2004]. From a statistical study of substorms using 3 months of Polar UV images, they showed that the majority of large substorms appears following periods when the IMF is strongly oriented southward. Our result is consistent with the view that large substorms follow the storage of a large amount of magnetic energy and thus follow a growth phase with a pronounced equatorward displacement.

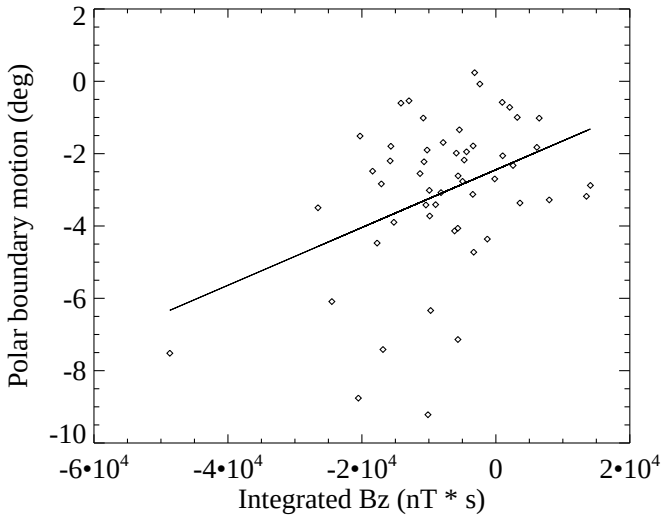


Figure 3.11: Equatorward displacement of the auroral polar boundary versus the IMF $B_z$ integrated over the growth phase time period.

[24] Figure 3.11 shows that substorms can also occur following periods with mainly positive $B_z$ (as was shown in section 3.2.3). Such events were emphasized by e.g. *Lui et al.* [1976]; *Kamide and Winningham* [1977]. In these cases, the orientation of $B_y$ influences the accumulation of energy. Moreover, the solar wind velocity and/or dynamic pressure are expected to also control the efficiency of the energy transfer from the solar wind. Various coupling functions have been proposed by different authors to account for these other factors. *Vasyliunas et al.* [1982] searched for a functional dependence on solar wind parameters of the rate of energy transfer from dimensional analysis constraints. They found

that the energy transfer depends on the solar wind dynamic pressure, velocity, and transverse IMF orientation. *Wygant et al.* [1983] found best agreement for a dependence on $\theta_c$, the angle between the transverse component of the IMF and the Earth's magnetic field at the magnetopause using a fourth power of $\sin\theta_c$. *Liou et al.* [1998] conducted a correlative study of the auroral power derived from Polar UVI observations with the concurrent solar wind and IMF observations from the Wind satellite. *Coumans et al.* [2006] showed that the most appropriate functions to describe the energy released in the proton aurora are $VB_t\sin(\theta_c/2)$ , $VB_tsin^2(\theta_c/2)$, $P^{1/3}VB_t^2sin^4(\theta_c/2)$ and $P^{1/6}VB_tsin^4(\theta_c/2)$, where $B_t$ is the transverse magnetic field. The first two are alternative proxies based on the transverse solar wind electric field in the Y-Z plane, while the others assume that the amount of energy transferred from the solar wind to the magnetosphere is proportional to the solar wind kinetic energy intercepted by the magnetopause. We now examine the relation between these four coupling functions and the latitudinal motion of the proton oval boundaries, in the onset MLT sector, during the growth phases of our database.

[25] We tested the relationship between the 4 coupling functions emphasized by *Coumans et al.* [2006], integrated over the growth phase time period and the linear regression on the equatorward motion of the polar boundary. For each of the growth sequences, the value of the coupling function was evaluated based on shifted ACE data at the time of each individual SI12 image. The values were then integrated over the growth phase time period. Figure 3.12 shows the scatterplot of slope value of the linear regression for the equatorward motion of the polar boundary versus the coupling function $P^{1/3}VB_t^2sin^4(\theta_c/2)$ integrated over the growth phase time period. The correlation coefficient of the linear regression is 0.54. This implies that even if the scatter of points is quite large, the trend is that the intensity of the coupling function plays a role on the latitudinal motion and thus on the storage of energy by the magnetosphere. The study was repeated with expressions $VB_t\sin(\theta_c/2)$ , $VB_tsin^2(\theta_c/2)$ and $P^{1/6}VB_tsin^4(\theta_c/2)$ and showed very similar results. When we correlated the equatorward boundary motion with these 4 coupling functions, we found lower correlation coefficients. This result indicates that the opening of magnetic flux on the front of the magnetosphere and the energy transfer from solar wind to the magnetosphere have much less influence on the equatorward boundary motion than on the polar boundary.

[26] *Shukhtina et al.* [2005] showed a good correlation (CC = 0.95) between the tail magnetic flux, stored during the growth phase, and the merging electric field $E_m = V_{SW}B_tsin^3(\theta/2)$, where $B_t$ is the transverse magnetic field. The estimate of the tail magnetic flux they used was based on direct or inferred measured lobe magnetic field and an empirical dependence of the tail radius on solar wind parameters. We also analyzed the relation between this function and the slope value of the linear regression of the equatorward motion of the polar and the equatorial boundaries. Correlation coefficients were respectively 0.40 and 0.34 for polar and equatorial boundaries, that is, less than with other functions. This difference in correlation coefficients from those of *Shukhtina et al.* [2005] probably stems from the fact that the tail radius they used arises from solar wind parameters, making their flux highly dependent on them. Our study does not introduce such

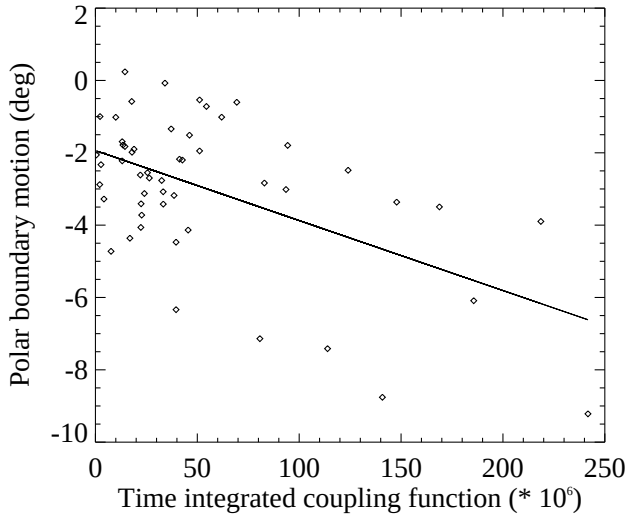


Figure 3.12: Equatorward displacement of the auroral polar boundary versus the value of the coupling function $P^{1/3}VB_t^2 sin^4(\theta_c/2)$ integrated over the growth phase time period.

a dependence, and suggests a much weaker correlation.

**Global or local motion.**

[27] The IMAGE-SI12 imager provided a global picture of the proton precipitation every 2 minutes, which we used to characterize the global equatorward motion of both boundaries during the growth phase. For each nightside 1-hour wide MLT sector, we calculated the average rate of the equatorward motion in deg/hour. Figure 3.13 presents samples of our analysis of the global nightside motion during the growth phase. A local variation was identified as a local displacement exceeding 2 deg/hour in 5 MLT sectors at most and no motion in other sectors ($0 \pm 1$ deg/hour). A global displacement is characterized by a quasi identical motion in every night sector, with typical values between $-2 \pm 1$ deg/hour and $-5 \pm 1$ deg/hour. As an example of global displacement, Figure 3.13-a shows the growth phase of January 15, 2001 with an onset at 0804 UT. The squares show the rate of the equatorial boundary motion (in MLAT deg/hour) and the diamonds represent the polar boundary motion rate. In this example, the onset occurs in the 2230-2330 MLT sector, and the motion of the polar boundary is nearly identical in all nightside sectors, close to -2.5 deg/hour. The nightside polar boundary thus retains the same shape while moving in latitude. The equatorial boundary behaves similarly in sectors between 2030 and 0330 MLT. The motion in the dusk sector and in the dawn sector is less and reaches, at the minimum, about -1.5 deg/hour.

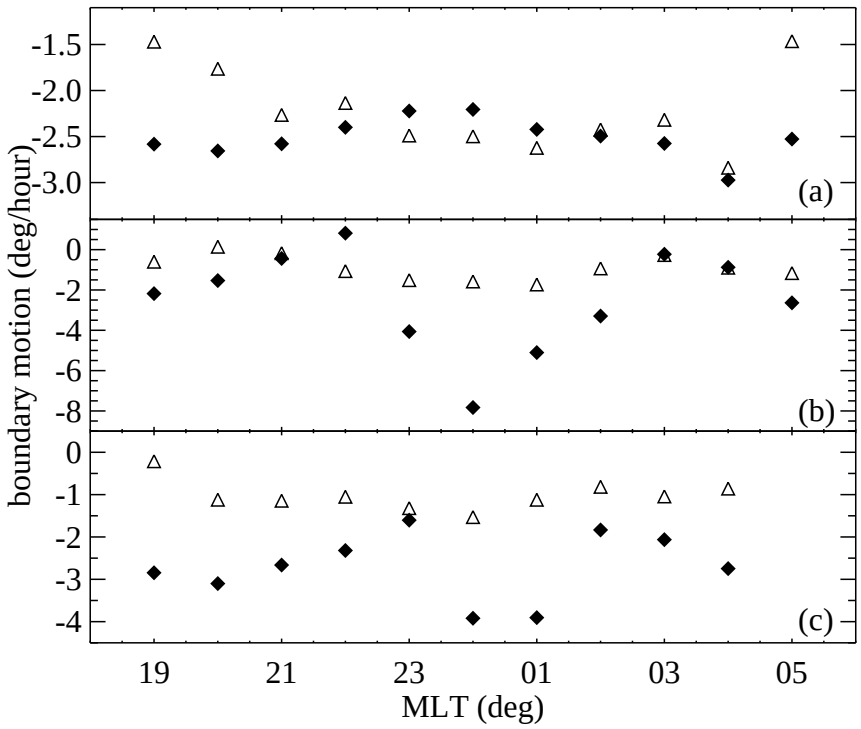


Figure 3.13: Rate of equatorward displacement of the polar (⧫) and the equatorial (△) boundaries in the nightside MLT sectors, for (a) the growth phase of January 15, 2001 preceding the onset at 0804 UT, (b) the growth phase of the December 7, 2000 preceding the onset at 2147 UT, and (c) the growth phase of March 13, 2001 preceding the onset at 0615 UT.

[28] In contrast, Figure 3.13-b presents the results for the period of December 7, 2000 preceding the onset at 2147 UT in the 2230-2330 MLT sector. In this case, the equatorward motion of the equatorial boundary was localized to a limited sector and this is thus an example of local motion. The motion was very small in the 1930-2130 MLT and 0230-0330 MLT sectors. Between these two sectors, the boundary moved equatorward, with a maximum in the 0030-0130 MLT sector. The polar boundary exhibited a large equatorward motion in the midnight sector (of about -8 deg/hour), in the sector next to the onset, while no motion occurred in the 2030-2130 MLT and the 0230-0330 MLT sectors. In the dusk sector, the rate of motion was about -2 deg/hour. The polar boundary moved poleward in the 2130-2230 MLT sector and moved strongly equatorward for MLT sectors closer to midnight. In the dawn sector, the equatorward motion was also about 2 deg/hour. The motion of the polar boundary was thus mostly restricted to the midnight sector. Solar wind measurements for this case showed no atypical behavior, with $B_z$ between 0 and -2 nT during the growth phase (except $\sim$10 minutes before the onset, where it turned slightly northward during 3 minutes), $B_y$ around -4 nT, the dynamic pressure between 4 and 4.5 nPa, the velocity around 450 km/s, and the density between 12 and 13 $cm^{-3}$.

[29] Both types of motion, local and global, are thus observed but we also describe a third type of global dynamics that is a superposition of both types of motions. This third type ('non-uniform global motion') is the most frequently observed for the polar boundary. The boundary moves equatorward in all sectors, but with different amplitudes. Figure 3.13-c shows an example for March 13, 2001. The growth phase preceded the onset at 0615 UT, which occurred in the midnight sector. The equatorial boundary moved equatorward nearly globally, at a rate of about 1 deg/hour. The polar boundary motion was equatorward in all nightside sectors, but the rate of motion varied in the different MLT sectors. The largest motion was observed in the 2330-0130 MLT onset sector, with a rate close to -4 deg/hour. At other local times, the rate of displacement varies between -3 and -1.5 deg/hour. We have checked the interplanetary magnetic field, the solar wind data and the activity level for each event. We could not identify any obvious differences that could characterized the different kind of motions.

[30] Of the 55 analyzed growth phases, the equatorial boundary had global motion in 38% of the cases, local motion in 16% of cases and non-uniform global motion in 46% of cases. The polar boundary motion was global for 17% of the cases, local for 5% of the cases and non-uniform global for 78% of the cases. In conclusion, the equatorial boundary generally moves equatorward with a global (uniform or not) motion, while the polar boundary motion is mainly non-uniform but global. Finally, we also observe that, occasionally (e.g. Figure 3.13-c), one or both boundaries move poleward in some MLT sectors. This feature does not contradict the fact that the open magnetic flux globally increases during these growth phases, since the motion is equatorward in other sectors.

[31] The maximum displacement of the polar boundary is statistically located around midnight MLT, but in no nightside local time sector does the motion of the equatorial

boundary appear be more pronounced than in others. The maximum equatorward displacement may occur in any sector from 1800 to 0600 MLT. A value between -4 and -12 deg/hour is typical for a local motion or the maximum displacement in the case of 'non-uniform global motion' for both boundaries. Furthermore, we did not find any relation between the onset sector and the sector where the boundary motion is more pronounced. Among the 55 events, the onset occurs in the 1 hour-wide sector of the largest equatorward displacement of the polar boundary for only 11 events (20%), mostly between 2300 and 0000 MLT. For 11 other events (20%), the onset occurs eastward from the sector of the maximum polar boundary motion. All other cases (33 events, 60%) exhibit an onset appearing westward of the maximum displacement of the polar limit (as far as 7 MLT hours westward). The distribution is quite similar for the equatorial boundary, with some additional cases showing an onset eastward of the maximum displacement of the equatorial boundary. In conclusion, no correlation is found between the motion of the oval boundaries and the substorm onset location.

### 3.2.5 Discussion

#### Proportion of triggered substorms

[32] *Lyons* [1996] argued, based on ground magnetometer data, that 'most, and perhaps all, expansions are triggered by IMF changes'. *Henderson et al.* [1996] demonstrate that substorms may occur solely as the result of an internal magnetospheric instability, without any external triggering. A statistical study by *Hsu and McPherron* [2003] indicated that 60% of all substorms are triggered. In their study, substorms were identified based on a sudden, persistent decrease in the AL geomagnetic index. The percentage they found is higher than the ∼40% of triggered events described in this work. Moreover, they also found that about 90% of the non-triggered substorms occur while the IMF is southward. The difference of proportion with the present work may be explained by the fact that, in this study, the events are initially selected based on the presence of a marked growth phase. The visual selection relying on the latitudinal motion of at least one of the oval boundaries probably introduces some bias on the type of subsequent substorm. We showed, in section 3.2.4, as previously indicated by *Kullen and Karlson* [2004], that the equatorward motion is controlled, in part, by the intensity of $B_z$. Since our database was selected on this motion, we mostly selected events with southward $B_z$, which is the IMF condition to accumulate open magnetic flux in the magnetosphere and generate an internal instability. Other events with $B_z$ values close to zero or mainly positive are represented in small proportion in our statistics. These are mainly triggered substorms occurring before an internal instability can occur and develop a substorm onset spontaneously, since the magnetosphere had not accumulated a large amount of open magnetic flux before onset.

**Evolution of the open flux during the growth phase**

[33] The statistical study of the evolution of the open flux during 55 growth phases (section 3.2.4) shows that the open magnetic flux increases during this phase of the auroral substorm development. This feature is the signature of the storage of magnetic energy in the magnetosphere originating from the solar wind through dayside magnetic reconnection between the geomagnetic field and the IMF. Statistically, onsets triggered by a sudden reversal of the $B_z$ component toward positive values occur for lower open flux that non-triggered onsets, whereas the mean open flux at the onset is the same for non-triggered events and events triggered by $B_y$ change. The Student's t tests was used to determine whether two means are distinct, for small samples. The difference between the means at the onset time for the non-triggered (0.74 GWb) and the $B_z$-triggered (0.66 GWb) data sets was found to be significant with a probability largely higher than 99 %. The difference between the means at the onset for non-triggered and $B_y$-triggered events is not significant. This result implies that only a sudden reversal of $B_z$ is sufficient to trigger a substorm before the magnetosphere has time to accumulate enough open magnetic flux to spontaneously develop a substorm. A change in the IMF $B_y$ component can trigger a substorm, but the magnetosphere has to be in an unstable state, characterized by a large value of the open magnetic flux. In other words, with a such level of instability, the magnetosphere is conditioned to develop a substorm onset, with or without a change in the $B_y$ component. This level of instability of the magnetosphere is probably somewhat different for each substorm, and depends on the previous state of the magnetosphere.

[34] We demonstrated that the difference in averaged open flux at the onset for $B_z$-triggered and non-triggered events does not stem from a difference in solar wind input. We first estimated the average value of $B_z$ for the $B_z$-triggered and non-triggered substorm growth phases and observed that both average values are negative and that the intensity of $|B_z|$ is highest for non-triggered onset. This result is expected since the open magnetic flux at non-triggered onset is higher and the condition to open magnetic flux is the southward turning of $B_z$. The flux would continue to increase if the change in IMF conditions did not trigger the onset. To verify that other solar wind characteristic values did not influence the flux values, we checked the average value of the coupling functions integrated on the growth phases (described in section 3.2.4) for $B_z$-triggered and non-triggered onset. For two of them ( $VB_t \sin(\theta_c/2)$ and $VB_t sin^2(\theta_c/2)$), the average values were higher for non-triggered onset growth phases, while for the 2 others ($P^{1/3}VB_t^2 sin^4(\theta_c/2)$ and $P^{1/6}VB_t sin^4(\theta_c/2)$), they were higher for $B_z$-triggered. This result indicates that, in our sample, the difference in open flux values cannot be attributed to a difference of coupling between the solar wind and the magnetosphere due to solar wind input difference (others than $B_z$).

[35] The statistical study indicates that, during the 20 minutes following onset, the open flux did not decrease for a large number of substorms (since the open flux did not drop on average). This result is somewhat unexpected since, following the onset, reconnection in the magnetotail is expected to close magnetic flux. Figure 3.10 shows that the rate

of increase of open flux is much reduced after the onset. This is likely explained by the fact that dayside reconnection continues even though the (possibly explosive) closure process associated with the substorm expansion phase development has started. The rate of dayside reconnection may be higher than the rate of reconnection in the tail. Thus, although the magnetic flux closure rate is increasingly larger in the tail after the onset, the total open flux continues to slowly increase. This assumption may be verified by examining the IMF $B_z$, which is one of the parameters controlling the rate of dayside reconnection. We verified this scenario for an event that occurred on September 30, 2000 05:42 UT characterized by an increase of the open flux after the onset. The solar wind electric field $E_{SW}$ may be estimated from ACE observations by $E_{SW} = -V_{SW}B_z$ (see *Milan et al.* [2004], and references therein). Then, as in *Milan et al.* [2004], we assume that the dayside reconnection rate (reconnection voltage) can be determined by applying this electric field across a constant portion of the dayside magnetopause $L_{MP}$, and that reconnection only takes place if the IMF is directed southwards, $B_z < 0$, such that

$$V_o = \begin{cases} L_{MP}E_{SW} & if B_z < 0 \\ 0 & if B_z > 0 \end{cases} \tag{3.2}$$

where $V_o$ is the potential of flux opening. In this case, at the onset time, the IMF $B_z$ component drops from -9.5 to -10 nT, and the velocity $V_{SW} \sim 420$ km/s. If we consider that $L_{MP} \sim 8$ $R_E$, the mean value obtained by *Hubert et al.* [2006] at the onset time, the potential of flux opening on the dayside magnetosphere is estimated about 215 kV, while the potential of flux closure in the tail has never been observed higher than 150 kV [*Hubert et al.*, 2006]. This suggests that the open flux continues to increase because the solar wind electric field is so large that the efficiency of dayside reconnection is higher than in the tail.

[36] We now compare the open magnetic flux estimates with the values obtained previously. According to DE1 measurements of the polar cap area during a large substorm by *Baker et al.* [1997], the polar cap magnetic flux increased during the growth phase from 0.78 GWb to 1.1 GWb prior to the substorm, and dropped after onset to 0.66 GWb, which are higher values than our results in general. According to *Petrinec and Russell* [1996], the lobe magnetic flux at substorm onset is 1-1.4 GWb. Polar cap area measurements using Polar UVI images [*Brittnacher et al.*, 1999] gave much smaller flux values (0.5-0.7 GWb) at substorm onset, whereas *Milan et al.* [2003], who also used Polar UVI images, but combined them with ground based data, estimated the flux at ∼1 GWb at two substorm onsets. *Shukhtina et al.* [2004] evaluated the tail magnetic flux from the lobe magnetic field and a tail radius based on solar wind parameters, between 0.85 and ∼1.4 GWb. The increase of the open flux before onset was estimated as ∼0.1-0.4 GWb in the work by *Brittnacher et al.* [1999], as 0.4-0.6 GWb in the work by *Milan et al.* [2003], and as 0-0.3 in the work by *Shukhtina et al.* [2004]. These open flux values roughly correspond to our results or perhaps exceed them in general in the cases of *Milan et al.* [2003] and *Shukhtina et al.* [2004]. Our values are in general agreement with previous estimates of the tail magnetic flux, which show a large scatter.

**Global or local motion**

[37] Our observations concerning the local or global character of the equatorward motion of the polar or equatorial boundary of the oval indicate that both types of motions are observed with SI12. The local motion corresponds to a displacement localized in an MLT sector, while the global motion is observed over the entire nightside sector. During the global motion, the boundary keeps the shape and only moves in latitude. *Jayachandran et al.* [2005] explained the global motion of the equatorward boundary of the proton oval by a global stretching of the tail magnetic field topology. By contrast, the local motion is explained by a stretching of the inner magnetosphere that is most pronounced around the onset meridian. The localized stretching indicates that the onset finds its origin in the near-Earth plasma sheet and is not triggered by any external process. We observed 9 cases where the equatorial boundary exhibited a local motion. We classify 7 of them as a non triggered onset substorms, which is consistent with the *Jayachandran et al.* [2005]'s explanation, except that we did not find that the local motion is more pronounced at the onset meridian. For last the two cases, the onset was classified as triggered by $B_z$ changes.

[38] Another phenomenology, the 'Global Non-Uniform' motion has also been observed in this study. It corresponds to a global motion all over the nightside sector, during which the boundary does not keep the same shape. The rate of motion varies according the MLT sector. The largest motion frequently occurs in the onset sector or in a sector adjacent to it, but it is also observed in the dusk or dawn sectors. Most frequently, the polar boundary is subject to a global non-uniform motion, and the equatorial boundary motion is global (uniform or not). The proportion between local or global motion of the equatorial boundary found by *Jayachandran et al.* [2005] is about 1/3. The results we found are somewhat lower since we found that about 1/6 of our examples are dominated by a local motion. Furthermore, because we selected the events with observable boundary drift at midnight, it is possible that we removed with this selection some events in which expansion is mostly outside of the near-midnight region. Therefore, for about $\sim$84% of the cases, the equatorial boundary motion is global uniform or non-uniform. *Jayachandran et al.* [2005] could not distinguish between the two types of motion, since the data they used in their study did not cover the whole nightside oval. Considering that the number of cases analyzed in this study is limited, we consider that our results for the equatorial boundary motion are not in disagreement with *Jayachandran et al.* [2005]'s results. The non-uniform global motion may be viewed as a global motion on which a local motion (that can control the position of the onset or not) is superposed.

[39] Global tail stretching is generally agreed to be a consequence of the loading of magnetic flux into the magnetotail. It stems from the accumulation of magnetic energy into the magnetospheric system through dayside reconnection at a larger rate than it can be transported through the nightside magnetotail via the standard convection and released by flux closure. To explain the local stretching, *Jayachandran et al.* [2005] proposed the idea that localized stretching reflects more the local properties within the central plasmasheet

(CPS) than the external drivers. Building on this idea, we suggest that the non-uniform global motion is a signature of the energy storage by the magnetotail on which CPS internal processes also act.

### 3.2.6 Conclusions and summary

[40] Our study is based on the analysis of the global motion of the proton aurora during 55 growth phases observed with the SI12 imager on board the IMAGE satellite. This sample was selected from visual inspection of all substorm events which occurred between June, 2000 and December, 2002. The global view provided by FUV imagers makes it possible to characterize the equatorward motion of the poleward and equatorward boundaries simultaneously at all local times and to determine the time evolution of the open magnetic flux from the size of the polar cap. The combination of the FUV global viewing with measurements of the solar wind and IMF characteristics has made it possible to reach the following conclusions concerning the solar wind control of the growth phases.

[41] We derive two main results.

- The average open flux at the substorm onset is smallest when the substorm is triggered by a sudden reversal of $B_z$. This is the sign that the accumulation of energy by the magnetosphere is perturbed by changes in $B_z$. The energy accumulation would continue to increase if this trigger did not happened.

- The equatorward motion during the growth phase may be global, restricted to local time sectors or a combination of both. No nightside local time sector appears favored where the motion of the equatorial boundary would be more pronounced. The maximum displacement of the polar boundary is statistically located around midnight MLT. The global non-uniform motion is due to a superposition of a global stretching of the tail magnetic field topology and a stretching of the inner magnetosphere finding its origin in the near-Earth plasma sheet.

[42] We also emphasize the following results:

- The sector of maximum proton precipitation during the growth phase is on average located between 2200 and 2300 MLT. It rapidly moves in local time by about 1.2 hour toward midnight at the time of the onset.

- Proxies characterizing the growth phase such as the stretching of magnetic field lines, mesured by GOES, in the geomagnetic tail have been observed in parallel with the equatorward motion of the precipitation.

- $\sim$ 40% of the substorm events selected for this study are triggered by an external cause, i.e. a solar wind or IMF characteristic variation.

- The open magnetic flux increases by as much as a 33% during the growth phase. The mean value of the open flux at the end of the growth phase, immediately preceding the substorm, onset is about 0.74 GWb for non-triggered substorms. Among the external (solar wind) factors we considered, only a sudden reversal of $B_z$ towards positive values is able to trigger a substorm for a lower value of the open flux (0.66 GWb). Indeed, the mean open flux at the onset is noticeably the same for non-triggered events and events triggered by $B_y$ (0.75 GWb).

- The open magnetic flux continues to increase, during the 20 minutes following the onset, for a large number of events (the open flux does not drop on the average, as would be expected). We interpret this behavior as an indication that the rate of opening of closed field line on the dayside can exceed that of the nightside reconnection after the onset in non-triggered substorms.

- The equatorward displacement is statistically correlated with the time integrated magnitude of the $B_z$ component of the IMF. It is also correlated with transfer functions describing the efficiency of solar wind energy transfer involving the transverse electric field carried by the solar wind.

# Chapitre 4

# Global auroral conductance distribution

## 4.1 Introduction

Ce chapitre est consacré à la détermination des conductivités ionosphériques à partir des observations du satellite IMAGE. Nous rappelons d'abord quelques notions théoriques qui n'ont pas été décrites dans l'article mais qui sont indispensables pour comprendre notre démarche scientifique.

### Les processus de transport dans l'ionosphère

Dans ce paragraphe, nous décrivons certains processus qui entrainent le mouvement des particules ionisées de l'ionosphère. Nous verrons à la fin qu'une partie de ces mouvements sont régis par la précipitation aurorale et que les caractéristiques de l'ionosphère sont donc fortement influencées par celle-ci.

Comme les autres gaz, le plasma ionosphérique est sujet à la gravité et aux forces de collisions [1], mais aussi aux forces électriques et magnétiques. Pour étudier l'effet de ces forces, il est nécessaire de construire l'équation de mouvement des particules du plasma. En supposant que les collisions entre les particules sont assez fréquentes, le plasma peut être traité comme un fluide et les équations du mouvement du plasma sont similaires aux équations de mouvement des fluides. Les processus de transport jouant un rôle important dans l'ionosphère sont décrits ci-dessous.

- Dans les régions E et F, le mouvement des particules chargées est controlé en partie par le champ magnétique terrestre. L'équation de mouvement comprend donc un terme de Lorentz ($\mathbf{V} \times \mathbf{B}$).
- Le mouvement des ions et des électrons est aussi influencé par le champ électrique. Le mouvement résultant des particules (et donc les courants électriques) dépend du champ

[1] Dans l'ionosphère, la densité de plasma est suffisante pour que les collisions ne puissent être négligées

magnétique et des fréquences de collisions, qui déterminent la mobilité et la conductivité électrique des particules chargées.
- Les particules chargées sont aussi entrainées par les vents neutres [2]. Les forces produites sont proportionnelles à la différence entre la vitesse du vent neutre ($U$) et les vitesses des ions ($V_i$) et électrons ($V_e$), et dépendent des fréquences de collisions.
- La variation de température journalière influence également le mouvement des particules chargées.
- Le plasma (comme n'importe quel gaz) diffuse sous l'action de la gravité et des gradients des pressions partielles du gaz. Mathématiquement, les pressions partielles des ions et des électrons peuvent s'exprimer $p_i = N_i k T_i$ et $p_e = N_e k T_e$.

Considérant les mouvements à grande échelle dans l'ionosphère, l'accélération peut être égalée à zéro. Les équations de mouvement peuvent alors s'écrire :

$$\begin{aligned} m_i \frac{d\mathbf{V}_i}{dt} = 0 = m_i \mathbf{g} - N_i^{-1} \nabla(N_i k T_i) + e(\mathbf{E} + \mathbf{V}_i \times \mathbf{B}) - m_i \nu_{in}(\mathbf{V}_i - \mathbf{U}) - m_e \nu_{ei}(\mathbf{V}_i - \mathbf{V}_e) \\ m_e \frac{d\mathbf{V}_e}{dt} = 0 = m_e \mathbf{g} - N_e^{-1} \nabla(N_e k T_e) - e(\mathbf{E} + \mathbf{V}_e \times \mathbf{B}) - m_e \nu_{en}(\mathbf{V}_e - \mathbf{U}) - m_e \nu_{ei}(\mathbf{V}_e - \mathbf{V}_i) \end{aligned} \tag{4.1}$$

où les indices i, e et n représentent respectivement les ions, les électrons et les espèces neutres de l'atmosphère. $m_i$ et $m_e$ sont les masses ionique et électronique et $\nu_{ab}$ sont les fréquences de collisions [3] entre les espèces $a$ et $b$.

## Le terme de collision dans l'équations de mouvement

Nous allons ici examiner de plus près le terme de collision des équations de mouvement. La force par unité de volume subie par les particules $a$ qui rencontrent les particules de type $b$ peut s'écrire :

$$\mathbf{F}_{ab} = -\mathbf{F}_{ba} = N_a m_a \nu_{ab}(\mathbf{V}_b - \mathbf{V}_a) \tag{4.2}$$

L'accélération des particules de type $a$ due aux collisions avec les particules de type $b$ peut alors s'écrire :

$$[\frac{\partial \mathbf{V}_a}{\partial t}]_{ab} = \nu_{ab}(\mathbf{V}_b - \mathbf{V}_a) \tag{4.3}$$

Pour décrire le taux de transfert de moment par unité de volume, définissons les coefficients $K_{ab}$. Ces coefficients interviennent dans la définition des fréquences de collisions comme

[2] L'atmosphère neutre à ces altitudes est soumise à des vents dus principalement à un mouvement de marée et à des variations de pression liées aux variations de températures journalières.

[3] Les fréquences de collisions que nous utilisons ici ne représentent pas exactement la fréquence réelle des collisions entre les particules $a$ et $b$, mais plutôt un coefficient indiquant le taux de transfert de moment, comme utilisé par *Rishbeth and Garriott* [1969]. Certains auteurs utilisent un paramètre de collision différent, plus proche des fréquences de collision de la théorie cinétique. Dans ce cas, ils remplacent la masse $m_a$ par la masse réduite $\frac{m_a m_b}{m_a + m_b}$.

suit :

$$\begin{aligned} \nu_{in} &= N_n K_{in} & \nu_{ni} &= N K_{ni} \\ \nu_{en} &= N_n K_{en} & \nu_{ne} &= (\frac{m_e}{m_n}) N K_{en} \\ \nu_{ei} &= N K_{ei} & \nu_{ie} &= (\frac{m_e}{m_i}) N K_{ei} \end{aligned} \tag{4.4}$$

avec $N = N_e = N_i$ la concentration électronique et ionique et $N_n$ la concentration en espèce neutre. Ces formules supposent que $m_i = m_n \gg m_e$. Les valeurs numériques des coefficients $K_{ab}$ sont données par *Rishbeth and Garriott* [1969] et valent en unité m.k.s. :

$$\begin{aligned} K_{in} &= 2.6 \times 10^{-15} M^{-1/2} \\ K_{en} &= 5.4 \times 10^{-16} T^{1/2} \\ K_{ei} &= [59 + 4.18 \log(\frac{T^3}{N})] 10^{-6} T^{-3/2} \end{aligned} \tag{4.5}$$

où $M$ est la masse des ions et espèces neutres exprimée en u.m.a. et $T$, la température, est supposée être égale pour toutes les espèces.

## Le mouvement des particules chargées dans un champ électrique

Nous pouvons déterminer le mouvement des ions et des électrons ionosphériques dans un champ électrique à partir des équations 4.1. Ces équations peuvent être simplifiées si nous négligeons la gravité, les forces de gradient de pression et les collisions ions-électrons. Nous pouvons alors écrire :

$$\begin{aligned} m_i \frac{d\mathbf{V}_i}{dt} &= eE + e\mathbf{V}_i \times \mathbf{B} - m_i \nu_{in} (\mathbf{V}_i - \mathbf{U}) \\ m_e \frac{d\mathbf{V}_e}{dt} &= -eE - e\mathbf{V}_e \times \mathbf{B} - m_e \nu_{en} (\mathbf{V}_e - \mathbf{U}) \end{aligned} \tag{4.6}$$

Négligeons le terme lié à la vitesse du vent neutre et analysons le mouvement des ions et des électrons. Si $E \parallel B$, les mouvements ne sont pas affectés par la présence du champ magnétique. Si $E \perp B$, les trajectoires sont cycloïdales. Elles sont représentées à la Figure 4.1 où on a supposé que les particules revenaient au repos après un laps de temps égal à $1/\nu$. Les trajectoires sont tracées pour plusieurs valeurs du rapport $\nu/\omega$, où $\omega$ est la fréquence de giration angulaire et est définie par $\omega = \frac{eB}{m}$ avec $e$ la valeur absolue de la charge de l'électron. Le mouvement des ions et des électrons est plus complexe si on ne néglige pas le vent neutre.

### Résolution mathématique des équations de mouvement

Pour résoudre mathématiquement les équations de mouvements 4.6, négligeons d'abord le terme de collision et supposons que le champ magnétique s'écrit $\mathbf{B} = (0, 0, B)$ et le

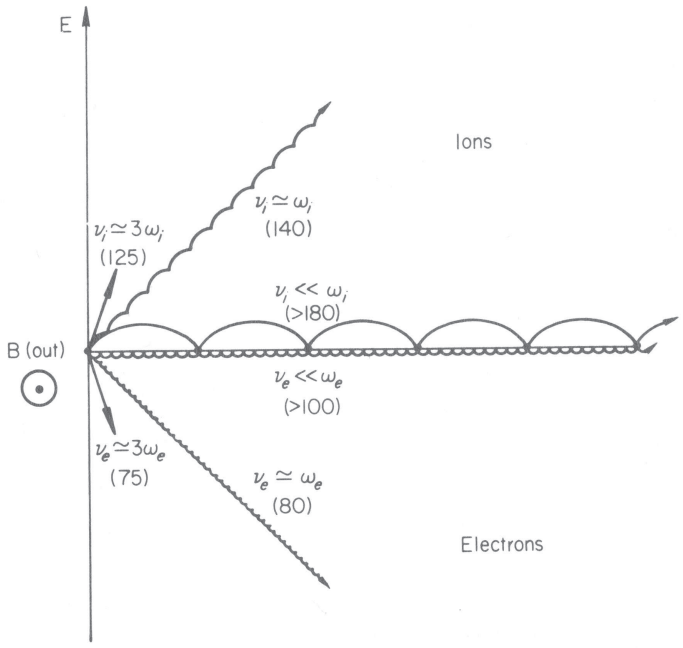


FIG. 4.1 – Trajectoires des ions et des électrons dans un champ électrique (**E** dans le plan du diagramme) et dans un champ magnétique (**B** sortant du schéma). Les particules chargées sont supposées entrer en collision avec les particules neutres à intervalles réguliers $1/\nu$ et posséder une vitesse nulle après chaque collision. Dans le but de montrer les mouvements des ions et des électrons, le diagramme est tracé de sorte que $\omega_e/\omega_i = 10$ (au lieu de $\sim 10^4$ dans la réalité). Toutes les trajectoires font référence au même intervalle de temps, c'est-à-dire 5 périodes de giration ioniques (ou 50 pour les électrons). Les nombres entre parenthèse indiquent les altitudes approximatives en km auxquelles les conditions sont remplies. Figure tirée du livre *Rishbeth and Garriott* [1969]

champ électrique $\mathbf{E} = (E_x, 0, E_z)$. Si nous ne considérons qu'une seule espèce, de charge q et de masse m, l'équation s'écrit :

$$m\frac{d\mathbf{V}}{dt} = qE + q\mathbf{V} \times \mathbf{B} \tag{4.7}$$

Si on décompose cette équation selon les trois composantes x, y et z, on obtient le système suivant :

$$\begin{aligned} m\frac{dv_x}{dt} &= qE_x + qv_yB \\ m\frac{dv_y}{dt} &= -qv_xB \\ m\frac{dv_z}{dt} &= qE_z \end{aligned} \tag{4.8}$$

La résolution de ce système donne :

$$\begin{aligned} v_x &= v_{x0}\cos\omega t + \frac{v_{y0} + qE_x}{qB}\sin\omega t \\ v_y &= \frac{v_{y0} + qE_x}{qB}\cos\omega t - v_{x0}\sin\omega t - \frac{qE_x}{qB} \\ v_z &= v_{z0} + \frac{qE_z}{m}t \end{aligned} \tag{4.9}$$

où $v_{x0}$,$v_{y0}$ et $v_{z0}$ sont les vitesses initiales de la particule au temps $t = 0$. Ces solutions décrivent en fait le mouvement de giration de la particule et la dérive du centre de guidage sous la contrainte du champ électrique.

Si on superpose maintenant le phénomène de collisions, les solutions 4.9 ne sont plus valables qu'entre les collisions. Le mouvement générale est perturbé. Supposons qu'après chaque collision, la particule repart du repos dans une direction au hasard ($v_{x0} = v_{y0} = v_{z0} = 0$). Supposons également que les collisions se produisent aléatoirement dans le temps. La distribution de probabilité des processus de collisions est alors proportionnelle à $e^{-\nu t}$ et la probabilité qu'une particule ne subisse pas de collision dans le temps compris entre $t$ et $t + dt$ vaut $\nu e^{-\nu t}dt$. Pendant ce temps sans collision, la particule subit un mouvement de dérive sous l'influence du champ électrique tel que décrit par les équations 4.9. Les vitesses moyennes de dérive sont donc données par les équations suivantes :

$$\begin{aligned} < v_x > &= \frac{\int \nu e^{-\nu t}(qE_x/qB)\sin\omega t dt}{\int \nu e^{-\nu t}dt} = \frac{E_x}{B}\frac{\omega\nu}{\nu^2 + \omega^2} \\ < v_y > &= \frac{\int \nu e^{-\nu t}(qE_x/qB)(\cos\omega t - 1)dt}{\int \nu e^{-\nu t}dt} = -\frac{E_x}{B}\frac{\omega^2}{\nu^2 + \omega^2} \\ < v_z > &= \frac{\int \nu e^{-\nu t}(qE_z/m)t dt}{\int \nu e^{-\nu t}dt} = \frac{qE_z}{m\nu} \end{aligned} \tag{4.10}$$

On obtient donc une solution pour les ions et une pour les électrons qui s'écrivent comme suit :

$$\begin{aligned} < v_{xi} >&= \frac{E_x}{B}\frac{\omega_i \nu_{in}}{\nu_{in}^2 + \omega_i^2} & < v_{xe} >&= -\frac{E_x}{B}\frac{\omega_e \nu_{en}}{\nu_{en}^2 + \omega_e^2} \\ < v_{yi} >&= -\frac{E_x}{B}\frac{\omega_i^2}{\nu_{in}^2 + \omega_i^2} & < v_{ye} >&= \frac{E_x}{B}\frac{\omega_e^2}{\nu_{en}^2 + \omega_e^2} \\ < v_{zi} >&= \frac{eE_z}{m_i \nu_{in}} & < v_{ze} >&= \frac{-eE_z}{m_e \nu_{en}} \end{aligned} \tag{4.11}$$

## Les conductivités ionosphériques

Définissons d'abord la densité de courant pour un plasma constitué d'électrons et d'ions :

$$\mathbf{j} = eN(\mathbf{V}_i - \mathbf{V}_e) \tag{4.12}$$

La loi d'Ohm reliant la densité de courant au champ électrique s'écrit :

$$\mathbf{j} = \boldsymbol{\sigma} \cdot \mathbf{E} \tag{4.13}$$

avec

$$\boldsymbol{\sigma} = \begin{bmatrix} \sigma_1 & -\sigma_2 & 0 \\ \sigma_2 & \sigma_1 & 0 \\ 0 & 0 & \sigma_0 \end{bmatrix}$$

$\sigma$ est le tenseur de conductivité. Cette forme tensorielle vient du fait que le plasma ionosphérique est un milieu anisotrope. Les courants ne circulent donc généralement pas uniquement dans la direction parallèle au champ électrique appliqué. Les composantes du tenseur définissent en fait trois conductivités :

- $\sigma_0$ est la **conductivité longitudinale**. Si le champ électrique est appliqué parallèlement au champ magnétique, la conductivité $\sigma_0$ dépend uniquement des fréquences de collision. (En résumé, $\sigma_0 \parallel \mathbf{B}$ et $\parallel \mathbf{E}$)
- $\sigma_1 = \sigma_P$ est la **conductivité de Pedersen**. Si le champ électrique appliqué est perpendiculaire au champ magnétique, $\sigma_P$ est la conductivité dans la direction du champ électrique (En résumé, $\sigma_P \perp \mathbf{B}$ et $\parallel \mathbf{E}$)
- $\sigma_2 = \sigma_H$ est la **conductivité de Hall**. Si le champ électrique appliqué est perpendiculaire au champ magnétique, $\sigma_H$ est la conductivité dans la direction perpendiculaire au champ électrique (En résumé, $\sigma_H \perp \mathbf{B}$ et $\perp \mathbf{E}$)

En combinant les solutions des équations du mouvements des électrons et des ions (Equations 4.11) avec les équations 4.12 et 4.13, on trouve que les conductivités peuvent s'écrire :

$$\sigma_0 = \frac{Ne}{B}\left(\frac{\omega_e}{\nu_{en}} + \frac{\omega_i}{\nu_{in}}\right) \tag{4.14}$$

$$\sigma_P = \frac{Ne}{B}\left(\frac{\nu_{en}\omega_e}{\nu_{en}^2+\omega_e^2} + \frac{\nu_{in}\omega_i}{\nu_{in}^2+\omega_i^2}\right) \tag{4.15}$$

$$\sigma_H = \frac{Ne}{B}\left(\frac{\omega_e^2}{\nu_{en}^2+\omega_e^2} - \frac{\omega_i^2}{\nu_{in}^2+\omega_i^2}\right) \tag{4.16}$$

Ce sont ces équations 4.14, 4.15 et 4.16 que nous avons utilisées pour modéliser les conductivités ionosphériques à partir des observations du satellite IMAGE

Trois types de courants sont associés à ces conductivités :
– le courant parallèle (dans la direction $\parallel \mathbf{B}$ et $\parallel \mathbf{E}$)
– le courant de Pedersen (dans la direction $\parallel \mathbf{B}$ et $\perp \mathbf{E}$)
– le courant de Hall (dans la direction $\perp \mathbf{B}$ et $\perp \mathbf{E}$)
Le courant de Pedersen est dissipatif (échauffement de Joule) puisque $\mathbf{J} \cdot \mathbf{E} \neq 0$, alors que le courant de Hall ne l'est pas.

## 4.2 Résumé introductif

Dans les chapitres précédents, l'analyse des observations IMAGE-FUV avait pour but d'expliquer les processus de précipitation des protons, c'est-à-dire les processus prenant place dans la magnétosphère qui accélèrent les protons vers l'atmosphère terrestre. Dans ce chapitre, j'utilise les observations SI12 (et WIC [4]) pour analyser les conséquences sur l'ionosphère de cette précipitation.

A partir des cartes instantanées de flux énergétiques des protons et des électrons incidents (calculées à partir des observations SI12 et WIC et des modèles de transport et de dégradation d'énergie des particules aurorales, comme expliqué au chapitre 1), j'ai développé une méthode pour calculer les conductivités ionosphériques de Hall et de Pedersen induites par les protons et les électrons auroraux, basée sur les équations 4.14, 4.15 et 4.16. L'intégration des profils de conductivité permet de calculer des cartes globales de conductances ionosphériques dues à la précipitation instantanée de protons : nouveau résultat permis grâce à SI12. J'ai analysé la contribution des protons dans la conductance totale induite par les particules aurorales. J'ai montré que la contribution des protons est relativement plus grande pendant les périodes calmes que pendant les sous-tempêtes. Ainsi, la contribution des protons est plus grande pendant la phase de croissance précédant l'onset et diminue fortement durant la phase d'expansion. Cette méthode est adaptée pour analyser l'évolution temporelle des conductances ionosphériques au-dessus des régions aurorales.

Ces résultats sont décrits explicitement et illustrés dans l'article repris dans les pages suivantes (publié dans la revue *Annales Geophysicae* en 2004).

[4] puisque j'ai également analysé les conséquences de la précipitation électronique

# 4.3 Global Auroral Conductance Distribution due to Electron and Proton Precipitation from IMAGE-FUV observations

V. Coumans, J.-C. Gérard, B. Hubert, M. Meurant
Laboratoire de Physique Atmosphérique et Planétaire, Université de Liège

S. B. Mende
Space Science Laboratory, University of California

*Published in Annales Geophysicae (April 8, 2004).*

## Abstract

[1] *The Far Ultraviolet (FUV) imaging system on board the IMAGE satellite provides a global view of the north auroral region in three spectral channels including the SI12 camera sensitive to Doppler shifted Lyman-α emission. FUV images are used to produce instantaneous maps of electron mean energy and energy fluxes for precipitated protons and electrons. We describe a method to calculate ionospheric Hall and Pedersen conductivities induced by auroral proton and electron ionization based on a model of interaction of auroral particles with the atmosphere. Different assumptions on the energy spectral distribution for electrons and protons are compared. Global maps of ionospheric conductances due to instantaneous observation of precipitating protons are calculated. The contribution of auroral protons in the total conductance induced by both types of auroral particles is also evaluated and the importance of proton precipitation is evaluated. This method is well adapted to analyze the time evolution of ionospheric conductances due to precipitating particles over the auroral region or in particular sectors. Results are illustrated with conductance maps of the north polar region obtained during four periods with different activity levels. It is found that the proton contribution to conductance is relatively higher during quiet periods than during substorms. The proton contribution is higher in the period before the onset and strongly decreases during the expansion phase of substorms. During a substorm which occurred on 28 April, 2001, a region of strong proton precipitation is observed with SI12 around 1400 MLT at ∼75° MLAT. Calculation of conductances in this sector shows that neglecting the protons contribution would produce a large error. We discuss possible effects of the proton precipitation on electron precipitation in auroral arcs. The increase of ionospheric conductivity induced by a former proton precipitation can reduce the potential drop along field lines in the upward field aligned currents by creating an opposite polarization electric field. This feedback mechanism possibly reduces the electron acceleration.*

### 4.3.1 Introduction

[2] The calculation of the ionosphere height integrated conductivities is important in evaluating the ionosphere electrodynamics and in modeling the interactions between magnetosphere, ionosphere and thermosphere. In particular, the Pedersen conductance is useful to calculate the Joule heating rate. Thus, it is crucial in studies of the ionospheric electrodynamics to be able to determine the global distribution of conductance and its time evolution.

[3] Conductivities are usually estimated from the electron density height profile which is controlled by the EUV solar radiation and the auroral precipitation. One experimental approach is to use the height profile of electron density measured from the ground with incoherent-scatter radars, such as the Chatanika or EISCAT radars, or derived from scanning photometers data. *Horwitz et al.* [1978] and *Vickrey et al.* [1981, 1982] provided examples of ionospheric Hall and Pedersen conductances evaluated from Chatanika radar measurements. *Mende et al.* [1984] compared the conductances derived from auroral spectroscopic measurements obtained with meridian scanning photometers and derived from the incoherent scatter radar at Chatanika. *Robinson et al.* [1989] compared the latter with the auroral luminosities observed with the auroral imagers on board the DEI satellite. EISCAT radar measurements of the electron density were used by *Schlegel* [1988], *Brekke and Hall* [1988], *Brekke et al.* [1989] and *Lester et al.* [1996] to calculate ionospheric conductances. Another method to evaluate ionospheric conductances from the ground uses observations of **B** and **E** fields from, for example, the STARE coherent radar system and the IMS Scandinavian Magnetometer Array [*Inhester et al.*, 1992].

[4] In situ measurements also allow to calculate conductances. *Evans et al.* [1977] determined the Hall and Pedersen conductivities of the auroral ionosphere produced by the particle precipitation from the auroral electron data obtained during the flight of Polar 3 over an auroral arc. *Vondrak and Robinson* [1985] compared the height-integrated conductivities inferred from the AE-C satellite measurements and those computed from the Chatanika radar measurements. These studies were localized in space since instruments have restricted fields of view which do not permit observations of the auroral zone at all latitudes and local times. An effort was done to extrapolate the EISCAT Pedersen conductances to other parts of the sky [*Kosch et al.*, 1998].

[5] In order to properly estimate the instantaneous three-dimensional current system, its variations during auroral substorms and the spatial distribution of Joule heating, an accurate knowledge of instantaneous ionospheric conductances over the entire polar region is required. For electrons three approaches have been applied so far.

[6] 1) Several empirical models of conductances were developed and validated with in situ particle measurements. These empirical formulas for SP and SH depend on the mean energy and the energy flux of the incident particles. *Spiro et al.* [1982] used data from

the AE-C and AE-D particle detectors to develop an empirical model of electron auroral zone conductances from patterns of energy influx and characteristic energy. The global distribution of the auroral enhancement portion of the Pedersen and Hall conductances was inferred from the data by means of empirical fits to detailed energy deposition calculations. *Robinson et al.* [1987] estimated the validity of their empirical conductances formulas using precipitating electron measurements made by the Hilat satellite during a pass over Greenland. *Gjerloev and Hoffman* [2000a,b] evaluated Hall and Pedersen conductances from 31 individual DE-2 substorm crossing measurements using a monoenergetic conductance model, which divides the energy flux into energy bands each centered at the energy Ei and then integrates over the energy spectrum. From these results, *Gjerloev and Hoffman* [2000c] developed an empirical model of conductances.

[7] 2) Statistical conductivity patterns have been constructed on the basis of statistical maps of auroral precipitation. *Wallis and Budzinski* [1981] presented patterns based on ISIS 2 satellite data. *Hardy et al.* [1987] used the *Hardy et al.* [1985] statistical global patterns of the integral energy flux and average energy of precipitating auroral electrons to determine the global pattern of electron-produced, height-integrated Hall and Pedersen conductivities. This approach cannot provide an accurate picture of the instantaneous effect of the auroral precipitation on the ionosphere since they only depend on geomagnetic activity through the 3-hour Kp index. *Fuller-Rowell and Evans* [1987] used the particle influx into the atmosphere monitored by the series of polar-orbiting National Oceanic and Atmospheric Administration TIROS, NOAA 6, and NOAA 7 spacecraft to construct statistical global patterns of height-integrated Pedersen and Hall conductivities for a discrete set of auroral activity ranges.

[8] 3) Auroral images acquired from high altitude, such as those from the Dynamic Explorer 1 satellite, coupled with an auroral model, provide instantaneous ionospheric conductance patterns. *Lummerzheim et al.* [1991] constructed maps from DE-1 data and *Rees et al.* [1988]'s model.

[9] In global models of auroral precipitation-induced conductances [*Wallis and Budzinski*, 1981; *Spiro et al.*, 1982; *Fuller-Rowell and Evans*, 1987; *Hardy et al.*, 1987] energetic protons have been either neglected or treated as if they were electrons. However, several studies [*Basu et al.*, 1987; *Galand et al.*, 1999; *Coumans et al.*, 2002] have shown that protons play a major role on the ionospheric densities at given locations and times. Recently *Galand and Richmond* [2001] proposed a simple way to parameterize the Pedersen and Hall conductances due to auroral proton precipitation and applied them to the *Hardy et al.* [1989] statistical patterns of precipitating proton flux and mean energy [*Galand et al.*, 2001]. The derivation is based on a proton transport code to calculate the electron production rate, which assumes a Maxwellian distribution of the incident proton energy flux. This approximation may however underestimate the high-energy tail of precipitating protons [*Decker et al.*, 1996; *Codrescu et al.*, 1997]. Since *Galand et al.* [2001]'s results are based on statistical patterns of precipitating particle characteristics, their conductances

cannot show the time variation due to auroral particles. Those patterns are only related to geomagnetic activity through 9 levels of Kp index.

[10] *Liou et al.* [2001] performed a statistical study of the seasonal variation of auroral electron precipitation using POLAR UVI observations. Their results indicated that dayside and nightside regions of electron aurora reveal different seasonal effects which are local time and latitude dependent. First, they showed that the nightside auroral power is suppressed in summer while the dayside auroral power is enhanced and reveal the so-called postnoon auroral bright spot in the sunlit hemisphere. Second, they concluded that the energy of the precipitating electrons is higher in winter than in summer and, third, that the electron number flux is smaller in winter than in summer. Based on DMSP satellite measurements, *Newell et al.* [1996b] also emphasized the suppression of discrete electron aurora in sunlit regions. They interpreted the observations in terms of an ionospheric conductivity feedback mechanism [*Atkinson*, 1970; *Sato*, 1978; *Lysak*, 1986]. The ionospheric 'background conductance', which is an approximately steady ionospheric conductance which is largely due to solar ionization, plays a role in the creation of the aurora. In this study we also examine if conductances due the auroral proton precipitation can also influence the electron precipitation as the background ionospheric conductance. If the proton precipitation produces an important enhancement in the ionospheric conductances, the feedback conductivity mechanism may produce or reduce the acceleration of auroral electrons.

[11] We propose to evaluate instantaneous conductance global distribution from IMAGE - FUV observations separately for electrons and for protons. The IMAGE (Imager for Magnetopause-to-Aurora Global Exploration) satellite, launched in March 2000, is a mission for remote sensing simultaneously of all regions of the Earth's magnetosphere. On board the IMAGE satellite, the FUV imaging system globally observes the north auroral region in the far ultraviolet [*Mende et al.*, 2000a]. The imagers are designed to monitor the electron and proton precipitation and discriminate between the two types of particles. Previous studies have shown the quantitative and qualitative validity of FUV instruments from comparisons with in situ auroral particle measurements [*Frey et al.*, 2001; *Gérard et al.*, 2001; *Coumans et al.*, 2002].

[12] Section 4.3.2 briefly describes the method used to extract the particle energy and energy flux characteristics from the FUV observations. In section 4.3.3 the conductance model we developed is described step by step. The validation of the conductivity model and of the complete method to construct conductance maps is discussed in section 4.3.4. We present some case studies in section 4.3.5. We show instantaneous conductance maps and discuss the relative importance of proton-induced conductivities. In section 4.3.6 we show some results obtained by using electron mean energy evaluated from FUV observations and we discuss the reliability and the relevance of this method. Finally, section 4.3.7 summarizes the method and discusses the role of proton induced conductances and its possible effect on field aligned currents associated with discrete electron aurora.

### 4.3.2 The FUV imagers and the auroral precipitation

[13] The FUV experiment on board the IMAGE satellite includes three different imagers: the Wideband Imaging Camera (WIC) and two Spectrographic Imagers (SI12 and SI13). One characteristic of the FUV imager is its capability to simultaneously observe the North hemisphere in all three spectral regions. The Spectrographic Imager is a narrow-band imager of far ultraviolet auroral emissions at 121.8 nm and 135.6 nm. The SI12 imager measures the brightness of the Doppler shifted Lyman-$\alpha$ auroral emission. SI12 is the first FUV imager able to detect incident proton flux without contribution from electrons. SI13 images the OI 135.6 nm line produced by incident primary electrons and protons and secondary electrons colliding with neutral atoms. The WIC imager has a passband between 140-180 nm with a low sensitivity below 140 nm which covers a spectral region including emissions excited by both protons and electrons. It is mostly sensitive to the LBH bands and the 149.3 nm NI line with small contributions from the NI 174.3 nm doublet and the OI 135.6 nm line. More information about the IMAGE mission can be found in *Burch* [2000] and the FUV experiment is described in *Mende et al.* [2000a].

[14] *Frey et al.* [2001] used in situ measurements from two orbits of the FAST satellite to model the auroral brightness and compared them with simultaneous FUV-WIC observations. They concluded to a good agreement between predicted and observed emission rates both in morphology and in intensity. *Gérard et al.* [2001] presented a comparison with SI12 observations for FAST and DMSP satellite overflights. This comparison showed an underestimation of the simulated SI12 response with the latitudinally integrated brightness. This discrepancy was tentatively attributed to high-energy protons above the 30 keV upper limit of the detectors, suggesting that higher energy protons could be important in producing this emission. *Coumans et al.* [2002] used in situ particle measurements from NOAA-15 and NOAA-16 satellites to check this possibility and assess the role of proton excitation of FUV emissions. The NOAA sets of detectors offers the advantage of observing electrons in the energy range 50 eV-1000 keV and protons from 50 eV to 800 keV, including all relevant auroral energies. The comparison was made for both WIC and SI12 data. Taking in consideration all possible sources of error, WIC observations showed agreement with in situ induced auroral brightness within 70% but SI12 observations coupled with simulation from the Monte Carlo code predicted proton fluxes twice as large as the in situ measurements [*Coumans et al.*, 2002]. Consequently, in this work, the proton energy fluxes are adjusted by a factor 2 to account for this overestimate of the SI12 derived proton flux.

[15] Using proton and electron transport models we can extract the proton and electron energy flux from auroral brightness images of respectively WIC and SI12 imagers. This procedure requires an hypothesis on the particle mean energy. The method to extract the precipitating electron energy flux is based on simulations with the GLOW model [*Solomon et al.*, 1988] extended to higher energies for auroral calculations [*Hubert et al.*, 2001]. This model based on a two-stream approximation calculates the auroral electron energy degradation and excitation by electron-induced process. The electron energy distribution is

assumed to be Maxwellian. The electron energy flux patterns are calculated from WIC observations, the electron transport code and the mean energy of electron. The proton energy transport code was described in detail by *Gérard et al.* [2000]. It is based on the direct Monte Carlo method [*Marov et al.*, 1997], which is a stochastic implementation of the solution of the Boltzmann equations, applied to the $H^+$ - H beam.

[16] The main limitation in this work is that the particle mean energy is not available. We consider the electron and proton mean energy patterns from *Hardy et al.* [1985, 1989]. These maps were computed from a statistical study using data collected over several years with detectors on board the Defense Meteorological Satellite Program (DMSP) satellites. The empirical model depends on the magnetic activity indexed by Kp. We discuss later the relevance of this approximation. For electrons, the combined WIC and SI13 simultaneous observations make it possible to evaluate the mean energy. A discussion of this method and some results are given in section 4.3.6. In a first step, since SI12 only images proton precipitation, we use the SI12 data to remove the proton contribution from the WIC and SI13 images. Then from the proton transport code and some assumption on the proton mean energy we calculate the proton energy flux maps from SI12 images. Another difficulty stems from the airglow contribution in the WIC and SI13 observations. This contribution must be removed before deriving the precipitating flux since we seek evaluation of the contribution of auroral particles only. This important step when using the WIC and SI13 observations to evaluate the electron mean energy is discussed in section 4.3.6. The background removal was done using the method described by *Immel et al.* [2000]. The airglow is determined from an average quiet-time airglow, individually for each instrument.

### 4.3.3 The conductance model

[17] From the electron and proton averaged energy and the energy flux maps, we developed a model to calculate the Hall and Pedersen conductances. The method can be separated in different steps. First the ionospheric ionization rate is evaluated from the incident particle characteristics. We then compute the electron and ion density profiles. The last step is the calculation of the conductances.

#### Ionization rates

[18] The calculation of the ionization height profiles requires the use of particle transport and energy degradation models described in the previous section. For electrons, the two-streams code calculates the secondary electron production rate from an incident energy flux and a mean energy of electrons, which is equivalent to the total ionization rate due to electrons. The calculations are made for a range of different mean energies and an incident energy flux of 1 $mW/m^2$. We multiply by the energy flux to evaluate the total ionization

profile due to precipitating electrons.

[19] For protons, the Monte Carlo code gives the primary electron production rate which can be introduced in the GLOW model to estimate the secondary electron population. The sum of primary and secondary electron production rate is the total ionization rate. The calculations are made for different energy bands with the central energy as particle mean energy and for an energy flux of 1 $mW/m^2$. The energy distribution of incident protons is assumed to be a Kappa function with $\kappa$=3.5, as recommended by *Hubert et al.* [2001]. The ionization profiles for each monoenergetic band are added to reconstruct the total contribution of the Kappa distribution. In this way, we obtain the total ionization profile for an energy flux of 1 $mW/m^2$ and multiply it by the actual incident energy flux to evaluate the total ionization profile due to precipitating protons. The total ionization height profile due to the total incident charged particle is the sum of the electron and proton ionization height profiles.

**Electron and ion density profiles**

[20] The electron density is derived from the continuity equations for the electron concentration $N_e$:

$$\frac{dN_e}{dt} = q_e - l_e - \mathrm{div}(N_e \mathbf{V}), \tag{4.17}$$

where $q_e$ is the electron production term, le is the electron loss term and the third term describes the change due to transport, if the transport processes result in a net drift velocity $\mathbf{V}$.The transport term is neglected since the diffusion time in the E and F1-regions exceeds the time between collisions. At steady state:

$$q_e = l_e = \bar{\alpha} N_e^2 \tag{4.18}$$

and

$$N_e = \sqrt{\frac{q_e}{\bar{\alpha}}}, \tag{4.19}$$

where $\bar{\alpha}$ is the effective recombination coefficient. The electron density height profile is calculated from equation 4.19 using the calculated electron production profile. The mean recombination coefficient is derived from

$$\bar{\alpha} = \frac{\sum_i \alpha_i(T_e) N_i}{N_e} \tag{4.20}$$

where i indicates $N_2^+$, $O_2^+$ or $NO^+$, $N_i$ is the density of the ion species i and $\alpha_i$ is the individual ion recombination coefficient. We use the ion proportion from the International Reference Atmosphere-1990 (IRI-90) model [*Bilitza*, 1990] to obtain the ion density $N_i$ from the electron density $N_e$. The ion recombination coefficients as a function of the electron temperature are from *Rees* [1989] and the electron temperature is taken from the MSIS-90

model atmosphere [*Hedin*, 1991] using the approximation that the electron temperature is equal to the neutral particle temperature.

### Conductivity profiles

[21] The Pedersen and Hall conductivities height profiles are computed from :

$$\sigma_P = \frac{N_e e}{B}\left(\frac{\nu_{en}\omega_e}{\nu_{en}^2+\omega_e^2} + \frac{\nu_{in}\omega_i}{\nu_{in}^2+\omega_i^2}\right) \tag{4.21}$$

$$\sigma_H = \frac{N_e e}{B}\left(\frac{\omega_e^2}{\nu_{en}^2+\omega_e^2} - \frac{\omega_i^2}{\nu_{in}^2+\omega_i^2}\right) \tag{4.22}$$

where conductivities are in $mho\ m^{-1}$ or in $S\ m^{-1}$, $e$ is the electron charge, $B$ the magnitude of the geomagnetic field, $N_e$ is the electron density, $\omega_i$ and $\omega_e$ the angular gyrofrequencies of respectively ions and electrons in the geomagnetic field. The ion gyrofrequency is calculated using an averaged mass evaluated for each altitude step. This mean ion mass is computed from the IRI-90 ion proportions and the mass of the ions. The geomagnetic field $B$ is calculated from the International Geomagnetic Reference Field model (IGRF-2000) [*Olsen et al.*, 2000] for the appropriate geographic position. $\nu_{in}$ and $\nu_{en}$ are the collision frequencies between the ion or the electron and the neutral species [*Rishbeth and Garriott*, 1969]. $\nu_{en}$ depends on the neutral density $N_n$ and on the temperature $T$ which is assumed equal for all species. The neutral atmosphere O, $O_2$ and $N_2$ densities are given by the MSIS-90 model atmosphere [*Hedin*, 1991].

[22] The conductivity profiles and the conductances are computed for electrons and protons of different mean energy for an incident energy flux of 1 $mW/m^2$. The profiles are calculated for a geographic latitude of 75°, a geographic longitude of 0° and for a geomagnetic index $A_p$=6, solar activity conditions $F_{10.7}$=191, $\bar{F}_{10.7}$=216 . We find that the Hall conductivity is maximum at lower altitudes than the Pedersen component both for incident electrons and protons and that the altitude of the maximum in $\sigma_P$ and $\sigma_H$ profiles decreases with increasing mean energy. A proton flux of 1 $mW/m^2$ of 1 keV mean energy induces a peak in the Pedersen conductivity around 140 km reaching $1.2\times10^{-4}$ $mho\ m^{-1}$, while at 30 keV, $\sigma_P$ peaks at 130 km with $2\times10^{-4}$ $mho\ m^{-1}$. The intensity of the Pedersen conductivity maximum does not vary as much with increasing mean energy as the maximum Hall conductivity. For electrons, with a mean energy of 1 keV, the maximum in $\sigma_P$ occurs near 130 km with $8\times10^{-5}$ $mho\ m^{-1}$ and in $\sigma_H$ around 120 km with $7\times10^{-5}$ $mho\ m^{-1}$. For $<E_{el}>$ = 4 keV, the Pedersen conductivity profiles peaks between 120 and 125 km and reaches $1.8\times10^{-4}$ $mho\ m^{-1}$ while the Hall conductivity profile peaks around 115 km with a value of $3\times10^{-4}$ $mho\ m^{-1}$. Finally for a higher mean energy the maximum of Pedersen conductivity decreases while still it increases for the Hall conductivity. For example, when $<E_{el}>$ = 20 keV, $\sigma_P \approx 7\times10^{-5}$ $mho\ m^{-1}$ around 120 km and $\sigma_H \approx 3.5\times10^{-4}$ $mho\ m^{-1}$ for altitudes less than 100 km.

[23] The Pedersen and Hall conductances are obtained by height integration of the respective conductivities between 80 and 200 km. They are shown in Figure 4.2 and Fig.-ure 4.3 respectively. Figure 4.2 shows that the Pedersen conductance reaches a maximum for electron mean energy between 2 and 4 keV and decreases for increasing energy, while the Hall conductance reaches a maximum for energy around 20 keV. For protons (Figure 4.3), the Pedersen conductivity varies slightly between 6 and 8 mho in the energy range of 1 keV to 40 keV. The Hall conductance increases in this energy range and reaches 9.5 mho for <Epr> = 40 keV.

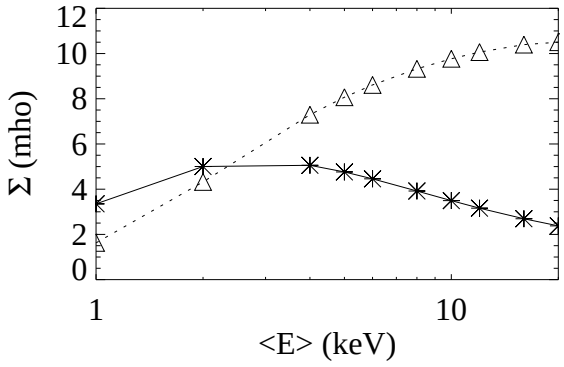


Figure 4.2: Hall and Pedersen conductances due to auroral electrons. Conductances are evaluated for an incident energy flux of 1 $mW/m^2$. The Pedersen conductance is presented with stars and the Hall conductance with triangles.

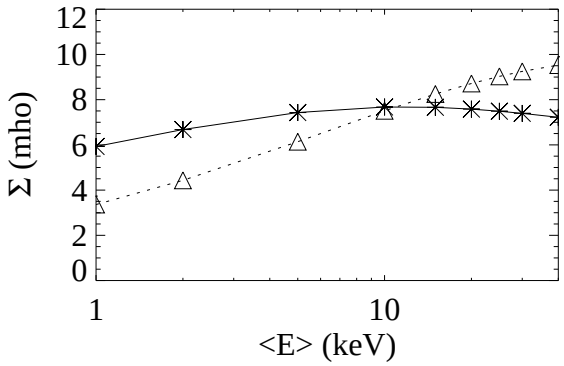


Figure 4.3: Hall and Pedersen conductances due to auroral protons Conductances are evaluated for an energy flux of 1 $mW/m^2$. The Pedersen conductance is presented with stars and the Hall conductance with triangles.

**Conductance maps**

[24] Hall and Pedersen conductivity height profiles and conductances are calculated for each pixel of the FUV images. We use the geomagnetic field B from the IGRF-2000 model [*Olsen et al.*, 2000] evaluated separately for each pixel of each analyzed FUV image. The MSIS input parameters are adapted to the geophysical and geographic conditions of each pixel of each observation.

[25] The EUV solar radiation also exerts an influence on the ionospheric conductances. The solar EUV radiation is the main source of ionization in the dayside ionosphere. The contribution of the EUV radiation is added in the auroral conductance maps. The determination of these empirical formulas is based on a photochemical equilibrium model of ionospheric conductivities and measurements of the Arecibo and Chatanika radars [*Rasmussen et al.*, 1988]

$$\Sigma_P^{sun} = \frac{4.5}{B}(1 - 0.85\nu^2)(1 + 0.15u + 0.05u^2) \tag{4.23}$$

$$\Sigma_H^{sun} = \frac{5.6}{B}(1 - 0.9\nu^2)(1 + 0.15u + 0.05u^2) \tag{4.24}$$

where $\nu = \chi/90^\circ$, $u = F_{10.7}/90$. The solar zenith angle is in degrees, the 10.7-cm solar flux is in units of $10^{-22}Wm^{-2}Hz^{-1}$, the magnetic field strength in gauss, and the conductance in mho. These formulas are normally applicable for $0 \leq \chi \geq 85^\circ$ and $70 \leq F_{10.7} \geq 250$ but for each pixel we extrapolate them for higher solar zenith angles. Knowing the solar zenith angle, we calculate the solar-EUV contribution to the conductances and combine it with particle-induced conductances using

$$\Sigma_{total} = \sqrt{\Sigma_{sun}^2 + \Sigma_{particles}^2} \tag{4.25}$$

The combination of two conductances produced by distinct sources is discussed in *Galand and Richmond* [2001]. *Wallis and Budzinski* [1981] estimated the error produced by this approximation to 7% for $\Sigma_P$ and 15% for $\Sigma_H$.

### 4.3.4 Sources of uncertainties

[26] The results of the conductivity model we developed can be compared with results from the literature. For electrons a comparison is made with results of the *Robinson et al.* [1987] conductance model. Figure 4.4 presents the ratio of *Robinson et al.* [1987]'s results to the results from our model as a function of the electron mean energy. Between 3 keV and 10 keV, differences are in a range of a few percent. Under 2 keV and above 10 keV the disagreement between the models can reach 30%. Statistical models of auroral electron precipitation [*Hardy et al.*, 1985] show that the mean energy of auroral electrons is usually between 1.5 and 10 keV where our model is quite close to *Robinson et al.* [1987] results.

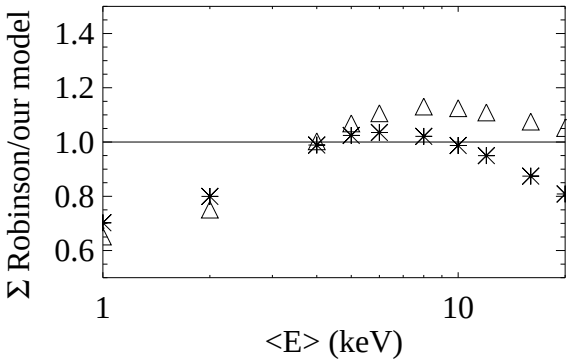


Figure 4.4: Ratio between conductances due to electrons calculated with *Robinson et al.* [1987]'s model and values calculated with this model. The ratio for the Pedersen conductance is presented with stars and the one for the Hall conductance with triangles.

[27] Our conductance model for protons was compared with *Galand and Richmond* [2001] using the same activity and geographic conditions. Our results are systematically 20 to 30% higher then *Galand and Richmond* [2001]'s. This is possibly due to the different assumptions on the distribution of the incident proton energy flux: *Galand and Richmond* [2001] assume the distribution to be Maxwellian while we use Kappa functions which appear to better represent the high-energy tail of protons.

**Uncertainties in the particle mean energy and energy flux.**

[28] Uncertainties are introduced by using empirical model of particle mean energy. The empirical model cannot show individual details of the instantaneous particle precipitation. This is another potential source of error of our model of conductivity. Since the energy flux computation used the mean energy values, some error is also introduced in the conductance calculation through the energy flux. *Meurant et al.* [2003b] evaluate the uncertainty on the electron mean energy and energy flux comparing them with in situ measurements, when the spatial distribution of the mean energy is computed from simultaneous WIC and SI13 images. *Meurant et al.* [2003b] showed that the precipitation characteristics derived from IMAGE-FUV data agreed with in situ measurements of two NOAA-16 passes within about 45%.

[29] To evaluate the error on the particles characteristics, the mean energy from *Hardy et al.* [1985, 1989]'s models and the energy flux deduced from FUV data were compared with in situ measurements of the FAST and DMSP satellites. Moreover, the electron mean energy computed from WIC and SI13 observation is also compared with in situ measurements and is discussed in section 4.3.6. Two comparisons are described next.

**Comparison with DMSP in situ measurements**

[30] Figure 4.5 shows an example of comparisons between the particle mean energies and energy fluxes evaluated from FUV and measured by DMSP F15 satellite for October 21, 2001. DMSP F15 is in a near circular, sun-synchronous, polar orbit. The on-board SSJ/4 detectors measure the flux of precipitating electrons and protons in the range of 32 eV to 30 keV in 20 channels. The total energy flux is computed by adding the flux from all channels and the mean energy is obtained by dividing the total energy flux by the total particle flux. The calculation of particle energy and flux from FUV data was described in section 4.3.2. The comparisons are made after following proper smoothing of the DMSP in situ flux measurements to account for the difference in spatial and time resolutions between in situ data and the FUV observation. Figures 4.5(b) and (c) show respectively comparisons of electron mean energy and energy flux while the DMSP-F15 satellite crossed the auroral oval. Characteristics of proton precipitation are shown in Figures 4.5 (d) and (e). In this example, the DMSP satellite crosses the auroral region in the prenoon sector from 2200 to 2130 MLT and from 44° to 71° MLAT. Figure 4.5 (a) shows the track of DMSP-F15 mapped to 120 km reported on the WIC image at 2335:29 UT.

[31] In Figure 4.5 (d), the proton mean energies measured by DMSP present a maximum around 25 keV between 2336:50 and 2337:00 UT. The values are quite constant, around 15 keV, between 2337:00 and 2339:40 UT. After 2339:40 UT the proton mean energy values reach 30 keV. The mean energies from *Hardy et al.* [1989]'s model are in the same range of value but do not show two maxima. When the measured mean energy is about 15 keV around 2338:20 UT, the empirical model overestimates it and indicates a maximum energy of 25 keV. The disagreement between the empirical model and the in situ measurements in this region is 66%. The comparison of the proton energy flux measured by DMSP satellite and evaluated from the *Hardy et al.* [1989] mean energy and SI12 observations is plotted in Figure 4.5 (e). The maximum in the flux computed from FUV data is shifted in comparison with the measurements. Moreover, the measured energy flux is overestimated during the time range 2337:30 and 2339:20 UT. This is probably due in part to the difference of spatial and time resolutions of instruments, and in part to the disagreement between used energy and real energy in this time range. The global agreement between the energy fluxes measured in situ and evaluated from FUV observation is ∼19%.

[32] For electrons, Figure 4.5 (b) shows that the *Hardy et al.* [1985] statistical mean energies are in good agreement with the DMSP measurements. The values are in the same range: around 0 and 2 keV between 2336:00 and 2338:20 and between 2 keV and 5 keV after. Around 2339:50 and 2340:40 measurements show respectively a minimum and a maximum in the energy that the statistical model cannot present. In Figure 4.5 (c) the energy fluxes computed from the statistical mean energy and the WIC data underestimate the DMSP energy flux between 2338:10 and 2339:30. In this case, the error is of a factor 2. The agreement is good elsewhere along the trajectory. The dash dot dot line in Figure 4.5

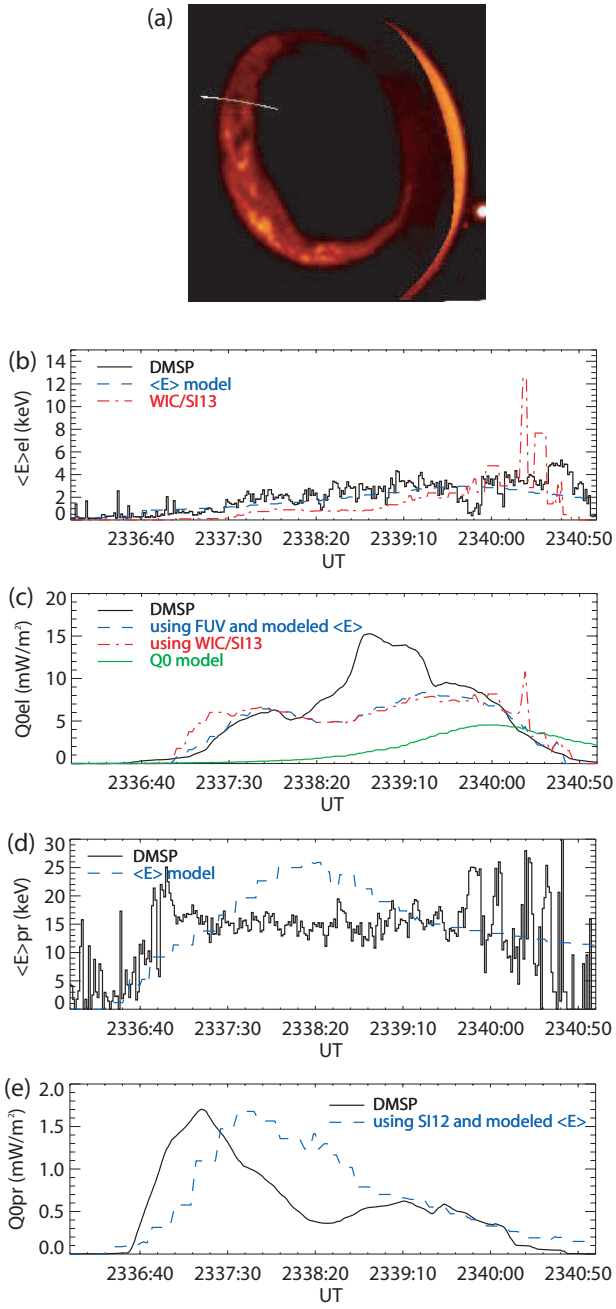


Figure 4.5: Comparison between the particle precipitation characteristics evaluated from the FUV data and measured by the DMSP F15 satellite for 21 October, 2001. (a) The mapped position of the DMSP F15 satellite is drawn on the WIC image. (b) The electron mean energy from *Hardy et al.* [1985] (blue curve) is compared with mean energy in situ measurement (black curve) and with mean energy evaluated from the ratio between WIC and SI13 images (red curve). (c) The electron energy flux evaluated using FUV and *Hardy et al.* [1985] mean energy (blue curve) and the one evaluated using the mean energy from WIC/SI13 ratio (red curve) are compared with DMSP energy flux measurement (black curve) and with *Hardy et al.* [1985] electron energy flux (green curve). (d) The proton mean energy from *Hardy et al.* [1991] (blue curve) is compared with the DMSP proton mean energy (black curve). (e) The energy flux evaluated from FUV - SI12 and the *Hardy et al.* [1991] mean energy (blue curve) is compared with in situ measurement (black curve).

(c) shows the electron energy flux from *Hardy et al.* [1985]'s model. The morphology of the precipitation is very different when using the statistical model's outputs. The statistical flux is nearly null until 2338:10 UT, while DMSP measurements show that it reaches a first maximum at 6 $mW/m^2$ around 2338:00 UT. The statistical flux increases up to 5 $mW/m^2$ at 2340:00 and then decreases while in situ measurements peaks up to 15 $mW/m^2$ at 2338:50 UT and decreases down to 0 at 2341:00 UT. This comparison shows that the *Hardy et al.* [1985] energy flux model is not a good estimation of the instantaneous energy flux.

**Comparison with FAST in situ measurements**

[33] In a second step, we compare the mean energy measurements determined from the FAST satellite detectors with the statistical model outputs for 23 December, 2000. Figures 4.6 (b) and (c) present the comparison for electron and for proton mean energies respectively. In this example, the FAST satellite crosses the auroral oval in the dawn sector from 0418 to 0830 MLT between 57° and 81° MLAT. Figure 4.6 (a) shows the track of the FAST satellite mapped to 120 km traced on the WIC image obtained at 2100 UT.

[34] The comparison of the electron mean energy (Figure 4.6 (b)) shows that the agreement between the *Hardy et al.* [1989]'s model mean energies and the in situ measurements is very good. The electron mean energies measured by FAST and computed from the statistical model follow the same evolution. Around 2102:30 UT the maximum values in both measured and modeled energies are about 4.5 keV. In the region crossed after 2105:50 UT, both energies are under 1 keV, even if the measurements show some very local peaks. Globally the statistical energy is 35% higher then the FAST measurement even if, very locally, the disagreement can reach up to 100%.

[35] For protons, Figure 4.6 (c) shows that globally the empirical model and the measurements are in the same range. Around 2103:20 UT the statistical mean energy reaches 11 keV while the in situ measurements are equal to 7 keV. After 2112:30 UT the measured energy is null while the statistical energy increases. However, this is of no consequence on the conductance calculation because the associated energy flux is negligible. The final conductance is very low so that the relative error is not so important.

**Uncertainties in the conductance model**

[36] We now try to evaluate the error on the conductance calculation introduced by the uncertainties on the particle mean energy. For electrons, we noted in the previous section that the error can be locally very important. As an example, we consider an error of 50% and calculate the propagated error on conductance. Figure 4.2 indicates that an error of ±50% at 1 keV induces an error of +33% or -57% on the Pedersen conductance, and +89% or -76% on the Hall conductance evaluation. If the electron mean energy is 5 keV, the error is -15% and +9% for Pedersen conductance, and +14% and -34% for Hall conductance.

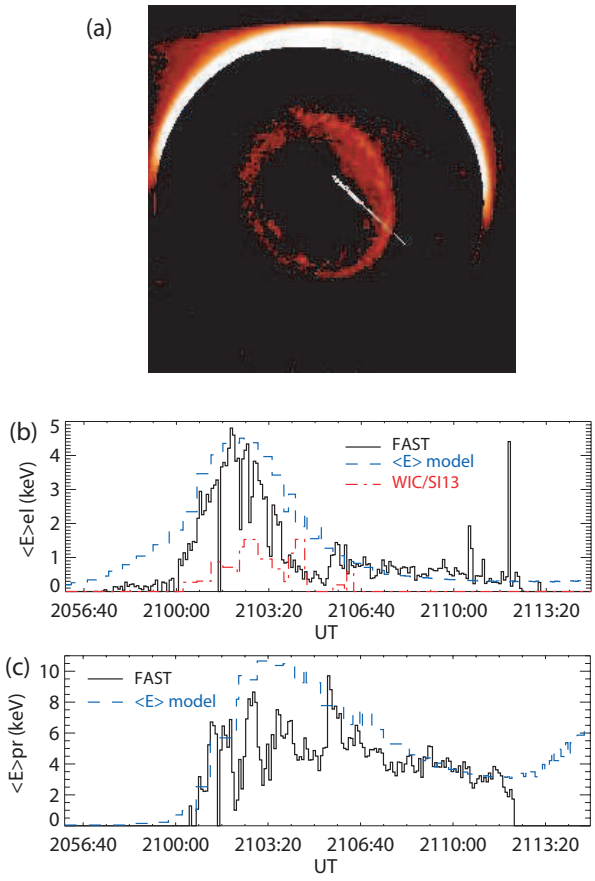


Figure 4.6: Comparison between the particle precipitation characteristics evaluated from the FUV data and measured by the FAST satellite for 23 December, 2000. (a) The mapped position of the FAST satellite is drawn on the WIC image. (b) The electron mean energy from *Hardy et al.* [1985] empirical model (blue curve) is compared with mean energy in situ measurement (black curve) and with mean energy evaluated from the ratio between WIC and SI13 images (red curve). (c) The proton mean energy from *Hardy et al.* [1991] (blue curve) is compared with the FAST proton mean energy (black curve).

At 10 keV, the error is between -20% and +36% for Pedersen conductance and +6% and -17% for Hall conductance.

[37] The error on the proton mean energy evaluated from comparison between in situ measurements and the statistical model outputs for the cases described before is around 65%. Using Figure 4.3, it is possible to evaluate the error introduced by the method. If we use 10 keV while the real mean energy is 30 keV, the Pedersen conductance is overestimated by 4% and the Hall conductance underestimated by 19%. Using 50 keV for calculation while the proton mean energy is 30 keV leads to an underestimation of the Pedersen conductance by 4% and an overestimation of the Hall conductance by 5%. For energy around 30 keV an error of 66% in the mean energy introduces an error of 19% at most in the conductance determination. For lower energies, the relative error is higher. For example, using $<E_P>$=1 keV in calculation while the proton mean energy is 3 keV introduces a 16% error in the Pedersen conductance and a 35% error in the calculated Hall conductance. Generally, the uncertainty on the particle mean energy leads to a larger error in the Hall conductance determination than in the Pedersen conductance, both for electrons and protons.

[38] An uncertainty in the particle mean energy introduces an error in the energy flux which can influence the conductance estimation. As we discussed in the comparison with DMSP measurements (firt subsection of section 4.3.4) the error in the proton energy flux is around 19%. In the comparison in section 4.3.4 the discrepancy is locally more important.

### Influence of geomagnetic activity

[39] The particle energy transport models uses a MSIS-90 [*Hedin*, 1991] atmosphere with fixed geomagnetic and activity level conditions. The MSIS parameters for 24 December, 2000, 1630 UT, a latitude of 65°, a longitude of 0°, solar maximum conditions with $F_{10.7} = 205$, $\bar{F}_{10.7} = 216$, and a geomagnetic index Ap=6. We now analyze the influence on the conductance evaluation of the use of fixed atmospheric conditions. For protons, the Monte Carlo code was run for four different situations encompassing a range of solar activity conditions: (i) Ap = 5, $F_{10.7} = \bar{F}_{10.7} = 200$, (ii) Ap = 40, $F_{10.7} = \bar{F}_{10.7} = 200$, (iii) Ap = 5, $F_{10.7} = \bar{F}_{10.7} = 80$, and (iv) Ap = 20, $F_{10.7} = \bar{F}_{10.7} = 80$. The other parameters were fixed to 24 December, 2000, 0000 UT, a latitude of 60°, a longitude of 0° for a monoenergetic proton incident beam of 1 $mW/m^2$ with an energy of 10 keV. Cases (i) and (ii) present solar maximum conditions while cases (iii) and (iv) are characteristic of the solar minimum activity. Using condition of case (i), the calculated conductances were: $\Sigma_P = 8.71$ mho and $\Sigma_H = 5.74$ mho. An increase of the Ap index for solar maximum conditions (case (ii)) gives $\Sigma_P = 8.63$ mho and $\Sigma_H = 5.13$ mho which means a decrease of 0.8% for the Pedersen conductance and of 10% for the Hall conductance. An increase of the Ap index for solar minimum conditions (case (iv) compared with case (iii)) induces respectively an increase of 0.3% and a decrease of 7.8% of the Pedersen and Hall conductances. A change in the $F_{10.7}$ index (case (iii) compared with case (i)) produces a variation of 5.1% for Pedersen

conductance and 11.6% for Hall conductance. We conclude that for protons the variation of solar and geomagnetic activity introduces effects of ∼5% and 12% for Pedersen and Hall conductances. For electrons a similar study shows that the maximum uncertainties associated with the Ap index and/or the $F_1 0.7$ index is ∼11% for the Pedersen conductance and around 2% for the Hall conductance.

[40] This discussion presented the uncertainties sources that appear in our method of conductance calculation. The use of averaged solar activity and geomagnetic conditions induced a maximal error of 12% while the uncertainty on the particle mean energy can induce a more important error. This is the main source of error in the conductance calculation. In section 4.3.6, we describe another method to obtain the instantaneous electron mean energy and we discuss the results.

### 4.3.5 Global conductance maps

[41] In this section, we present 4 selected cases with different Kp index value, observed in the northern hemisphere. We illustrate different auroral activity levels at different seasons. We first present instantaneous conductance maps calculated for 12 August, 2000 and 23 December, 2000. The specificity of this work is that instantaneous conductance maps are evaluated each 2 minutes so that the evolution of conductances during substorms can be followed. It is thus possible to assess the evolution of the role of protons in the conductances. In a second step we present the evolution of conductances in different magnetic sectors during two selected substorms which occurred on 27 November, 2000 and 28 April, 2001. For each case and for both conductances, we calculate the increase in conductance when protons are considered in comparison with a pure electron precipitation assumption.

#### 12 August, 2000

[42] The first example shown in Plate 4.7 occurred during the expansion phase of a summer substorm (Kp = 8) on 12 August, 2000 at 0832 UT. The top panels show the calculated Pedersen (Plate 4.7a) and Hall (Plate 4.7b) conductances induced by auroral electron precipitation. Central panels show Pedersen (Plate 4.7c) and Hall (Plate 4.7d) conductances induced by protons. Bottom panel (Plate 4.7e and Plate 4.7f) shows conductance maps induced by auroral particles and the solar EUV contribution. Adding the proton contribution in the conductance calculation globally increases the Hall conductance by 5.5% and the Pedersen conductance by 4.8% in comparison with the calculation for electrons only. In the sector between 2100 and 2400 MLT, the proton contribution is ∼8% for $\Sigma_P$ and $\Sigma_H$, while in the post noon sector protons contribute for less then % in both $\Sigma_P$ and $\Sigma_H$. The EUV contribution to the conductances can be more important than the proton contribution during this summer substorm. The maximum in the EUV contribution to the Hall conductance near 1200 MLT and 55° MLAT is ∼13 mho, while the maximum in the Hall

conductance due to protons is less than 6 mho. The Hall conductance can locally reach 40 mho and the Pedersen conductance ∼28 mho.

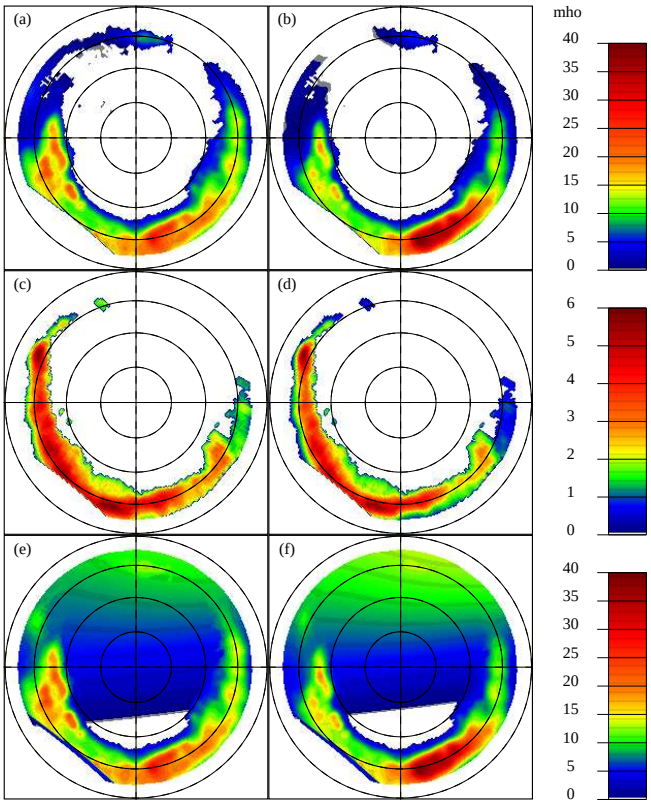


Plate 4.7: Conductance maps for 12 August 2000, 08:32 UT corresponding to a summer substorm (Kp =8). Panels (a) and (b) show, respectively, Pedersen and Hall conductances induced by auroral electron precipitation. Panels (c) and (d) show, respectively, Pedersen and Hall conductances induced by protons and panel (e) and (f) show conductance maps induced by both auroral particles and EUV solar radiation. Circles show 50°, 60°, 70° and 80° MLAT. The local midnight is located downward.

### 23 December, 2000

[43] The second example (Plate 4.8) is a winter situation with a low magnetic activity level (Kp = 2) which occurred on 23 December, 2000 at 2104 UT. It corresponds to a quiet phase between two weak substorms. The particle mean energies were locally validated by comparison with FAST in situ measurements (described in section 4.3.4). A feature of this case, fairly typical of non substorm situation, is that the proton contribution to both

Hall and Pedersen conductances is maximum in the dusk sector, whereas the electron contribution is close to zero. The maximum in the electron induced conductances is located near 0700 MLT in the dawn sector. Electron precipitation is relatively important in the entire prenoon sector. The maximum in the Hall and Pedersen conductances induced by electrons are 8.2 mho and 5.3 mho respectively while the maximum in conductance induced by protons are 3.1 mho and 3 mho respectively. We note that the conductance values are small in this case. Globally over the entire auroral oval, the protons increase the Hall conductance by 40% and the Pedersen conductance by 53%, mostly as a consequence of the effect of proton precipitation in the dusk sector. In comparison to the substorm case discussed before, the proton contribution in conductances is globally significantly more important.

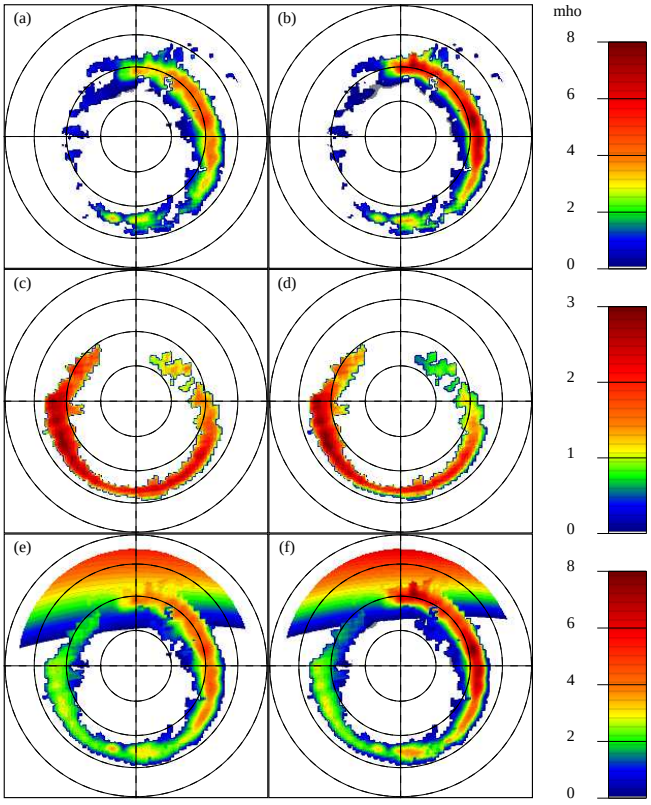


Plate 4.8: Idem Plate 4.7 for 23 December 2000, 21:04 UT with Kp=2. Circles show 50°, 60°, 70° and 80° MLAT. The local midnight is located downward.

[44] Another example (not shown) of quiet winter situation corresponding to 1 November, 2000 at 1701 UT has been analyzed. The Kp index for this period was equal to 2. In this example, the auroral injection is close to zero in the dayside and weak in the nightside. The

maximum in the Pedersen conductance map due to auroral particles is 7.0 mho and 7.3 mho in the Hall conductance map. Adding the contribution of proton in the conductance calculation globally increases the Hall and the Pedersen conductances by 13% in comparison with the calculation with electrons only.

[45] During periods of quiet magnetic activity the relative contribution of auroral protons in conductances can be much more important than during active period. As an example, during the substorm of 12 August, 2000 their contribution reached a few percent, while in the low Kp example, it can reach more than 50% and, it is even close to 100% locally. This result reflects that the relative contribution of the protons to the auroral hemispheric power is larger during quiet time periods.

[46] To test the sensitivity of the method, conductance maps were constructed for the case of 23 December, 2000 using a constant particle mean energies for all FUV pixels instead of the statistical mean energies. Plate 4.9 shows the result using $<E>_{el}$ = 6.4 keV and $<E>_{pr}$ = 8 keV. The value for electron is chosen as the maximal value of the prenoon sector average energy for Kp =3 in the *Hardy et al.* [1987]'s empirical precipitation model. For protons a mean energy of 8 keV is a plausible value for low activity conditions according to *Hardy et al.* [1991]. The results (Plate 4.9b) show an increase in the Hall conductance maximum of about 20% for the electron contribution when using 6.4 keV instead of the statistical average energy (Plate 4.8b). On the poleward limit of the auroral zone in the morning sector, the Hall conductance value is around 5 or 6 mho, while using the statistical mean energies the values are around 1 mho. Thus when the constant energy case is very different from the statistical energy, the differences in the Hall conductance computation can be locally very important. This effect was discussed in section 4.3.4. The effects on the Pedersen conductance computation are much less significant. The maximum in Pedersen conductance (Plate 4.9a) has a value nearly identical using statistical average energy (Plate 4.8a) and the morphology of the induced conductance is similar. The calculation of conductances induced by proton precipitation with a constant mean energy is presented in Plates 4.9 c and d. Comparing with Plates 4.8 c and d, the conductances values globally decrease when using $<E>_{pr}$ = 8 keV and the morphology of the pattern also exhibits some variations. With the statistical mean energy, the maximum in both conductance patterns is near 2000 MLT and 65.5° MLAT. With the constant energy, this value decreases by 46% for Pedersen and 30% for Hall conductance. Moreover the location of the maximum in the conductance is changed. When using the constant energy, the peak in conductances is around 0325 MLT and 65.4° MLAT. As already mentioned in section 4.3.4, the uncertainties on the mean energy is the main source of errors of the method and can induce important errors. Globally the conductance values are close to each other and the morphology is quite similar for both cases.

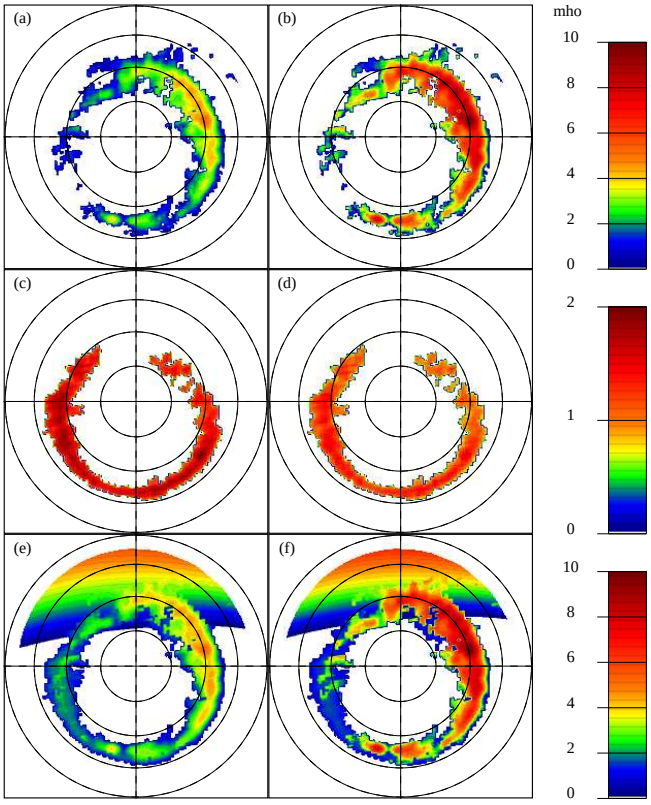


Plate 4.9: Conductance maps for 23 December 2000, 21:04 UT (same as Plate **??**) using constant particle mean energy over the entire auroral region. $< E >_{el} = 6.4$ keV and $< E >_{pr} = 8$ keV. Circles show 50°, 60°, 70° and 80° MLAT. The local midnight is located downward.

**27 November, 2000**

[47] A specific advantage of this approach is that the evolution of conductances during substorms can be analyzed. On 27 November, 2000, two substorms followed each other: the first one started around 0355 UT and the second one around 0725 UT. The events were described by *Hubert et al.* [2002], who calculated the evolution of the hemispheric power and related the auroral events to solar wind variations detected by the ACE satellite. We consider the second substorm only. The onset was observed by the three FUV instruments at ∼0725 UT near 0000 MLT. It is related to a sudden increase in the solar wind density. The WIC observations show that for electrons, the substorm expansion extended both duskward and dawnward. The proton aurora observed by SI12 predominantly extended dawnward with a less significant duskward extension. *Hubert et al.* [2002] showed that the contribution of proton in the hemispheric power reached 45% before the substorm onset decreasing under 15% after breakup. The minimum in the proton contribution took place around 0830 UT when the total hemispheric power was maximum. The instantaneous Hall and Pedersen conductance maps were evaluated each 2 or 4 minutes before the onset and during the beginning of the substorm and then each 10 or 20 minutes during the substorm development. The evolution of conductances averaged in different MLAT-MLT sectors are illustrated in Figures 4.10, 4.11 and 4.12. The time evolution of the average conductances was calculated over the entire north polar region (Figure 4.10). It presents two main peaks: a first one between 0755 and 0806 UT and a second one around 0836 UT which is as important as the first one for Pedersen conductance, reaching 3.6 mho, while for Hall conductance the first maximum was the highest, reaching 3.3 mho. The contribution of electrons and protons is ∼1 mho for both conductances before the visually estimated onset (∼0725 UT). The calculation of conductances including protons is 60% higher then using electrons only, before the onset. It decreases to ∼20% during the substorm. After 0900 UT, conductances due to electrons decreased while the value of the ratio $(\Sigma_{aur} - \Sigma_{el})/\Sigma_{el}$ increased. In the sector between 2330 and 0030 MLT and 60° and 65° MLAT (Figure 4.11), the increase of conductances due to electron and proton around 0725 UT corresponds to the substorm onset which was visually identified from the FUV observations. The averaged Pedersen conductance due to auroral particles reaches 19.5 mho in that sector and averaged Hall conductance around 21 mho. Between ∼0700 and ∼0711 UT, the contributions of both conductances remain quite constant. Between ∼0711 UT and ∼0725 UT conductances in this sector decrease and reach a minimum just before the onset. At that time the contribution of proton in conductances is maximum. Before ∼0711 UT including the protons in conductances evaluation increases the Pedersen conductance by about 65% and the Hall conductance by about 55%. Just before the substorm onset, the Pedersen conductance increases by about 95% when adding the proton contribution, and the Hall conductance by about 80%. After 0725 UT, the proton precipitation increase both conductances by ∼10% and after 0800 UT this contribution decreases below 5%. Figure 4.12 shows the evolution of conductances in the dusk and night sector. The electron induced conductances start increasing at 0746 UT when the substorm activity reaches that sector. Before 0746 UT the increase in both conductances due to protons is between 100 and 50%

but it decreases under 30% after 0746 UT and under 20% after 0820 UT.

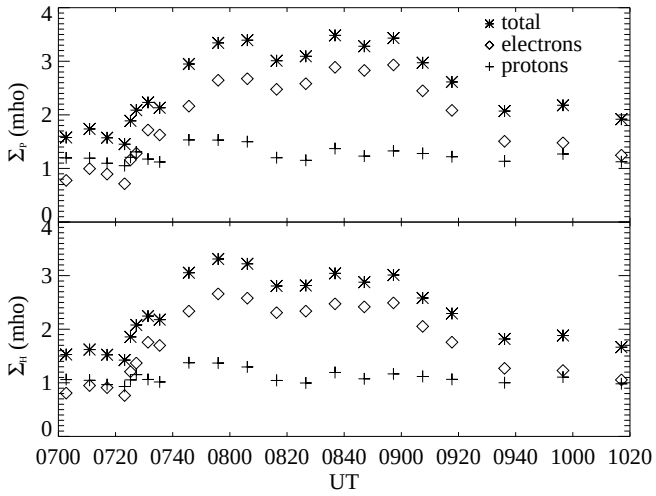


Figure 4.10: Time evolution of the Pedersen (top panel) and Hall (bottom panel) conductances during a substorm which occurred on 27 November, 2000. The conductances are averaged over all the auroral region.

**28 April, 2001**

[48] The example of 28 April, 2001 illustrates a particular feature. Before 0500 UT the measurements of the FUV instruments were close to their sensitivity threshold. Auroral activity increased after 0500 UT and SI12 imaged a sudden brightening in the postnoon sector. This signal was also observed by WIC and much less intensely by SI13. At 0508 UT a very bright spot was observed by SI12 at $\sim 74^{\circ}$ MLAT and 1415 MLT, its luminosity gradually decreased and at 0512 UT the spot disappeared. At 0521 UT the spot reappeared in the SI12 images at the same location in the same time as the auroral signal intensified near 0000 MLT. Two minutes later, the spot had vanished while the midnight sector activity was still strong. A spot was also observed with the WIC and SI13 instruments at the same location and at the same time. In view of the intensity of the signal observed by SI12, it appears that the spot in the postnoon sector is essentially due to protons. The evaluation of conductance maps from FUV observations at 0508 UT shows that the maximum of the Pedersen and Hall conductances induced by protons occurred in the postnoon sector and reached 7.7 mho and 5.9 mho respectively while the maximum in the Pedersen conductance due to electron occurs around 1930 MLT and $73^{\circ}$ MLAT and reached 8 mho (5 mho for Hall conductance at the same location). The evolution of conductances in the postnoon sector is shown in Figure 4.13. The increase in both conductances induced by protons at 0500 UT coincides with the onset of the substorm. The conductance due to protons averaged

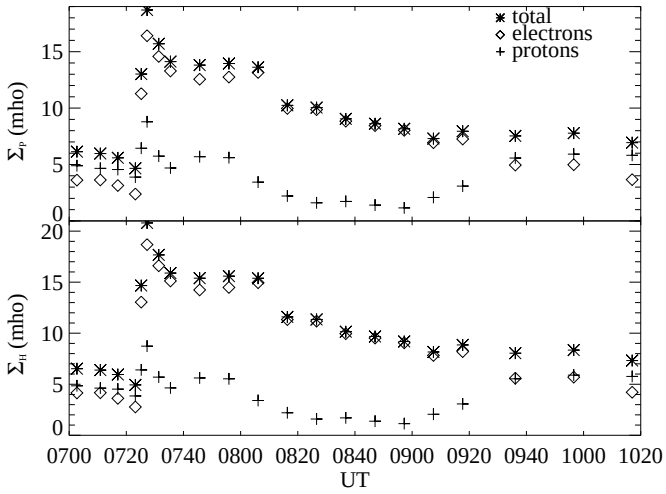


Figure 4.11: idem Figure 4.10. In this example, the conductances are averaged over the midnight sector (MLAT between 60° and 65° and MLT between 2330 and 0030).

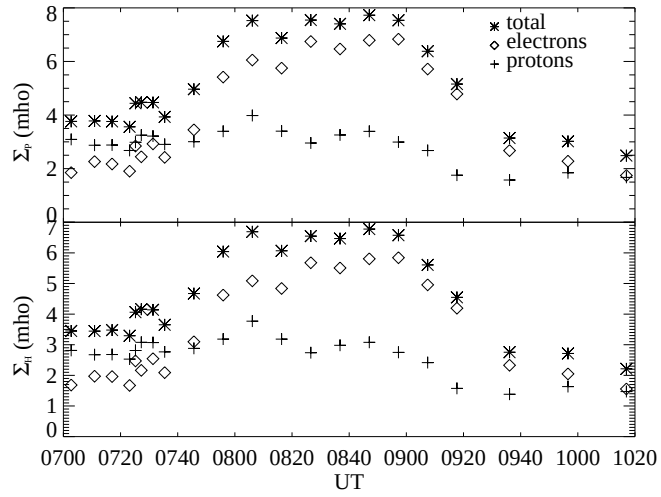


Figure 4.12: idem Figure 4.10 with conductances averaged over the dusk sector (MLAT between 60° and 70° and MLT between 1800 and 2100).

over the sector between 71° and 77° MLAT and 1400 and 1430 MLT peaked a first time at 0508UT up to 5.6 mho for Pedersen and 4 mho for Hall conductance and a second time at 0521 UT up to 6 mho for Pedersen and 4.6 mho for Hall conductances. After 0521 UT, the Pedersen and Hall proton induced conductances are around 2 and 1.5 mho respectively. During the event, the averaged Pedersen and Hall conductances due to electrons in the postnoon sector remained quite constant, respectively around 0.6 mho and 0.2 mho. The total value of conductances due to both types of particles is very close to the value of the proton induced component in the postnoon sector. This clearly illustrates that neglecting protons in this particular case would induce a very large error in conductances evaluation in this sector.

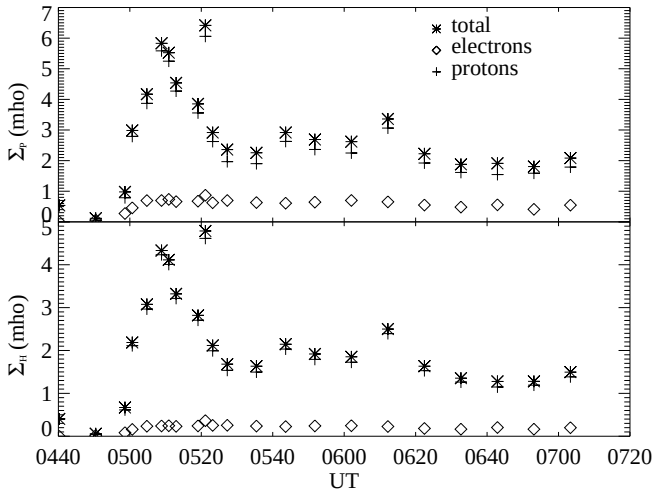


Figure 4.13: Time evolution of the Pedersen (top panel) and Hall (bottom panel) conductances during a substorm which occurred on 28 April, 2001. The conductances are averaged over the sector between 71° and 77° MLAT and 1400 and 1430 MLT.

### 4.3.6 Electron mean energy from the WIC to SI13 ratio

[49] Using the electron transport models described in section 4.3.2, the electron mean energy can be derived from WIC and SI13 observations. The method to determine the mean electron energy and energy flux characteristics from FUV observations and the uncertainties associated with this method were thoroughly described by *Hubert et al.* [2002] and *Meurant et al.* [2003b]. The determination of the electron mean energy is based on the ratio between WIC and SI13 images. The WIC/SI13 ratio was modeled as a function of the energy of the precipitating electrons using the GLOW model [*Solomon et al.*, 1988] extended to higher energies for auroral calculations [*Hubert et al.*, 2001].

[50] In the calculation of conductance maps, the *Hardy et al.* [1985] electron mean energy can be replaced by the mean energy evaluated from the WIC to SI13 ratio. An upper threshold of the electron mean energy was fixed to 15 keV. Uncertainties are associated with this method. *Meurant et al.* [2003b] compared the electron energy determined using the WIC/SI13 ratio with the electron energy measured by the detectors on board the NOAA-16 satellite and found agreement within about 45%. In addition, we compared the FUV derived electron mean energy with the DMSP and FAST in situ measurements. In Figure 4.5 (b) the electron mean energy deduced from the WIC/SI13 ratio is compared with the *Hardy et al.* [1985]'s model and DMSP measurement. In the region between 2336:00 and 2339:40 UT the electron mean energy from the WIC/SI13 ratio underestimates the in situ measurement. Between 2337:30 and 23339:40 UT the disagreement is about 50% or more. After 2340:00 UT the FUV extracted energy presents two maxima: a first one peaks up to 12.5 keV and the second one up to 7.5 keV, which are not measured by DMSP. Such peaks are generally induced by the background signal subtraction in the WIC data. However, in this case, DMSP crossed the auroral oval in the night sector. The WIC signal is thus not contaminated by dayglow signal. Figure 4.5 (c) illustrates the influence of the use of FUV extracted electron mean energy on the calculated energy flux. Between 2337:40 UT and 2340:10 UT the energy flux from the mean energy of *Hardy et al.* [1987]'s model and from the WIC/SI13 ratio are very similar. Near 2340:20 UT the energy flux shows a maximum up to 11 $mW/m^2$ which is induced by the peak in mean energy. The spatial resolution of the in situ data is much higher than the FUV instrumental resolution and therefore, in situ data were properly smoothed to account for this difference. Nevertheless a difference between the theoretical and effective value may stem from the fact that in situ measurements are made along the orbital track, while FUV globally observes the auroral region. Each FUV pixel includes contributions from emissions adjacent to the low latitude satellite track owing to its 2-3 pixel wide point spread function.

[51] Figure 4.6 (b) showed the comparison between the electron mean energy calculated from FUV observations with the FAST measurements and the values from *Hardy et al.* [1985]. Between 2100:00 and 2104:10 UT, the measured and the FUV evaluated mean energies follow the same evolution: they first increase until 2102:10 UT and then decrease. However, the maximum energy in the measurements is about three times larger than the calculated one.

[52] The WIC/SI13 ratio is a good global indicator of the morphology of the energy of auroral precipitation. The mean energy computed from the ratio is a good way to represent the spatial and the time evolution of the auroral electron precipitation. Fast and local fluctuations can be determined with the energy computed from this ratio while the *Hardy et al.* [1985]'s statistical mean energy cannot represent them. As discussed in section 4.3.4, the uncertainties in the mean energy is the main source of error in the calculation of conductances.

[53] Plates 4.14 a and b show the electron induced conductance maps evaluated using the

WIC/SI13 ratio to calculate the mean energy for the case of 23 December, 2000. The peak in the Hall conductance reaches 17 mho and is thus globally higher than when calculated with the statistical mean energy (Plate 4.8b). The WIC observation shows two local maxima in the auroral precipitation in the sector between 0000 and 0600 MLT. They create two maxima in the Hall conductance not present in Plate 4.8b. The Pedersen conductance maps (Plate 4.14a and Plate 4.8a) induced by precipitating electrons show that the use of the mean energy computed from the FUV observations (4.9 mho) or statistical mean energy (5.4 mho) gives results quite similar. As discussed in section **??**, the error induced by the electron mean energy value is larger for the Hall than for the Pedersen conductance.

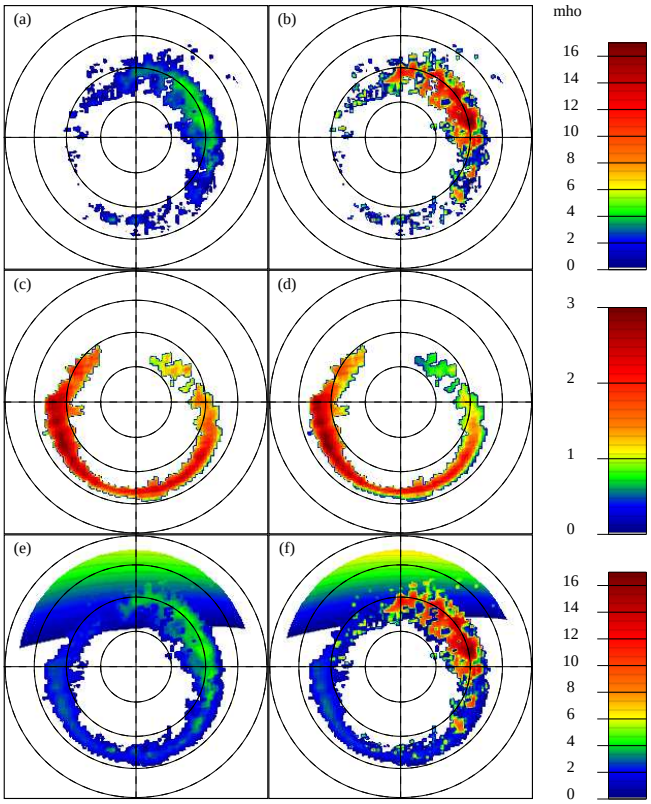


Plate 4.14: Conductance maps for 23 December 2000 21:04 UT (same as Plate 4.9) using electron mean energy computed from the ratio of WIC and SI13 simultaneous observations. Circles show 50°, 60°, 70° and 80° MLAT. The local midnight is located downward.

[54] The upper limit set for the maximum mean energy is also a source of uncertainties. We evaluated the error on the conductances when the electron mean energy is limited to 15 keV. If the mean energy was 20 keV, the error induced by the threshold would be 1.4% for the Hall and ∼18% for the Pedersen conductance. For increasing mean energy, the error

increases for the Pedersen conductance and remains around 1.5% for the Hall conductance.

### 4.3.7 Discussion and conclusions

[55] We developed a model using IMAGE-FUV observations to evaluate instantaneous ionospheric conductivity profiles and conductances induced by auroral precipitation on a global scale. The instantaneous Hall and Pedersen conductances produced by precipitating protons are computed on a global scale. The model requires assumptions on the auroral particles mean energy. We use the statistical models *Hardy et al.* [1985] for the electron and *Hardy et al.* [1989] for the proton mean energies. During quiet periods the statistical model values are close to the actual particle mean energies. However, during substorms when the precipitation changes rapidly, the instantaneous variations in the auroral precipitation are not well represented by these statistical models. In these cases the ratio of simultaneous WIC and SI13 images may be used as an indicator of the electron energy. The morphology is then better represented but in some cases the quantitative values of the computed conductances are too high. The validity of using the precipitating particle characteristics from statistical model was tested by comparing the particle energy flux and mean energy evaluated from FUV observations with in situ measurements from the FAST and DMSP satellites. Comparisons show that the mean energies from *Hardy et al.* [1985, 1989]'s models are reasonably close to the in situ measurements. The electron mean energy deduced from the WIC to SI13 ratio often provides a better morphology than the statistical mean energy, meaning that the evolution of the mean energy and the energy flux along the low altitude satellite track are better reproduced. However the values are often overestimated, presumably as a consequence of the large sensitivity of the method to the background subtraction in the images.

[56] As we discussed in section 4.3.4, the main source of error in the conductance calculation is due to the uncertainties on the particle mean energy. Globally, the error in the Pedersen conductance is smaller than the one in the Hall conductance. Our calculated Pedersen conductance is thus more reliable than our calculated Hall conductance.

[57] The application of the conductivity model to different cases for various magnetic activity level shows that the contribution of auroral protons in the total ionospheric conductances induced by auroral precipitation strongly depends on the location and mostly on the geomagnetic activity level. The contribution of protons is significant during quiet time periods. During substorms, the increase of conductances due to protons is globally less than 6% even though locally it can reach ∼10%. During quiet time periods, the increase due to proton can reach globally up to 50% and locally nearly 100%. In a study based on POLAR UVI images [*Liou et al.*, 2001] protons were considered as electrons as the UVI imager does not offer the possibility to discriminate between the two types of particle. We have calculated conductances without proton contribution in WIC and SI13 signals from two observations with different magnetic activity conditions. For the low Kp case, the Pedersen

and Hall conductances calculated discriminating between electron and proton contribution ($\Sigma_{p+e}$) can locally be 10 times higher than conductances calculated considering protons as electrons ($\Sigma_{p=e}$), mainly in the dusk sector and for the equatorward limit of the auroral region, which reflects that the proton auroral oval is shifted equatorward of the electron oval in the dusk sector. For the case with higher Kp, the region where the difference is a factor 10 or more is much smaller. Over nearly all the auroral region, $\Sigma_{p=e}$ is nearly identical to $\Sigma_{p+e}$. This was expected during substorms as the electron precipitation is large.

[58] The variations of auroral electron precipitation with season [*Liou et al.*, 2001] or sunlight conditions [*Newell et al.*, 1996b] were interpreted in terms of an ionospheric conductivity feedback mechanism [*Atkinson*, 1970; *Sato*, 1978; *Lysak*, 1986]. The feedback conductivity mechanism assumed that the ionospheric 'background conductance' plays a role in the creation of the aurora. The ionosphere supports a large-scale electric field associated with plasma convection in the magnetosphere, which drives a large-scale electric current and the Pedersen part of which may be connected to a large-scale field-aligned current. Precipitating particles create a density perturbation and an increase in the Pedersen conductivity. Depending on the ionosphere state, it reacts to this enhancement either as a voltage generator or as a current generator. If the background ionospheric conductivity is high, the ionosphere responds by a polarization field which reduces the large-scale convection electric field. If the background conductivity is low, the ionosphere responds by an increase in the Pedersen current which must be closed by field-aligned currents flowing at the conductivity gradient. The field aligned-current is associated with Alfvén waves [*Lysak*, 1986]. More currents flow between the magnetosphere and the ionosphere. A field-aligned potential drop is required to pull more electrons from the low-density magnetosphere. It accelerates electrons and produces high energy electron precipitation and thus intense electron auroral arcs. As the electrons are accelerated by field aligned electric field, protons are decelerated or accelerated upward. The observation of the seasonal variation of the upward ion beam was described in *Collin et al.* [1998]. Observations with the TIMAS instrument onboard the POLAR satellite are similar to the seasonal variations of the intense electron aurora and are in agreement with the mechanism. Moreover, observations from ground were also in the favor of the feedback conductivity mechanism. *Nakano et al.* [2002] analyzed local characteristics of the geomagnetic field to extract information on the field aligned current variation. They shown that the net field-aligned currents are upward in the nightside region and downward in the dayside. In the nightside region, the background conductivity is low and the feedback mechanism implies that a more intense field-aligned current is flowing upward and the integration along the field line gives an important upward net field-aligned current.

[59] We show that in some cases proton precipitation is very localized and very intense as shown by the example of 28 April, 2001. The increase in conductance due to protons is very high in this sector. The ionospheric conductivity feedback mechanism is plausibly also operative in this case. Proton precipitation produces a local increase of ionospheric conductivity which presumably causes more current to flow between the ionosphere and

the magnetosphere and increases or decreases the field aligned electric field and modifies the auroral precipitation. The ionosphere is primed for the feedback instability only when the background conductivity is low. In the case where proton precipitation is important, the background conductivity is high and the enhancement of Pedersen conductivity due to electron precipitation creates a polarization electric field reducing the total convection electric field. The conditions are not suitable to create intense aurora. A very intense localized proton injection can influence the electron precipitation by reducing the electron acceleration. Thus, intense electron aurora is not expected to take place efficiently in regions where proton precipitation was important. The verification is beyond the scope of this study but the question requires further investigation. *Lyons* [1992] assumed that the potential variation which is the cause of the formation of electron auroral arcs generally occurs between about 5000 and 10000 km altitude. Can enhancement of ionospheric conductivity due to proton precipitation create effect up to this altitude?

# Chapitre 5

# Modèle de transport des protons auroraux et comparaison avec ARGOS-HITS

## 5.1 Résumé introductif

Cette étude n'est pas immédiatement liée aux observations de l'aurore à protons par le satellite IMAGE, mais s'inscrit plutôt dans une démarche d'utilisation du modèle de transport et de dégradation d'énergie des protons auroraux. Ce modèle, décrit au chapitre 1.1, repose sur une simulation de Monte Carlo. Les protons pour lesquels on choisit une hypothèse de distribution en angle d'attaque et en énergie (dans le cas présent, une distribution kappa) sont introduits dans un modèle d'atmosphère MSIS-90 [*Hedin*, 1991] et leur transport au travers de l'atmosphère neutre est décrit en résolvant les équations de Boltzmann. Le modèle considère les collisions élastiques et inélastiques, les ionisations et les échanges de charge. J'ai comparé l'emission Lyman-$\alpha$ aurorale simulée par ce modèle avec des observations spectrales du satellite ARGOS. Les premiers résultats furent encourageants, mais des désaccords dans certains cas ont été observés et n'ont pu être résolus.

## 5.2 ARGOS-HITS

L'instrument HITS (**H**igh Resolution **I**onospheric and **T**hermospheric **S**pectrograph), à bord du satellite ARGOS (**A**dvanced **R**esearch and **G**lobal **O**bservation **S**atellite) fournit des mesures spectrales à haute résolution de l'aurore à protons. HITS est un spectrographe dont la bande passante de 100 Å peut être fixée entre 500 et 1700 Å, ce qui permet donc des observations détaillées dans le domaine UV lointain. Chaque spectre a une résolution temporelle de 1 seconde bien qu'ils soient typiquement moyennés sur de plus longues périodes afin d'améliorer la statistique de comptage. Sur une période de 60 secondes, HITS balaye approximativement 200 km le long de l'empreinte du satellite. Le champ de vue de

HITS s'étend sur ∼230 km dans la direction perpendiculaire à la trajectoire.

Les observations HITS fournissent deux avantages dans l'étude de l'aurore à protons :

- La résolution spectrale de HITS vaut ∼1.5 Å (FWHM). Cette résolution est suffisante pour séparer l'émission géocoronale (Lyman-$\alpha$ au repos) et l'émission Lyman-$\alpha$ déplacée par effet Doppler due à la précipitation de protons.

- Les mesures de l'aurore à protons par HITS sont disponibles dans les régions nocturne et diurne et dans les deux hémisphères. Le satellite ARGOS se trouve sur une orbite quasi-polaire de 98.7 ° d'inclinaison, dans la direction 0230/1430 MLT. Son altitude vaut 850 km. L'instrument HITS peut être utilisé selon deux modes de fonctionnement : un mode balayage ou un mode de vue fixe. Dans le cas de notre étude, l'orientation d'observation est maintenue fixe avec un angle d'environ 60° entre le vecteur d'observation HITS et la direction du nadir du satellite.

## 5.3 Etude de l'émission Lyman-$\alpha$ produite par les protons auroraux et corrélation avec les observations ARGOS-HITS.

Dans le but de déduire les énergies caractéristiques des protons incidents à partir des observations spectrales, j'ai comparé les observations spectrales de la raie Lyman-$\alpha$ déplacée par HITS et celles simulées par le modèle de transport et de dégradation d'énergie des protons auroraux (voir chapitre 1.1).

Pour caractériser la forme des spectres observés et simulés et ainsi obtenir un indicateur univoque de l'énergie caractéristique des particules à partir des observations, j'ai utilisé les longueurs caractéristiques des ailes rouge et bleue du spectre Doppler, définies comme suit :

$$\Delta\lambda_{red} = \frac{\int_{\lambda_{Ly\alpha}}^{\lambda_{max}} \lambda I(\lambda) d\lambda}{\int_{\lambda_{Ly\alpha}}^{\lambda_{max}} I(\lambda) d\lambda} - \lambda_{Ly\alpha} \tag{5.1}$$

$$\Delta\lambda_{blue} = \lambda_{Ly\alpha} - \frac{\int_{\lambda_{min}}^{\lambda_{Ly\alpha}} \lambda I(\lambda) d\lambda}{\int_{\lambda_{min}}^{\lambda_{Ly\alpha}} I(\lambda) d\lambda} \tag{5.2}$$

où $\lambda_{Ly\alpha}$ est la longueur d'onde au repos H Lyman-$\alpha$, $I(\lambda)$ est le taux d'émission spectrale à chaque longueur d'onde observée, et $\lambda_{min}$ et $\lambda_{max}$ sont les limites d'intégration des largeurs rouge et bleue et valent respectivement 1210 Å et 1230 Å.

Les premier résultats de cette analyse furent encourageants. Ils ont été publiés dans un article dans la revue Geophysical Research Letters (article joint en annexe). Pour cette étude, nous avions supposé que les protons incidents avaient une distribution en angle d'attaque isotrope et une distribution en énergie de type kappa ($\kappa$=3.5). Nous avons testé des protons incidents dont l'énergie caractéristique $E_0$ variait entre 100 eV et 25 keV. Les résultats, présentés à la figure B.3 (voir annexe B) , montrent que le modèle reproduit assez bien le pic d'émission dans le spectre auroral . Pourtant, la suite de cette analyse ne fut pas concluante car dans plusieurs cas, il fut impossible de modéliser l'aile rouge du spectre observé.

Deux approches ont été mises en place pour trouver une explication à ce désaccord : dans un premier temps, l'hypothèse sur la distribution énergétique des protons incidents a été analysée. Les comparaisons ont été effectuées en supposant que les protons étaient distribués selon un faisceau monoénergétique ou selon une fonction maxwellienne. Ces résultats n'ont pas permis d'expliquer le désaccord. Dans un second temps, le modèle numérique de dégradation de l'énergie des protons a été modifié de sorte à mieux prendre en considération la statistique des collisions entre $H^+$ ou H et les constituants neutres de l'atmosphère. Mais ces nouveaux résultats ne permettent toujours pas de modéliser correctement l'aile rouge des spectres Ly-$\alpha$ observés.

J'ai également analysé l'aurore du côté jour en comparaison avec l'aurore du côté nuit. Trois comparaisons ont été effectuées : elles montrent de nouveau un désaccord flagrant dans la partie spectrale aux plus grandes longueurs d'onde, comme on peut le remarquer à la figure 5.1.

Deux hypothèses pour expliquer ce désaccord sont plausibles :

- ARGOS-HITS observe une raie d'émission due à un autre constituant atmosphérique, qui n'est pas prise en compte lors des comparaisons.

- Avec les données ARGOS-HITS, la valeur de l'angle d'observation lors de la mesure nous est fournie . La valeur de cet angle est nécessaire pour intégrer, le long de la ligne de visée, les taux d'émissions modélisées, et ainsi reproduire au mieux les observations. La valeur de cet angle montre que l'observation est très souvent proche d'une vue perpendiculaire aux lignes de champs. Dans ces conditions d'observation, le modèle que j'utilise ne pourra en aucun cas reproduire un spectre dissymétrique car le déplacement par effet Doppler dû à l'éloignement des particules du point d'observation est nul. L'erreur pourrait alors provenir de la valeur fournie de cet angle.

Il n'a pas été possible de trouver une solution à ce problème, ni de déterminer la cause de ces désaccords.

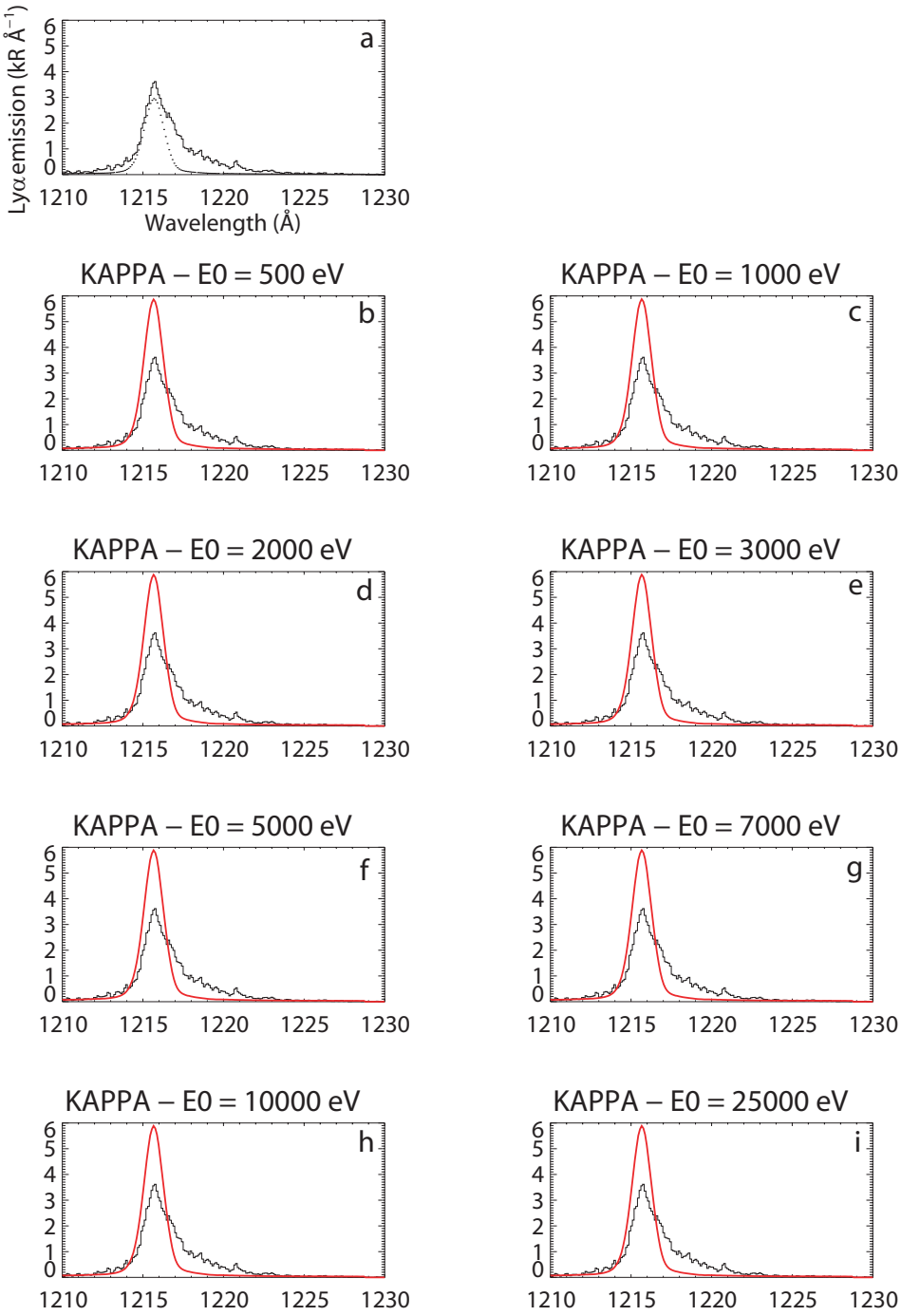


FIG. 5.1 – Comparaison des spectres entre 1210 et 1230 Å observés par ARGOS-HITS (trait noir) et simulés (trait rouge) utilisant une distribution énergétique du type Kappa. Le trait pointillé sur la figure 5.1a montre la composante due à l'émission géocoronale. Les figures 5.1b à 5.1i sont fonction de l'énergie caractéristique $E_0$ des protons (énergie indiquée au-dessus de chaque figure). On remarquera que le spectre simulé présente une quasi-symétrie due à l'orientation de la ligne de visée presque normale aux lignes de champ. De son côté, le spectre observé est nettement dissymétrique.

# Conclusions

Les études décrites dans ce travail sont mon apport personnel à une meilleure compréhension des processus de précipitation de protons, entrant en jeu dans le phénomène auroral. Ce travail s'inscrit dans la cadre de la mission IMAGE dont un des buts principaux est de montrer comment la magnétosphère répond globalement aux variations du vent solaire. Par le passé, la précipitation de protons était étudiée à l'aide de mesures optiques ou radars au sol ou par des mesures de satellites in situ, ce qui ne permettait qu'une vue localisée de celle-ci. L'observation globale de l'ovale auroral et l'étude de la précipitation de protons dans tous les secteurs simultanément sont rendues possible grâce à l'imageur spectral SI12 embarqué à bord du satellite IMAGE. Utilisant ce nouvel outil, j'ai donc eu la possibilité d'analyser les relations entre la précipitation globale de protons et les variations du vent solaire, ainsi que leurs conséquences sur l'ionosphère.

La première étape de ce travail a consisté à valider les observations des instruments FUV (WIC et SI12 principalement). La camera WIC est sensible à l'émissions LBH de $N_2$ et aux émissions de l'azote atomique NI, alors que SI12 donne une image de l'émission Lyman-$\alpha$ déplacée par effet Doppler produite par les protons. J'ai comparé les observations de WIC et SI12 avec des prédictions de modèles combinées aux mesures des instruments TED et MEPED à bord des satellites NOAA. L'instrument MEPED mesure les protons qui précipitent avec des énergies supérieures à 30 keV et les comparaisons peuvent donc inclure toutes les énergies aurorales, au contraire de travaux précédemment publiés dans la littérature. Sur base des calibrations, les comparaisons avec SI12 montraient un (dés)accord de 50%, ce qui signifie que les observations SI12 couplées avec les simulations prédisaient des flux de protons deux fois plus important que les mesures in situ. Sur base de ce résultat, j'ai décidé de recalibrer la méthode et pour la suite du travail, les flux d'énergie de protons ont été ajustés par un facteur 2 pour prendre en considération cette surestimation des flux. Outre ce résultat pratique et très utile pour la suite des travaux, cette étude a également montré que (i) la précipitation des protons peut contribuer significativement à l'émission aurorale FUV à des moments et des localisations précis et ne peut être négligée, (ii) et dans certaines régions, spécialement dans le secteur du crépuscule, les protons de hautes énergies dominent le flux énergétique de protons et comptent pour une large part dans le signal Lyman-$\alpha$ observé.

Dans la suite du travail, les observations SI12 couplées aux simulations de Monte Carlo

ont été utilisées pour établir une vue statistique de la précipitation globale de protons. Des cartes de flux énergétiques de protons ont été générées pour les périodes proches des solstices d'hiver et d'été. La morphologie globale instantanée et statistique de l'aurore à protons déduite de SI12 est très semblable à celle basée sur le modèle empirique de DMSP. Ce résultat n'était pas évident a priori puisque les deux études sont basées sur des observations très différentes. L'analyse de la puissance aurorale en fonction de la valeur de l'indice Kp, calculée sur base des données DMSP (modèle empirique de *Hardy et al.* [1989]) et des observations SI12 présente un accord remarquable, même si cette étude montre que la grandeur fondamentale dans le contrôle de la précipitation de protons est la pression dynamique plutôt que l'indice Kp. Enfin, un effet saisonnier dans la précipitation de protons a été mis en évidence. L'extension en latitude de l'ovale est plus grande en été qu'en hiver et la puissance des protons précipités est supérieure d'au moins 1.5 fois en été qu'en hiver. La fréquence d'aurores à protons intenses est 3 fois plus importante en été qu'en hiver. Cet effet saisonnier a été mis en évidence sur les observations dans l'hémisphère nord de deux hivers (2000-2001 et 2001-2002) et deux étés (2000 et 2001) et est en opposition avec celui observé pour les électrons. Le mécanisme proposé pouvant engendrer ce type de comportement pour les protons est lié à la présence de champs électriques alignés qui accélèrent les électrons vers l'ionosphère et suppriment le flux de protons incidents dans ces mêmes régions. La présence de tels potentiels de champs alignés dépend de la différence d'illumination entre l'été et l'hiver.

La relation entre la précipitation de protons, le vent solaire et le champ magnétique interplanétaire a également été analysée. L'intensité de l'aurore à protons observée par SI12 aux périodes proches des solstices d'hiver et d'été a été corrélée avec les caractéristiques du vent solaire et du champ magnétique IMF mesurées par les instruments du satellite ACE. Une forte corrélation est mise en évidence entre la puissance des protons précipités et la pression dynamique du vent solaire moyennée sur une heure. La puissance des protons augmente également avec l'intensité de $|B_z|$. Les corrélations entre l'aurore à protons du côté nuit et les fonctions de couplage ont également été analysées. Ces fonctions de couplages sont des approximations qui traduisent les mécanismes de couplage entre le champ magnétique interplanétaire et la magnétosphère, ainsi que l'énergie transmise à la magnétosphère via ces mécanismes. Les coefficients de corrélation les plus élevés sont obtenus pour les expressions contenant la pression dynamique et le champ électrique transverse (dans le plan YZ) du vent solaire. En dehors des sous-tempêtes aurorales, l'influence de la pression dynamique sur l'aurore à protons semble provenir de l'effet de la pression dynamique sur la forme de la magnétosphère, provoquant l'étirement de la queue de la magnétosphère et la précipitation des protons par le phénomène de stochastisation, mais aussi par d'autres processus de couplage entre le vent solaire et la magnétosphère. De plus, l'étude comparative des réactions des protons et des électrons a montré que les mécanismes de précipitations des particules sont identiques pour des degrés d'activités élevés, alors qu'ils apparaissent différents pour des conditions de plus faible activité.

J'ai appliqué cette étude de la précipitation aurorale protonique à un cas plus parti-

culier : je me suis intéressée à la précipitation aurorale des protons durant les phases de croissance précédant les sous-tempêtes aurorales. La phase de croissance est la phase la moins étudiée dans la littérature, probablement parce qu'elle est la moins spectaculaire dans ses conséquences visuelles. J'ai analysé la morphologie et la dynamique de l'ovale auroral à l'échelle globale, durant 55 phases de croissance, ainsi que l'évolution du flux magnétique ouvert dans la calotte polaire durant celles-ci. J'ai également examiné la relations entre la dynamique de l'ovale et les paramètres du vent solaire et du champ IMF au cours de ces événements. J'ai montré que le mouvement vers l'équateur des frontières de l'ovale durant les phases de croissance est corrélé statistiquement avec l'intensité de $B_z$, ainsi qu'avec l'intensité des fonctions de couplage, ce qui confirme que l'accumulation d'énergie durant la phase de croissance est fortement influencée par le couplage entre la vent solaire et la magnétosphère. J'ai également montré que cette accumulation d'énergie pouvait être interrompue, et donc la phase d'expansion déclenchée, par une variation dans le vent solaire ou par une instabilité interne dans la magnetosphère. SI12 a offert la possibilité d'observer globalement le comportement des frontières de l'ovale durant les phases de croissance. Le résultat de cette analyse montre que le mouvement peut être global, local ou une superposition des deux. Ce résultat est interprété comme la superposition d'un étirement global de la magnétosphère dû à l'influence du vent solaire et d'un étirement local trouvant son origine dans le feuillet de plasma interne à la magnétosphère.

Finalement, pour compléter l'analyse de la précipitation des protons auroraux et dans le but d'analyser leur influence sur la haute atmosphère, j'ai développé un modèle de conductance ionosphérique. Les observations IMAGE sont utilisées pour produire des cartes instantanées de conductances ionosphériques de Hall et de Pedersen, ainsi que les profils de conductivités dus aux protons et aux électrons auroraux. La contribution des protons dans les conductances peut ainsi être evaluée. J'ai montré que durant les périodes calmes, elle est relativement plus grande que durant les sous-tempêtes. La contribution des protons est également plus élevée durant la phase de croissance et diminue fortement durant la phase d'expansion. Négliger la contribution des protons lors de l'analyse des caractéristiques aurorales entrainerait une erreur importante dans certains secteurs et à certaines périodes. J'ai également montré que l'augmentation de la conductivité ionosphérique, induite par la précipitation de protons joue une rôle sur la précipitation d'électrons. En créant un champ électrique de polarisation inverse, l'augmentation de la conductivité ionosphérique réduit la chute de potentiel le long des lignes de champ dans le secteur des courants alignés dirigés vers le haut. Ce mécanisme de rétroaction pourrait réduire la précipitation d'électrons dans ce même secteur.

En résumé, notre étude a montré que :

– les protons ne peuvent être négligés dans l'étude des aurores, car leur contribution à la puissance et aux conductances aurorales peut être non négligeable par rapport à celle des électrons,

– leur précipitation est principalement influencée par les variations de pression dynamique du vent solaire ainsi que par l'orientation du champ magnétique interplanétaire, tant au point de l'énergie accumulée durant la phase de croissance, que des processus de déclenchement de leur précipitation et les processus de précipitation eux-mêmes,

– la précipitation de protons présente un effet saisonnier, avec un maximum dans l'hémisphère d'été,

– les conductivités de Hall et de Pedersen et leur évolution temporelle peuvent être déduites globalement de la contribution des trois imageurs ultraviolets de l'expérience.

De nouvelles études sont appelées à venir compléter ces recherches. Ainsi, il serait intéressant de mettre en relation l'énergie accumulée durant la phase de croissance avec l'énergie libérée durant la sous-tempête. Ces résultats donneraient de informations complémentaires quant aux mécanismes d'accumulation et de transfert d'énergie. De plus, l'analyse de la précipitation des protons dans l'hémisphère sud permettrait de compléter la compréhension des processus de saisonnalité.

La technologie des imageurs spectraux à bord du satellite IMAGE est un précurseur dans l'observation des protons. Les 5 années de fonctionnement de la mission ont été une réussite totale et ont permis une avancée importante dans la connaissance relative à leur précipitation vers la haute atmosphère. Ce travail n'est qu'une partie des résultats de la mission. Même si le satellite IMAGE a arrêté d'émettre en 2005, la base de données est tellement importante que de nombreux résultats sont encore attendus. De plus, l'espoir existe que la communication entre le satellite et la Terre soit rétablie en octobre 2007 [1]. En outre, de nouvelles missions sont amenées à se développer : Kuafu, mission chinoise en collaboration internationnale, propose d'envoyer deux satellites qui observeront simultanément un hémisphère et qui seront équipés de caméras SI. De tels satellites permettraient également l'études globale de la précipitation des protons et électrons dans les deux hémisphères et de mieux comprendre la complexité des mécanismes de précipitations. La possibilité serait offerte de vérifier si les mécanismes sont globaux dans la queue de la magnétosphère et donc si la précipitation présente une symétrie nord/sud ou si des mécanismes locaux entrent en jeu et influencent préférentiellement la précipitation vers un seul hémisphère. J'espère que l'avenir sera favorable au développement d'autres missions de ce type dans lesquelles la Belgique sera un acteur important.

[1] Le satellite subira alors une eclipse total de soleil et il est possible qu'une réinitialisation du système permette au satellite d'émettre à nouveau vers la Terre

# Annexe A

# Seasonal, Solar Flux, and Magnetic Activity Variations in Electron and Ion Auroral Energy Fluxes

B. A. Emery, W. Xu
High Altitude Observatory/NCAR

V. Coumans
Laboratoire de Physique Atmosphérique et Planétaire, Université de Liège

D. S. Evans, M. S. Greer
Space Environment Center/NOAA

G. A. Germany
University of Alabama in Huntsville

E. Holeman
Boston College

K. Kadinsky-Cade, F. J. Rich
Air Force Geophysics Laboratory

*Draft 25/08/07, for submission to Journal of Geophysical Research (Space Physics)*

## Abstract

[1] *Models for electron and ion auroral inputs usually ignore seasonal differences. This study shows, however, that there are significant seasonal variations in electron and ion auroral energy fluxes, which are opposite to each other. Electron auroral energy flux was characterized by electron hemispheric power (Hpe) estimated since 1978 from NOAA and DMSP satellites after the estimates were corrected for instrumental problems and adjusted to a common baseline in previous work. Similarly, intersatellite adjusted ion hemispheric power (Hpi) estimates came from four NOAA satellites beginning in 1998. NOAA/DMSP adjusted Hpe and Hpi estimates compare well with POLAR UVI Hpe and IMAGE FUV Hpe and Hpi estimates from imagers. Seasonal variations were expressed in terms of hemispheric power (Hp) magnitudes. Electron particle precipitation was ∼20-50% stronger at winter solstice than in summer for Hpe>∼25 GW, with the highest winter excess for high solar fluxes (10.7 cm adjusted solar flux Sa). Hpe summer values were larger than winter ∼35% of the time starting at Hpe<∼10 GW, increasing to ∼25-35% summer excess at the lowest Hpe magnitudes. Ion precipitation was ∼20-30% larger during summer solstice compared to winter solstice. Seasonal, Sa, Kp, ap, $B_z$, and $V_{sw}$ relations were found for Hpe and Hpi and compared with previous work. Hpe and Hpi increased with Kp, solar wind speed ($V_{sw}$) and negative Interplanetary Magnetic Field (IMF) $B_z$. Hpi increased strongly with positive $B_z$. At low $V_{sw}$ and $B_z$>-3 nT, Hpe increased with increasing Sa, while Hpi increased with Sa up to ∼115 for all conditions.*

### A.0.1 Introduction

[2] Several models of auroral energy input assume hemispheric conjugacy and thus no seasonal variations. *Hardy et al.* [1985, 1987] and *Fuller-Rowell and Evans* [1987] modeled electron and total auroral energy fluxes and mean energies from Defense Meteorological Satellite Program (DMSP) and National Oceanic and Atmospheric Administration (NOAA) satellites, respectively. Ion energy fluxes and mean energies were modeled as a function of Kp using DMSP data by *Hardy et al.* [1989, 1991]. In all these studies, seasonal or interhemispheric differences were neglected and bin statistics were increased by adding both hemispheres together. The present study examined the seasonal and solar flux variations in the auroral electron and ion inputs.

[3] The level of auroral activity can be characterized by an estimate of the area integrated particle energy deposition into each high-latitude hemisphere. The estimated energy input is called the 'hemispheric power' (Hp) [*Fuller-Rowell and Evans*, 1987]. The estimate relies on a set of statistical auroral ovals, constructed from NOAA Space Environment Monitor 1 (SEM-1) observations and ordered by Hp. The statistical ovals were constructed without regard to hemisphere or season, simply binning all observations within a given Hp interval by magnetic latitude and magnetic local time. These empirical ovals provide the basis for an extrapolation of the local measurements of particle energy fluxes made by any satellite to a global estimate. The extrapolation takes into account the manner that a satellite passage samples the auroral oval, an extrapolation that depends upon the hemisphere sampled and the Universal Time (UT) of the sample. The empirical patterns do not replicate the very intense, but localized regions of particle energy input that may occur during dynamic activity, for example the onset of substorms. In such circumstances the estimate of Hp can be a significant over- or under-estimate depending upon whether or not the satellite passed through the region of large energy fluxes. The results presented here use hourly and daily median values of hemispheric power estimates from a number of satellites to minimize the effect of estimates made during such dynamic periods.

[4] A hemispheric power index $I$ is based on $Hp$ in a geometric fashion, with the approximate relation [*Maeda et al.*, 1989]:

$$I = 2.09 \ln(Hp) \tag{A.1}$$

where $Hp$ is in GW. *Maeda et al.* [1989] found a Kp relation using NOAA data from 1978 to 1985:

$$Hp(GW) = -2.78 + 9.33Kp \tag{A.2}$$

where $Hp$ must be larger than 1 GW at the lower limit. This Kp relation is used in global models such as the Whole-Atmosphere Community Climate Model (WACCM) to specify the auroral energy input [*Marsh et al.*, 2007]. The potential drop imposed on the polar cap was estimated using Millstone Hill incoherent scatter radar ion drift velocities as a function of the hemispheric power index I [*Foster et al.*, 1986]. This ion convection model and

the auroral input model of *Fuller-Rowell and Evans* [1987] were used as statistical models in the Assimilative Model of Ionospheric Electrodynamics (AMIE) [e.g., *Lu et al.* [1994, 2001]; *Knipp et al.* [1993]], and in the Coupled Thermosphere-Ionosphere Model (CTIM) [e.g., *Codrescu and Kutiev* [1997]; *Fuller-Rowell et al.* [1998]].

[5] The original hemispheric power estimates from the NOAA data combined the contributions of electrons and ions to the energy input to produce a 'total' estimate, called Hpt in this paper. The present study strives to distinguish between the hemispheric power input from electrons (Hpe) and that from ions (Hpi). Hpi is obtained from NOAA SEM-2 observations by computing hemispheric power estimates using electron observations only (Hpe) and subtracting that value from Hpt. This procedure does not take into account the fact that the global pattern of ion precipitation differs from the pattern of total (electron plus ion) precipitation and so there are greater uncertainties in the values of Hpi. Hpe is estimated with electron observations from DMSP satellites using the global NOAA Hpt maps. Other DMSP studies [e.g. *Hardy et al.* [1989]; *Brautigam et al.* [1991]] bin the electron and ion data into global maps of energy flux as a function of magnetic local time (MLT) and magnetic latitude and calculate Hpe and Hpi from an area integration of the energy fluxes.

[6] Estimates of NOAA Hpt are available at http://www.sec.noaa.gov/ftpdir/lists/hpi, which is linked to the near-real-time website (http://www.sec.noaa.gov/pmap). NOAA Hpt and DMSP Hpe estimates are also in the Coupling, Energetics and Dynamics of Atmospheric Regions (CEDAR) Database (http://cedarweb.hao.ucar.edu), with further descriptions appearing at http://cedarweb.hao.ucar.edu/instruments/ehp.html on the 'Estimated Hemispheric Power' (ehp) web page. Estimates of Hpe (and Hpi = Hpt-Hpe) from NOAA Space Environment Monitor 2 (SEM-2) satellites are in the CEDAR Database. DMSP Hpe estimates are also located at the webpage for DMSP in the CEDAR Database (http://cedarweb.hao.ucar.edu/dmsp/dmspssj4_hp.html). Twenty-eight years of Hpe or Hpt estimates from 11 NOAA and 11 DMSP satellites were adjusted to produce consistent estimates of Hpe by *Emery et al.* [2006], hereafter referred to as Paper 1. Paper 1 also produced intersatellite adjusted estimates of Hpi (and thus Hpt) from four NOAA SEM-2 satellites.

[7] This paper reviews Paper 1. Estimates of the ion contribution to Hpt are made including other data sets at different energy ranges. Comparisons are made with Hpe and Hpi estimates from imagers on different satellites, and seasonal variations in Hpe and Hpi are analyzed. The seasonal variations were expressed mathematically as functions of the magnitudes of Hpe and Hpi, including any solar flux variations expressed as the daily 10.7 cm solar flux adjusted to 1 AU (Sa) in solar flux units (sfu) of $10^{-22}$ W m$^{-2}$ Hz$^{-1}$. Hpe and Hpi were binned in Kp, Interplanetary Magnetic Field (IMF) $B_z$, solar wind speed ($V_{sw}$), and solar flux (Sa). Polynomial fits in Kp were found for the total southern hemisphere (SH) Hpe and Hpi hourly average composite estimates and independent fits were found for Hpe and Hpi as a function of $B_z$ and $V_{sw}$. Variations with respect to Sa were found for

Hpe and Hpi binned in $B_z$ and $V_{sw}$.

## A.0.2 Background

### Satellite Observations

[8] The NOAA low-energy Total Energy Detector (TED) SEM-1 electron and ion precipitation instruments measured 11 energy bands between 300 eV and 20 keV to produce estimates of Hpt. These satellites are listed in Table A.1a. The NOAA SEM-2 satellites listed in Table A.1b with 16 energy levels between 50 eV and 20 keV were used to estimate Hpt using ion and electron detectors and also to estimate Hpe using only electron energy bands. The ion hemispheric power (Hpi) is the difference between Hpt and Hpe (Hpi = Hpt - Hpe). A multiplicative consistency factor (NOAA Y0 in Table A.1) is usually calculated for each new NOAA satellite, so that the first six months of the estimated Hpt from the new satellite agrees with the Hpt estimates from older concurrent satellites. The first NOAA standard was TIROS, launched in 1978, and the second NOAA standard was NOAA-12, launched in 1991 after a gap starting in 1989 when Hpt estimates from NOAA-10 were abandoned due to a spurious response problem. Although the NOAA satellites also carry Medium Energy Proton and Electron Detector (MEPED) instruments to measure electrons in three integral or differential energy bands above 30 keV and protons in five (SEM-1) or six (SEM-2) energy bands [*Codrescu et al.*, 1997], the present study was limited to the TED instruments.

[9] DMSP satellites listed in Table A.2 estimated Hpe starting in 1983 using the electron energy detectors of the SSJ/4 and SSJ/5 (Special Sensor for flux J) instruments with 19 energy levels between 32 eV and 30 keV. The DMSP instruments have both pre-flight calibration and post-flight calibration corrections for sensor degradation and are not adjusted to agree between satellites.

[10] *Hardy et al.* [1985] and *Fuller-Rowell and Evans* [1987] showed the electron and total energy fluxes to be lowest around 12-14 MLT, highest on the nightside, and increasing with activity (Kp or I). *Liou et al.* [2001] showed that electron mean energies in winter from the UVI experiment on POLAR could be as high as 10 keV on the equatorward edge of the oval near dawn and near the poleward edge in the pre-midnight sector. This is similar to the 'characteristic energy' maps of *Fuller-Rowell and Evans* [1987]. Using the highest DMSP energy level, Paper 1 found the electron energy flux between 20 and 30 keV to be 5-6% of the 32 eV to 30 keV total for most Kp levels, increasing to as much as 12% for Kp 0. Thus the absolute difference between NOAA and DMSP Hpe estimates is usually less than 10%, and intersatellite adjusted Hpe from NOAA (<20 keV) and DMSP (<30 keV) can be considered to represent Hpe < 30 keV.

[11] *Hardy et al.* [1989] binned the ion energy flux from DMSP-F6 and F7 as a func-

tion of Kp and found the minimum ion energy flux around 10-11 MLT. The ion (mostly proton) auroral oval is shifted toward the duskside compared to the electron aurora, so protons add most to the hemispheric power on the equatorward duskside of the auroral oval [*Hardy et al.*, 1989; *Galand et al.*, 2001; *Coumans et al.*, 2004a]. A significant portion of the ion energy flux is at energies above 30 keV [*Hardy et al.*, 1989; *Coumans et al.*, 2002].

### Adjusted Hpe from NOAA and DMSP

[12] Operation times for all satellites are listed in Tables A.1 and A.2 along with their intersatellite adjustments. Most of these are the same as in Paper 1 except as noted. Two new satellites are DMSP-F17 (F17) and the European Meteorological Operational satellite MetOp-02 (M02). MetOp-02 carries the NOAA SEM-2 instruments and so this study treated M02 like a NOAA satellite. Corrections to data from various satellites were made for sunlight contamination, data dropouts over the auroral oval, degradation of sensors over time, high spurious count rates, and increased noise at the end of a satellite lifetime as listed in the footnotes of Tables A.1 and A.2. With a 98 degree inclination, most of the polar orbiting satellites were placed to take cloud cover pictures in the daytime over the northern hemisphere (NH), so that the nighttime auroral coverage was better in the SH.

[13] Figure A.1a shows SH daily median Hpt from NOAA SEM-1 satellites and Hpe from NOAA SEM-2 and DMSP satellites, where the original NOAA estimates have been divided by 'NOAA Y0' multiplicative consistency factors listed in Tables A.1a and A.1b to show the real range in the NOAA estimates. Figure A.1a shows some anomalies such as summer SH sunlight contamination (high values of Hpe from DMSP-F09 and F10 in 1988-1993), and spurious noise (high Hpt from NOAA-10 in 1988). Some satellite estimates appear to be low (low X1 divisor adjustments in Tables A.1 and A.2), e.g., NOAA-8 Hpt (black N8 from 1983-1985) and DMSP-F11 Hpe (black F11 from 1991-1999). Other estimates appear to be high, e.g., the NOAA standard NOAA-12 Hpt (green N12 from 1991-2002 and 2005-2006).

[14] The adjustment divisors X1 in Tables A.1 and A.2 are often different for each hemisphere because one adjustment required the SH/NH median daily ratio of Hpe and Hpi to be close to 1.0 over the lifetime of the satellite. The original interhemispheric biases could be due to different MLT coverage in the two hemispheres, to biases in the initial NOAA total precipitation patterns that were used, to the lack of seasonal variations in the patterns, or to unknown reasons. The original Hpi interhemispheric biases appeared to be related to the MLT orbits of the satellites, but no pattern was found for the original Hpe interhemispheric biases.

[15] Adjusted SH Hpe are shown in Figure A.1b. The largest Hpe values in Figure A.1b are in the declining phase of the solar cycle for the three solar cycles shown. The differences among these three solar cycles in the Hpe will be addressed in a follow-up study.

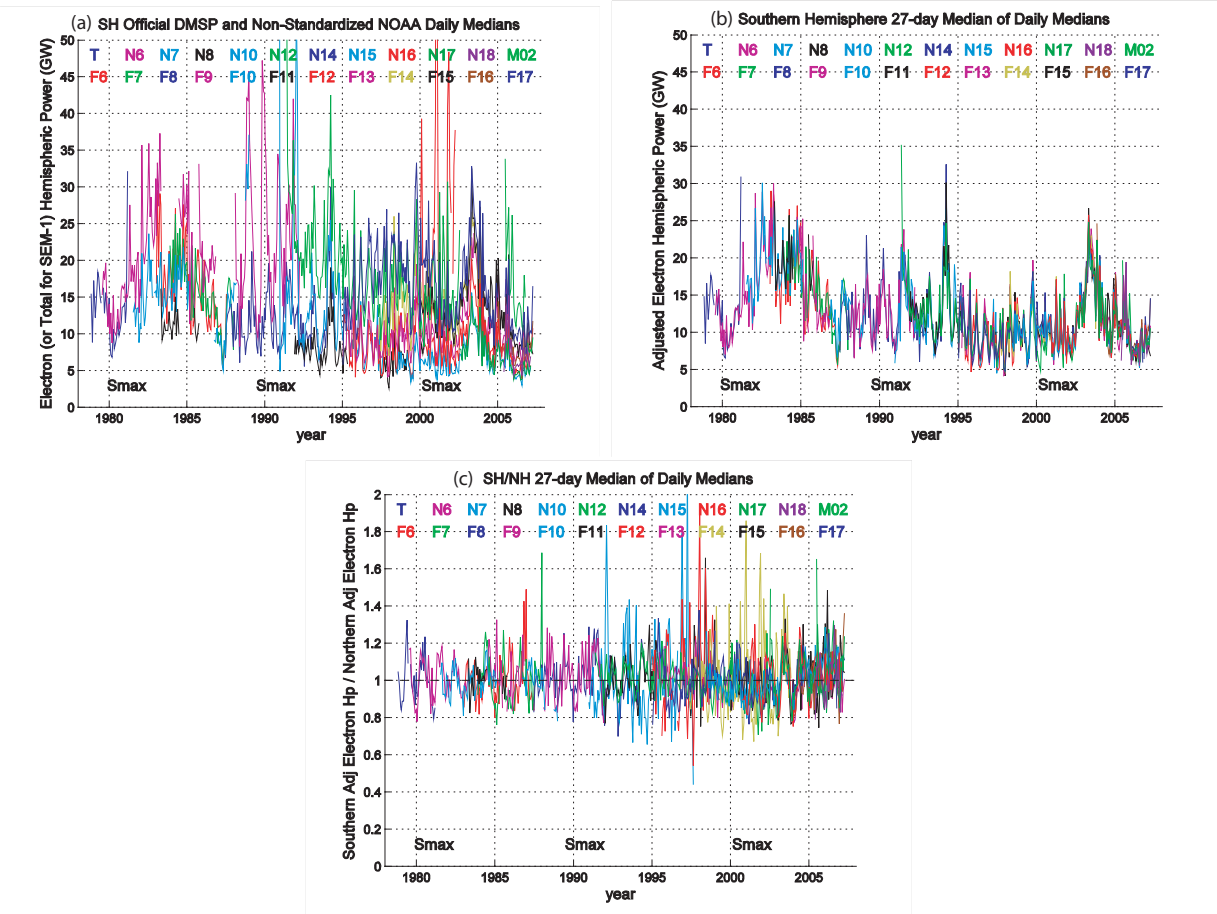


Figure A.1: (a) Southern hemisphere (SH) 27-day medians of the total (SEM-1) or electron hemispheric power from daily medians for 24 NOAA and DMSP satellites where the NOAA standards of TIROS or NOAA-12 have been removed to reveal the different satellite calibrations. (b) Southern hemisphere (SH) 27-day medians of the daily median adjusted electron hemispheric power (Hpe) for 24 NOAA and DMSP satellites after corrections, deletions and adjustments are made to a new Hpe baseline magnitude. (c) Southern hemisphere (SH) / northern hemisphere (NH) ratios of the daily median adjusted electron hemispheric power (Hpe) plotted as 27-day medians for 24 NOAA and DMSP satellites after corrections, deletions and adjustments are made to a new Hpe baseline magnitude.

[16] The baseline magnitude for Hpe was chosen to be close to the median of the original DMSP Hpe estimates. The closest satellite estimates to the baseline Hpe were from DMSP-F13. NH adjusted Hpe estimates are similar to those from the SH, but Hpe intersatellite cross-correlation coefficients of the daily median values are 0.775 for the NH compared to 0.845 for the SH Hpe [Table 6 of Paper 1]. SH Hpe estimates are better correlated because all but DMSP-F06 through F09 orbits sampled the nighttime aurora best in the SH. Many of the figures and analyses in the present study therefore use SH estimates of Hpe and Hpi.

[17] Figure A.1c plots the ratio of the SH/NH daily median adjusted Hpe estimates for each of the 24 satellites. The seasonal variation shows as a maximum in the ratio for SH winter and as a minimum in the ratio for SH summer. Seasonal variations in this ratio appear to be clearer in solar maximum when SH winter values are up to 25% greater than at equinox and SH summer values are as much as 25% less than at equinox. The seasonal variation is smaller in solar minimum and masked by problems in the ratio mostly due to inadequate auroral coverage in the NH. Hpe estimates from all satellites were combined each hour to produce hourly median, average, and maximum estimates of Hpe. The 28-year SH median Hpe from hourly medians was 12.1 GW and the average from hourly averages was 17.4 GW.

[18] *Ridley* [2007] estimated the median Hpt from NOAA to be ∼18 GW from 10 years of TIROS standardized Hpt and 15 years of NOAA-12 standardized Hpt. From Table A.1a, the average X1 divisor for TIROS is 1.05, and the average X1 divisor for NOAA-12 is 1.75, for a combined divisor over 25 years of 1.47. The resulting revised median Hpt from the *Ridley* [2007] study is 12.2 GW (18/1.47), which is very close to our median Hpe estimate of 12.1 GW. We examine seasonal variations in hourly average Hpe in Section A.0.5.

### Adjusted Hpi from NOAA SEM-2

[19] Paper 1 studied 123 days of DMSP-F13 and F15 ion energy flux data in 2001 and showed that the along-track fraction of the 0.5-30 keV ion energy flux coming from energies <20 keV ranged between 72 and 82% (77±5%) for Kp 1-3. Thus the baseline magnitude for NOAA SEM-2 Hpi (<20 keV) was set so that the ratio of the SH Hpi (<20 keV) over the Hpi (<30 keV) of Hardy et al. [1989] for Kp 1-3 was 77±1%.

[20] Figure A.2 shows the adjusted SH and NH Hpi estimates from the NOAA SEM-2 satellites. The adjusted 27-day median Hpi estimates are between ∼0.5 GW and ∼2.0 GW and increase about 50% from 1998 to post-solar-maximum conditions in 2003. The SH Hpi has an annual variation maximizing in summer, while the NH Hpi estimates appear to have equinoctial peaks, leading to a semiannual variation. Both hemispheres exhibit equinox activity peaks between about 2001 and 2004.

[21] There are significant differences in the Hpi estimates between the two hemispheres

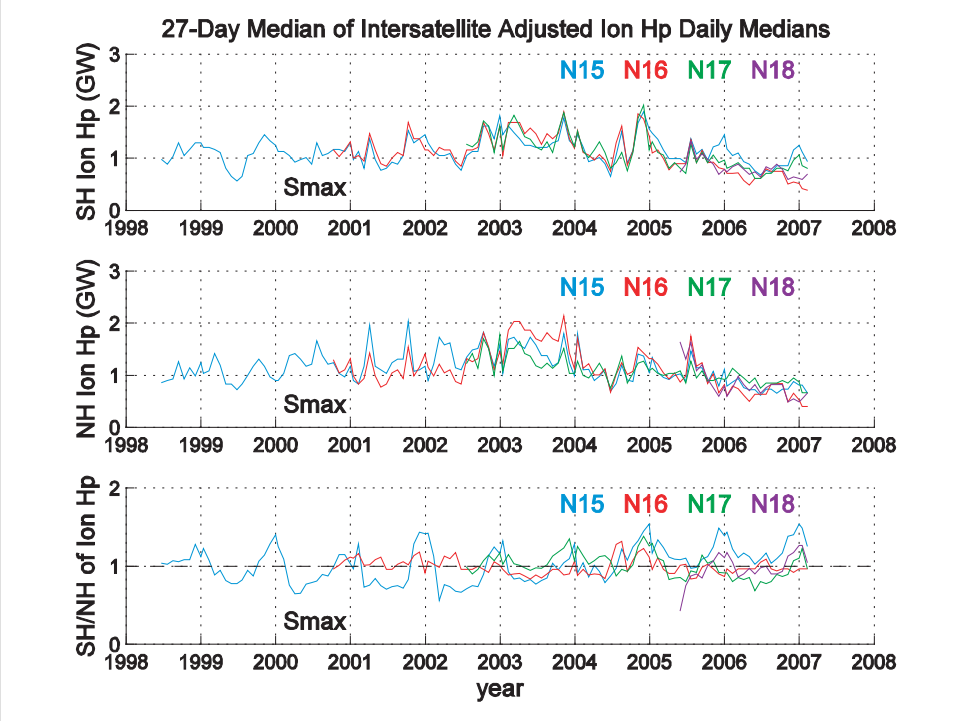


Figure A.2: Southern hemisphere (SH, top panel), northern hemisphere (NH, middle panel), and SH/NH ratios (bottom panel) of the 27-day medians of the ion hemispheric power (Hpi) from daily medians for four NOAA SEM-2 satellites after problems are removed and the adjustments in Table A.1b are applied.

and between different satellites in the NH. SH cross-correlation coefficients of daily median Hpi are ∼0.90, while NH cross-correlation coefficients are ∼0.85 among different SEM-2 satellites [Paper 1]. Because of MLT sampling problems in NH Hpi estimates, we primarily used SH estimates.

[22] The bottom panel of Figure A.2 plots the ratio of the SH/NH daily median adjusted Hpi estimates. Unlike the SH/NH Hpe ratio shown in Figure A.1c, the seasonal variation in the Hpi ratio shows a maximum in the SH summer and a minimum in the SH winter. The Hpi estimates during each UT hour in both the SH and NH from all four NOAA SEM-2 satellites were combined to provide minimum, maximum, median, and average Hpi and standard deviations of the average values. The 8-year SH median of hourly median Hpi (<20 keV) values was 1.10 GW, while the 8-year average was 1.45 GW. Compared to the 28-year median and average Hpe values of 12.1 GW and 17.4 GW, Hpi contributes ∼8% to the total Hpt. The next section examines the fraction content of ions using this and other data sets. The seasonal variations in hourly averaged Hpi are examined in Section A.0.5.

### A.0.3 Hpi Fractional Contribution to the Total Auroral Particle Energy Input

[23] In the present study, the ion fraction (<20 keV) of the total Hpt in the SH varied from a high of ∼19% for Kp 0, summer, $B_z$ positive, and low $V_{sw}$ to a low of ∼5% for Kp 2-7, winter, $B_z$ negative and high $V_{sw}$. *Hubert et al.* [2002] used NOAA-15 (<20 keV) normalized by NOAA-12 in 2000 and found Hpi to be about 22% of the total Hpt for low Kp and about 9% of the total for high Kp. Hpi (<30 keV) in Table 7 of *Hardy et al.* [1989] was used to calculate the ratio of Hpi/Hpt (<30 keV) in Table 5 of Paper 1. The ratio ranged from 13% for Kp 0 and 1 to 6-7% for Kp 3 and above. From Table 3 of *Brautigam et al.* [1991], the ratio of DMSP Hpi (<30keV) to Hpt excluding the bins with poor statistics varied from 17 for $B_z$ positive and low $V_{sw}$ to 8% for $B_z$ negative and high $V_{sw}$. The *Brautigam et al.* [1991] study and the present study found the highest ion fractions for $B_z$ positive and low $V_{sw}$ and the lowest ion fractions for $B_z$ negative and high $V_{sw}$.

[24] The ion contribution to the total particle energy input will increase as higher ion energies are included. Paper 1 calculated the ratio of Hpi/Hpt using Hpi (<2.5 MeV) and Hpe (<1 MeV) estimates from NOAA MEPED instruments using background material for *Fang et al.* [2007] from *Fang* [private communication] together with our estimates of Hpi (<20 keV) and Hpe (<30 keV). The ion fraction of the total particle energy input was 28% at Kp 1, 12-14% at Kp 2-3, and 8-11% at Kp 4-6. *Hubert et al.* [2002] used the IMAGE UVI imagers to study four substorm periods and concluded that protons (>1 keV) contribute 20-50% of the total hemispheric power before and after substorms and 10-20% in active substorm periods. *Coumans et al.* [2002] reduced the IMAGE SI12 Hpi calibration by a factor of 2, which reduces these proton contribution estimates to 10-25% of the total

Hpt in quiet periods and to 5-10% in active substorm periods, which are similar to our estimates of the period from the *Fang et al.* [2007] study.

### A.0.4 Comparisons with Images

#### POLAR UVI

[25] The Ultraviolet Imager (UVI) on the POLAR satellite measured the $N_2$ Lyman-Birge-Hopfield (LBH) emissions within its spectral bandpass of 124-200 nm [*Torr et al.*, 1995]. The $N_2$ LBH emissions were separated into two regions: one at shorter wavelengths (LBHs, 140-160 nm) with significant $O_2$ absorption, and one at longer wavelength emissions with less $O_2$ absorption loss (LBHl, 160-180 nm). In the absence of dayside photoelectrons, $N_2$ LBH intensities are a direct diagnostic of the incident auroral electron flux. The LBHl sensitivity peaked for electrons ∼5 keV, with a range of ∼20 eV to 70 keV. Hpe was estimated after dayglow removal from LBHl images that showed the full auroral oval or the nightside auroral oval in the field of view (FOV). *Codrescu et al.* [1997] found that NOAA MEPED electrons >30 keV contribute ∼0.05-6 GW to Hpe (50 eV to 1 MeV) between low and high activities, which is <10% of Hpe found for comparable activities from low-energy DMSP and NOAA instruments. Therefore the UVI LBHl Hpe estimates <70 keV should be similar to Hpe estimates from DMSP (<30 keV) and NOAA (<20 keV) satellites.

[26] UVI POLAR images are available at http://uvi.nsstc.nasa.gov and UVI Hpe estimates approximately every 10 minutes are found at http://csds.uah.edu/uvi-ost. The POLAR satellite was launched on 24 February (day 54) 1996, with apogee over the NH polar cap. Images from the primary UVI detector are available from days 83 to 268. The primary detector suffered operational anomalies between days 212 and 289 when it was shut down, so images from the secondary detector were certified starting on about day 339 of 1996. The challenge of creating robust, unsupervised, automated processing algorithms prevented a thorough validation of UVI Hpe estimates. Full or nightside oval NH UVI Hpe estimates between 97001 and 01365 were used to create median hourly Hpe estimates, which were then used to create median daily UVI Hpe estimates.

[27] Figure A.3 is median hourly NH UVI Hpe estimates combined into median daily Hpe estimates and plotted as 27-day medians (x's). Equivalent median hourly adjusted NOAA and DMSP NH Hpe estimates are combined into median daily Hpe estimates and then into 27-day medians, plotted as a blue line. Hourly medians were used in this comparison to eliminate outliers. UVI and NOAA/DMSP Hpe estimates show equinox maxima, with similar magnitudes except in the NH fall equinox. A preliminary analysis of the UVI images indicates a bright source on the nightside (e.g., a light leak) at certain UTs (orbit location). The late summer period also presents some of the strongest dayglow periods. These two factors probably affected the automated processing routines that compiled the UVI Hpe database used here.

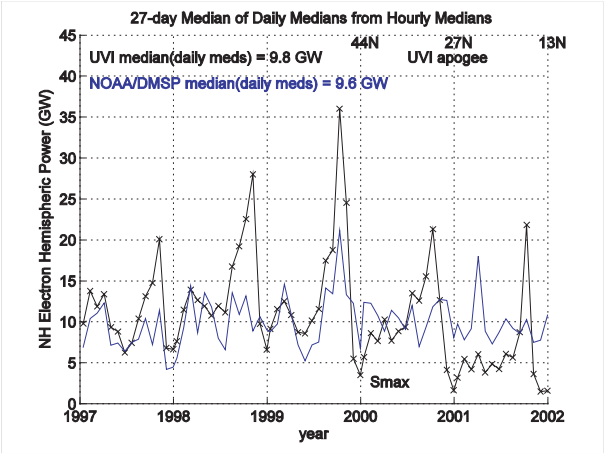


Figure A.3: Median daily northern hemisphere (NH) estimates of the electron hemispheric power (Hpe) from hourly medians from POLAR UVI (black x's) using full (0) and nightside (1) auroral fields-of-view (FOV) compared to median daily Hpe estimates from the NH NOAA/DMSP median hourly composite (blue) plotted as 27-day medians. The POLAR apogee on day 1 of 2000 to 2002 is listed at the top. For UVI apogee equatorwards of the aurora, Hpe estimates are low because a smaller portion of the aurora is in the FOV. The fall equinox UVI Hpe peaks are probably due to a light leak at certain viewing locations.

[28] Starting in 2000 when the POLAR apogee moved equatorward of 45 N, UVI Hpe estimates are less than adjusted NOAA/DMSP Hpe as a result of viewing the oval on the Earth's limb, where part of the oval is hidden from view. Apart from these questionable NH fall and low-latitude apogee UVI Hpe estimates, the general correspondence with the NOAA/DMSP intersatellite Hpe composite is good.

[29] *Lummerzheim et al.* [1997] compared standardized NOAA-12 and 14 estimates of Hpe to POLAR Hpe estimates from the primary UVI detector in the NH on 19-20 May 1996 in their Figure 3. This comparison is repeated in Figure A.4 with adjusted Hpe from NOAA and DMSP satellites as stars (NH) or x's (SH). SH Hpe estimates are included because seasonal differences in Hpe are not large in solar minimum conditions, as shown in Section A.0.5. The hourly average NOAA/DMSP Hpe is shown as a solid green line for the NH and as a dashed line for the SH. NOAA and DMSP Hpe have peaks at the same time as UVI Hpe, and the magnitudes are comparable below 20 or 30 GW. The UVI peak of the first substorm is ∼50 GW, which is close to the largest SH estimate from F12 of ∼40 GW. The second UVI substorm peak is greater than 120 GW briefly, with an average peak of ∼80 GW between 0030 and 0230 UT, while the largest NH F10 estimate is ∼50 GW. Short-term localized intense regions of precipitation are often missed by individual

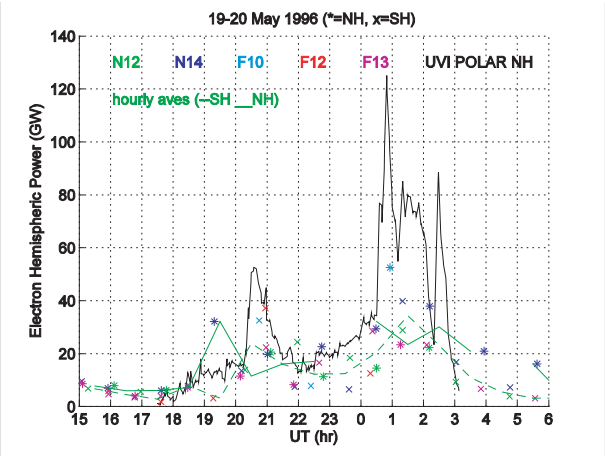


Figure A.4: POLAR UVI estimates of electron hemispheric power (Hpe) in the NH (black line) on 19-20 May 1996 compared to adjusted Hpe estimates from NOAA and DMSP in the NH (*) and SH (x). Also shown in dark green are Hpe average hourly composite estimates in the NH (solid line) and SH (dashed line).

satellite tracks across the aurora that use averaged global auroral patterns to estimate Hpe.

## IMAGE FUV

[30] The IMAGE satellite was launched on 25 March 2000 (00085 in year-daynumber). Summary FUV auroral images are available at http://sprg.ssl.berkeley.edu/image from 00139 to 05352. The IMAGE FUV experiment estimates Hpi [e.g., *Hubert et al.* [2002]] from the Spectrograph Imager (SI), assuming a model ion mean energy as a function of Kp from *Hardy et al.* [1989]. The SI instrument was composed of two narrowband detectors: one centered at 121.8 nm (SI12) to measure the hot Doppler-shifted Lyman-$\alpha$ hydrogen, and the second detector centered at the OI 135.6 nm (SI13) emission [*Mende et al.*, 2000b]. SI12 was minimally sensitive to electron precipitation but was sensitive to proton precipitation with peak sensitivity ~8 keV. The SI12 proton energy range was between ~1 keV [*Mende et al.*, 2001] and ~30 keV [*Gérard et al.*, 2001], but protons >30 keV could contribute significantly.

[31] Hpe was estimated using the Wideband Imaging Camera (WIC) with a pass-band between 140 and 190 nm [*Mende et al.*, 2000a], similar to POLAR UVI. As described by *Hubert et al.* [2002], the SI13 image was mapped to the WIC image and electron mean energy was determined from the ratio of WIC/SI13 using efficiency versus electron average energy curves. Hpe was then found from the WIC signal. These calculations were performed after the proton-induced signals in WIC and SI13 were removed based on the

proton estimates from SI12. The contribution of electrons with energies >30 keV was negligible [*Coumans et al.*, 2002]. Therefore IMAGE FUV WIC Hpe estimates should be similar to NOAA/DMSP Hpe estimates from the present study, while IMAGE SI12 Hpi estimates miss lower ion energies (<1 keV) and include ions with higher energies (>20 keV), as compared to Hpi estimates from the NOAA SEM-2 instruments.

[32] Paper 1 estimated from Figure 11 of *Coumans et al.* [2002] that NOAA TED SEM-2 proton energy fluxes (0.3-20 keV) in the total auroral oval had approximately the same magnitude as MEPED (30-240 keV) modeled ion energy fluxes for a median Kp of 4. Similarly, *Fang et al.* [2007] showed in their Figure 9 that NOAA MEPED Hpi (30-240 keV) had about the same magnitude as the adjusted NOAA TED SEM-2 Hpi (0.3-20 keV) for Kp values between 4- and 7+ on 17-18 April 2002. The high-energy contribution to the total Hpi (0.3-240 keV) decreased for lower Kp in the *Fang et al.* [2007] study, where MEPED Hpi (30-240 keV) was ∼15% of the SEM-2 Hpi (0.3-20 keV) for Kp ∼3, ∼10% for Kp ∼2, and dropped to ∼1% for Kp ∼1-. Therefore IMAGE FUV Hpi (>1 keV) should be larger than NOAA SEM-2 Hpi (<20 keV) for medium and high Kp levels. For Kp <1, NOAA SEM-2 Hpi might be higher than IMAGE FUV Hpi because of the contribution to Hpi of protons <1 keV.

[33] Figures A.5a and A.5c show NH Hpe estimates from IMAGE FUV images compared with adjusted Hpe estimates from NOAA and DMSP satellites from both hemispheres for 02-03 January 2001 and for 30 January 2001. Previous IMAGE Hpe and Hpi estimates and standardized NOAA Hpe estimates for 30 January were also shown in Figure 6a of *Hubert et al.* [2002]. The format for Figures A.5a and c is the same as that in Figure A.4 for the POLAR UVI comparison. SH NOAA and DMSP Hpe estimates ("x"s) are similar to NH Hpe estimates ("*"s), although there are fewer NH estimates between 3 and 9 UT because the NH MLT satellite tracks do not sample the auroral oval well. Like the UVI Hpe comparison in Figure A.4, the FUV Hpe peaks above ∼20-30 GW are usually larger than the equivalent NOAA/DMSP Hpe composite. However, the SH average hourly composite Hpe (dashed dark green line) replicates the FUV peak around 3-6 UT on 2-3 January, while the maximum SH Hpe estimates from N12 (green x) at 2240 UT on 2 January and N16 (red x) at 1145 UT on 3 January are close to the FUV peaks at those times. Where FUV Hpe estimates are less than 5 GW on 30 January, NOAA and DMSP Hpe estimates are higher.

[34] Figures A.5b and A.5d show the same periods, but for Hpi. The initial calibration for the IMAGE Hpi used in *Hubert et al.* [2002] was halved in the present study because of the NOAA MEPED/TED and IMAGE FUV comparisons of *Coumans et al.* [2002]. Summer SH ("x") Hpi values are usually larger than winter NH ("*") Hpi as explained later. SEM-2 NOAA-15 and 16 adjusted Hpi estimates for proton energies <20 keV are about the same as Hpi estimates from SI12 from about 1 to 4 GW, but N16 (red) and N15 (blue) Hpi (<20 keV) estimates between 0400 and 0530 UT on 3 January fall short of SI12 observations that peak ∼7 GW when Kp was 4-, when ions >20 keV can contribute half the total ion

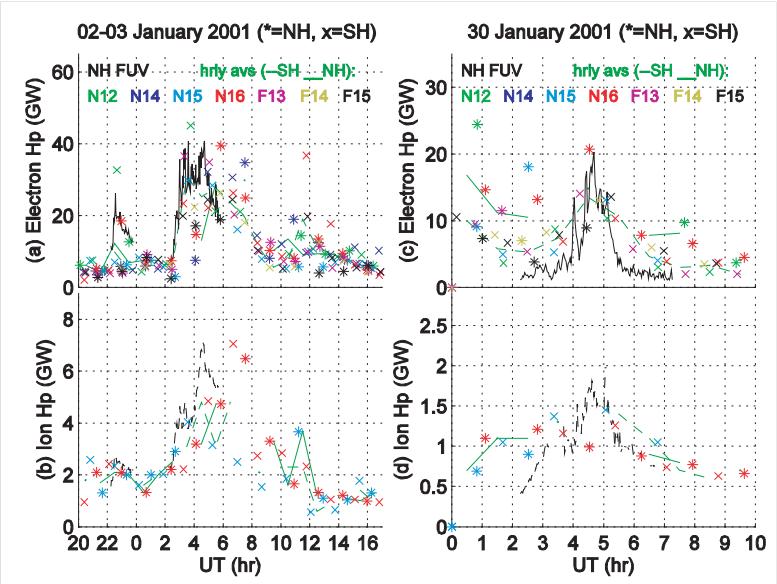


Figure A.5: Same as Figure A.4 except the black line is NH (a,c) electron or (b,d) ion hemispheric power estimates from IMAGE FUV for (a,b) 02-03 January 2001 and for (c,d) 30 January 2001.

flux. SEM-2 (<20 keV) Hpi estimates are higher than IMAGE FUV Hpi estimates in the quiet period at the beginning of 30 January, when IMAGE Hpi estimates fall below 1 GW for a Kp of 2. Because SI12 images are not sensitive to protons <1 keV, they miss soft ion precipitation, particularly around the cusp on the dayside, which is increasingly important for periods of low ion energy flux.

[35] The good agreement between Hpe and Hpi measurements obtained from global imagery and those obtained by extrapolation to global patterns using in situ NOAA/DMSP observations give confidence that the NOAA/DMSP estimates are reasonable characterizations of hemispheric energy input except during dynamic periods with localized intense energy fluxes.

## A.0.5 Interhemispheric Seasonal Variations

### SH/NH Variations in Time

[36] The top panel of Figure A.6 plots as 27-day averages, the ratio of daily average Hpe(SH)/Hpe(NH) estimates, while the bottom panel shows the SH/NH daily ratio for Hpi. The daily Hp estimates were averaged from hourly Hp averages. The means of the

ratios of the daily Hp averages are listed at the top of each plot. The 28-year mean of the ratio of daily Hpe median SH and NH values (not shown) is 1.0000, because one of the adjustments made in Paper 1 was to require that the median daily Hpe SH/NH ratios be approximately 1.0 over the lifetime of each satellite, as shown in Tables A.1 and A.2. However, daily average SH Hpe estimates were ∼2% larger than in the NH, and NH Hpi estimates were ∼2% larger than in the SH. Larger NH Hpi estimates can be traced back to NOAA-15 in Figure A.2, whose NH estimates were larger than in the SH for most of the years before 2004 as seen in the SH/NH ratio of the plot and as listed in Table A.1b.

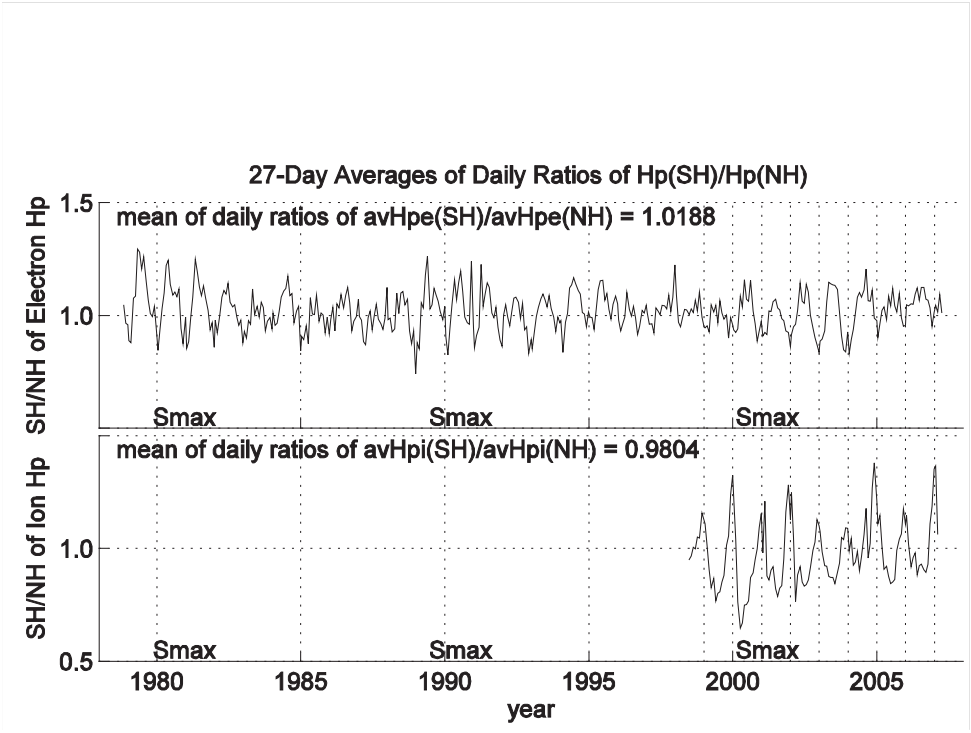


Figure A.6: Daily ratios of the daily average southern hemisphere (SH) Hpe (top panel) and Hpi (bottom panel) divided by daily average northern hemisphere (NH) Hp values are plotted as 27-day averages. The daily Hp averages are calculated from hourly Hp averages. The means of the daily SH/NH Hp ratios over the observation periods are listed. The seasonal variations of the electrons and ions are opposite to each other.

[37] Year boundaries, which occur during the SH summer, are shown as dotted lines in Figure A.6 for 1999-2007 and clearly demonstrate that Hpi is largest in the summer hemisphere while Hpe is smallest in the summer hemisphere. The seasonal variations are more distinct in the hourly average composites than in the individual satellite SH/NH ratios plotted in Figures A.1c and A.2. However, as in Figure A.1c, Hpe seasonal differences

appear to be as much as ±25% of the yearly average (or equinox values) in solar maximum and ∼ ±5% in solar minimum. For Hpi, solar cycle effects are not as easy to discern, and summer-winter extremes vary between ∼ ±10% in 2003-2004, to ∼ ±30% in 2000 or 2005. The Hpi seasonal variation is opposite to that of Hpe, and it appears to be larger.

### Interhemispheric Differences as Functions of Hemispheric Power Magnitudes

[38] *Ridley* [2007] calculated the difference between median daily NH Hpt and SH Hpt (<20 keV) as a function of daynumber from 25 years of NOAA estimates. The interhemispheric differences showed that winter solstice Hpt was ∼20% larger than summer solstice Hpt. Hpt is similar to Hpe since the Hpi component for <20 keV is ∼8% of Hpt (from Sections A.0.2 and A.0.3, and *Hubert et al.* [2002]). In the present study, we similarly binned adjusted composite hourly averaged NH and SH Hpe (<30 keV) and Hpi (<20 keV) and their interhemispheric differences as a function of daynumber according to the magnitudes of SH or NH Hpe and Hpi. The data were further separated into three Sa bins (Sa<100, 100-160, Sa>160). Ordering by Hp magnitude is consistent with how *Fuller-Rowell and Evans* [1987] ordered Hpt as a function of the magnitude of Hpt.

[39] The top panel of Figure A.7 displays the annual variation in the interhemispheric differences between hourly averaged SH Hpe and NH Hpe binned in daynumber and then averaged each day over 28 years. Global averages of Hpe (or the average of each hourly SH and NH Hpe) were confined to be between 10 and 12 GW for daily 10.7 cm solar flux (Sa) values of 160 or more. The bottom panel shows the same for 9 years of Hpi, where hourly average SH+NH Hpi were between 1.0 and 1.2 GW. Like *Ridley* [2007], we anticipate an annual cosine variation with a peak on daynumber 173, which is the winter solstice for the SH. The fitted cosine amplitude is 0.80 GW for Hpe and -0.18 GW for Hpi, representing a 1.60 GW (15%) increase in the winter solstice Hpe over summer, and a 0.36 GW (34%) increase of the summer solstice Hpi compared to winter.

[40] Figures A.8a and A.8b plot the seasonal variations as $Hpe_{ws}$ [1] and $Hpi_{ws}$ [2], where the winter-summer differences are twice the average of the fitted annual cosine magnitudes. Three Sa ranges are plotted for $Hpe_{ws}$, but Sa was not significant for $Hpi_{ws}$. Positive values are winter excesses while negative values are summer excesses. The lowest Hpe magnitudes exhibit summer excess Hpe compared to winter, while for global average Hpe >10 GW, winter Hpe values are larger than summer Hpe values. For global average Hpe >40 GW, the winter excesses in Hpe are ∼40%. The highest winter excesses are for the highest Sa values. *Ridley* [2007] estimated a 20% winter excess NOAA Hpt, which we would expect to be similar to Hpe. However, when we average the fractional seasonal variation over all magnitudes of global Hpe, weighting with the number of hourly values in each magnitude bin, we calculate an average Hpe winter excess of only 7% because the summer Hpe exceeds

[1] $Hpe_{ws} = [Hpe(winter) - Hpe(summer)]/Hpe(globalannualaverage)$
[2] $Hpi_{ws} = [Hpi(winter) - Hpi(summer)]/Hpi(globalannualaverage)$

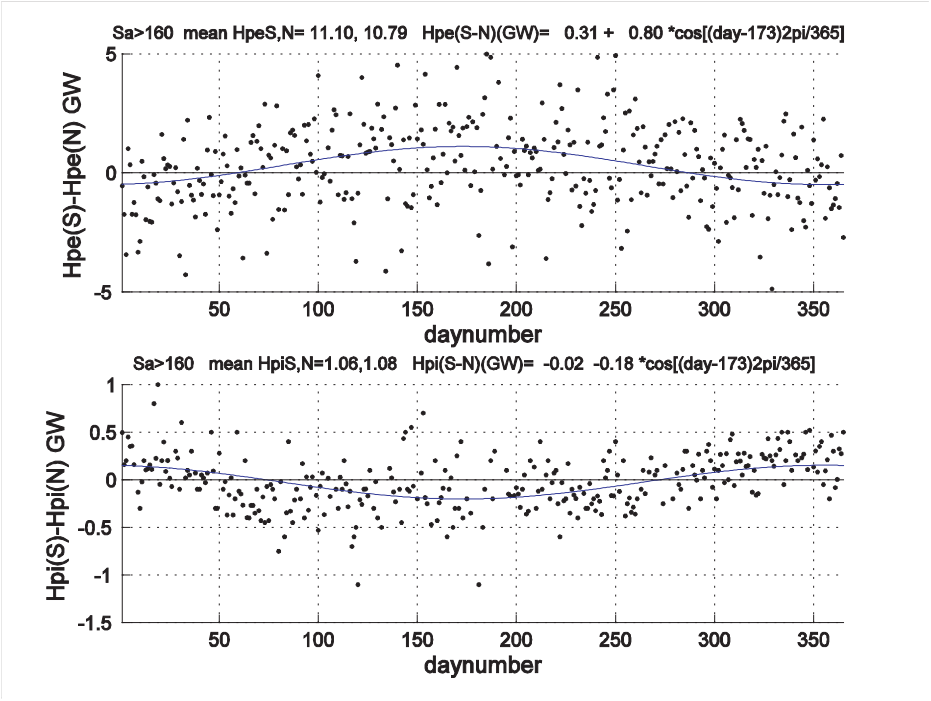


Figure A.7: NOAA/DMSP differences between SH and NH Hpe averaged in daynumber for hourly average (SH+NH) Hpe between 10 and 12 GW for Sa values above 160 sfu are in the top panel. The bottom panel show similar differences between NOAA SEM-2 SH and NH Hpi averaged in daynumber for hourly average (SH+NH) Hpi between 1 and 1.2 GW. Annual cosine fits to the differences for a peak at SH summer solstice are listed above the figures and are plotted as smooth curves.

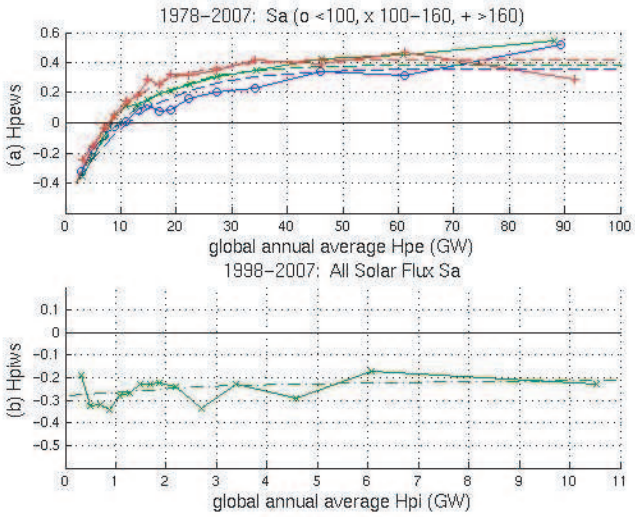


Figure A.8: (a) $\text{Hpe}_{ws}$ and (b) $\text{Hpi}_{ws}$ represent the fractional difference between winter and summer. The annual cosine amplitude is divided by the annual global average Hpe or Hpi. Three solar flux (Sa) levels are shown for Hpews, with dashed lines for the parameterizations at Sa=81, 131 and 199.

the winter Hpe ∼35% of the time. The largest summer Hpi excesses compared to winter in Figure A.8b are ∼35% for global Hpi<1 GW. Above ∼2 GW, the summer excess Hpi compared to winter is ∼20%. The average Hpi summer excess weighted by the number of hourly values in each magnitude bin is 28%.

[41] The fits of $Hpe_{ws}$versus the global annual average Hpe in Figure A.8a are plotted as dashed lines for Sa values of 81, 131 and 199 as

$$Hpe_{ws} = [0.32 + 0.0005\min(Sa, 250)] - [0.81 + 0.001min(Sa, 250)] * \exp\{-[0.06 + 0.00025\min(Sa, 250)]Hpe(global\ average)\} \quad \text{(A.3)}$$

The dashed line in Figure A.8b for $Hpi_{ws}$ is

$$Hpi_{ws} = -0.21 - 0.073 * \exp[-0.30Hpi(global\ average)] \quad \text{(A.4)}$$

### Discussion of Seasonal Variations

[42] The seasonal differences in Hpe of ∼ ±40% from Figure A.8a are within the range of the largest intersatellite adjustment factors listed in Tables A.1 and A.2, and so were not noted until *Ridley* [2007] and the present study. The electron aurora is composed mostly of diffuse precipitation from the central plasma sheet, with discrete arcs of usually higher

energies and larger energy fluxes on the poleward edge [e.g., *Heelis et al.* [1980]]. *Newell et al.* [1996b] used DMSP data to examine discrete aurora with intense electron acceleration events (i.e., energy fluxes >5 mW $m^{-2}$). The largest probability of finding these intense electron fluxes was ~6% in darkness from 20 to 23 MLT. *Coumans et al.* [2004a] found a similar probability of 7% between 21 and 24 MLT from 15 winter days of IMAGE FUV data. *Newell et al.* [1996b] found that these intense discrete auroral arcs are suppressed in sunlight by a factor of three. They suggested that the nightside seasonal variation is related to an ionospheric conductivity feedback mechanism where higher energy electrons from the magnetosphere are accelerated along field line potential drops into dark regions of low conductance. *Liou et al.* [2001] showed an increase in the typical pre-midnight auroral intensity from ~1.5 mW $m^{-2}$ in NH summer to ~2 mW $m^{-2}$ in NH winter from POLAR UVI images during solar minimum conditions.

[43] Using NH UVI images, *Liou et al.* [1997] found increasing electron energy flux from April to July during the day-time hours ~9 MLT and ~15 MLT. *Liou et al.* [2001] similarly found an increase in the dayside summer electron energy flux compared to winter, especially in the pre- and post-noon sectors. In Plate 3 of *Hardy et al.* [1985], DMSP electron energy fluxes on the dayside are approximately equal to the energy fluxes on the nightside for Kp 0. The nightside contribution to the total energy flux increases with increasing Kp, with the largest local energy fluxes in the post midnight sector. Thus for low magnitudes of Hpe, the summer dayside enhancements of the electron energy flux compared to equinox or winter found by *Liou et al.* [1997, 2001] outweigh the winter nightside increases in electron energy flux compared to summer found by *Liou et al.* [2001] and *Newell et al.* [1996b]. For higher Hpe magnitudes, the nightside winter increases in electron energy flux are more important compared to summer, leading to larger winter Hpe compared to summer Hpe. Figure A.8a shows summer Hpe exceeds winter Hpe ~35% of the time with low Hpe. However, winter Hpe usually exceeds summer Hpe, as seen in Figures A.1c, A.6, A.7, and A.8a.

[44] *Newell et al.* [2005] used DMSP data and *Coumans et al.* [2004a, 2006] used IMAGE FUV data to study seasonal variations in the ion energy flux. *Newell et al.* [2005] reported on ion fluxes >0.25 mW $m^{-2}$ based on 11 years of DMSP SSJ/4 observations from 1 January 1984 to 31 December 1994. NH winters (SH summers) from 1 December to 10 January were combined with SH winters (NH summers) from 1 June to 10 July. The largest ion energy fluxes were in the nighttime sector between 21 and 2 MLT. *Newell et al.* [2005] found an increase in the intense ion aurora in winter between 0 and 6 MLT compared to summer. This winter ion energy flux increase was ~15% in the most active post solar maximum years (1992-1994), and was ~31% in solar minimum (1984-1986). There was no summer/winter difference in ion energy input between 18 and 24 MLT, but there was an increase in dayside ion auroral flux in summer compared to winter. The summer dayside ion energy fluxes between 15 and 18 MLT in the solar minimum case were 57% larger than in winter. We estimated from the information in *Newell et al.* [2005], that their total DMSP Hpi (<30 keV) was approximately the same for summer and winter in solar minimum because summer dayside increases compensated for summer nightside decreases.

In solar maximum years, both winter and summer seasons showed an increase in the ion energy flux of nearly a factor of six in the pre-midnight region from 18 to 24 MLT compared to solar minimum years, thus reducing the importance of the dayside ion energy flux in solar maximum. From the information from *Newell et al.* [2005] presented above, we estimated DMSP Hpi to be ∼7% larger (half of the post-midnight 15% increase) in winter compared to summer during solar maximum. Using NOAA SEM-2 Hpi (<20 keV), our findings show summer Hpi to be larger than winter Hpi.

[45] *Coumans et al.* [2004a] compared SI12 proton images for 12 summer days (14-17, 21-28 June) and 15 winter days (15-29 December) in the northern hemisphere in 2000. The integrated proton flux of *Coumans et al.* [2004a] was ∼21% larger in summer than in winter for Kp ≤3 and ∼16% larger for Kp ≥4. The summer Hpi increase was mainly due to the increased latitudinal width of the precipitation from 8.3 degrees in winter to 13.5 degrees in summer. Figure 2 in *Coumans et al.* [2006] showed that the largest ion energy fluxes in both winter (77 days) and summer (82 days) during solar maximum (2000-2002) occurred between 0 and 2 MLT, which is similar to the result of *Newell et al.* [2005]. However, unlike the DMSP study of *Newell et al.* [2005], the ion energy fluxes in the post-midnight sector were larger in the two summers (2.6 and 3.0 GW) than in the two winters (1.3 and 1.4 GW). We calculated the SEM-2 summer and winter Hpi estimates (<20 keV) in the NH and SH for the same 159 days of the *Coumans et al.* [2006] IMAGE study and found the two NH summer and two SH summer Hpi estimates to be between 1.3 and 1.7 GW and the two NH winter and two SH winter estimates to be between 1.1 and 1.5 GW. These winter SEM-2 Hpi estimates were close to SI12 Hpi estimates, but the summer SEM-2 Hpi estimates were only ∼15-20% larger than winter and not a factor of two larger as found by *Coumans et al.* [2006].

[46] Similar to *Coumans et al.* [2004a], Figure 2 of *Coumans et al.* [2006] showed the nightside winter ion auroral oval was ∼8 degrees in width and expanded mostly poleward to 15-19 degrees wide for the 2000 summer and to 10-15 degrees wide for the 2001 summer. We estimated the nightside ion auroral widths from Figures 3-6 in *Newell et al.* [2005] for summer and winter to be ∼11 degrees in solar minimum and ∼15 degrees in post-solar-maximum. All three studies showed an increase in the latitude extent of ion aurora in summer on the dayside compared to winter.

[47] We found low-energy (<20 keV) Hpi to be larger in summer than in winter in Figures A.2, A.6, A.7, and A.8b, but we cannot determine the MLT variations or the width of the ion precipitation because the Hpi and Hpe estimates suppress such information. Our Hpi summer increases compared to winter are smaller than the IMAGE SI12 Hpi seasonal variations, and are opposite to the DMSP study by *Newell et al.* [2005] which found overall increases in the winter ion energy flux compared to summer in solar maximum.

## A.0.6 Hemispheric Power versus Kp

[48] The auroral energy input is well correlated to the level of magnetic activity represented by the Kp index, which is always available. Solar wind drivers of magnetic activity are the IMF $B_z$ component and the solar wind velocity ($V_{sw}$), which are not always available. For the present study, we binned the hourly average composite SH Hpe and Hpi values as a function of 3-hour Kp, hourly IMF $B_z$, hourly $V_{sw}$, and daily solar flux for two- or four-month seasons. The two-bin separation values for $B_z$ (- and +), $V_{sw}$ ($<$ and $>$ 430 km $s^{-1}$), and Sa ($<$ and $>$130) were chosen to have approximately the same number of statistics above and below. Multiple bins for $B_z$, $V_{sw}$, and Sa were chosen for other comparisons. Tables A.3a and A.3b list the hourly averaged SH NOAA/DMSP Hpe and SH NOAA SEM-2 Hpi values as a function of Kp and season for all conditions. All-season averages were found by first averaging the two-month fall and spring periods, which have similar Hpe and Hpi values, and then averaging over the three four-month seasons of winter, summer, and equinox. NH UVI Hpe all-season averages are also listed along with NH SI12 Hpi estimates from *Coumans et al.* [2006] and DMSP Hpe and Hpi estimates from *Hardy et al.* [1989].

### Electron Hemispheric Power as a Function of Kp

[49] Figure A.9a shows the SH hourly average Hpe ($<$30 keV) values binned in Kp. The diamonds are averages for all conditions (all-seasons in Table A.3a). The error bars represent $\pm 1$ standard deviation, and no symbol is plotted if there are less than 26 points in a Kp bin. A third-order polynomial fit to the diamonds, listed at the top of the plot is

$$Hpe(GW) = 2.5103 + 9.9207Kp - 2.1825Kp^2 + 0.3033Kp^3 \quad \text{(A.5)}$$

The seasonal variation is plotted around the polynomial fit as summer red dashed lines and winter blue dot-dashed lines using the formula

$$Hpe(GW) = Hpe(Kp)(1 \pm 0.5Hpe_{ws}) \quad \text{(A.6)}$$

where $Hpe(Kp)$ is from Eq. A.5 and Sa was assumed to be 130 in Eq. A.3 for $Hpe_{ws}$. The plus sign is for the winter curve and the minus sign is for the summer curve.

[50] The polynomial fit is relatively close to the linear fit for Kp 0-7 found by *Maeda et al.* [1989] using NOAA Hpt estimates between 1978 and 1985. The linear fit for Hpt is too small for Kp 8 and 9, but agrees well in general because the NOAA Hpt estimates were normalized to be consistent with NOAA-TIROS, which was close to the chosen Hpe baseline, as shown by the X1 factors close to 1.0 in Table A.1a. To keep the fit positive at Kp 0, an additional point of 3.55 GW was added at Kp=-0.2. A second-order polynomial fit of Hpe hourly averages to 3-hour ap (not plotted) was

$$Hpe(GW) = 8.8186 + 0.5457ap - 0.00053303ap^2 \quad \text{(A.7)}$$

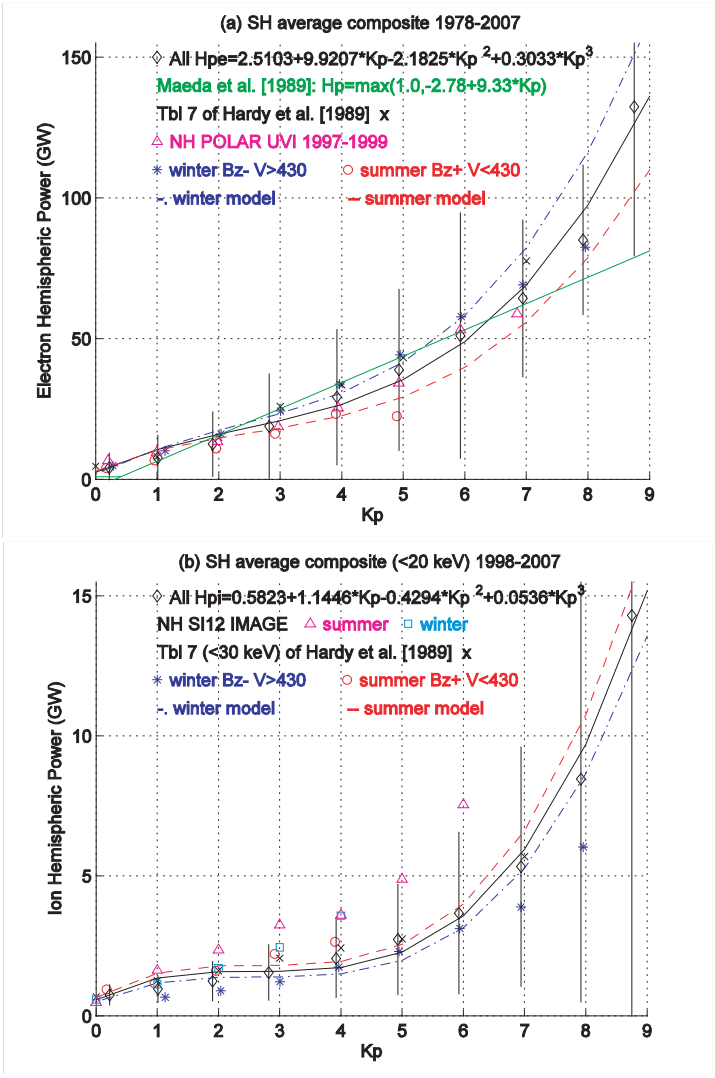


Figure A.9: (a) Southern hemisphere (SH) average hourly composite electron hemispheric power (Hpe) values are averaged in Kp bins between 1978 and 2007. The polynomial fit is to all the SH data, where the vertical bars are plus and minus one standard deviation. The model estimates for summer and winter are plotted as red dashed and blue dot-dashed lines about the polynomial fit where the solar flux (Sa) was assumed to be 130. No symbol is plotted if there are <25 hours in a bin. The dark green line is the linear fit from *Maeda et al.* [1989] using NOAA TIROS-standardized total hemispheric power estimates from 1978 to 1985. Hourly average Hpe estimates from UVI on POLAR in the NH from 1997-1999 are plotted as triangles. Values from DMSP-F6 and F7 between 1983-1984 from *Hardy et al.* [1989] are plotted as x's, where Kp $\geq$ 6- is arbitrarily plotted at Kp=7. (b) Similar to Figure A.9a except for SH ion hemispheric power (Hpi) values between 1998 and 2007 from four NOAA SEM-2 satellites. NH Hpi estimates from SI12 IMAGE in 2000 and 2001 are similar to *Coumans et al.* [2006], but separated into summer and winter.

[51] Seasonal variations are responsible for some of the variability within each Kp level, while IMF $B_z$ and $V_{sw}$ add additional variability. Each Kp level in Figure A.9a shows relatively low Hpe (red circles) during summer, $B_z$ positive, and low $V_{sw}$ conditions compared to relatively high Hpe (blue stars) during winter, $B_z$ negative, and high $V_{sw}$ conditions.

[52] Also plotted in Figure A.9a are the values from DMSP F6 (normalized to F7) and F7 in 1983-1984 from Table 7 of *Hardy et al.* [1989]. As shown in Table A.3a, the *Hardy et al.* [1989] DMSP Hpe are a little larger than the NOAA/DMSP Hpe over 28 years, which might be expected from Figure A.1b where the median Hpe is relatively large in 1983-1984.

[53] The average hourly NH POLAR UVI estimates of Hpe between 1997 and 1999 as a function of Kp are plotted in Figure A.9a, avoiding the periods around the fall equinoxes that were contaminated with light leaks. The UVI Hpe estimates are close to the NOAA/DMSP Hpe except for the lowest Kp levels where they are larger, possibly due to insufficient dayglow removal in the UVI images. Another possibility for the discrepancy could be an underestimate of low level quiet-time electron energy fluxes in the polar cap by NOAA and DMSP instruments.

[54] The fractional difference between four-month Hpe winter and summer over the average Hpe was computed (not plotted) as a function of Kp. Summer excess Hpe was seen for Kp 0 and 1 (at low magnitude Hpe), and winter excess Hpe was seen for Kp 2 to 6 with poor statistics for higher Kps. The NH UVI showed somewhat larger winter excess Hpe values than the SH NOAA/DMSP Hpe for Kp 1 to 5.

### Ion Hemispheric Power as a Function of Kp

[55] Figure A.9b shows all-season average Hpi values for all conditions from Table A.3b as diamonds. The third-order polynomial fit (black line) was achieved by adding an additional point at Kp=-0.2 of 0.73 GW to keep the Hpi value at Kp 0 positive:

$$Hpi(GW) = 0.5823 + 1.1446Kp - 0.4294Kp^2 + 0.0536Kp^3 \quad \text{(A.8)}$$

A first-order polynomial fit of hourly average Hpi estimates to 3-hour ap (not plotted) was

$$Hpi(GW) = 0.8290 + 0.0408ap \quad \text{(A.9)}$$

The seasonal variation in Hpi is plotted around the polynomial fit using the equation

$$Hpi(GW) = Hpi(Kp) * (1 \pm 0.5Hpi_{ws}) \quad \text{(A.10)}$$

which similar to Eq.A.6 for Hpe. Unlike Hpe in Figure A.9a, the summer Hpi curve is larger than the winter Hpi curve. Also unlike Hpe, the Hpi values at each Kp level for all seasons were slightly higher for $B_z$ positive conditions and low solar wind speeds, where

most of the $B_z$ positive and low $V_{sw}$ conditions were in the lower Kp levels. We will examine IMF $B_z$ and $V_{sw}$ conditions more in Section A.0.7.

[56] IMAGE SI12 Hpi estimates (>1 keV) from NH images for 40 days in summer (1 June - 10 July 2000) and 37 days in winter (3 Dec 2000 - 8 Jan 2001) were plotted in Figure 1 of *Coumans et al.* [2006] as a function of Kp. These IMAGE SI12 Hpi estimates were separated into summer and winter estimates and plotted in Figure A.7b, where statistics were good between Kp 1 and 5 for summer and between Kp 0 and 3 for winter. The SI12 values are larger than other estimates except at Kp 0, where they are ∼20% lower than other Hpi estimates, probably because SI12 Hpi estimates are insensitive to ion energies <1 keV. For Kp 1 and larger, the summer SI12 Hpi estimates are progressively larger than the Hpi estimates from DMSP (<30 keV) or from NOAA SEM-2 (<20 keV), which suggests ions of higher energies (>30 keV) become increasingly important in the total ion flux as Kp increases.

[57] The fractional difference between four-month winter and summer SH Hpi showed mostly summer excess Hpi in the entire Kp range (not plotted). The NH SI12 Hpi summer excess was a little larger than the NOAA SEM-2 SH Hpi summer excess.

### A.0.7 Electron and Ion Hemispheric Power as a Function of IMF $B_z$ and $V_{sw}$

[58] Many modelers prefer to use parameterizations in terms of IMF $B_z$ and solar wind velocity ($V_{sw}$) instead of Kp. *Brautigam et al.* [1991] binned DMSP electron and ion energy fluxes as a function of magnetic latitude and local time for various $B_z$ and $V_{sw}$ conditions to create global estimates of Hpe and Hpi. They found minimum values of Hpe for $B_z$ ∼4 nT, and minimum values of Hpi for $B_z$ ∼2 nT. The lines in Figure A.10 are similar to *Brautigam et al.* [1991], where we include 28 years of adjusted hourly averages of individual satellite track estimates of NOAA/DMSP Hpe and 9 years of NOAA SEM-2 Hpi. Both Hpe and Hpi increase strongly as a function of negative $B_z$. Hpi also increases strongly as a function of positive $B_z$ after a minimum around 1 nT. Hpe approximately doubles for $V_{sw}$ between 300 and 600 km/s in Figure A.10c, while the increases in Hpi with $V_{sw}$ in Figure A.10d are more modest except where the large increases in Hpi reflect larger magnitudes of $B_z$ at higher $V_{sw}$ velocities in the extreme $B_z$ bins. The same trends in Hpe and Hpi were also seen for each season (not shown). The minimum Hpe and Hpi values in Figure A.10 are not as low as the Hpe and Hpi values at Kp 0 in Figure A.9 or in Table A.3. Therefore, the quietest conditions are captured with Kp 0.

[59] DMSP Hpe and Hpi estimates (<30 keV) from Table 3 in *Brautigam et al.* [1991] (not plotted) were approximately the same magnitude as our NOAA/DMSP Hpe and Hpi for $B_z$ positive, but they were larger than our Hpe and Hpi for $B_z$ negative. The NH UVI

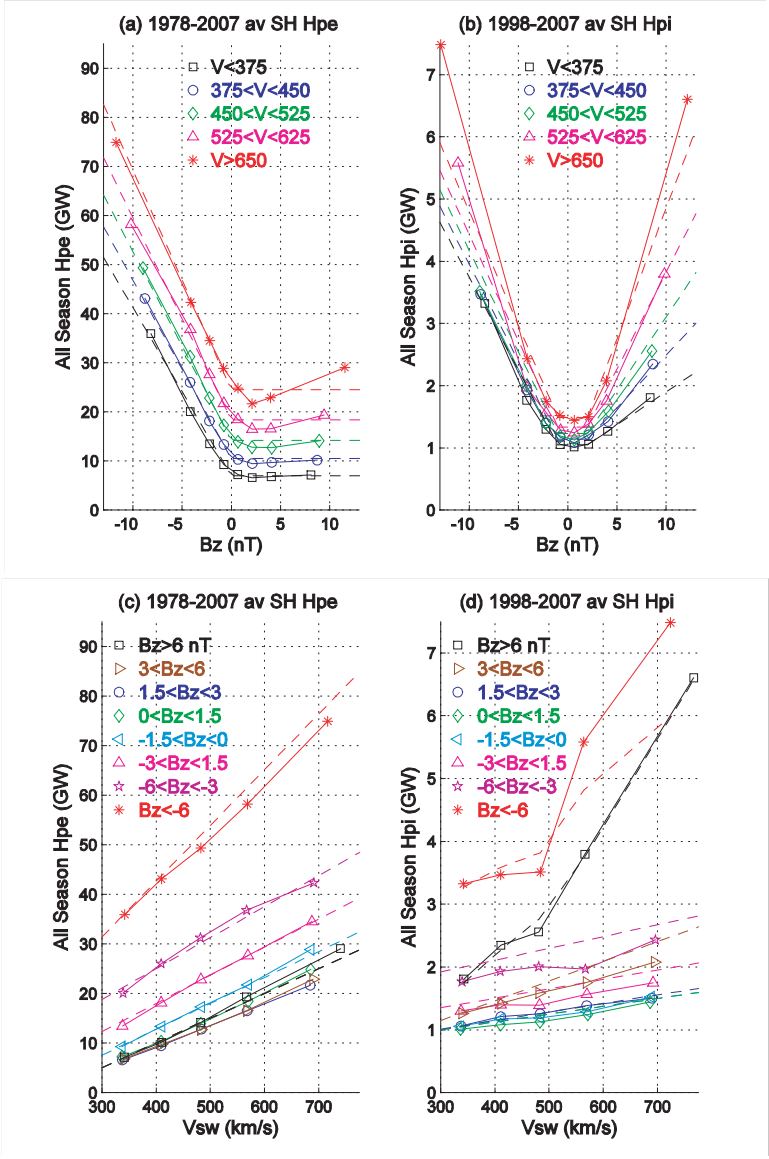


Figure A.10: Southern hemisphere (SH) average hourly composite (a) electron (Hpe) and (b) ion (Hpi) hemispheric power values are averaged in IMF $B_z$ and solar wind ($V_{sw}$) bins and plotted as solid lines as a function of $B_z$, similar to *Brautigam et al.* [1991]. Model parameterizations are dashed lines. Southern hemisphere (SH) average hourly composite (c) electron (Hpe) and (d) ion (Hpi) hemispheric power values are averaged in IMF $B_z$ and solar wind ($V_{sw}$) bins and plotted as solid lines as a function of $V_{sw}$, similar to *Brautigam et al.* [1991]. Model parameterizations are dashed lines.

Hpe (not shown) were similar in magnitude to our NOAA/DMSP Hpe for $B_z$ negative, but were ~3 GW higher for $B_z$ positive, which is similar to the excess UVI Hpe for Kp 0 and 1 in Table A.3a and in Figure A.9a.

[60] Hpe can be parameterized for negative $B_z$ as:

$$Hpe(B_z < 0) = 5.0 + 3.3|B_z\_neg| + (0.05 + 0.003|B_z\_neg|) * [\min(V_{sw}, 700) - 300] \quad \text{(A.11)}$$

where Hpe is in GW, $B_z$ in nT, and $V_{sw}$ in km $s^{-1}$. Hpe for zero or positive $B_z$ is:

$$Hpe(B_z \geq 0) = 5.0 + 0.05[\min(V_{sw}, 700) - 300] \quad \text{(A.12)}$$

which is the same as Eq. A.11 with $B_z$ set to zero. The model parameterizations are shown as dashed lines in Figures A.10a and A.10c.

[61] SEM-2 Hpi estimates in Figure A.10b for large positive $B_z$ are almost as large as those for large negative $B_z$. If we assume Hpi is a constant between $B_z$ -1 and +2 nT, Hpi can be parameterized as:

$$Hpi(B_z < -1nT) = 0.71 + 0.29|B_z\_neg| + (0.0002|B_z\_neg| + 0.00105)[\min(V_{sw}, 700) - 300] \quad \text{(A.13)}$$

and as:

$$Hpi(B_z > +2nT) = 0.86 + 0.07B_z\_pos + (0.0009B_z\_pos - 0.00055)[\min(V_{sw}, 700) - 300] \quad \text{(A.14)}$$

where these linear model estimates are plotted as dashed lines in Figures A.10b and A.10d using the actual binned values of $B_z$ as a function of $V_{sw}$ for the extreme $B_z$ bins in Figure A.10d. The constant values of Hpi between -1 and +2 nT are:

$$Hpi(-1 < B_z < +2nT) = 1.00 + 0.00125[\min(V_{sw}, 700) - 300] \quad \text{(A.15)}$$

[62] The Hpe and Hpi seasonal variations in Equations A.6 and A.10 can equally be applied to these parameterizations of Hpe and Hpi in $B_z$ and $V_{sw}$ in place of the Kp relations.

### A.0.8 Solar Flux Variations in Hemispheric Power

[63] We now examine how SH Hpe and Hpi change as a function of the 10.7 cm solar flux adjusted to 1 AU (Sa). The seasonal variations in Hpe are a function of Sa as shown in Figure A.8a, but do not show if Hpe decreases or increases with increasing Sa. Because Hpe and Hpi are very strong functions of $B_z$, we binned hourly Hpe and Hpi as a function of six Sa ranges (<85, 85-100, 100-130, 130-160, 160-190, >190) using the same $B_z$ and

$V_{sw}$ bins given in Figures A.10a and b. To increase statistics, we then combined various $B_z$ and $V_{sw}$ bins in Figure A.11 for winter and summer. Because the $B_z$ and $V_{sw}$ bins reflect the magnetic activity, the resulting variations of Hp with Sa should reflect the effect of the EUV flux.

[64] In Figure A.11a-f, Hpe increases with Sa for low $V_{sw}$and $B_z$>-3 nT. The increase is ∼25-30% for winter and ∼20% for summer for $V_{sw}$<375 km $s^{-1}$. We checked individual bins to see if there were biases in $B_z$ or $V_{sw}$. The $V_{sw}$ average varied up and down with increasing Sa, but $B_z$ generally decreased ∼0.05 nT from low to high Sa for -3<$B_z$<0 nT. Using the $B_z$_neg term in Eq. A.11, this corresponds to an increase of ∼0.2 GW, or ∼3% for Figure A.11c, which would exhibit the largest effect where the magnitude of Hpe is small. So, perhaps the Hpe increase with Sa for low $V_{sw}$ is really only ∼15-25% instead of ∼20-30%.

[65] For 375<$V_{sw}$<450 km $s^{-1}$, there was no Sa variation for $B_z$>3 nT. In winter for -3<$B_z$<3 nT in Figures A.11b and A.11d, Hpe increases ∼10% up to Sa ∼150. This is also characteristic of most winter seasons for $B_z$<3 nT. The summer Hpe in Figure A.11d increases ∼10% in the range. Most summer seasons are similar to Figure A.11b where the summer Hpe increases ∼10% up to Sa ∼100, and then drops to values similar to Sa ∼75. For $B_z$<-3 nT at all $V_{sw}$, the Hpe variations were similar to those in Figure A.11b, but with greater Hpe magnitudes and more separation between the seasons.

[66] The increasing difference between winter and summer Hpe with increasing Sa in the common pattern of Figure A.11b is the reason that there is a Sa variation in Figure A.8a. The winter to summer excess increases with Sa for Hpe>10 GW. Similarly, Figures A.11c and e show that winter and summer Hpe are similar over the Sa range for Hpe<8 GW, where Sa variations are not important in Figure A.8a.

[67] *Newell and Wing* [1998] found that discrete electron auroras in sunlight decrease with increasing 10.7 cm solar flux and also found that discrete auroras in darkness have no solar cycle dependence. Thus, summer aurora might be expected to decrease more than winter aurora with increasing solar flux. In our study, we find the opposite, where there is an increase of Hpe with Sa, especially for low $V_{sw}$, and that this increase is larger in winter than summer. Our increase with Sa is largest for low magnitudes of Hpe, or for low activities, and could reflect an increase in diffuse aurora with increasing EUV. For most conditions, the increase of Hpe with Sa is particularly strong for Sa<∼100, and then diminishes or is masked with increased magnetic activity.

[68] Figure A.11g shows the Hpi variation with Sa for -3<$B_z$<3 nT over all $V_{sw}$. The summer Hpi increases ∼50% from Sa 75-115, and then decreases to ∼33% by Sa 150. The winter Hpi increase is less at ∼35% up to Sa 115, and then decreases to ∼25% by Sa 175. More negative $B_z$ of ∼0.2 nT with increasing Sa result in an increase in Hpi from Eq. A.14 of ∼0.06 GW, or ∼8%, which is still less than the observed increase of Hpi with Sa. The

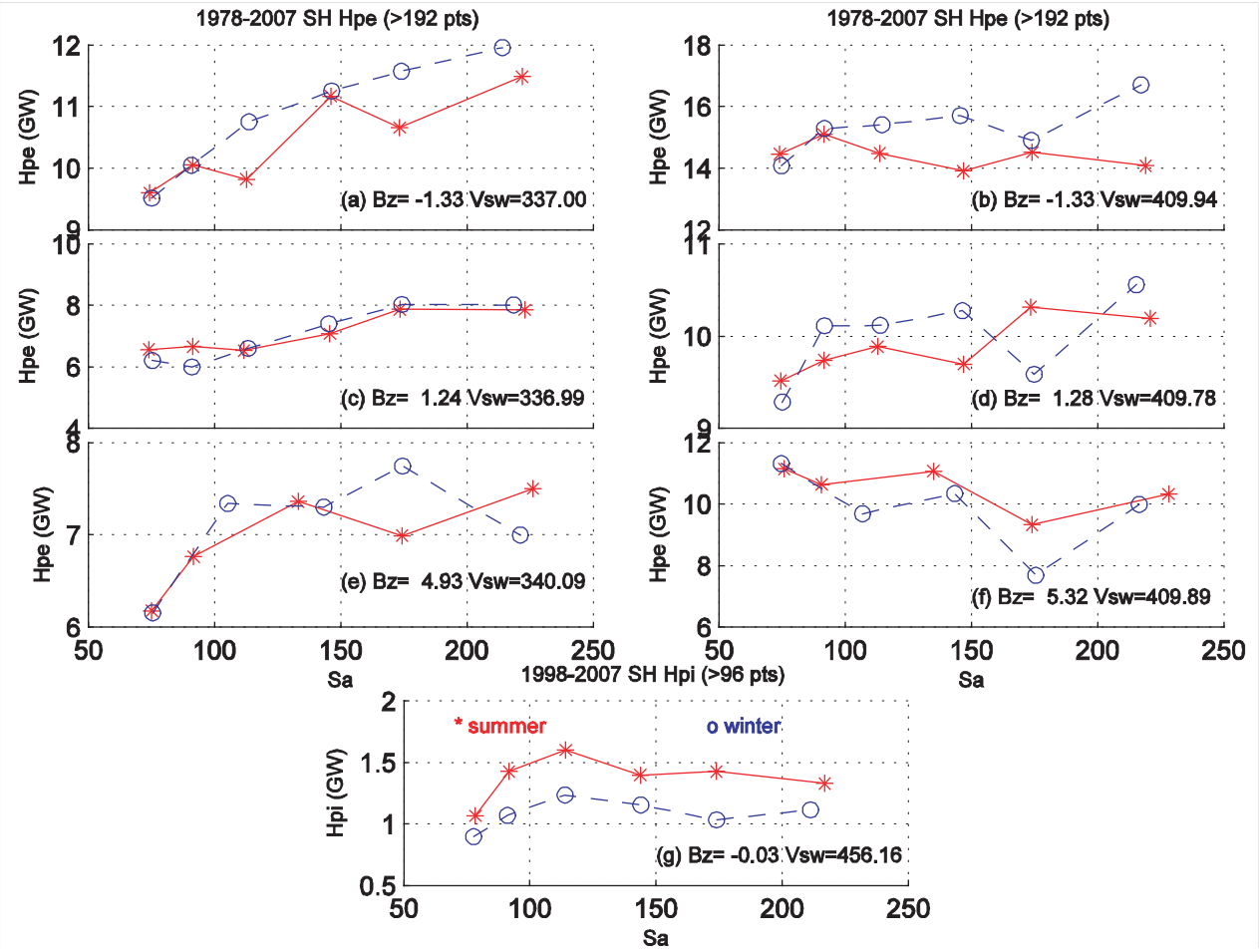


Figure A.11: (a-f) Hourly composite NOAA/DMSP SH Hpe are plotted for $V_{sw}$ <375 km $s^{-1}$ (left column) and 375<$V_{sw}$<450 km $s^{-1}$ (right column) as a function of Sa for summer (red stars) and winter (blue circles). The $B_z$ bins are different for each row at -3<$B_z$<0 nT (row 1), 0<$B_z$<3 nT (row 2), and $B_z$>3 nT (row 3). (g) Hourly composite NOAA SEM-2 SH Hpi are plotted for -3<$B_z$<3 nT and for all $V_{sw}$ as a function of Sa in summer and winter.

pattern in Figure A.11g is consistent for most of the individual $V_{sw}$ and $B_z$ bins. Because ions are more important at low activities (Section A.0.8), the increase of Hpi with EUV is more apparent for low Sa, and then could be masked by electrons or stronger activities at higher Sa. The increase of Hpi with increasing Sa is consistent with the study by *Newell et al.* [2005] which found that the ion energy flux in the 'active period' of 1992-1994 increased in the pre-midnight sector by a factor of six from solar minimum values 1984-1987.

[69] When we examined the Sa variation on bins based on the magnitude of the SH Hpe and Hpi, we found Hpe increased 8% (0.2 GW) with increasing Sa for all seasons for SH Hpe<4 GW, but no effect for larger magnitudes. This could reflect more active conditions with higher Sa, or an enhancement of Hpe with increasing EUV flux. For SH Hpi binned in magnitude, a 1-3% increase (0.01-0.02 GW) of SH Hpi with increasing Sa was found for SH Hpi magnitudes between 0.6-1.4GW.

## A.0.9 Modeling Hpe and Hpi

[70] The seasonal variations from Section A.0.5 can be combined with the estimated Sa variations in Section A.0.8 with any of the model Hpe parameterizations as:

$$Hpe(GW) = Hpe(Kp, ap, B_z/V_{sw}) * \{1 \pm 0.5 Hpe_{ws} \cos[(day - 173)2\pi/365] * \{1 + 0.0019 * [\min(Sa, 200) - 70]\}\} \ (if\ V_{sw} < 375 kms^{-1}\ and\ B_z > -3nT) \quad (A.16)$$

where the '+' is for the SH and the '-' is for the NH. A 25% increase in Hpe from Sa ~70 to ~200 is estimated in the last term for $V_{sw}$<375 km $s^{-1}$ and $B_z$>-3 nT. The ~10% winter increases in Hpe up to Sa ~150 for most other periods for $B_z$<3 nT are not included. Hpi can be modeled as:

$$Hpi(GW) = Hpi(Kp, ap, B_z/V_{sw}) * \{1 \pm 0.5 Hpi_{ws} \cos[(day - 173)2\pi/365] * \{1 + 0.008 * [\min(Sa, 115) - 70]\}\} \quad (A.17)$$

where the '+' is for the SH and the '-' is for the NH. The last term indicates a 35% increase in Hpi from Sa ~70 to ~115 in the last term. Hpe or Hpi($K_p$,ap,$B_z/V_{sw}$) are the Kp, ap, or $B_z$ and $V_{sw}$ approximations of the all-season (or equinox) Hp found in Eqs. A.5, A.7, A.8, A.9, A.11-A.12, A.13-A.15, or other formulae.

## A.0.10 Summary and Conclusions

[71] Estimates of the hemispheric power of precipitating auroral particles from different NOAA and DMSP satellites were recalibrated after correcting for sensor degradations, noise and other problems. The best intersatellite correlations were in the SH, where the

auroral coverage was better.

[72] The intersatellite adjustments to a baseline for Hpe (<30 keV) from Tables A.1 and A.2 were within a factor of two for all 24 satellites. The magnitude of the ion baseline (<20 keV) from four NOAA SEM-2 satellites was doubled (X1 divisors in Table A.1b ∼0.5) in order to be compatible with, i.e. ∼77% of, the DMSP Hpi (<30 keV) of *Hardy et al.* [1989] for Kp 1-3. SH/NH ratios of Hpe and Hpi were adjusted to be ∼1.0 over the lifetimes of the satellites. Individual adjusted satellite Hpe and Hpi estimates and hourly estimates from all satellites can be obtained from the CEDAR Database at http://cedarweb.hao.ucar.edu/. Using SH hourly averages, the 28-year average Hpe (<30 keV) was 17.4 GW, while the 9-year average Hpi (<20 keV) was 1.45 GW, or 8% of the total Hpt 'average' of 18.85 GW.

[73] In the present study, the largest ion fraction (<20 keV) of Hpt in the SH was ∼19% during Kp 0, summer, $B_z$ positive, and low $V_{sw}$ conditions, and the smallest was ∼5% during Kp 2-7, winter, $B_z$ negative, and high $V_{sw}$ conditions. This is consistent with the DMSP ion fraction (<30 keV) of ∼17% to ∼8% of the total found by *Brautigam et al.* [1991] for similar conditions. Inclusion of higher ion (<2.5 MeV) and electron (<1 MeV) energies increased the ion fraction of the total energy flux to ∼30% for low activities and to ∼10% for high activities.

[74] The median hourly POLAR UVI NH Hpe estimates from 1997-1999 agreed with similar estimates from NOAA/DMSP. In case studies, adjusted NOAA and DMSP Hpe agreed with POLAR UVI or IMAGE FUV Hpe ∼<25 GW, but were usually lower than UVI and FUV Hpe values for more active conditions. Adjusted NOAA SEM-2 Hpi (<20 keV) were similar to IMAGE SI12 Hpi (>1 keV) when Hpi estimates were between ∼1 and 4 GW. For quiet conditions, the SI12 Hpi missed ion energy fluxes <1 keV, and for active conditions, the NOAA Hpi values missed ion energy fluxes >20 keV.

[75] The ratio of daily average SH Hpe to NH Hpe is greater than 1.0 in June and less than 1.0 in December (Fig. A.6), corresponding to a solstice winter increase over summer. But ∼35% of the time, summer solstice Hpe exceeded winter Hpe, with maximum summer excesses of ∼30% for the lowest Hpe magnitudes (∼3 GW). Maximum winter solstice excesses were ∼35-40% for Hpe >∼40 GW, with the largest winter excesses for large Sa (Fig. A.8a). A weighted average of the fractional winter excess over all Hpe magnitudes was 7%. This is less than the estimate of ∼20% winter solstice increase compared to summer from *Ridley* [2007] using 25 years of NOAA Hpt estimates. The increase of winter Hpe compared to summer is consistent with the suppression of discrete arcs between 20 and 23 MLT in sunlight [*Newell et al.*, 1996b]. The increase of summer Hpe compared to winter for low Hpe (Fig. A.8a) is consistent with the summer sunlit enhancement of soft electron aurora in the pre- and post-noon sectors [*Liou et al.*, 1997, 2001] because the dayside contribution to the total aurora is greatest during quiet periods [e.g., *Hardy et al.* [1985]].

[76] The seasonal variation of the ratio of SH Hpi to NH Hpi is opposite to that for Hpe,

with values greater than 1.0 in December and less than 1.0 in June (Fig. A.6). Summer solstice Hpi excesses maximized ∼30% for Hpi <∼1.5 GW and decreased to ∼20% for larger Hpi. The summer over winter increase in NOAA SEM-2 Hpi agrees with the IMAGE SI12 FUV seasonal Hpi estimates of *Coumans et al.* [2004a, 2006], but disagrees with the DMSP Hpi estimates of *Newell et al.* [2005], who found extra winter ion energy fluxes compared to summer during solar maximum conditions.

[77] Average hourly SH NOAA/DMSP Hpe and NOAA SEM-2 Hpi were binned in Kp and as a function of IMF $B_z$ and $V_{sw}$. Hpe and Hpi estimates as a function of $B_z$ and $V_{sw}$ were similar to the results found by *Brautigam et al.* [1991]. Hpi minimized for $B_z$ around 1.5 nT, and increased almost as much for large positive $B_z$ as for large negative $B_z$. Hpe and Hpi increased with increasing $V_{sw}$, where the Hpi increases were relatively modest. NOAA/DMSP Hpe agreed with NH POLAR UVI Hpe for negative $B_z$ conditions. The UVI Hpe estimates were ∼2-3 GW larger than NOAA/DMSP SH Hpe for low Kp (Table A.3a) and for positive $B_z$ conditions. For Kp 4 and above, NH IMAGE FUV Hpi were approximately double NOAA SEM-2 Hpi (Table A.3b) because ions >30 keV contribute about half the total Hpi during active periods [*Fang et al.*, 2007].

[78] Hpe values increased ∼25% for Sa increasing from ∼70 to ∼200 for low $V_{sw}$ and $B_z$>-3 nT. At larger $V_{sw}$, winter Hpe increased ∼10% from Sa ∼70 to ∼150, while summer Hpe increased ∼10% from Sa ∼70 to ∼100, and then decreased. The winter-summer excess Hpe increased with Sa>100. The Hpe increase with increasing Sa is opposite to the observation by *Newell and Wing* [1998] that discrete aurora in sunlight decrease linearly with the 10.7 cm solar flux. However, our results show the biggest EUV (Sa in discrete $B_z/V_{sw}$ bins) responses for low activities when most of the aurora is diffuse. Hpi values increased ∼35-50% for Sa increasing from ∼70 to ∼115, and then decreased slightly. The increase of Hpi with increasing solar flux is consistent with the finding by *Newell et al.* [2005] of a six fold increase of ion energy flux in the post-midnight region from 0 to 6 MLT between low and high solar flux.

[79] This study confirms the finding of *Ridley* [2007] that seasonal (interhemispheric) variations are present in electron (total) hemispheric power estimates. We extend that study to show the seasonal Hpe variations change from summer to winter excesses with increasing Hpe magnitudes. This is the first time variations in Hpe and Hpi as a function of 10.7 cm solar flux (Sa) have been estimated. The seasonal, solar flux, and $B_z/V_{sw}$ fits to Hpe are new, as are the Kp/ap fits to Hpi.

[80] The global maps used to estimate DMSP electron and NOAA electron and total hemispheric power are based on NOAA total hemispheric power [*Fuller-Rowell and Evans*, 1987]. The ion and electron energy fluxes were added together from both hemispheres assuming conjugacy and did not allow for seasonal or interhemispheric differences. It would be useful if these global maps could be updated to include the observed seasonal differences, and separated into ion and electron ovals with different auroral locations, widths,

and characteristics.

[81] Several global models (e.g. *Marsh et al.* [2007]) currently use the *Maeda et al.* [1989] formula with Kp to estimate the auroral input. The linear formula of *Maeda et al.* [1989] for Hpt is relatively close to the third-order polynomial function we found for Hpe except at the highest Kp levels, where the Maeda formula underestimates Hpt. We presented various fits for Hpe ($<$30 keV) and for Hpi ($<$20 keV). These formulae can be used in global models to estimate both the electron and ion auroral inputs. Although we showed solar flux variations in this paper, a major question that remains is: 'Why were the variations in the electron auroral energy input so different in the last three solar cycles?' We will attempt to explain this in a future paper in terms of high speed solar wind streams.

| Name | Start-Stop | AscN LT +/- S/N | NOAA Y0 | SH/X1[] | NH/X1[] | Init/Adj SH/NH |
|---|---|---|---|---|---|---|
| TIROS | 78306-81058 | 1500 LT + S | 1.00 | 1.04 | 0.97 | 1.062/0.990 |
| NOAA-06[a] | 79190-86321 | 1929 LT - S | 0.80 | 1.244[0.995] | 1.238[0.99] | 1.016/1.012 |
| NOAA-07[b] | 81192-85041 | 1430 LT + S | 1.21 | 0.785[0.95] | 0.785[0.95] | 0.972/0.996 |
| NOAA-08 | 83129-85287 | 1931 LT + S | 1.63 | 0.583[0.95] | 0.638[1.04] | 0.925/1.012 |
| NOAA-10[c] | 86289-91125* | 1930 LT - S | 1.00 | 0.75 | 0.73 | 1.004/0.978 |
| NOAA-12[d] | 91155-06277* | 1930 LT - S | 1.00 | 1.72 | 1.78 | 0.972/1.001 |
| NOAA-14[e] | 95019-06277* | 1400 LT + S | 1.00 | 0.84 | 0.84 | 1.119/1.001 |

| Name | Start-Stop | AscN LT +/- S/N | NOAA Y0 | SH/X1[] | NH/X1[] | Init/Adj SH/NH |
|---|---|---|---|---|---|---|
| NOAA-15[f] | 98182-present | 2000 LT - S | 2.70 | 0.663[1.79] | 0.737[1.99] | 0.898/0.999 |
| | Electrons only | | | 0.604[1.63] | 0.667[1.80] | 0.906/1.004 |
| | Ions only | | | 0.459[1.24] | 0.537[1.45] | 0.842/0.985 |
| NOAA-16[g] | 00286-present | 1400 LT + S | 1.95 | 0.836[1.63] | 0.856[1.67] | 0.980/1.004 |
| | Electrons only | | | 0.785[1.53] | 0.805[1.57] | 0.973/0.999 |
| | Ions only | | | 0.487[0.95] | 0.467[0.91] | 1.000/0.966 |
| NOAA-17 | 02193-present | 2200 LT + S | 2.59 | 0.660[1.71] | 0.676[1.75] | 0.982/1.005 |
| | Electrons only | | | 0.610[1.58] | 0.618[1.60] | 1.000/1.013 |
| | Ions only | | | 0.382[0.99] | 0.409[1.06] | 0.929/0.994 |
| NOAA-18[h] | 05157*-present | 1400 LT - S | 1.80* | 0.844[1.52] | 0.833[1.50] | 1.046/1.032 |
| | Electrons only | | | 0.783[1.41] | 0.767[1.38] | 1.037/1.015 |
| | Ions only | | | 0.567[1.02] | 0.511[0.92] | 1.103/0.995 |
| MetOp-02[i] | 06337-present | 2130 LT S | 2.00* | 0.900[1.80] | 0.910[1.82] | 1.0003/1.011 |

Table A.1: NOAA Satellite Characteristics and Corrections to Baseline Electron or Ion Hemispheric Power

Table A.1 : Table of NOAA satellite names, operational dates (two-digit year and three-digit daynumber of year), ascending (Asc) local time (LT) at the equator towards the northern hemisphere (NH) where +/- means the orbit precesses to later/earlier LTs, various "correction" factors, and the lifetime ratio of the daily median hemispheric power (Hp) estimates of the southern hemisphere (SH) over the NH from the initial ("Init") data and from the final adjusted ("Adj") data. A "*" on the operational dates indicates a shorter period of good data. With a 98 degree inclination, the highest NH latitude is reached about 6 hours earlier in LT than the ascending time, and the highest SH latitude is about 6 hours later, so an "S" (or an "N") means the SH (or NH) nightside aurora is favored. All NOAA satellites favor the SH nightside aurora ("S"). Orbit characteristics are also located at http://www.osdpd.noaa.gov/PSB/NAVIGATION/navpage.html. The NOAA multipliers (Y0) achieve consistency with the TIROS or NOAA-12 "standards" for satellites that are not subject to spurious noise counts. The adjustment factors (X) in the present study are divisors, and there can be more than one adjustment (X1 to X5) if noise or data dropouts affect the data as listed in the footnotes. (For noise corrections, ydf is the year with fractional days.) The adjustment factors X in brackets are the corrections using the NOAA standard multiplier factors Y0 ([X1] = X1 x NOAA Y0), so the X factors outside the brackets give the real range of the calibration adjustments.

**Table A.1a**: NOAA SEM-1 satellites : The total hemispheric power estimates from the NOAA SEM-1 (300 eV to 20 keV) satellites are corrected to a common baseline electron hemispheric power.

**Table A.1b**: NOAA SEM-2 satellites :The total and electron hemispheric power estimates from the NOAA SEM-2 (50 eV to 20 keV) satellites are corrected to a common baseline electron hemispheric power and the remaining ion hemispheric power estimates are corrected to a common baseline ion hemispheric power. The adjustment factors X1 in brackets are the corrections using the NOAA standard multiplier factors Y0, so the X1 factors outside the brackets give the real range of the calibration adjustments ([X1] = X1 x NOAA Y0).

[a] After 1985.0, NOAA-06 experienced a 20%/yr increase from noise: SH, NH X=(X1*(1+ydf-1985.0)*0.20)

[b] After 83218, NOAA-07 experienced noise which was more in the NH: SH X2=0.87[1.05], NH X2=0.92[1.11]

[c] Spurious noise for NOAA-10; 80%/yr increase between 87136-88059: X=X1*(1+(ydf-1987.370)*0.80); a software "fix" started 88001, gap 88060-88274, but noise increased, 88275-88366: SH X2=3.03, NH X2=3.12; abandoned data after 88366*

[d] Analysis terminated for NOAA-12 after 02203*; less reliable in-flight analysis data from 05191 to 06277 with NH X2=1.59

[e] Analysis terminated for NOAA-14 after 04366*; less reliable in-flight analysis data from 05191 to 06277. Spurious noise changed frequently: 100%/yr increase 1995.0-1996.9: X=X1*(1+(ydf-1995.0)*1.00); stable 1996.9-1998.0: SH X2=2.38, NH X2=2.43; 23%/yr decrease 1998: X=X2*(1-(ydf-1998.0)*0.23); stable 99001-01036: SH X3=1.83, NH X3=1.87; mode change 01036 increased noise threshold, 2%/yr decrease 01037-04366: SH X4=1.38, NH X4=0.95, X=X4*(1-(ydf-2001.099)*0.02); 05001-06277 in-flight analysis: SH X5=1.23, NH X5=1.32

[f] Sensor degradation for NOAA-15 of ∼2%/yr after 2004.0: X=X1*(1-(ydf-2004.0)*0.02)

[h] Sensor degradation for NOAA-16 of ∼4%/yr from 2004.0 to 2005.5: X=X1*(1-(ydf-2004.0)*0.04); sensor degradation of ∼8%/yr after 2005.5: SH X2=1.53[t],1.44[e],0.89[i], NH X2=1.57,1.48,0.86, X=X2*(1-(ydf-2005.5)*0.08)

[h] Usable start date for NOAA-18 on 05180*; analysis completely revised in July 2006 with change in NOAA Y0.

[i] NOAA Y0 consistency factor for MetOp-02 assumed 2.00 until the end of the first six months of operation. No Hpe (or Hpi) calculated.

| Name | Start-Stop | AscN LT +/- S/N | SH/X1 | NH/X1 | Init/Adj SH/NH |
|---|---|---|---|---|---|
| DMSP-F06 | 83001-87203 | 0600 LT o N | 1.02 | 0.92 | 1.101/0.993 |
| DMSP-F07[a] | 83320-88117 | 1030 LT o N | 1.025 | 1.085 | 0.943/0.998 |
| DMSP-F08 | 87176-94213 | 0610 LT o N | 0.92 | 0.98 | 0.943/1.005 |
| DMSP-F09[b] | 88039-92094 | 0932 LT - N | 1.27 | 1.36 | 1.202/1.002 |
| DMSP-F10[c] | 90341*-97318 | 1944 LT + S | 0.83 | 0.77 | 1.024/0.989 |
| DMSP-F11[d] | 91337-00137* | 1659 LT + S | 0.63 | 0.565 | 1.094/0.993 |
| DMSP-F12[e] | 95005-02113* | 2049 LT - S | 0.88 | 0.81 | 1.188/1.001 |
| DMSP-F13 | 95089-present | 1711 LT + S | 0.99 | 1.01 | 0.977/0.996 |
| DMSP-F14[f] | 97118-present* | 2035 LT - S | 1.43 | 1.43 | 1.000/1.000 |
| DMSP-F15[g] | 99351-05094* | 2110 LT - S | 1.37 | 1.35 | 1.017/1.003 |
| DMSP-F16[h] | 03300-present | 2000 LT + S | 0.81 | 0.75 | 1.070/0.990 |
| DMSP-F17 | 06315-present | 1733 LT o S | 1.13 | 1.16 | 0.960/0.985 |

Table A.2: DMSP Satellite Characteristics and Corrections to Baseline Electron Hemispheric Power

Table A.2 : This table is similar to Table A.1 except for DMSP satellites which estimate the electron hemispheric power (Hpe) from two electron detectors (32 eV to 30.18 keV). The first four DMSP satellites (F06-F09) favor the NH nightside aurora while the later satellites favor the SH nightside aurora. Orbit LT crossings over a satellite lifetime are available at https://swx.plh.af.mil/dmsp/ssiesdmspgeneral.html with a login from AFRL, where satellites drift to earlier ("-") or later ("+") LTs, or drift very little in LT ("o"). The adjustment factors (X) in the present study are divisors, and there can be more than one adjustment (X1 to X4) if noise or data dropouts affect the data as listed in the footnotes. The summer sunlight contamination in the SH DMSP-F09 and F10 was initially deleted by eliminating the most affected UTs and daynumbers as listed in the footnotes. Later, the sunlight contamination was fitted to smooth curves as a function of UT and daynumber, and subtracted from all the affected UTs to recover the data and find the X divisor adjustments and SH/NH ratios listed below. The instrument package for the DMSP satellites is SSJ/4 for DMSP-F06 to F15, and is SSJ/5 for DMSP-F16 to F17. The SSJ/5 has 100 times the collection area of SSJ/4 so more background noise.

[a] DMSP-F07 data gap 88026-88115, some tape noise (not adjusted for)

[b] DMSP-F09 SH summer sunlight contamination for daynumbers $>$ 275 and $<$ 60 for all UTs except 1000-1659 UT which are acceptable

[c] Elliptical orbit for DMSP-F10, usable start date 90353*; SH sunlight contamination varied first 3 summers: 91001-91059 acceptable UTs 1000-1259, 91291-92059 acceptable UTs 1100-1259, 92291-93059 acceptable UTs 0800-1259; variable noise; 70%/yr increase1992.480-1992.70, X=X1*(1+(ydf-1992.480)*0.70); >1992.70 SH X3=0.96; 1992.70-1993.176 NH X3=0.89; after 1993.175 NH X4=1.09 because the Thule dropouts are severe after 93064.

[d] Tape noise on DMSP-F11 started 99087, delete data after 99105*

[e] DMSP-F12 NH summer gaps 95115-95228, 96116-96225; NH Thule dropouts after 98048, tape noise 1998, delete data after 98351*

[f] Sensor degradation on DMSP-F14 ∼11%/yr after 2001.0 not completely removed by AFRL post-flight yearly electron high energy detector (EHED) corrections so used annual adjustments X=X1*(Revised EHED*/DMSP EHED) where the ratio in parentheses multiplying X1 is (0.885/0.941) for 2001, (0.775/0.944) for 2002 and (0.665/0.866) for 2003; NH Thule dropouts after 98333; poor spectrograms starting in 2003, delete data after 03324 although have low Hpe values earlier and AFRL produces Hpe estimates up to 05094.

[g] Sensor degradation on DMSP-F15 ∼5.5%/yr after 2001.0 and ∼10.5%/yr after 2005.0 not completely removed by AFRL post-flight yearly electron high energy detector (EHED) corrections, so used annual adjustments X=X1*(Revised EHED*/DMSP EHED) where the ratio in parentheses multiplying X1 is (0.970/1.000) for 2001, (0.915/1.000) for 2002, (0.860/0.968) for 2003, (0.805/0.950) for 2004, (0.712/0.855) for 2005, (0.625/0.760) for 2006, and (0.591/0.760) for 2007. [h] Analysis for DMSP-F16 completely revised in May 2006.

Table A.3 : The composite adjusted NOAA/DMSP hourly averages of the southern hemisphere (SH) electron hemispheric power (Hpe <30 keV) and NOAA SEM-2 ion hemispheric power (Hpi <20 keV) in GW are shown as a function of Kp and season. The SH seasons and daynumbers for non-leap years are: summer (295-049), winter (112-231), fall (50-111) and spring (232-294), where the equinox periods are half the length of the solstice periods. All-season averages from three seasons, averaging fall and spring together into equinox, are also given. Estimates for periods with 25 hours are preceded by '∼'. The Hpe composite hourly averages are from November 1978 to February 2007, while the Hpi averages are from July 1998 to February 2007. Northern hemisphere (NH) UVI POLAR Hpe estimates are between 1997 and 1999 and are shown as a function of season where the fall period (*) includes 16-33 winter days with light leaks. The UVI fall equinox period exhibits the light leak enhancements, and is not included in the all-season average. The DMSP Hpe (extrapolated to 100 keV) and Hpi (<30 keV) estimates are from *Hardy et al.* [1989] using DMSP-F06 and F07 in 1983-1984 where the values for Kp=6- were included in Kp=7. The SI12 Hpi ( 1 keV to over 30 keV) all-season estimates are from *Coumans et al.* [2006], along with the summer and winter values used in our study where '∼' is for <100 images.

| Kp | SH summer | NH UVI summer | SH winter | NH UVI winter | SH fall | NH UVI fall* | SH spring | NH UVI spring | SH all-seas | NH UVI all-seas* | NH+SH DMSP |
|---|---|---|---|---|---|---|---|---|---|---|---|
| 0 to 0+ | 4.58 | 7.04 | 3.84 | 5.74 | 3.98 | 13.59 | 4.09 | 7.49 | 4.15 | 6.76 | 4.68 |
| 1- to 1+ | 7.92 | 8.68 | 7.53 | 10.03 | 7.25 | 15.22 | 7.69 | 10.05 | 7.64 | 9.59 | 8.14 |
| 2- to 2+ | 12.75 | 12.48 | 11.88 | 14.10 | 12.64 | 21.29 | 13.34 | 14.12 | 12.54 | 13.57 | 14.9 |
| 3- to 3+ | 17.75 | 17.68 | 18.82 | 19.23 | 19.52 | 29.21 | 20.45 | 19.30 | 18.85 | 18.74 | 25.9 |
| 4- to 4+ | 26.39 | 21.96 | 32.02 | 31.01 | 28.91 | 37.42 | 29.75 | 23.35 | 29.25 | 25.44 | 33.6 |
| 5- to 5+ | 36.10 | 29.53 | 42.35 | 36.65 | 38.12 | 43.19 | 38.60 | 36.52 | 38.94 | 34.23 | 43.2 |
| 6- to 6+ | 50.70 | 43.53 | 52.92 | 64.26 | 49.39 | 61.04 | 49.79 | ∼51.76 | 51.07 | 53.18 | |
| 7- to 7+ | 64.65 | ∼31.84 | 64.92 | ∼71.11 | 62.97 | 73.98 | 63.97 | ∼73.70 | 64.35 | 58.88 | 77.6 |
| 8- to 8+ | 89.60 | ∼13.82 | 73.58 | | 89.08 | ∼97.68 | 94.98 | | 85.07 | | |
| 9- to 9 | 129.39 | | 134.05 | | ∼137.33 | | ∼129.82 | | 132.34 | | |

| Kp | SH summer | NH SI12 summer | SH winter | NH SI12 winter | SH fall | SH spring | SH all-seas | NH SI12 all-seas | NH+SH DMSP |
|---|---|---|---|---|---|---|---|---|---|
| 0 to 0+ | 0.89 | 0.49 | 0.61 | 0.58 | 0.77 | 0.77 | 0.75 | 0.54 | 0.674 |
| 1- to 1+ | 1.08 | 1.63 | 0.85 | 1.13 | 0.95 | 0.98 | 0.96 | 1.35 | 1.26 |
| 2- to 2+ | 1.39 | 2.36 | 1.10 | 1.71 | 1.23 | 1.24 | 1.24 | 2.05 | 1.61 |
| 3- to 3+ | 1.67 | 3.25 | 1.46 | 2.45 | 1.51 | 1.57 | 1.55 | 2.98 | 2.06 |
| 4- to 4+ | 2.12 | 3.60 | 2.02 | 3.58 | 1.94 | 2.09 | 2.05 | 3.62 | 2.43 |
| 5- to 5+ | 2.98 | 4.88 | 2.59 | | 2.55 | 2.70 | 2.73 | 4.87 | 2.75 |
| 6- to 6+ | 4.23 | 7.54 | 3.34 | ∼3.23 | 3.61 | 3.27 | 3.67 | 6.56 | |
| 7- to 7+ | 6.36 | | 4.38 | | 4.99 | 5.51 | 5.33 | | 5.69 |
| 8- to 8+ | 10.70 | | 6.70 | | ∼10.80 | ∼5.16 | 8.46 | | |
| 9- to 9 | 15.33 | | ∼10.23 | | ∼21.99 | ∼12.67 | 14.30 | | |

Table A.3: (a) Electron and (b) Ion Hemispheric Power as a Function of Kp and Season

# Annexe B

# High resolution FUV observations of proton aurora

D. H. Chua, K. F. Dymond, S. A. Budzien
Thermospheric and Ionospheric Research and Applications Group, Naval Research Laboratory, Washington, DC

R. P. McCoy
Office of Naval Research, Arlington, Virginia

J.-C. Gérard, V. Coumans
Laboratoire de Physique Atmosphérique et Planétaire, Université de Liège

D. Bisikalo, and V. Shematovich
Institute of Astronomy, Russian Academy of Sciences, Moscow

*Published in Geophysical Research Letters (September 24, 2003)*

## Abstract

[1] *We present new FUV observations of Doppler-shifted Lyman-α emissions from proton aurora obtained from the High Resolution Ionospheric and Thermospheric Spectrograph (HITS) aboard the Advanced Research and Global Observation Satellite (ARGOS). The HITS instrument observes the Doppler-shifted H Lyman-a emissions from proton precipitation with 1.5 Å resolution. The high spectral resolution of these measurements allows the auroral Lyman-α emissions to be separated from the intense geocoronal background. The measured proton aurora Doppler spectra are modeled using a Monte Carlo simulation of proton flux transport. The forward modeling performed with this code allows us to infer the characteristic energies of the incident protons from the measured Lyman-α Doppler spectra. The inferred characteristics of dayside versus nightside proton precipitation are compared and used to identify the magnetospheric regions from which the particles likely originated.*

### B.0.11 Introduction

[2] Energetic protons originating from the ring current, radiation belts, and the plasma sheet precipitate into the upper atmosphere with some distribution in pitch angle and energy. The incident protons undergo collisions and experience charge exchange reactions with atmospheric constituents. Upon capturing an electron in a charge exchange interaction, a precipitating proton will propagate as an energetic hydrogen atom that preserves the velocity and direction of the original proton. If the hydrogen atom is in an electronically excited state, deexcitation may occur through photon emission. These emissions will be (red-) blue-shifted as it moves (away) toward an observer. Spectroscopic measurement of these Doppler shifts therefore provides a means of inferring precipitating proton energies, as was demonstrated by the pioneering work of *Vegard* [1939] and *Meinel* [1951] from ground-based measurements of H Balmer lines.

[3] Far-ultraviolet (FUV) measurements of H Lyman-$\alpha$ emissions from satellite-borne instruments have extended our capabilities for remote sensing of proton precipitation with greater spatial coverage and the ability to make observations under sunlit conditions in the dayside auroral regions. Recent efforts to better understand the synoptic structure of the proton aurora have been driven by the availability of global images of Doppler-shifted H Lyman-$\alpha$ emissions obtained by the IMAGE/SI-12 instrument [*Mende et al.*, 2000a, 2001]. To complement these global observations, high resolution spectral measurements of proton aurora with large spatial coverage are essential. Such data are obtained by the High Resolution Ionospheric and Thermospheric Spectrograph (HITS) aboard the Advanced Research and Global Observation Satellite (ARGOS) which provides detailed FUVobservations of both the airglow and aurora. The HITS instrument is a $f/5.4$ 1-meter Rowland circle spectrograph with a 100 Å selectable passband within the 500 - 1700 Å range. Individual HITS spectra have a time resolution of 1-second although these are typically averaged over longer time periods to improve the counting statistics. Over a 60-second interval HITS scans across approximately 200 km along the satellite track. The HITS field of view spans about 230 km in the cross track direction. The HITS observations offer two key advantages for proton aurora studies:

[4] (1) The spectral resolution of HITS achieved on orbit is about 1.5 Å (full-width, half-maximum). This is sufficient to separate the emissions from the geocorona at the Lyman-$\alpha$ rest wavelength and the Doppler-shifted Lyman-$\alpha$ emissions arising from proton precipitation. The inability to isolate these two Lyman-$\alpha$ components was a significant impediment toward detailed analyses of proton aurora spectra in previous studies.

[5] (2) The HITS proton aurora measurements from the ARGOS spacecraft are available in both dayside and nightside regions in both northern and southern hemispheres. The ARGOS spacecraft is in a 98.7 inclination, sun-synchronous 0230/1430MLT polar orbit at 850 km altitude. While HITS is usually a limb-scanning instrument, the observations shown in this study are taken when HITS was set in a fixed viewing orientation wherein

the angle between the HITS look vector and the spacecraft nadir vector is about 60 .

[6] The purpose of this report is to present the initial results from our study of high resolution spectral observations of proton aurora. The characteristics of proton aurora observed in the dayside auroral zone are contrasted with those seen in the nightside. The interpretation of the HITS proton aurora observations is aided with the use of a Monte Carlo model of proton and hydrogen transport and their interactions with the neutral atmosphere.

## B.0.12 HITS Observations

[7] HITS spectra obtained during the recovery phase of a substorm (AE $\geq$ 250 nT, Kp = $5^+$) on December 30, 1999 are shown in Figure B.1. The left-most panels show HITS auroral spectra in the northern (Figure B.1A) and southern (Figure B.1B) hemispheres. The wavelength scale (Å) and universal time are shown along each abscissa and ordinate respectively. The Apex magnetic latitude (MLAT) and magnetic local time (MLT) [*Richmond*, 1995] of the observations are shown along the secondary y-axes. Also shown is $\theta$, the angle between the HITS look vector and the local IGRF magnetic field. The spectral emission rates are color coded in units of kiloRayleighs per Angstrom (kR $Å^{-1}$).

[8] The H Lyman-$\alpha$ emissions are the most prominent feature in these HITS spectra. Two components of this emission can be distinguished here: the ubiquitous geocoronal Lyman-$\alpha$ airglow at the rest wavelength (1215.67 Å) and Doppler-shifted Lyman-$\alpha$ emissions arising from precipitating protons. The latter appear as enhanced emissions in the wings of the Lyman-$\alpha$ line within a narrow band of latitudes. In the southern hemisphere proton aurora are observed in the pre-midnight sector (2300 MLT) between -61° and -64° MLAT (Figure B.1B). During the pass over the northern polar cap HITS observes proton aurora emissions in both the dayside (1000 MLT) and nightside (0400 - 0500 MLT) auroral zones (Figure B.1A).

[9] Another important feature in the HITS dayglow and auroral spectra shown in Figure B.1 is the NI 1200 Å triplet. Since the 1200 Å emission arises in part from electron impact excitation, it serves as a useful indicator of the electron aurora's location relative to the proton aurora. Additional weak spectral features with emission rates less than 50 R$Å^{-1}$ are present in Figures B.1A and B.1B, including the NI 1167 Å, 1176 Å, 1243 Å, and OI 1172 Å emission lines.

[10] In order to extract the Doppler-shifted Lyman-$\alpha$ proton aurora emissions from the HITS spectra it is necessary to first remove the geocoronal Lyman-$\alpha$ background. We measure the peak emission rate of the geocoronal Lyman-$\alpha$ line as a function of solar zenith angle outside the auroral regions where there are no contributions from proton aurora. This variation is modeled using a cosine squared function given in equation (1)

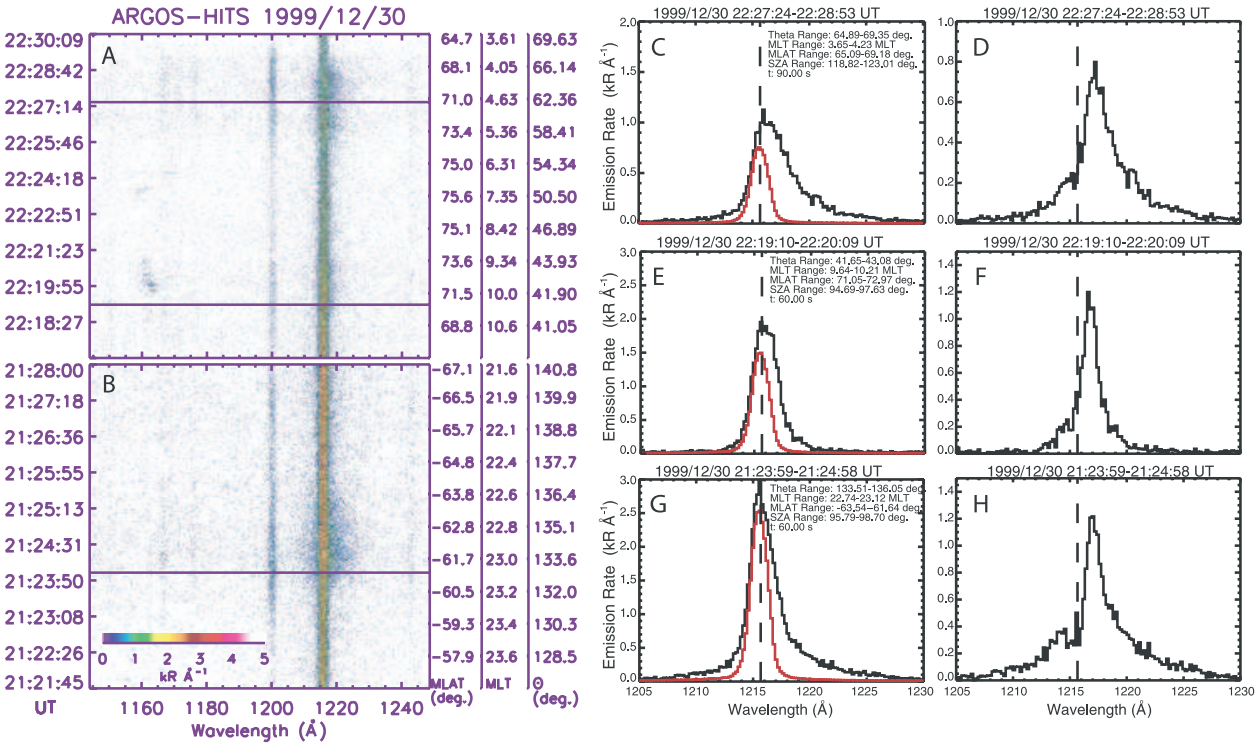


Figure B.1: HITS FUV auroral spectra in the northern (A) and southern (B) hemispheres. Panels C, E, and G show representative auroral spectra (black curves) and the estimated geocoronal Lyman-$\alpha$ contribution to the total line profile (red curves). Panels D, F, and H show the proton aurora Doppler spectra following subtraction of the geocoronal component. The vertical dashed lines in panels C-H denote the Lyman-$\alpha$ rest wavelength.

where $\Phi_{SZA}$ is the solar zenith angle and $A_{0,1,2}$ are the fit parameters.

$$I = A_0 \cos^2(A_1 \Phi_{SZA}) + A_2 \tag{B.1}$$

An example of the geocoronal Lyman-$\alpha$ peak intensity versus solar zenith angle and the model fit using equation B.1 is shown in Figure B.2. Once the model is fit to the data, the expected geocoronal Lyman-$\alpha$ peak intensity at the auroral location of interest is computed using the fit parameters. The geocoronal background Lyman-$\alpha$ line shape is formed by convolving a delta function valued at the modeled peak intensity at the auroral location with the HITS line spread function. The resulting geocoronal Lyman-$\alpha$ line is then subtracted from the HITS spectra to yield the Doppler profile of the proton aurora emissions.

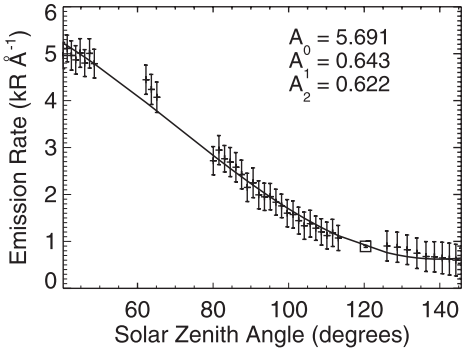


Figure B.2: Geocoronal Lyman-$\alpha$ peak intensity versus solar zenith angle. The model fit to the data using equation (1) is shown by the solid line. The data point near the solar zenith angle of 120 corresponds to the proton aurora location and shows the expected geocoronal Lyman-$\alpha$ peak intensity there based on the model fit.

[11] Three examples of proton aurora spectra are given in Figures B.1C, B.1E, and B.2G at the times indicated by the horizontal lines in Figures B.1A and B.1B. The auroral spectra (shown in black) are averaged over the amount of time, t, shown in each plot to improve the counting statistics. The red curve in each plot shows the modeled Lyman-$\alpha$ line used in subtracting the geocoronal background from the auroral spectra. The proton aurora Doppler spectra following geocoronal background subtraction are shown in Figures B.1D, B.1F, and B.1H. We quantify these profiles by defining characteristic widths for the red and blue wings of the Doppler spectra as follows: $\Delta\lambda_{red} = \frac{\int_{\lambda_{Ly\alpha}}^{\lambda_{max}} \lambda I(\lambda) d\lambda}{\int_{\lambda_{Ly\alpha}}^{\lambda_{max}} I(\lambda) d\lambda} - \lambda_{Ly\alpha}$ ; $\Delta\lambda_{blue} = \lambda_{Ly\alpha} - \frac{\int_{\lambda_{min}}^{\lambda_{Ly\alpha}} \lambda I(\lambda) d\lambda}{\int_{\lambda_{min}}^{\lambda_{Ly\alpha}} I(\lambda) d\lambda}$. Here $\lambda_{Ly\alpha}$ is the H Lyman-$\alpha$ rest wavelength and I($\lambda$) is the spectral emission rate at each observed wavelength. $\lambda_{min}$ and $\lambda_{max}$ are the lower and upper limits of integration for the blue and red widths. These are set to $\lambda_{min}$ = 1210.0Å and

$\lambda_{max}$ = 1230.0Å, corresponding to $H/H^+$ energies of 10.3 keV (upward propagating) and 64.4 keV (downward propagating) respectively. The characteristic red and blue widths indicate the hardness of the$H/H^+$ distributions giving rise to the measured emissions: larger spectral widths correspond to more energetic $H/H^+$ populations.

[12] During the orbit shown in Figure B.1A, dayside proton aurora is observed between 22:19 - 22:21 UT in the high latitude (70 - 73 MLAT) pre-noon sector (1000 MLT). Subtracting the modeled geocoronal Lyman-$\alpha$ line yields the dayside proton aurora Doppler spectrum shown in Figure B.1F. The red-shifted wing of this dayside proton aurora spectrum peaks at 1216.6 Å and is narrow with a characteristic width of 2.1 Å. The faint blue wing of this dayside proton Doppler spectrum indicates the presence of a weak backscattered $H/H^+$ component. The emission rates in the blue wing of the dayside proton spectrum are less than 150 Rayleighs and the characteristic width is 1.3 Å.

[13] Doppler-shifted $H/H^+$ emissions in the nightside proton aurora extend beyond 1225.0 Å which is indicative of higher energy proton precipitation. Near the equatorward region of the northern auroral zone (65 - 69 MLAT), between 22:27:24 - 22:28:53 UT, HITS observes a broad red wing in the proton aurora spectrum with a characteristic width of 3.4 Å (Figures B.1C and B.1D). The peak in the Doppler-shifted proton aurora spectra appears at 1217.2 Å. A stronger blue wing is seen here than on the dayside aurora with a characteristic blue width of 1.8 Å. The proton aurora observed by HITS between 21:24 - 21:25 UT in the southern hemsiphere, pre-midnight sector is similar to that measured in the post-midnight, northern hemisphere (Figures B.1G and B.1H). Here, the peak in the Doppler profile occurs at 1217.0 Å and the characteristic red and blue widths are 3.5 Å and 2.1 Å respectively (Figures B.1G and B.1H).

### B.0.13 Model Comparison

[14] In Figure B.3 the HITS proton aurora spectra (black curves) are compared to synthetic Doppler-shifted Lyman-$\alpha$ line profiles (gray curves) produced by a Monte Carlo simulation of proton and hydrogen transport. Protons with some distribution in pitch angle and energy (i.e. Maxwellian, kappa, mono-energetic) are input into a MSIS-90 model atmosphere [*Hedin*, 1991] and their transport through the neutral atmosphere is described by solving a set of coupled Boltzmann equations. The model includes elastic and inelastic collisions, ionization, and charge exchange. Further details of the model are described by *Gérard et al.* [2000]. The excitation of Lyman-$\alpha$ emissions is computed and a synthetic Lyman-$\alpha$ Doppler profile matching the HITS viewing geometry and convolved with the HITS line spread function is produced. The input parameters of the forward model are varied until the $\chi^2$ statistic is minimized when comparing the predicted and observed proton aurora spectra. In each case, the proton aurora line profile produced by the model is added to the geocoronal Lyman-$\alpha$ line (from Figures B.1C, B.1E, and B.1G) in order to reproduce the original HITS spectral measurement. For this study we assume an isotropic pitch angle distribution for the protons input into the model. The incident protons are given a kappa

energy distribution ($\kappa = 3.5$) and the proton characteristic energies ($E_0$) are varied between 100 eV and 25 keV.

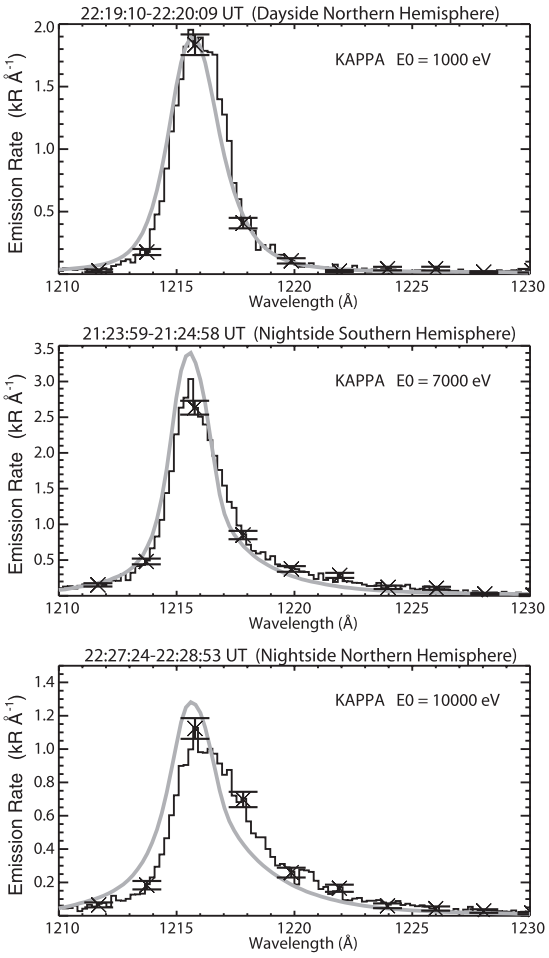


Figure B.3: Monte Carlo model fits to proton aurora Doppler spectra observed by HITS in the dayside northern hemisphere (top), nightside southern hemisphere (middle), and the nightside northern hemisphere (bottom).

[15] For the narrowly-peaked dayside proton spectrum the observed Doppler profile is best fit by an input proton distribution with a characteristic energy near 1 keV (Figure B.3, top panel). The model reproduces the peak in the auroral spectrum well, and we see good agreement in the predicted and observed red wing emissions longward of 1217 Å. The model predicts a larger backscattered $H/H^+$ component than the observed spectra shows, since the blue wing of the modeled spectrum is more intense than that measured.

[16] The proton aurora spectrum measured by HITS in the nightside southern hemisphere is best matched by precipitating protons with a characteristic energy of 7 keV (Figure B.3, middle panel). The model closely reproduces the observed blue wing of the proton spectrum, indicating that the fraction of backscattered $H/H^+$ from the input proton beam is estimated well. The model overestimates the peak in the auroral spectrum by 13% and underestimates the intensity of the red wing relative to the observations. The bottom panel of Figure B.3 shows the comparison of the spectrum measured by HITS in the northern, nightside auroral zone and the modeled Doppler profile arising from proton precipitation with a characteristic energy of 10 keV. While the general shape of the modeled proton aurora Doppler profile is similar to that of the observations, the HITS spectrum appears red shifted by about 1 Å relative to the model prediction. The peak of the modeled Lyman-$\alpha$ line profile is also about 20% more intense than the observed spectrum.

## B.0.14 Discussion and Conclusions

[17] The characteristics of the precipitating protons inferred from the HITS observations allude to their likely origins in the magnetosphere. With a narrow Doppler spectrum and an inferred characteristic energy near 1 keV, the precipitating protons observed by HITS in the dayside aurora near the northern polar cap probably represent a magnetosheath-like population originating from either the mantle or low-latitude boundary layer (LLBL). The observed dayside proton aurora is not likely to be associated with $H/H^+$ precipitation from the cusp since the HITS measurement was taken in the pre-noon sector during a period when the $B_y$ component of the interplanetary magnetic field (IMF) was strongly positive (not shown). Previous studies have shown that the cusp is located in the post-noon sector when the IMF $B_y$ component is positive [*Frey et al.* [2002], for example]. The nightside proton aurora seen by HITS is consistent with $H/H^+$precipitation from the plasma sheet, given the relatively broad Doppler profiles and inferred characteristic energies in the 7 - 10 keV range.

[18] The synthetic proton aurora spectra produced by the Monte Carlo $H/H^+$ transport model agreed well with the observed Doppler profiles in two of the three cases shown (Figure B.3). In the third case, the predicted and observed proton spectra had similar profiles but the measured spectrum appeared red-shifted relative to the model spectrum. One explanation for this is that the incident proton beam is not isotropic as we have assumed in the model. If the pitch angle distribution of the incident protons is more field-aligned, the fraction of incident particles that continue to be scattered downward to produce red-shifted emissions increases relative to the fraction that can undergo either magnetic mirroring or sufficient scattering to change their pitch angles beyond 90 . This produces Doppler spectra with peaks at longer red-shifted wavelengths and with diminished blue wings. Figure 4 of *Gérard et al.* [2000] illustrates this behavior.

[19] One situation in which the above scenario would be likely is if the nightside northern

hemisphere proton spectrum shown in Figures B.1C and B.3 was obtained equatorward of the proton isotropy boundary (IB) [*Sergeev et al.*, 1983] in a low-latitude proton precipitation (LLPP) region [*Gvozdevsky et al.* [1997], and references therein]. Normally the flux of trapped protons ($J_t$) and the flux of precipitating protons ($J_p$) are comparable poleward of the proton isotropy boundary (isotropic proton flux distribution). Equatorward of the isotropy boundary $J_t$ remains high while $J_p$ usually drops rapidly. However during LLPP events there is an enhanced flux of precipitating protons equatorward of the isotropic boundary caused by the partial filling of the loss cone by a moderate amount of pitch angle scattering. The proton pitch angle distributions in LLPP regions are usually anisotropic ($J_p/J_t < 1$). LLPP typically occur following substorms, as is the case for our observations.

[20] Further studies of proton aurora using HITS observations will include establishing a quantitative relationship between the observed red and blue widths of the Doppler profiles ($\Delta\lambda_{red}$, $\Delta\lambda_{blue}$) and the characteristic energies of the incident protons inferred by the Monte Carlo proton transport model. Coordinated observations between HITS and global images from the IMAGE/SI-12 instrument will also enrich our understanding of the large scale structure and dynamics of proton aurora.

# Bibliographie


Ahn, B. H., S.-I. Akasofu, and Y. Kamide (1983), The joule heat production rate and the particle energy injection rate as a function of the geomagnetic indices ae and al, *J. Geophys. Res.*, *88*, 6275.

Ajello, J. M., and D. E. Shemansky (1985), A reexamination of important $N_2$ cross sections by electron impact with application to the dayglow : The Lyman-Birge-Hopfield band System and N I (119.99 nm), *J. Geophys. Res.*, *90*, 9845.

Akasofu, S.-I. (1964), The development of the auroral substrom, *Planet. Space Sci.*, *12*, 273.

Akasofu, S.-I. (1981), Energy coupling between the solar wind and the magnetosphere, *Space Sc. Rev.*, *28*, 121.

Arnoldy, R. L. (1971), Signature in the interplanetary medium for substorms, *J. Geophys. Res.*, *76*, 5189.

Atkinson, G. (1970), Auroral arcs : Result of the interaction of a dynamic magnetosphere with the ionosphere, *J. Geophys. Res.*, *75*, 4764.

Baker, D. N., A. J. Klimas, D. Vassiliadis, T. I. Pulkkinen, and R. L. McPherron (1997), Reexamination of driven and unloading aspects of magnetospheric substorms, *J. Geophys. Res.*, *102*, 7169, doi :10.1029/96JA02627.

Baker, D. N., T. I. Pulkkinen, J. Büchner, and A. J. Klimas (1999), Substorms : A global instability of the magnetosphere-ionosphere system, *J. Geophys. Res.*, *104*, 14,601, doi : 10.1029/1999JA900162.

Banks, P. M., and A. F. Nagy (1970), Concerning the influence of elastic scattering upon photoelectron transport and escape, *J. Geophys. Res.*, *75*, 1902.

Banks, P. M., C. R. Chappell, and A. F. Nagy (1974), A new model for the interaction of auroral electrons with the atmosphere : Spectral degradation, backscatter, optical emission, and ionization, *J. Geophys. Res.*, *79*, 1459.

Basu, B., J. R. Jasperse, R. M. Robinson, R. R. Vondrak, and D. S. Evans (1987), Linear transport theory of auroral proton precipitation : A comparison with observations, *J. Geophys. Res.*, *92*, 5920.

Baumjohann, W., G. Paschmann, and C. A. Cattell (1989), Average plasma properties in the central plasma sheet, *J. Geophys. Res.*, *94*, 6597.

Bilitza, D. E. (1990), International Reference Ionosphere 1990, NSSDC 90-22.

Bisikalo, D. V., V. I. Shematovich, J.-C. Gérard, M. Meurant, S. B. Mende, and H. U. Frey (2003), Remote sensing of the proton aurora characteristics from IMAGE-FUV, *Ann. Geophys.*, *21*, 2165.

Borovsky, J. E. (1993), Auroral arc thicknesses as predicted by various theories, *J. Geophys. Res.*, *98*, 6101.

Brautigam, D. H., M. S. Gussenhoven, and D. A. Hardy (1991), A statistical study on the effects of imf $b_z$ and solar wind speed on aurora ion and electron precipitation, *J. Geophys. Res.*, *96*, 5525.

Brekke, A., and C. Hall (1988), Auroral ionospheric quiet summer time conductances, *Ann. Geophys.*, *6*, 361.

Brekke, A., C. Hall, and T. L. Hansen (1989), Auroral ionospheric conductances during disturbed conditions, *Ann. Geophys.*, *7*, 269.

Brittnacher, M., M. Fillingim, G. Parks, G. Germany, and J. Spann (1999), Polar cap area and boundary motion during substorms, *J. Geophys. Res.*, *104*, 12,251, doi : 10.1029/1998JA900097.

Burch, J. L. (2000), Image mission overview, *Space Science Reviews*, *91*, 1.

Carlson, C. W., R. F. Pfaff, and J. G. Watzin (1998), The Fast Auroral SnapshoT (FAST) mission, *Geophys. Res. Lett.*, *25*, 2013.

Chapman, S., and V. A. Ferraro (1930), A new theory of magnetic storms, *Nature*, *126*, 129.

Chua, D., G. Parks, M. Brittnacher, W. Peria, G. Germany, J. Spann, and C. Carlson (2001), Energy characteristics of auroral electron precipitation : A comparison of substorms and pressure pulse related auroral activity, *J. Geophys. Res.*, *106*, 5945.

Clemmons, J. H., et al. (2000), Observations of traveling pc5 waves and their relation to the magnetic cloud event of January 1997, *J. Geophys. Res.*, *105*, 5441.

Codrescu, M. V., T. J. Fuller-Rowell, R. G. Roble, and D. S. Evans (1997), Medium energy particle precipitation influences on the mesosphere and lower thermosphere, *J. Geophys. Res.*, *102*, 19,977.

Codrescu, M. V. T. J. F.-R., and I. S. Kutiev (1997), Modeling the f-layer during specific geomagnetic storms, *J. Geophys. Res.*, *102*, 14,315.

Collin, H. L., W. K. Peterson, O. W. Lennartsson, and J. F. Drake (1998), The seasonal variation of the auroral ion beams, *Geophys. Res. Lett.*, *25*, 4071.

Coumans, V., J. C. Gérard, B. Hubert, and D. S. Evans (2002), Electron and proton excitation of the fuv aurora : Simultaneous image and noaa observations, *J. Geophys. Res.*, *107*(A11), 1347, doi :10.1029/2001JA009233.

Coumans, V., J.-C. Gérard, B. Hubert, S. B. Mende, and S. W. H. Cowley (2004a), Morphology and seasonal variations of global auroral proton precipitation observed by IMAGE-FUV, *J. Geophys. Res.*, *109*(A12205), doi :10.1029/2003JA010348.

Coumans, V., J.-C. Gérard, B. Hubert, M. Meurant, and S. B. Mende (2004b), Global auroral conductance distribution due to electron and proton precipitation from IMAGE-FUV observations, *Ann. Geophys.*, *22*, 1595.

Coumans, V., J.-C. Gérard, B. Hubert, and M. Meurant (2006), Global auroral proton precipitation observed by IMAGE - FUV : Noon and midnight brightness dependence on solar wind characteristics and IMF orientation, *J. Geophys. Res.*, *111*, doi : 10.1029/2005JA011317.

Cowley, S. W. H., and E. J. Bunce (2001), Origin of the main auroral oval in Jupiter's coupled magnetosphere-ionosphere system, *Planet. Space Sci.*, *49*, 1067.

Decker, D. T., B. V. Kozelov, B. Basu, J. R. Jasperse, and V. E. Ivanov (1996), Collisional degradation of the proton-H atom fluxes in the atmosphere : A comparison of theoretical techniques, *J. Geophys. Res.*, *101*, 26,947.

Delcourt, D. C., J. A. Sauvaud, R. F.-J. R. F., Jr. Martin, and T. E. Moore (1996), On the nonadiabatic precipitation of ions from the near-Earth plasma sheet, *J. Geophys. Res.*, *101*(A8), 17,409.

Dungey, J. W. (1961), Interplanetary magnetic field and the auroral zones, *Phys. Rev. Lett.*, *6*, 47.

Eastes, R. W. (2000), Modeling the $N_2$ Lyman-Birge-Hopfield bands in the dayglow : Including radiative and collisional cascading between the singlet states, *J. Geophys. Res.*, *105*, 18,557.

Eastes, R. W., and A. V. Dentamaro (1996), Collision-induced transitions between the $a^1\Pi_g$, $a'^1\Sigma_u^-$, and $w^1\Delta_u$ states of $N_2$ : Can they affect auroral $N_2$ Lyman-Birge-Hopfield band emissions ?, *J. Geophys. Res.*, *101*, 26,931.

Emery, B. A., D. S. Evans, M. S. Greer, K. Kadinsky-Cade, E. Holeman, F. J. Rich, and W. Xu (2006), The low energy auroral electron and ion hemispheric power after noaa and dmsp intersatellite adjustments, *NCAR Scientific and Technical Report, TN-470+STR (http ://cedarweb.hao.ucar.edu/instruments/str470.pdf).*

Emery, B. A., V. Coumans, D. S. Evans, G. A. Germany, M. S. Greer, E. Holeman, K. Kadinsky-Cade, F. J. Rich, and W. Xu (2007), Seasonal and kp variations in the auroral electron and ion hemispheric power after intersatellite adjustments, *submited to J. Geophys. Res.*

Ergun, R. E., et al. (1998), FAST satellite observations of electric field structures in the auroral zone, *Geophys. Res. Lett.*, *25*, 2025.

Evans, D. S., N. C. Maynard, J. Trøim, T. Jacobsen, and A. Egeland (1977), Auroral vector electric field and particle comparisons : 2. Electrodynamics of an arc, *J. Geophys. Res.*, *82*, 2235.

Fairfield, D. H., and J. D. Scudder (1985), Polar rain : Solar coronal electrons in the earth's magnetosphere, *J. Geophys. Res.*, *90*, 4055.

Fang, X., M. W. Liemohn, J. U. Kozyra, D. S. Evans, A. D. DeJong, and B. A. Emery (2007), Global 30-240 kev proton precipitation in the 17-18 april 2002 geomagnetic storms : 1. Patterns, *J. Geophys. Res.*, *112*, doi :10.1029/2006JA011867.

Fitzgerald, G. F. (1892), Sunspots and magnetic storms, *The Electrician*, *30*, 48.

Foster, J. C., J. M. Holt, R. G. Musgrove, and D. S. Evans (1986), Ionospheric convection associated with discrete levels of particle precipitation, *Geophys. Res. Lett.*, *13*, 656.

Frank, L. A., and J. D. Craven (1988), Imaging results from Dynamics Explorer 1, *Rev. Geophys.*, *26*, 249.

Frey, H., et al. (2003a), Summary of quantitative interpretation of IMAGE far ultraviolet auroral data, *Space Sci. Rev.*, *109*, 255.

Frey, H. U., S. B. Mende, C. W. Carlson, J.-C. Gérard, B. Hubert, J. Spann, R. Gladstone, and T. J. Immel (2001), The electron and proton aurora as seen by IMAGE-FUV and FAST, *Geophys. Res. Lett.*, *28*, 1135.

Frey, H. U., S. B. Mende, T. J. Immel, S. A. Fuselier, E. S. Claflin, J.-C. Gérard, and B. Hubert (2002), Proton aurora in the cusp, *J. Geophys. Res.*, *107*, doi : 10.1029/2001JA900161.

Frey, H. U., S. B. Mende, S. A. Fuselier, T. J. Immel, and N. Østgaard (2003b), Proton aurora in the cusp during southward imf, *J. Geophys. Res.*, *108*, 1277, doi : 10.1029/2003JA009861.

Frey, H. U., S. B. Mende, V. Angelopoulos, and E. F. Donovan (2004), Substorm onset observations by IMAGE-FUV, *J. Geophys. Res.*, *109*, doi :10.1029/2004JA010607.

Fuller-Rowell, T. J., and D. S. Evans (1987), Height-integrated Pedersen and Hall conductivity patterns inferred from the TIROS-NOAA satellite data, *J. Geophys. Res.*, *92*, 7606.

Fuller-Rowell, T. J., M. V. Codrescu, E. A. Araujo-Pradere, and I. Kutiev (1998), Progress in developing a storm-time ionospheric correction model, *Adv. Space Res.*, *22*, 821.

Fuselier, S. A., et al. (2001), Ion outflow observedby IMAGE : Implications for source regions and heating mechanisms, *Geophys. Res. Lett.*, *28*, 1163.

Galand, M., and A. D. Richmond (2001), Ionospheric electrical conductances produced by auroral proton precipitation, *J. Geophys. Res.*, *106*, 117.

Galand, M., R. G. Roble, and D. Lummerzheim (1999), Ionization by energetic protons in Thermosphere-Ionosphere Electrodynamics General Circulation Model, *J. Geophys. Res.*, *104*, 27,973.

Galand, M., T. J. Fuller-Rowell, and M. V. Codrescu (2001), Response of the upper atmosphere to auroral protons, *J. Geophys. Res.*, *106*, 127.

Gasda, S., and A. D. Richmond (1998), Longitudinal and interhemispheric variations of auroral ionospheric electrodynamics in a realistic geomagnetic field, *J. Geophys. Res.*, *103*, 4011.

Gjerloev, J. W., and R. A. Hoffman (2000a), Height-integrated conductivity in auroral substorms. 1. Data, *J. Geophys. Res.*, *105*, 215.

Gjerloev, J. W., and R. A. Hoffman (2000b), Erratum : Height-integrated conductivity in auroral substorms, 1. data, *J. Geophys. Res.*, *105*, 10,675.

Gjerloev, J. W., and R. A. Hoffman (2000c), Height-integrated conductivity in auroral substorms, 2. modeling, *J. Geophys. Res.*, *105*, 227.

Gladstone, G. R., et al. (2000), Stellar calibration of the WIC and SI imagers and the GEO photometer on IMAGE-FUV, *Eos Trans. AGU*, *81*(48), fall Meet. Suppl., Abstract SM72A-06.

Gonzales, W. D., and F. S. Mozer (1974), A quantitative model for the potential resulting from reconnection with an arbitrary interplanetary magnetic field, *J. Geophys. Res.*, *79*, 4186.

Gonzales, W. D., J. A. Joselyn, Y. Kamide, H. W. Kroehl, G. Rostoker, B. T. Tsurutani, and V. M. Vasyliunas (1994), What is a geomagnetic storm ?, *J. Geophys. Res.*, *99*, 5771.

Gérard, J.-C., B. Hubert, D. V. Bisikalo, and V. I. Shematovich (2000), A model of Lyman-$\alpha$ line profile in the proton aurora, *J. Geophys. Res.*, *105*, 795.

Gérard, J.-C., B. Hubert, M. Meurant, D. V. Bisikalo, V. I. Shematovich, H. U. Frey, S. B. Mende, G. R. Gladstone, and C. W. Carlson (2001), Observation of the proton aurora with IMAGE-FUV imager and simultaneous ion flux in-situ measurements, *J. Geophys. Res.*, *106*, 28,939.

Gérard, J.-C., B. Hubert, A. Grard, M. Meurant, and S. B. Mende (2004), Solar wind control of auroral substorm onset locations observed with the IMAGE-FUV imagers, *J. Geophys. Res.*, *109*, doi :doi :10.1029/2003JA010129.

Grodent, D. (2000), Modeling of the auroral thermal structure and morphology of Jupiter, Dissertation présentée en vue de l'obtention du grade de Docteur en Sciences.

Gvozdevsky, B. B., V. A. Sergeev, and K. Mursula (1997), Long lasting energetic proton precipitation in the inner magnetosphere after substorms, *J. Geophys. Res.*, *102*, 24,333.

Hardy, D. A., M. S. Gussenhoven, and E. Holeman (1985), A statistical model of auroral electron precipitation, *J. Geophys. Res.*, *90*, 4229.

Hardy, D. A., M. S. Gussenhoven, R. Raistrick, and W. J. McNeil (1987), Statistical and functional representations of the pattern of auroral energy flux, number flux, and conductivity, *J. Geophys. Res.*, *92*, 12,275.

Hardy, D. A., M. S. Gussenhoven, and D.Brautigam (1989), A statistical model of auroral ion precipitation, *J. Geophys. Res.*, *94*, 370.

Hardy, D. A., W. McNeil, M. S. Gussenhoven, and D. Brautigam (1991), A statistical model of auroral ion precipitation, 2, functional representation of the average patterns, *J. Geophys. Res.*, *96*, 5539.

Hecht, J. H., D. L. McKenzie, A. B. Christensen, D. J. Strickland, J. P. Thayer, and J. Watermann (2000), Simultaneous observations of lower thermospheric composition change during moderate auroral activity from Kangerlussuaq and Narsarsuaq, Greenland, *J. Geophys. Res.*, *105*, 27,109.

Hedin, A. E. (1987), MSIS-86 thermospheric model, *J. Geophys. Res.*, *92*, 4649.

Hedin, A. E. (1991), Extension of the MSIS thermosphere model into the middle and lower atmosphere, *J. Geophys. Res.*, *96*, 1159.

Heelis, R. A., J. D. Winningham, W. B. Hanson, and J. L. Burch (1980), The relationships between high-latitude convection reversals and the energetic particle morphology observed by Atmosphere Explorer, *J. Geophys. Res.*, *85*, 3314.

Henderson, M. G., G. D. Reeves, R. D. Belian, and J. S. Murphree (1996), Observations of magnetospheric substorms occurring with no apparent solar wind/IMF trigger, *J. Geophys. Res.*, *101*, 10,773, doi :10.1029/96JA00186.

Horwitz, J. L., J. R. Doupnik, and P. M. Banks (1978), Chatanika radar observations of the latitudinal distributions of auroral zone electric fields, conductivities, and currents, *J. Geophys. Res.*, *83*, 1463.

Hsu, T. S., and R. L. McPherron (2003), Occurrence frequencies of imf triggered and nontriggered substorms, *J. Geophys. Res.*, *108*, 1307, doi :10.1029/2002JA09442.

Hubert, B., J. C. Gérard, D. V. Bisikalo, V. I. Shematovich, and S. C. Solomon (2001), The role of proton precipitation in the excitation of the auroral FUV emissions, *J. Geophys. Res.*, *106*, 21,475.

Hubert, B., J. C. Gérard, D. S. Evans, M. Meurant, S. B. Mende, H. U. Frey, and T. J. Immel (2002), Total electron and proton energy input during auroral substorms : Remote sensing with IMAGE-FUV, *J. Geophys. Res.*, *107*(A8), 1183, doi : 10.1029/2001JA009229.

Hubert, B., J.-C. Gérard, A. Fuselier, and S. B. Mende (2003), Observation of dayside subauroral proton flashes with the IMAGE-FUV imagers, *Geophys. Res. Lett.*, *30*, 1145, doi :10.1029/2002GL016464.

Hubert, B., S. E. Milan, A. Grocott, C. Blockx, S. W. Cowley, , and J.-C. Gérard (2006), Dayside and nightside reconnection rates inferred from IMAGE FUV and Super Dual Auroral Radar Network data, *J. Geophys. Res.*, *111*, doi :10.1029/2005JA011140.

Hultqvist, B. (2002), Downward ion acceleration at auroral latitudes : Cause of parallel electric field, *Ann. Geophys.*, *20*, 1117.

Immel, T., J. Craven, and A. Nicholas (2000), An empirical model of the OI FUV dayglow from DE-1 images, *J. Atmos. Solar-Terr. Phys.*, *62*, 47.

Inhester, B., J. Untiedt, M. Segatz, and M. Kürschner (1992), Direct determination of the local ionospheric hall conductance distribution from two-dimensional electric and magnetic field data, *J. Geo-phys. Res.*, *97*, 4073.

Jacobsen, B., P. E. Sandholt, W. J. Burke, W. F. Denig, and N. C. Maynard (1995), Optical signatures of the prenoon auroral precipitation : Sources and responses to solar wind variations, *J. Geophys. Res.*, *100*, 8003.

Jayachandran, P. T., E. F. Donovan, J. W. MacDougall, D. R. Moorcroft, K. Liou, P. T. Newell, and J.-P. St-Mauri (2005), Global and local equatorward expansion of the ion auroral oval before substorm onsets, *J. Geophys. Res.*, *110*, doi :10.1029/2004JA010837.

Kamide, Y., and J. D. Winningham (1977), A statistical study of the 'instantaneous' nightside auroral oval : The equatorward boundary of the electron precipitation as observed by the Isis 1 and 2 satellites, *J. Geophys. Res.*, *82*, 5573.

Kan, J. R., and L. C. Lee (1979), Energy coupling functions and solar wind magnetosphere dynamo, *Geophys. Res. Lett.*, *6*, 577.

Kanik, I., L. W. Beegle, J. M. Ajello, and S. C. Solomon (2000), Electron-impact excitation/emission and photoabsorption cross sections important in the terrestrial airglow and auroral analysis of rocket and satellite observations, *Phys. Chem. Earth*, *25*, 573.

Kaufmann, R. L. (1987), Substorm currents - growth phase and onset, *J. Geophys. Res.*, *92*, 7471.

Klumpar, D. M., M. Boehm, R. J. Strangeway, C. W. Carlson, J. P. McFadden, and M. A. Temerin (2000), Structured proton precipitation : A particle source for discrete proton aurora, *Eos Trans. AGU*, *81*(48), Fall Meet. Suppl., Abstract SM11C-11.

Knight, S. (1973), Parallel electric field, *Planet. Space Sci.*, *21*, 741.

Knipp, D. J., et al. (1993), Ionospheric convection response to slow, strong variations in a northward interplanetary magnetic field : A case study for january 14, 1988, *J. Geophys. Res.*, *98*, 19,273.

Kosch, M. J., T. Hagfors, and K.Schlegel (1998), Extrapolating EISCAT Pedersen conductances to other parts of the sky using ground-based TV auroral images, *Ann. Geophys.*, *16*, 583.

Kullen, A., and T. Karlson (2004), On the relation between solar wind, pseudobreakups, and substorms, *J. Geophys. Res.*, *109*, doi :10.1029/2004JA010488.

Landau, L. D., and E. M. Lifshitz (1960), Mécanique, Volume 1, p. 126.

Lasen, K., and C. Danielsen (1978), Quiet time pattern of auroral arcs for different directions of the interplanetary magnetic field in the Y-Z plane, *J. Geophys. Res.*, *83*, 5277.

Lemaire, J., and M. Scherer (1974), Ionosphere-plasmasheet field-aligned currents and parallel electric fields, *Planet. Space Sci.*, *22*, 1485.

Lester, M., J. A. Davies, and S. Virdi (1996), High-latitude Hall and Pedersen conductances during substorm activity in the SUNDIAL-ATLAS campaign, *J. Geophys. Res.*, *101*, 26,719.

Liou, K., P. T. Newell, C.-I. Meng, A. T. Y. Lui, M. Brittnacher, and G. Parks (1997), Synoptic auroral distribution : A survey using Polar ultraviolet imagery, *J. Geophys. Res.*, *102*, 27,197.

Liou, K., P. T. Newell, C.-I. Meng, M. Brittnacher, and G. Parks (1998), Characteristics of the solar wind controlled auroral emissions, *J. Geophys. Res.*, *103*, 17,543.

Liou, K., P. T. Newell, C.-I. Meng, T. Sotirelis, M. Brittnacher, and G. Parks (1999), Source region of 1500 MLT auroral bright spots : Simultaneous Polar UV-images and DMSP particle data, *J. Geophys. Res.*, *104*, 24,587.

Liou, K., P. T. Newell, and C.-I. Meng (2001), Seasonal effects on auroral particle acceleration and precipitation, *J. Geophys. Res.*, *106*, 5531.

Lodge, O. (1900), Sun spots, magnetic storms, comets tails, atmospheric electricity, and aurorae, *Electrician*, *46*, 249.

Lu, G., A. Richmond, J. Ruohoniemi, R. Greenwald, M. Hairston, F. Rich, and D. Evans (2001), An investigation of the influence of data and model inputs on assimilative mapping of ionospheric electrodynamics, *J. Geophys. Res.*, *106*, 417.

Lu, G., et al. (1998), Global energy deposition during the january 1997 magnetic cloud event, *J. Geophys. Res.*, *103*, 11,685.

Lu, G. A. D. R., et al. (1994), Interhemispheric asymmetry of the high-latitude ionospheric convection pattern, *J. Geophys. Res.*, *99*, 6491.

Lui, A. T., S.-I. Akasofu, E. W. H. Jr., and S. J. Bame (1976), Observation of the plasma sheet during a contracted oval substorm in a prolonged quiet period, *J. Geophys. Res.*, *81*, 1415.

Lummerzheim, D., M. H. Rees, D. J. Craven, and L. A. Frank (1991), Ionospheric conductances derived from DE-1 auroral images, *J. Atm. Terr. Phys.*, *53*, 281.

Lummerzheim, D., M. Brittnacher, D. Evans, G. A. Germany, G. K. Parks, M. H. Rees, and J. F. Spann (1997), High time resolution study of the hemispheric power carried by energetic electrons into the ionosphere during the May 19/20, 1996 auroral activity, *Geophys. Res. Lett.*, *24*, 987.

Lundin, R., and I. Sandahl (1978), Some characteristics of the parallel electric field acceleration of electrons over discrete auroral arcs as observed from two rocket flights, in Symposium on European Rocket Research, ESA SP-135, p.125, Eur. Space Agency, Noordwijk, Netherlands.

Lyons, L. R. (1992), Formation of auroral arcs via magnetosphere-ionosphere coupling, *Rev. Geophys.*, *30*, 93.

Lyons, L. R. (1995), A new theory for magnetospheric substorms, *J. Geophys. Res.*, *100*, 19,069, doi :10.1029/95JA01344.

Lyons, L. R. (1996), Substorms : Fundamental observational features, distinction from other disturbances, and external triggering, *J. Geophys. Res.*, *101*, 13,011, doi : 10.1029/95JA01987.

Lyons, L. R., and D. S. Evans (1984), An association between discrete aurora and energetic particule boundaries, *J. Geophys. Res.*, *89*, 2395.

Lyons, L. R., D. S. Evans, and R. Lundin (1979), An observed relation between magnetic field aligned electric fields and downward electron energy fluxes in the vicinity of auroral forms, *J. Geophys. Res.*, *84*, 457.

Lysak, R. L. (1986), Coupling of the dynamic ionosphere to auroral flux tubes, *J. Geophys. Res.*, *91*, 7047.

Maeda, S., T. J. Fuller-Rowell, and D. S. Evans (1989), Zonally averaged dynamical and compositional response of the thermosphere to auroral activity during september 18-24, 1984, *J. Geophys. Res.*, *94*, 16,869.

Makita, K., C.-I. Meng, and S.-I. Akasofu (1983), The shift of the auroral electron precipitation boundaries in the dawn-dusk sector in the association with geomagnetic activity and interplanetary magnetic field, *J. Geophys. Res.*, *88*, 7967.

Marklund, G., L. Blomberg, C.-G. Fälthammer, and P.-A. Lindqvist (1994), On intense diverging electric fields associated with black aurora, *Geophys. Res. Lett.*, *21*, 1859.

Marklund, G., T. Karlsson, and J. Clemmons (1997), On low-altitude particle acceleration and intense electric fields and their relationship to black aurora, *J. Geophys. Res.*, *102*, 17,509.

Marov, M. Y., V. I. Shematovich, D. V. Bisikalo, and J.-C. Gérard (1997), Nonequilibrium processes in planetary and cometary atmosphere : Theory and applications.

Marsh, D. R., R. R. Garcia, D. E. Kinnison, B. A. Boville, F. Sassi, S. C. Solomon, and K. Matthes (2007), Modeling the whole atmosphere response to solar cycle changes in radiative and geomagnetic forcing, *J. Geophys. Res.*, *112*, in press, doi : 10.1029/2006JD008306.

Maynard, N. C., and A. J. Chen (1975), Isolated cold plasma regions : observations and their relation to possible production mechanisms, *J. Geophys. Res.*, *80*, 1009.

McComas, D. J., S. J. Bame, P. Barker, W. C. Feldman, J. L. Phillips, P. Riley, and J. W. Griffee (1998), Solar Wind Electron Proton Alpha Monitor (SWEPAM) for the Advanced Composition Explorer, *Space Sci. Rev.*, *86*, 563.

McFadden, J. P., C. W. Carlson, and R. E. Ergun (1999), Microstructure of the auroral acceleration region as observed by FAST, *J. Geophys. Res.*, *104* (14), 453.

McPherron, R. L. (1970), Growth phase of magnetospheric substorms (Magnetospheric substorms model modification for growth phase inclusion prior to explosive expansion phase), *J. Geophys. Res.*, *75*, 5592.

McPherron, R. L., C. T. Russel, and M. P. Aubry (1973), Satellite studies of magnetospheric substorms on augustus 15, 1968, *J. Geophys. Res.*, *78*, 3131.

Meier, R. R. (1991), Ultraviolet spectroscopy and remote sensing of the upper atmosphere, *Space Science Reviews*, *58*, 1.

Meinel, A. B. (1951), Doppler shifted auroral hydrogen emission, *Astrophys. J.*, *113*, 50.

Mende, S. B., R. R. Vondrak, R. H. Eather, M. H. Rees, and R. M. Robinson (1984), Optical mapping of ionospheric conductance, *J. Geophys. Res.*, *89*, 1757.

Mende, S. B., H. U. Frey, M. Lampton, J.-C. Gérard, B. Hubert, S. Fuselier, J. Spann, R. Gladstone, and J. L. Burch (2001), Global observations of proton and electron auroras in a substorm, *Geophys. Res. Lett.*, *28*, 1139.

Mende, S. B., H. U. Frey, T. J. Immel, D. G. Mitchell, P. C :son-Brandt, and J.-C. Gérard (2002), Global comparison of magnetospheric ion fluxes and auroral precipitation during a substorm, *Geophys. Res. Lett.*, *29*(12), 1609, doi :10.1029/2001GL014143.

Mende, S. B., et al. (2000a), Far ultraviolet imaging from the IMAGE spacecraft. 1. System design., *Space Science Reviews*, *91*, 243.

Mende, S. B., et al. (2000b), Far ultraviolet imaging from the IMAGE spacecraft. 2. Wideband FUV imaging, *Space Science Reviews*, *91*, 271.

Meurant, M., J.-C. Gérard, B. Hubert, C. Blockx, N. Østgaard, and S. Mende (2003a), Dynamics of global scale electron and proton precipitation induced by a solar wind pressure pulse, *Geophys. Res. Lett.*, *30*(20), 2032, doi :10.1029/2003GL018017.

Meurant, M., J.-C. Gérard, B. Hubert, V. Coumans, V. I. Shematovich, D. V. Bisikalo, D. S. Evans, G. R. Gladstone, and S. B. Mende (2003b), Characterization and dynamics of the auroral precipitation during substorms deduced from IMAGE-FUV, *J. Geophys. Res.*, *108*(A6), 1247, doi :10.1029/2002JA009685.

Milan, S. E., M. Lester, S. W. H. Cowley, K. Oksavik, M. Brittnacher, R. A. Greenwald, G. Sofko, and J.-P. Villain (2003), Variations in the polar cap area during two substorm cycles, *Ann. Geophys.*, *21*, 1121.

Milan, S. E., S. W. H. Cowley, M. Lester, D. M. Wright, J. A. Slavin, M. Fillingim, C. W. Carlson, and H. J. Singer (2004), Response of the magnetotail to changes in the open flux content of the magnetosphere, *J. Geophys. Res.*, *109*, doi :10.1029/2003JA010350.

Mozer, F. S., and A. Hull (2001), Origin and geometry of upward parallel electric fields in the auroral acceleration region, *J. Geophys. Res.*, *106*, 5763.

Nakano, S., T. Iyemori, and S. Yamashita (2002), Net field-aligned currents controlled by the polar ionospheric conductivity, *J. Geophys. Res.*, *107*, doi :10.1029/2001JA900177.

Newell, P. T., and C.-I. Meng (1994), Ionospheric projections of magneospheric regions under low and high solar wind pressure conditions, *J. Geophys. Res.*, *99*, 273.

Newell, P. T., Y. I. Feldstein, Y. I. Galperin, and C. I. Meng (1996a), Morphology of nightside precipitation, *J. Geophys. Res.*, *101*, 10,737.

Newell, P. T., C.-I. Meng, and K. M. Lyons (1996b), Suppression of discrete aurorae by sunlight, *Nature*, *381*, 766.

Newell, P. T., R. A. Greenwald, and J. M. Ruohoniemi (2001), The role of the ionosphere in aurora and space weather, *Rev. Geophys.*, *39*, 137.

Newell, P. T., K. Liou, J. P. Skura, and C.-I. Meng (2002), The distribution of auroral power increases and decreases, *Geophys. Res. Lett.*, *29*, 2209, doi :10.1029/2002GL016288.

Newell, P. T., S. Wing, T. Sotirelis, and C.-I. Meng (2005), Ion aurora and its seasonal variations, *J. Geophys. Res.*, *110*(A01215), doi :10.1029/2004JA010743.

Newell, P. T., T. Sotirelis, K. Liou, C.-I. Meng, and F. J. Rich (2007), A nearly universal solar wind-magnetosphere coupling function inferred from 10 magnetospheric state variables, *J. Geophys. Res.*, *112*, doi :10.1029/2006JA012015.

Newell, P. T. C.-I. M., and S. Wing (1998), Relation to solar activity of intense aurorae in sunlight and darkness, *Nature*, *393*, 342.

Olsen, N., T. J. Sabaka, and L. L. Tøffner-Clausen (2000), Determination of the IGRF 2000 model, *Earth Planets Space*, *52*, 1175.

Østgaard, N., J. Stadsnes, J. Bjordal, R. R. Vondrak, S. A. Cummer, D. L. Chenette, G. K. Parks, M. J. Brittnacher, and D. L. McKenzie (1999), Global-scale electron precipitation features seen in UV and X rays during substorms, *J. Geophys. Res.*, *104*, 10,191.

Østgaard, N., J. B. J Stadsnes and, R. R. Vondrak, S. A. Cummer, D. L. Chenette, M. Schultz, and J. G. Pronko (2000), Cause of the localized maximum of X-ray emission in the morning sector : A comparison with electron measurements, *J. Geophys. Res.*, *105*, 20,869.

Parks, G. K. (2004), Physics of space plasmas - An introduction, Westview Press, Perseus Books Group, Boulder and Oxford.

Perreault, P., and S.-I. Akasofu (1978), A study of geomagnetic storms, *Geophys. J. R. astr. Soc.*, *54*, 547.

Petrinec, S. M., and C. T. Russell (1996), Near-Earth magnetotail shape and size as determined from the magnetopause flaring angle, *J. Geophys. Res.*, *101*, 137, doi : 10.1029/95JA02834.

Petrukovich, A. A., W. Baumjohann, R. Nakamura, T. Mukai, and O. A. Troshichev (2000), Small substorms : Solar wind input and magnetotail dynamics, *J. Geophys. Res.*, *105*, 21,109, doi :10.1029/2000JA900057.

Rasmussen, C. E., R. W. Schunk, and V. B. Wickwar (1988), A photo-chemical equilibrium model for ionospheric conductivity, *J. Geophys. Res.*, *93*, 9831.

Rees, M. H. (1989), Physics and chemistry of the upper atmosphere, Cambridge Univ. Press, New York.

Rees, M. H., D. Lummerzheim, R. G. Roble, J. D. Winningham, J. D. Craven, and L. A. Frank (1988), Auroral energy deposition rate, characteristic electron energy, and ionospheric parameters derived from dynamics explorer, 1. images, *J. Geophys. Res.*, *93*, 12,841.

Richmond, A. D. (1995), Ionospheric electromagnetics using magnetic apex coordinates, *J. Geomagn. Geoelectr.*, *47*, 191.

Richmond, A. D., Y. Kamide, and S.-I. Akasofu (1990), Global measures of ionospheric electrodynamic activity inferred from combined incoherent scatter radar and ground magnetometer observations, *J. Geophys. Res.*, *95*, 1061.

Richmond, A. D., et al. (1988), Mapping electrodynamic features of the high-latitude ionosphere from localized observations - combined incoherent-scatter radar and magnetometer measurements for january 18-19, 1984, *J. Geophys. Res.*, *93*, 5760.

Ridley, A. J. (2007), Effects of seasonal changes in the ionospheric conductances on magnetospheric field-aligned currents, *Geophys. Res. Lett.*, *34*, doi :10.1029/2006GL028444.

Rishbeth, H., and O. K. Garriott (1969), Introduction to ionospheric physics, Academic Press, New York and London.

Robinson, R. M., R. R. Vondrak, K. Miller, T. Dabbs, and D. Hardy (1987), On calculating ionospheric conductances from the flux and energy of precipitating electrons, *J. Geophys. Res.*, *92*, 2565.

Robinson, R. M., R. R. Vondrak, J. D. Craven, L. A. Frank, and K. Miller (1989), A comparison of ionospheric conductances and auroral luminosities observed simultaneously with the Chatanika radar and the DE 1 auroral imagers, *J. Geophys. Res.*, *94*, 5382.

Sandahl, I. (1995), Norrsken, Budbäre från rymden, Institutet för rymdfysik, Kiruna.

Sato, T. (1978), A theory of quiet auroral arcs, *J. Geophys. Res.*, *83*, 1042.

Schlegel, K. (1988), Auroral zone E-region conductivities during solar minimum derived from EISCAT data, *Ann. Geophys.*, *6*, 129.

Senior, C., J. R. Sharber, J. D. Winningham, O. de la Beaujardière, R. A. Heelis, D. S. Evans, M. Sugiura, and W. R. Hoegy (1987), E and F region study of the evening sector auroral oval : A Chatanika/Dynamics Explorer 2/NOAA 6 comparison, *J. Geophys. Res.*, *92*, 2477.

Sergeev, V., E. M. Sazhina, N. A. Tsyganenko, J. A. Lundblad, and F. S. raas (1983), Pitch-angle scattering of energetic protons in the magnetotail current sheet as the dominant source of their isotropic precipitation into the nightside ionosphere, *Planet. Space Sci.*, *31*, 1147.

Sergeev, V., M. Malkov, and K. Mursula (1993), Testing the isotropic boundary algorithm method to evalueat the magnetic field configuration in the tail, *J. Geophys. Res.*, *98*, 7609.

Sergeev, V. A., P. Tanskanen, K. Mursula, A. Korth, and R. C. Elphic (1990), Current sheet thickness in the near-Earth plasma sheet during substorm growth phase, *J. Geophys. Res.*, *95*, 3819.

Sergeev, V. A., G. R. Bikkuzina, and P. T. Newell (1997), Dayside isotropic precipitation of energetic protons, *Ann. Geophys.*, *15*, 1233.

Shelley, E. G., et al. (1995), The Toroidal Imaging Mass-Angle Spectrograph (TIMAS) for the POLAR mission, *Space Science Reviews*, *71*, 497.

Shue, J.-H., P. T. Newell, K. Liou, and C.-I. Meng (2002), Solar wind density and velocity control of auroral brightness under normal interplanetary magnetic field conditions, *J. Geophys. Res.*, *107*, 1428, doi :10.1029/2001JA009138.

Shukhtina, M. A., N. P. Dmitrieva, and V. A. Sergeev (2004), Quantitative magnetotail characteristics of different magnetospheric states, *Ann. Geophys.*, *22*, 1019.

Shukhtina, M. A., N. P. Dmitrieva, N. G. Popova, V. A. Sergeev, A. G. Yahnin, and I. V. Despirak (2005), Observational evidence of the loading-unloading substorm scheme, *Geophys. Res. Lett.*, *32*, doi :10.1029/2005GL023779.

Smith, C. W., J. L'Heureux, N. F. Ness, M. H. Acuna, L. F. Burlaga, and J. Scheifele (1998), The ACE magnetic fields experiments, *Space Sci. Rev.*, *86*, 613.

Solomon, S. C. (2001), Auroral particule transport using monte carlo and hybrids methods, *J. Geophys. Res.*, *106*, 107.

Solomon, S. C., P. B. Hays, and V. Abreu (1988), The auroral 6300 Å emission : observation and modeling, *J. Geophys. Res.*, *93*, 9867.

Spann, J. F., M. Brittnacher, R. Elsen, G. A. Germany, and G. K. Parks (1998), Initial response and complex polar cap structures of the aurora in response to the January 10, 1997 magnetic cloud, *Geophys. Res. Lett.*, *25*, 2577.

Spiro, R. W., P. H. Reiff, and L. J. Maher (1982), Precipitating electron energy flux and auroral zone conductances - an empirical model, *J. Geophys. Res.*, *87*, 8215.

Stolarski, R. S. (1972), Analytic approach to photoelectron transport, *J. Geophys. Res.*, *77*, 2862.

Strickland, D. J., R. E. Daniell, J. R. Jasperse, and B. Basu (1993), Transport-theoretic model for the electron-proton-hydrogen atom aurora 2. Model results, *J. Geophys. Res.*, *98*, 21,533.

Torr, M. R., et al. (1995), A far ultraviolet imager for the international solar-terrestrial physics mission, *Space Sci. Rev.*, *71*, 329.

Tsurutani, B. T., et al. (2001), Auroral zone dayside precipitation during magnetic storm initial phases, *J. Atmos. Sol. Terr. Phys.*, *63*, 513.

Tsyganenko, N. (), Quantitative models of the magnetospheric magnetic field : methods and results, *Space Sci. Rev.*, *54*.

Tsyganenko, N. A. (2002), A model of the near magnetosphere with a dawn-dusk asymmetry : 2. Parameterization and fitting to observations, *J. Geophys. Res.*, *107*, 1176, doi :10.1029/2001JA000220.

Vallance-Jones, A., F. Creutzberg, R. L. Gattinger, and F. A. Harris (1982), Auroral studies with a chain of meridian scanning photometers, 1, Observations of proton and electron aurora in magnetospheric substorms, *J. Geophys. Res.*, *87*, 4489.

Vasyliunas, V. M., J. R. Kan, G. L. Siscoe, and S.-I. Akasofu (1982), Scaling relations governing magnetospheric energy transfer, *Planet. Space Sci*, *30*, 359.

Vegard, L. (1939), Hydrogen showers in the auroral region, *Nature*, *144*, 1089.

Vickrey, J. F., R. R. Vondrak, and S. J. Matthews (1981), The diurnal and latitudinal variation of auroral zone ionospheric conductivity, *J. Geophys. Res.*, *86*, 65.

Vickrey, J. F., R. R. Vondrak, and S. J. Matthews (1982), Energy deposition by precipitating particles and joule dissipation in the auroral ionosphere, *J. Geophys. Res.*, *87*, 5184.

Volland, H. (1973), A semiempirical model of large-scale magnetospheric electric fields, *J. Geophys. Res.*, *78*, 171.

Vondrak, R. R., and R. M. Robinson (1985), Inference of high-latitude ionization and conductivity from AE-C measurements of auroral electron fluxes, *J. Geophys. Res.*, *90*, 7505.

Voronkov, I., E. Friedrich, and J. C. Samson (1999), Dynamics of the substorm growth phase as observed using CANOPUS and SuperDARN instruments, *J. Geophys. Res.*, *104*, 28,491.

Wallis, D. D., and E. E. Budzinski (1981), Empirical models of height integrated conductivities, *J. Geophys. Res.*, *86*, 125.

Weimer, D. R. (2004), Correction to "predicting interplanetary magnetic field (IMF) propagation delay times using the minimum variance technique", *J. Geophys. Res.*, *109*, doi :10.1029/2004JA010691.

Weimer, D. R., D. M. Ober, N. C. Maynard, W. J. Burke, M. R. Collier, D. J. McComas, N. F. Ness, and C. W. Smith (2002), Variable time delays in the propagation of the interplanetary magnetic field, *J. Geophys. Res.*, *107*, 1211, doi :10.1029/2001JA009102.

Weimer, D. R., D. M. Ober, N. C. Maynard, M. R. Collier, D. J. McComas, N. F. Ness, C. W. Smith, and J. Watermann (2003), Predicting interplanetary magnetic field (IMF) propagation delay times using the minimum variance technique, *J. Geophys. Res.*, *108*, 1026, doi :10.1029/2002JA009405.

Wygant, J. R., R. B. Torbert, and F. S. Mozer (1983), Comparison of the S3-3 polar cap potential drops with the interplanetary magnetic field and models of magnetopause reconnection, *J. Geophys. Res.*, *88*, 5727.

Zelenyi, L., A. Galeev, and C. F. Kennel (1990), Ion precipitation from the inner plasma sheet due to stochastic diffusion, *J. Geophys. Res.*, *95*, 3871.

Zhou, X., and B. T. Tsurutani (1999), Rapid intensification and propagation of the dayside aurora : Large scale interplanetary pressure pulses (fast shocks), *Geophys. Res. Lett.*, *26*, 1097.

Zhou, X.-Y., R. J. Strangeway, P. C. Anderson, D. G. Sibeck, B. T. Tsurutani, G. Haerendel, H. U. Frey, and J. K. Arballo (2003), Shock aurora : FAST and DMSP observations, *J. Geophys. Res.*, *108*(A4), 8019, doi :10.1029/2002JA009701.